

# The Dynamics of Non-Equilibrium Gliding in Flying Snakes

Isaac J. Yeaton

Dissertation submitted to the Faculty of the  
Virginia Polytechnic Institute and State University  
in partial fulfillment of the requirements for the degree of

Doctor of Philosophy  
in  
Mechanical Engineering

Shane D. Ross, Chair  
John J. Socha, Co-Chair  
Mark R. Paul  
Nicole T. Abaid  
Craig A. Woolsey

February 13, 2018  
Blacksburg, Virginia

Keywords: Flying snake, animal locomotion, gliding flight, dynamical systems

Copyright 2018, Isaac J. Yeaton

# The Dynamics of Non-Equilibrium Gliding in Flying Snakes

Isaac J. Yeaton

## Academic Abstract

This dissertation addresses the question, how and why do ‘flying’ snakes (*Chrysopelea*) undulate through the air? Instead of deploying paired wings or wing-like surfaces, flying snakes jump, splay their ribs into a bluff-body airfoil, and undulate through the air. Aerial undulation is the dominant feature of snake flight, but its effects on locomotor performance and stability are unknown. Chapter 2 describes a new non-equilibrium framework to analyze gliding animals and how the pitch angle affects their translational motion. Chapter 3 combines flying snake glide experiments and detailed dynamic modeling to address what is aerial undulation and how each kinematic component affects rotational stability and translational performance. Chapter 4 combines the kinematic data of Chapter 3, with elements of the non-equilibrium framework of Chapter 2, to examine the kinematics of snake flight in greater detail. This chapter also tests if our current understanding of flying snake aerodynamics is sufficient to explain the observed center of mass motion.

This work was partially supported by the National Science Foundation under grants 1351322, 1150456, and 0966125.

# The Dynamics of Non-Equilibrium Gliding in Flying Snakes

Isaac J. Yeaton

## General Audience Abstract

Flying snakes can move unlike any other flying or slithering animal. Flying snakes have evolved the ability to glide safely to the ground by undulating through the air. Flapping flyers, like birds, bats, and insects, move through the air using wings and powerful flight muscles. In contrast, gliding animals fall through the air, using gravity to increase their speed, and air resistance to produce lift and drag forces such that they move over the ground. Flying snakes glide by jumping, flattening their bodies (similar to a cobra hooding), and undulating through the air using an ‘S’-shaped body. This dissertation addresses the question, how and why do flying snakes undulate through the air? First, I describe a new mathematical analysis of gliding animals, which provides a framework to understand how an animal’s size and orientation to the oncoming airflow affect its glide performance. Second, I describe glide experiments where the bodies of flying snakes were measured as they flew through a large indoor glide arena. From these measurements, we quantified how the body bends in the horizontal and vertical directions. Next, I describe a detailed mathematical model used to test how the different body configurations we measured affect glide performance and flight stability. The model results indicate that flying snakes likely use aerial undulation to stabilize their rotational motion. Third, I tested if our current measurements of the lift and drag properties of flying snakes, based on the quasi-steady assumption, can account for the trajectories we recorded. The force analysis suggests that flying snakes produce more force than the quasi-steady assumption can account for, and that future work is needed to understand unsteady aerodynamic mechanisms relevant for snake flight.

This work was partially supported by the National Science Foundation under grants 1351322, 1150456, and 0966125.

# Dedication

For Caitlin and Amayla.

# Acknowledgments

I would like to acknowledge the many people who have made this dissertation work possible. My advisors, Jake Socha and Shane Ross, were instrumental in encouraging me to ask broader scientific questions and to push my analyses farther. My committee members, Mark Paul, Nicole Abaid, and Craig Woolsey, provided valuable guidance throughout this whole process and were always encouraging. I owe a special thanks to my labmates for numerous discussions, assistance setting up and conducting experiments, and providing valuable feedback on my presentations and writing. From the Socha Biomechanics Lab, I would like to thank Grant Baumgartner, Hodjat Pendar, Talia Weiss, Sharri Zamore, Farid Jafari, Jack Whitehead, Michelle Graham, Catherine Twyman, Joel Garrett, Melissa Kenny, and Khaled Adjerid. From the Ross Dynamics Lab, I would like to thank Gary Nave, Shibabrat Naik, Peter Nolan, Kristen Tetreault, Jun Zhong, and Nathaniel Hall. Lastly, I would like to acknowledge the American tax payer for funding my stipend and scientific work.

This work was supported by NSF PHY (PoLS) grant 1351322 to co-Chair J.J.S., “CAREER: Gliding flight in snakes: How wingless gliders produce force, maintain stability, and maneuver,” NSF CMMI grant 1150456 to Chair S.D.R., “CAREER: Integrating Geometric, Probabilistic, and Topological Methods for Phase Space Transport in Dynamical Systems,” NSF DGE grant 0966125, “IGERT: MultiScale Transport in Environmental and Physiological Systems (MultiSTEPS),” Virginia Tech Biological Transport (BIOTRANS), Virginia Tech Institute for Creativity, Arts, and Technology (ICAT), Virginia Tech Center for the Arts, and Virginia Tech Graduate School Interdisciplinary Graduate Education Programs (IGEPs).

Isaac Yeaton  
Baltimore, MD  
February, 2018

# Contents

Title page . . . . .	i
Academic Abstract . . . . .	ii
General Audience Abstract . . . . .	iii
<b>Dedication</b>	<b>iv</b>
<b>Acknowledgments</b>	<b>v</b>
<b>Contents</b>	<b>vi</b>
<b>List of Figures</b>	<b>xiii</b>
<b>List of Tables</b>	<b>xxxv</b>
<b>1 Introduction</b>	<b>1</b>
1.1 Overview of flying snakes . . . . .	2
1.2 Dissertation overview . . . . .	3
References . . . . .	5
<b>2 Global dynamics of non-equilibrium gliding in animals</b>	<b>8</b>
Abstract . . . . .	8
2.1 Introduction . . . . .	9

2.2	Methods . . . . .	12
2.2.1	Rigid-body model equations of motion . . . . .	12
2.2.2	Dimensional analysis . . . . .	14
2.2.3	Rescaling and final equation form . . . . .	15
2.2.4	Equilibrium gliding . . . . .	16
2.2.5	Equilibria type and stability analysis . . . . .	17
2.2.6	Model input from experimentally measured lift and drag curves . . . . .	18
2.2.7	Model assumptions . . . . .	21
2.3	Results . . . . .	21
2.3.1	Structure of the velocity polar diagrams . . . . .	21
2.3.2	Pitch bifurcation diagrams . . . . .	23
2.3.3	Velocity polar diagrams from kinematics data . . . . .	26
2.4	Discussion . . . . .	31
2.4.1	Effect of lift and drag coefficients . . . . .	31
2.4.2	Comparison to other modeling studies of gliding . . . . .	32
2.4.3	Implications for animals that glide . . . . .	35
2.5	Conclusions . . . . .	36
	References . . . . .	37
<b>3</b>	<b>Undulation enhances stability, enabling gliding in flying snakes</b>	<b>42</b>
	Abstract . . . . .	42
	Significance statement . . . . .	43
3.1	Introduction . . . . .	43
3.2	Results and Discussion . . . . .	46
3.2.1	Flying snakes use orthogonal bending waves when gliding . . . . .	46

3.2.2	A new model of limbless flight . . . . .	50
3.2.3	Undulation enhances rotational stability, increasing glide performance	51
3.2.4	Dorsoventral bending controls pitching motion in flying snakes . . . .	55
3.2.5	Inertial maneuvering in flying snakes . . . . .	60
3.3	Conclusions . . . . .	62
	References . . . . .	62
<b>4</b>	<b>Body configuration and force production in flying snakes</b>	<b>66</b>
	Abstract . . . . .	66
4.1	Introduction . . . . .	67
4.2	Methods . . . . .	69
4.2.1	Measurements of snake kinematics . . . . .	69
4.2.2	Reconstructing the body position . . . . .	70
4.2.3	Center of mass motion . . . . .	73
4.2.4	Reconstructing the wing-body orientation . . . . .	74
4.2.5	Lift and drag forces . . . . .	75
4.2.6	Aerodynamic force errors . . . . .	76
4.2.7	Corrections to the lift and drag forces . . . . .	78
4.2.8	Gap and stagger . . . . .	78
4.2.9	Gap and stagger from previous kinematic measurements . . . . .	79
4.2.10	Assumptions . . . . .	80
4.3	Results . . . . .	81
4.3.1	Center of mass motion . . . . .	81
4.3.2	Lift and drag forces . . . . .	84
4.3.3	Aerodynamic force errors and corrections . . . . .	85

4.3.4	Lift and drag distributions . . . . .	85
4.3.5	Gap and stagger . . . . .	92
4.4	Discussion . . . . .	96
4.4.1	Center of mass motion . . . . .	96
4.4.2	Lift and drag forces . . . . .	97
4.4.3	Gap, stagger, and airflow orientation . . . . .	98
4.4.4	Future work . . . . .	99
4.5	Conclusions . . . . .	100
	References . . . . .	100
<b>5</b>	<b>Conclusions</b>	<b>104</b>
5.1	Future work . . . . .	106
5.1.1	Non-equilibrium framework of gliding . . . . .	106
5.1.2	Dynamic model of snake flight . . . . .	106
5.1.3	Flying snake kinematic experiments . . . . .	109
5.1.4	Additional flying snake measurements . . . . .	109
	References . . . . .	111
<b>Appendix A <i>Supplemental Information</i> – Global dynamics of non-equilibrium gliding in animals</b>		<b>113</b>
	Code repository . . . . .	113
A.1	Linear stability analysis . . . . .	113
A.2	Conversion between dimensional, non-dimensional, and rescaled quantities . . . . .	114
A.3	Velocity polar diagram when $C_L$ and $C_D$ are constant . . . . .	116
A.4	Kinematic lift and drag coefficient curves . . . . .	118
A.5	Numerical implementation of Velocity Polar Diagrams . . . . .	122

A.6	Stability Analysis and Terminal Velocity Manifold Computation . . . . .	122
A.6.1	Expansion about the equilibrium . . . . .	123
A.6.2	Hopf bifurcation case . . . . .	128
A.6.3	Stable node case . . . . .	132
A.6.4	Saddle case . . . . .	134
A.6.5	Terminal velocity manifold as slow manifold . . . . .	140
A.6.6	Acceleration along the terminal velocity manifold . . . . .	141
	References . . . . .	142

**Appendix B *Supporting Information* – Undulation enhances stability, enabling gliding in flying snakes** **143**

B.1	Flying snake glide experiments . . . . .	143
B.2	3D data processing . . . . .	145
B.2.1	Complex orthogonal decomposition . . . . .	146
B.2.2	Quantifying aerial undulation . . . . .	147
B.3	Snake morphometrics . . . . .	149
B.4	Theoretical model of snake flight . . . . .	149
B.4.1	Kinematic model — Aerial serpenoid curve . . . . .	150
B.4.2	Airfoil coordinate system . . . . .	151
B.4.3	Dynamic model — Variable-geometry rigid-body formulation . . . . .	152
B.4.4	Orientation of the body . . . . .	153
B.4.5	Aerodynamic lift and drag . . . . .	156
B.4.6	Extending the lift and drag coefficients . . . . .	157
B.4.7	Complete dynamical model . . . . .	159
B.4.8	Glide simulations . . . . .	159

B.4.9	Simulation initial conditions . . . . .	159
	References . . . . .	168
<b>Appendix C</b>	<b>Reconstructing the flying snake from motion capture data</b>	<b>170</b>
C.1	Overview of data processing . . . . .	170
C.2	Trial selection using trajectory summary plots . . . . .	171
C.3	Gap filling with Kalman filters . . . . .	183
C.4	Butterworth filtering and filter cutoff frequency calculation . . . . .	186
C.4.1	Ball drop experiments to test cutoff frequency calculation and error in the measurement system . . . . .	188
C.5	Global natural cubic spline fitting to the snake’s body . . . . .	193
C.5.1	Spline evaluation . . . . .	194
C.6	Linear mass distribution and calculating center of mass . . . . .	200
C.6.1	Sectioning measurements . . . . .	200
C.6.2	Analysis of linear mass distribution data . . . . .	201
C.6.3	Smoothed mass density used in the dynamical model . . . . .	201
C.7	Flying snake morphometrics . . . . .	209
C.8	Performance comparison between Cube trials and previous flying snake ex- periments from Socha (2005) . . . . .	210
C.9	Effect of missing data . . . . .	213
	References . . . . .	218
<b>Appendix D</b>	<b>Variable-geometry rigid-body model of snake flight</b>	<b>219</b>
D.1	Dynamic model . . . . .	219
D.1.1	Overview . . . . .	219
D.1.2	Conservation of linear momentum . . . . .	222

D.1.3	Conservation of angular momentum . . . . .	223
D.1.4	Alternative derivation of the moment equation . . . . .	223
D.1.5	Matrix formulation . . . . .	224
D.1.6	Initial conditions . . . . .	226
D.1.7	General form of Euler’s equation . . . . .	227
D.1.8	Center of pressure . . . . .	229
D.2	Effects of snake size and undulation frequency on glide dynamics . . . . .	230
D.3	Effects of corrected lift and drag forces on glide dynamics and stability . . .	236
	References . . . . .	241

# List of Figures

- 2.1 Construction of the velocity polar diagram. (a)–(d) Time histories of position, velocity, acceleration, and glide angle from one simulated glide. The solid circle denotes the location of maximum glide angle, marking the end of the ballistic phase. The open circle denotes an increase in acceleration near the end of the trajectory. The dashed line in (d) indicates the equilibrium glide angle,  $\gamma^*$ . (e) Horizontal ( $x$ ) and vertical ( $z$ ) glide path of the simulated glider, where equally spaced points in time are indicated by the ‘x’ markers, and arrows indicate the direction of forward travel. (f) Schematic of the rigid-body glider model with pitch control analyzed and simulated in this study. (g) Velocity polar diagram, with the simulated trajectory overlaid in black and motion in forward time indicated by the arrow on the trajectory. Gray lines indicate trajectories with different initial conditions of velocity. The end of the ballistic phase occurs when the velocity trajectory transitions onto the terminal velocity manifold. The terminal velocity manifold is surrounded by a low acceleration magnitude region,  $\sqrt{a_x^2 + a_z^2} < 0.1 \text{ g}$ , indicated by the purple shading. The animal accelerates along the manifold, indicated by loss of shading and denoted with the open circle. The stable equilibrium is denoted by the blue circle; the equilibrium glide angle is the angle subtended between the horizontal axis and a line from the origin to the equilibrium point. The empty wedge-shaped area results from of the angle of attack limitations of the experimentally measured lift and drag coefficients (see Supplemental Information). . . . . 13

2.2	Pitch as a bifurcation parameter. Increasing the body pitch angle $\theta$ shifts the lift-to-drag ratio curves horizontally to the left, which changes the number of intersections with $\cot \gamma$ . Each intersection is an equilibrium point, which are indicated by round markers at the intersection points for varying pitch angles. Force coefficient data are for a flying snake cross-sectional shape [14] at $Re=11,000$ . . . . .	16
2.3	Summary of equilibrium type as a function of lift and drag curves. The equilibrium type is uniquely determined by the lift and drag curves and their slopes evaluated at the equilibrium angle of attack. Previous models of animal gliding, which assumed constant lift and drag coefficients, only observed stable node and stable focus type equilibrium points, as indicated by the horizontal gray line. . . . .	17
2.4	Lift, drag, and lift-to-drag ratio coefficient curves used in this study. Airfoil-based curves for (a) flying squirrels [35], (b) flying snakes [14], and (c) chukar partridge [44], and whole-animal curves for (d) sugar gliders [42], (e) dragonflies [45], and (f) flying fish [43]. Measured values are indicated with markers, and spline-fit values are indicated with solid lines. . . . .	20
2.5	Caption on next page. . . . .	24
2.5	(Previous page.) Velocity polar diagrams. Two different pitch values, indicated by (i) and (ii), are shown for (a) flying squirrels, (b) flying snakes, (c) chukar partridge, (d) sugar gliders, (e) dragonflies, and (f) flying fish. Pitch values are specified by vertical lines in figure 2.6. Gray lines are simulated glide trajectories, and arrows indicate motion along the trajectory through time. Equilibrium gliding is indicated by circle markers, and the glide angle is read as the angle subtended from the horizontal axis as before to the equilibrium point(s). Saddle points and their stable and unstable branches are indicated in red, with separatrices running vertically to the saddle points. The inset in (bii) shows 2 <sup>nd</sup> and 3 <sup>rd</sup> -order accurate analytical approximations of the terminal velocity manifold in the vicinity of the saddle point equilibrium. Vertical velocity nullclines, where the vertical acceleration is zero, are shown in (bi), (ci), and (cii), as the solid purple line passing though the equilibrium points and near the terminal velocity manifold. . . . .	25

2.6	Caption on next page. . . . .	27
2.6	(Previous page.) Pitch bifurcation diagrams for equilibrium glide angle $\gamma^*$ as pitch angle $\theta$ varies. Diagrams correspond to (a) flying squirrels, (b) flying snakes, (c) chukar partridge, (d) sugar gliders, (e) dragonflies, and (f) flying fish. Equilibrium glide angles are found as intersection(s) of the bifurcation curve with vertical lines at a specified pitch angle, with multiple intersections indicating multiple equilibrium points. Colors correspond to different equilibrium types; cool colors are locally attracting and warm colors are locally repelling. Vertical lines indicate pitch angles used in the velocity polar diagrams in figure 2.5, and the arrows on these lines indicate the passive directional change of glide angle. Not all angles of attack were available in the original data; these regions are indicated with gray shading. . . . .	28
2.7	Caption on next page. . . . .	29
2.7	(Previous page.) Non-equilibrium glide framework applied to kinematics data of flying squirrels from ref. [26]. (a) Aerodynamic coefficients derived from an ensemble of kinematics measurements. Solid points are mean $\pm$ s.e.m. (b) Pitch bifurcation diagram. (ci, cii) Velocity polar diagrams at zero and positive pitch angles, respectively. The closed contour in (ci) is a periodic orbit due to a Hopf bifurcation. (d, e) Velocity polar diagrams derived from individual glide trials. The calculated velocity trajectory is indicated in blue and equal time points are indicated at 0.08 s intervals. Note that all velocity polar diagrams have the same limits because the kinematics data have been non-dimensionalized and rescaled. . . . .	30
2.8	Universal glide scaling parameter $\epsilon$ for gliding animals. Mammalian data for flying squirrels, sugar gliders, and colugos are from refs. [26, 27, 36, 47, 54], <i>Draco</i> data are from refs. [28, 29], flying fish ( <i>Cypselurus hiraii</i> ) data are from ref. [43], dragonfly ( <i>Sympetrum sanguine</i> ) data are from ref. [45], flying squid ( <i>Sthenoteuthis ptrepus</i> ) data are from ref. [22, 55], and flying snake ( <i>Chrysopelea paradisi</i> ) data are from refs. [8, 9, 22]. . . . .	34

3.1	Measurements of gliding in snakes. (A) The flying snake, <i>Chrysopelea paradisi</i> , in the mid-glide posture, with a flattened body and infrared (IR) markers placed along the dorsal surface and tail. (B) The body's flattened cross-sectional shape when gliding [13]. (C) Front view of the glide arena from the top of the launch platform. The floor is covered with white foam padding and a tree is placed in the center to encourage jumps. Motion capture cameras are placed around the perimeter. Photo courtesy of Mike Diersing. (D) Morphing wing-body seen from snapshots of an overhead view of aerial undulation as the snake glides through the indoor glide arena. Motion is from bottom to top, with the snake appearing smaller as it moves away from the camera. (E) Side view of a <i>C. paradisi</i> glide showing the out-of-plane twisting at the 'U'-bends due to the vertical wave, indicated by the white oval. . . . .	45
3.2	Caption on next page. . . . .	47

3.2 (Previous page.) Measured body kinematics in flying snakes. (A) Horizontal and vertical bending waves with the overhead view of snake’s backbone (B) near halfway through a glide. The large-amplitude flat-top horizontal wave and the small-amplitude vertical wave travel together down the body. The vertical wave has twice the spatial and temporal frequencies as the horizontal wave. Zero crossings of the horizontal wave (red markers) correspond to ‘U’-bend of the snake, as well as peaks in the vertical wave (black markers). (C and D) Space-time bending plots showing the traveling waves of bending. The time-point indicated in (A) and (B) is denoted by the vertical lines. (E-H) Results of the complex orthogonal decomposition analysis to quantify the spatial and temporal characteristics of aerial undulation. (E) Ratios of temporal and spatial frequencies of the horizontal and vertical waves. The black ‘+’ is the overall average, indicating that the vertical wave has twice the spatial and temporal frequencies as the horizontal wave. (F) The average horizontal wave amplitude is tightly coupled with the number of spatial periods of the horizontal wave (gray line). Individual glides from seven different animals are shown with small colored markers and individual averages are shown with large markers and one standard deviation bars. The size of the average marker indicates the snake’s mass. (G) Average vertical wave amplitude vs. number of spatial periods of the horizontal wave. (H) Average dorsoventral bending angle (out-of-plane gross body bending) is not coupled with the number of spatial periods of the horizontal wave, but is non-zero, indicating that the flying snakes body is not always parallel to the ground while gliding. (I and J) Definition of the local horizontal and vertical bending angles shown from the top and side view of the snake. The horizontal angle,  $\theta$ , is defined as the angle between the blue unit vector in the  $-\hat{y}$  direction and the projection of the yellow tangent vector into the horizontal plane (black vector). The local vertical bending angle,  $\psi$ , is the angle between the yellow tangent vector and the horizontal projection. On the snake images, the gray markers indicate the location of the IR markers, dark green is the dorsal surface, and yellow-green is the ventral surface. (K) Definition of the dorsoventral bending angle as the slope of the best-fit line (black) to the vertical wave amplitude (yellow) as a function of distance along the body. . . . .

3.3	<p>Simulated flying snake glides. (A) Horizontal wave shape space used for simulated glides. Gray and black boxes indicate counts (one or two, respectively) of experimentally observed body shapes (figure 3.2F). The shape space is naturally demarcated along the diagonal of observed body shape, “open” shapes in the lower left, and “closed” shapes in the upper right. The different regions are separated by the black borders. (B) Height fallen during short glides before becoming unstable with no undulation. A ‘10’ denotes a stable glide, and the black borders demarcate the observed body shapes observed in the kinematic measurements. Many shapes within the observed diagonal are unstable. (C) Height fallen during short glides before becoming unstable with undulation. Undulation improves the stability properties of shapes within the observed region. (D) Horizontal glide distance without undulation. (E) Horizontal glide distance with undulation. Undulation generally increases the glide distance, especially within the observed region. . . . .</p>	54
3.4	<p>Caption on next page. . . . .</p>	58

3.4 (Previous page.) Effect of dorsoventral bending,  $d_\psi$ , on glide dynamics and controlling pitching motion. (A) Side views of simulated snake kinematics, where motion would be from left to right, for  $d_\psi$  ranging from  $-20^\circ$  to  $20^\circ$  and a vertical wave amplitude  $\psi_m=20^\circ$  (same as for glides in figure 3.3). The head of the snake is indicated with the green circle. Negative  $d_\psi$  causes the posterior body to fall below the head (“tail down”); both negative a positive values are seen in snake glides. (B) Side view of the center of mass trajectory, where colors indicate different  $\nu_\theta$  and  $\theta_m$  combinations (see (E) for the color key). The performance peaks at  $d_\psi=10^\circ$ , and is worst at  $d_\psi=20^\circ$ . The stability is worst for  $-20^\circ$ , as some glides do not reach the ground. (C) Pitch angle during full simulations vs. normalized time (physical time multiplied by the undulation frequency). Most glides pitch down, especially for negative dorsoventral bending. Best performing glides occur for  $d_\psi$  of  $10^\circ$ , where the pitch angle is near zero. (D) Terminal landing position vs. phased-averaged pitch moment for different dorsoventral bending angles and number of spatial periods. Dorsoventral bending has a large effect on the glide performance by affecting the pitch moment. (E and F) The effect of the number of spatial periods and dorsoventral bending on the phase-averaged pitch moment. (E) Different colored lines indicate different  $d_\psi$  combinations, while colored points indicate different  $\nu_\theta$  and  $\theta_m$  combinations along the best-fit line of figure 3.2F. The sign of the pitch moment depends on the dorsoventral bending angle, while the magnitude depends on the number of spatial periods. (F) Alternative view of (E), where lines indicate different  $\nu_\theta$  and  $\theta_m$  combinations. The point of zero pitch moment occurs for positive  $d_\psi$  and is indicated by the black oval. Varying  $d_\psi$  is more effective than varying  $\nu_\theta$  to change the sign and amplitude of the pitch moment. . . . .

3.5	<p>Inertial maneuverability in flying snakes. (A) Aerodynamic pitch, roll, and yaw moments from the phase averaging analysis (Eq. 3.2.5). Periodic traces indicate the moment time series for one phase, while gray bands indicate the extrema for all phases. The magnitude increases with time because the speed increases as the simulated snake falls due to gravity. The black line is the phase-averaged pitch moment (used in figure 3.4D-F), which is non-zero. The phase-averaged roll and yaw moments are always zero. (B) Inertial moments from the phase averaging analysis. The extrema do not change with time because inertial moments are independent of the animal’s speed. (C) Relative contribution of inertial-to-aerodynamic moments (the peak-to-peak ratio of the moment time series) throughout a glide for different dorsoventral bending angles and number of spatial periods, with the vertical wave amplitude constant at 20°. Colors indicate different <math>\nu_\theta</math> combinations and are the same as in figure 3.4. The black line is the parameter combination of <math>\nu_\theta</math> and <math>d_\psi</math> shown in (A) and (B). Inertial moments always dominate at the beginning of the glide. Inertial yaw moments always dominate, suggesting a mechanism of maneuvering. . . . .</p>	61
4.1	<p>Indoor glide arena and glide trial experiments. (A) View of the “Cube”, showing the blackbox theatre equipped with launch platform, high-speed motion capture cameras, and target tree. (B,C) Rear and top views of the motion capture camera coverage cones. The IR marker trajectories for one trial are shown, with the jump and landing locations indicated by the red markers. (D) <i>C. paradisi</i> in an ‘S’-shaped glide posture. The flattened body and airfoil cross-sectional shape twist along the body. The infrared markers are shown along the dorsal surface of the animal. . . . .</p>	70

4.2	Method of reconstructing the morphing wing-body of flying snakes from recorded infrared marker (IR) trajectories. Each image shows the reconstruction step from one trial at the same time instance. (A) The measured IR markers provide a discrete representation of the body. (B) Cubic splines are fit to the IR markers, providing a continuous representation. (C) The tangent vector, $\hat{T}$ , is used, along with the vertical direction, to define the airfoil coordinate system in (D). The width of the body is taken to define the chord-line, $\hat{C}$ , and $\hat{B}$ points upward through the backbone. (E) Mass distribution overlaid on the spline, visualized as spherical markers with radius proportional to the mass. The head and mid-body are relatively more massive; the tail only accounts for $\approx 9\%$ of the animal mass. (F) Complete reconstruction of the morphing wing-body, showing the <i>C. paradisi</i> cross section overlaid on the spline, incorporating the orientation from (D) and the width distribution. . . . .	71
4.3	Quasi-steady aerodynamics and gap and stagger calculations. (A) Quasi-steady lift and drag coefficients for different angles of attack and Reynolds number, based on Holden et al. (2014). The coefficients for $\alpha > 60^\circ$ are polynomial extrapolations such that the lift and drag coefficients match a triangular bluff body at $\alpha = 90^\circ$ [90, 91]. (B) Simple sweep theory and sweep angle calculation. The perpendicular velocity component is used in the force calculations, and is found by removing the velocity component parallel to the local tangent direction. (C) Definition of gap, stagger, and angle of attack of the snake in the trajectory reference frame. Gap is the horizontal spacing and stagger is the vertical spacing. Both the front and rear airfoils have different angles of attack, sweep angles, and different local velocities. (D,E) Two time instances from a glide showing intersections of the body with the plane through the center of mass. The location of these intersections is used to calculate gap and stagger. The body is rotated to the trajectory reference frame, with the center of mass velocity in the $+y$ -direction, denoted by the black arrow. The time point in (D) is from 53% through the glide, while (E) is from 90%. The dorsal surface is indicated in green and the ventral surface in yellow. . . . .	72
4.4	Caption on next page. . . . .	82

- 4.4 (Previous page.) Overview of trajectory dynamics for 43 trials from seven flying snakes. (A) Side view of the glide path in the straightened frame. Three of the panels are for three individuals that gave the greatest number of usable glides and spanned the entire mass range of snakes used. The last panel shows glides for four additional individuals. Different trials for each snake are indicated by different colors and the trial number is labelled. The first number of the trial identification is the day of testing. The best performing glides are trial 618 from snake 95 and trial 505 from snake 88. (B) Overhead view of the glide path showing the unfiltered center of mass position in the inertial frame. The glides are generally not straight and show broad arcing behavior. (C) Velocity polar diagrams of forward and vertical velocity in the straightened frame. The glide angle is the angle subtended from the horizontal downward. (D) Velocity polar diagrams that has been non-dimensionalized and rescaled to remove the effects of animal size. Velocity trajectories show a characteristic vertical portion during the ballistic phase, followed by an upward hook onto the terminal velocity manifold near a rescaled velocity of 1. The lightest snake (snake 95) progresses farthest on the diagram and had the best glide performance (in trial 618). . . . . 83
- 4.5 Aerodynamic force estimates and center of mass acceleration, normalized by body weight, as functions of height for three snakes. The left column is determined from the left hand side of equation (4.2.24), which consists of the integrated lift and drag forces. The right column is determined from the right-hand side of equation (4.2.24) and consists of the accelerations and gravity. The black line is the average for all trials and the colored band is  $\pm 1$  standard deviation. (A) Lateral direction force and acceleration components are close to zero. (B) Forward forces, responsible for horizontal motion over the ground, are smoother than forward accelerations, but the force estimates are too low. (C) Vertical forces, responsible to offset the animal's weight, are too high compared to vertical accelerations. The dashed line indicates the equilibrium configuration when the aerodynamic forces balance the weight. . . . . 87

4.6	<p>Aerodynamic force errors and corrections. (A) Absolute force errors normalized by body weight about the lateral, forward, and vertical directions given by equation (4.2.25) for 43 glide trials from seven snakes. The average errors are shown in black, with the colored bands indicating <math>\pm 1</math> standard deviation. Lateral errors are near zero. Forward force errors are positive, with a maximum error of 0.25 BW, indicating insufficient forward force. The vertical force error is negative, with a minimum of approximately -0.5 BW, indicating too much vertical force. (B) Corrections to the quasi-steady lift and drag forces to reduce the forward and vertical force errors to zero. The left column is the multiplier needed for the lift force and the right column is the multiplier needed for the drag force. The drag multiplier is constant throughout the glides and is approximately <math>0.6\times</math>, while the lift multiplier decreases throughout the glide. The average lift multiplier is approximately <math>1.35\times</math>. . . . .</p>	88
4.7	<p>Caption on next page. . . . .</p>	89
4.7	<p>(Previous page.) Corrected quasi-steady lift and drag force distributions for two snakes from the best performing glides. For each snake, lift force distribution (blue) and drag force distribution (yellow) are shown from the side and top view (left and right columns). Progress through the glide (height fraction) is marked by the rows, with 0.9 being closest to the launch branch. The instantaneous forces have been corrected using the force multipliers from figure 4.6B. The instantaneous center of mass velocity is shown with the black arrow, and the center of mass location by the axes. Each image is scaled such that the green coordinate axis is 10 cm. The smaller snake, snake 95, had more out-of-plane motion of the posterior body and a tighter body profile than the larger snake 88. For both animals, the drag force is continuous and large over the whole body, with the straight and ‘U’-bend segments contributing similar amounts. The lift force is lowest at the ‘U’-bends, but the symmetric airfoil produces force along the interior of the bend. The tail produces little force due to its small width. . . . .</p>	90

4.8	Space-time plots of Reynolds number, angle of attack, sweep angle, and dynamic pressure fraction for the glides shown in figure 4.7. The locations of the time points in figure 4.7 are indicated by the vertical black marks. (A,B) Reynolds number distribution, where the gray dotted lines denote the ‘U’-bends, found as zero crossings of the horizontal wave. The Reynolds number increases as the animal accelerates, with snake 88 having higher Reynolds numbers because it is wider than snake 95. The tail has a much lower Reynolds number because of its small width. (C,D) Angle-of-attack distributions, where the ‘U’-bends are ridges of high angle of attack. (E,F) Sweep angle distribution, where ridges of high sweep at the ‘U’-bends are surrounded by sweep angles near 0°. Both the angles of attack and sweep angles generally decrease as the glide shallows. (G,H) Fraction of the dynamic pressure, $U_{\perp}^2/U^2$ , due to simple sweep theory. Regions where over 75% of the dynamic pressure is maintained are dark and outlined with the white contour; these regions generally occur along the straight segments between the ‘U’-bends. . . . .	91
4.9	Caption on next page. . . . .	94

4.9	(Previous page.) Distributions of gap, stagger, angle of attack, and sweep angle of the 43 glide trials analyzed. Columns (A)–(C) show the distributions for different height fractions through the glide. (A) Distributions of stagger vs. gap, with the median, first, and third quartiles marked in yellow. The red ‘+’ symbols denote measurement locations for wake interaction effects [16]. Measurement configurations where wake interaction effects are greatest are enclosed in the red box. Initially, the gap and stagger distributions are relatively disperse, but coalesce as the glides progress. (B) Angle of attack of the rear airfoil vs. angle of attack of the front airfoil. The angles of attack are correlated and initially spread along the diagonal. The angles of attack decrease as the glides progress, which results in more lift and less drag. (C) Sweep angle of the front and rear airfoils do not follow a clear trend, indicating the airflow is not usually perpendicular to the body, even along the straight segments. (D) Comparison of gap and stagger from this study (first panel) and from Socha et al. (2010) [11] (second panel). The third panel displays the same information as the first panel, but with the same color bar range as the second panel to highlight the spread of the data. The tandem effects test locations are overlaid on each plot. Each study has measured gaps and staggers in the wake interaction region. . . . .	95
5.1	Modifying the vertical wave to more closely resemble the observed kinematics. (A) Horizontal (blue) and vertical wave (yellow) from one trial at one time point. Notice the peaked vertical wave with broad troughs. (B) Modeled horizontal and vertical waves. The horizontal wave is a flat-topped sinusoid, while the vertical wave is a standard sinusoid. (C) Proposed modification of the vertical wave (solid line) compared to the current sinusoidal model (dashed line). The proposed model has sharper peaks and broad troughs. The flatness of the valleys can be tuned with one parameter ( $\beta$ in equation 5.1.2). The dashed line is for $\beta = 0$ (standard sine curve) and the solid line is for $\beta = 0.5$ .	108
A.1	Velocity polar diagram for constant lift and drag coefficients. The equilibrium condition proposed by Socha <i>et. al</i> (2010). . . . .	117
A.2	Mean kinematics-based lift, drag, and lift-to-drag ratio coefficient curves. . .	121

A.3	Acceleration along the terminal velocity manifold for the airfoil snake at a pitch angle of $\theta = 5^\circ$ . . . . .	141
B.1	Summary of complex orthogonal decomposition analysis. (A) The explained variance fraction for the different animals for the horizontal and vertical waves. Summing all modes results in a variance fraction of 1 (explaining all of the modal activity). The blue dots are the explained variance fraction for the first mode, while the red dots are the explained variance of the first and second modes combined. The horizontal wave is more organized, with a single mode accounting for much of the variance. (B) The number of modes required to account for 95% of the variance. Generally two modes are required for the horizontal, while three or four modes are required for the vertical wave. . . .	161
B.2	Caption on next page. . . . .	162
B.2	(Previous page.) Simulated flying snake glides. (A) Shape space used for simulated glides. Gray and black boxes indicate counts (one or two, respectively) of experimentally observed body shapes (figure 3.2F). The purple box indicates the shape shown in detail in (C)-(E) (B) The shape space is naturally demarcated along the diagonal of observed body shape, “open” shapes in the lower left, and “closed” shapes in the upper right. (C) Horizontal and vertical bending angles for a simulated glide with 1.4 spatial periods and a $96^\circ$ horizontal wave amplitude. (D) Center of mass trajectory with and without undulation (red and gray, respectively). Snapshots of the body orientation are shown, with the lift (blue) and drag (yellow) forces overlaid at the start, $1/3$ , $2/3$ , and the end of the trajectories. (E) Yaw, pitch, and roll Euler angles for the glides shown in (D), with no undulation indicated by dashed lines and undulation with solid lines. Without undulation, this particular glide becomes unstable in roll. (F,G) Summary of height fallen before becoming unstable for different body shapes, undulation frequency, and launch heights. The gray bands demarcate the observed body shapes from the kinematics measurements. (H) Increase in height fallen in meters due to undulation from a 75m launch height. (I,J) Horizontal glide distance with and without undulation. (K) Increase in horizontal glide distance in meters due to undulation. . . .	163

- B.3 Effect of the vertical wave amplitude  $\psi_m$  and dorsoventral bending  $d_\psi$  (columns) on glide performance for different dorsoventral flexion angles and number of spatial periods. See figure 3.4 for details. (A) Simulated glides with planar undulation performed worst, although the behavior for different dorsoventral bending angles (moving across the columns) is the same in (B) for  $\psi_m=10^\circ$ . Negative dorsoventral bending is associated unstable glides and poor performance due to pitching down and a net negative phase-averaged pitch moment. Positive dorsoventral bending is associated with stable glides with poor performance due to pitching-up. The pitch moment is in physical units of Nmm. 164
- B.4 Overview of complex orthogonal decomposition analysis for the glide shown in figure 3.2 of the main paper. (A) First scaled complex orthogonal model,  $\sqrt{\lambda_1} \mathbf{w}_1$  for the horizontal ( $\theta$ ) and vertical ( $\psi$ ) waves. The diameter of the circular spectrum is roughly the peak-to-peak amplitude of the waves (figure 3.2A). One revolution indicates one complete period of bending on the body. (B) First row of the complex modal coordinate ensemble matrix  $\mathbf{q}$  encompassing the undulation frequency information. One revolution indicates one complete period of undulation of the mode. (C) The complex numbers indicated in (A) are visualized as unwrapped angles to quantify the average whirl rate. The slope of the best-fit line is the number of spatial periods  $\nu$ . The slope for the vertical wave  $\psi$  is twice as great as for the horizontal wave  $\theta$ . (D) The slope of the line indicates the number of undulation periods during the glide. The slope of the vertical bending wave line is twice as great as the horizontal bending wave line. . . . . 165
- B.5 Width and mass distributions of flying snakes. (A) Width distribution along the length of the animal as percent of the snout-vent length (SVL) of the snake for three different animals, and a parabolic fit. (B) Density distribution as percent of the average snake density,  $\bar{\rho} = m_{tot}/SVL$  for three different snakes. The head has higher density than the body, but both are modeled by two parabolas. The tail is included, although the tail dynamics was not modeled. . . . . 166

B.6	Lift and drag coefficients of flying snakes. The data is from [14]. (A) Definition of the angle of attack, $\alpha$ , as the angle between the chord-line direction $\hat{c}$ and the velocity component locally perpendicular to the body. (B) Lift and drag coefficients as functions of angle of attack and Reynolds number. The extrapolated region is demarcated by the gray band on the horizontal axis between $60^\circ$ and $90^\circ$ . (C) Lift-to-drag ratio, with the characteristic peak at an angle of attack of $35^\circ$ . . . . .	167
B.7	Ensuring the correct angle of attack and lift vector direction based on the orientation of the body with the free-stream airflow. (A)-(D) match the cases in (B.4.34). . . . .	168
C.1	Quantified selection criteria from the trajectory summary plots. Red markers are trials that were excluded, green markers are trials that were selected for further processing, and blue markers were used in the complex orthogonal decomposition (COD) analysis. The shaded areas are the convex hulls of the respective markers. (A) The time component of selection. The abscissa indicates the total length of usable time series and the ordinate indicates the largest gap length. (B) The marker component of selection. The abscissa indicates the maximum number of missing markers on the snake's body, normalized by the total number of markers on the body. The ordinate indicates the median number of missing markers, normalized by the total number of markers on the body. . . . .	173

C.2	Summary histograms of missing data, including the number of gaps in the time series, the length of the individual gaps, where the gaps occur in the time series, the amount of vertical glide distance recorded, and the horizontal glide distance, for the different trials analyzed. The first row are for 36 trials used for the complex orthogonal decomposition analysis, which are a subset of the 52 trials shown on the second row that were analyzed in detail. These 52 trials are indicated by bold labels in figures C.3–C.14. The third row indicates the 79 trials that were excluded from further analysis. These trials generally had more gaps, with longer lengths, shorter heights recorded, and much shorter glide distances recorded. The last row is the summary histograms for all of the recorded trials. Note that the first three columns treat each marker time series separately (i.e. between 11 and 17 time series per trial per snake), while the last two columns are summaries for each trial and calculated from the head marker position at the start and end of the usable data region (between the red and purple vertical lines in the trajectory summary plots). . . . .	174
C.3	<i>Chrysopelea paradisi</i> 81. . . . .	175
C.4	<i>Chrysopelea paradisi</i> 91. . . . .	176
C.5	<i>Chrysopelea paradisi</i> 95. . . . .	177
C.6	<i>Chrysopelea paradisi</i> 88. . . . .	178
C.7	<i>Chrysopelea paradisi</i> 90. . . . .	178
C.8	<i>Chrysopelea paradisi</i> 86. . . . .	179
C.9	<i>Chrysopelea paradisi</i> 94. . . . .	179
C.10	<i>Chrysopelea ornata</i> 30. . . . .	180
C.11	<i>Chrysopelea ornata</i> 31. . . . .	180
C.12	<i>Chrysopelea ornata</i> 32. . . . .	181
C.13	<i>Chrysopelea ornata</i> 33. . . . .	181
C.14	<i>Chrysopelea ornata</i> 35. . . . .	182

C.15	Filter cutoff frequency selection for a forward-backward Butterworth filter. (a-c) Root-mean-square errors for the head (blue) and tip of the tail (green) marker time series for different filter cutoff frequency, with the selected cutoff frequencies indicated by the vertical red lines. The times series (d-f) for marker about each direction has different characteristics and results in different cutoff frequencies. In (a-c), the frequency selection algorithm begins by calculating the RMS error residual line for cutoff frequencies from $1 \leq f_c \leq 35$ Hz in 0.5 Hz increments, as indicated by the thick blue and green lines. Then, beginning at 35 Hz and decreasing, points are added to a linear regression (open markers), until the $r^2$ of the fit drops below 0.95; the proceeding frequency is then used such that $r^2 \geq 0.95$ . Next, the linear fit is extended to the $y$ -intercept (thin blue and green lines), giving the RMS value of the noise [89]. Next, the intercept is projected (black line) onto the residual line; the frequency of this intersection is the selected cutoff frequency (red line). Using this approach, the signal distortion (the distance between the residual intercept and the linear fit) is equal to the noise passed through the filter. . . . .	187
C.16	Ball drop locations used to test the accuracy of the motion capture system. (a) Overhead view of the $5 \times 5$ measurement grid, where the three ball drops at each site are indicated by the colored markers. Gray lines are the $X - Y$ center of mass position of the recorded snake glides. The majority of the glides fall within at 7 drop location near the launch height. (b) Three-dimensional analogue of (a). (c) Position residuals for different filter cutoff frequencies for each ball drop trajectory. . . . .	188
C.17	Ball drop acceleration errors vs. heigh within the Cube.. The small multiples correspond to the grid of drop locations in figure C.16. Errors are reported in units of gravitational constant $g$ , and printed values for each plot are the average errors of the solid lines. The markers indicate the errors for the first 8 and last 10 time points, which we determined contributed larger errors and were excluded from the analysis. The vertical gray line indicates the average jump height of 8.4 m. . . . .	190
C.18	Ball drop velocity errors found by fitting linear polynomials to the time series data of velocity. . . . .	191

C.19	Ball drop position errors found by fitting quadratic polynomials to the time series data of filtered position. . . . .	192
C.20	Numerical test of global natural cubic splines on a 2D serpenoid curve. (a) Prescribe curvature $\kappa$ (black) and tangent angle $\theta$ (magenta). (b) Reconstructed curvature and tangent angle from the spline. Note that the curvature is non-smooth. The tangent angle is. (c) Analytical serpenoid curve and the subsampled “measurement” locations (red dots) that the spline were fit to. The spline was sampled at 100 locations and closely matches the body. (d) The error in the arc length of each segment (ss) and the length of the segment parameters ( $ts = \Delta t$ ). The length errors are small. . . . .	197
C.21	Digitized snake image to calculate landmark positions along the body. (A) Overhead image of snake 91 at the end of day 4 of trials that was digitized manually. Splines were fit to the digitized points, and separated by different regions of the body, with the head in blue, the body in green, and the tail in purple. The landmarks along the body are denoted by circles, the vent as a square marker, and the landmarks along the tail as diamonds. (B and C) The position between the landmark points was found by integrating along the arc length of the spline in physical units (B) and in units of snout-vent length in (C). . . . .	199
C.22	Snake 87 immediately removed from the lab freezer, shown in (a) dorsal and (b) ventral views. The specimen was kept in the plastic bag and run under warm water to thaw the body. (c) Cross section from a fresh specimen (image from Jake Socha). . . . .	201
C.23	Raw linear mass density measurements. (a) Measured mass of each $\approx 10$ mm segment. Specimen 87 showed signs of tissue degradation, so larger sections were used along the posterior section of the body, hence the larger masses of the individual segments. Also, there is more variation with this measurement than the other specimens. (b) Density of each individual segment. (c) Normalized density (density divided by the average density) for each specimen, and the average value (in black) used for mass calculations from the Cube data.	202

C.24 Parabolic fits to the linear mass density distributions. (a) The head (blue) and body (green) were separated and the data from each specimen grouped together. The parabolic fit for each region is shown with the black line. (b) Comparison of the parabolic fit to the normalized density for each specimen. (c) Comparison of the parabolic fit to the density in physical units for each specimen. (d) Comparison of the parabolic fit to the average normalized density (figure C.23c. . . . .	203
C.25 Image processing steps to calculate the width of the snake as a function of distance along the body. . . . .	205
C.26 Pseudo-color images of six snapshots from three individuals used in the width calculations. . . . .	206
C.27 Build-up for the width distribution. (A) Six width distribution from the image processing steps. (B) Width distributions, where the two measurements per animal have been averaged. (C) Parabolic fit to the width distributions. (D) The width distribution and parabolic fit after the $1.13\times$ scaling correction has been applied. (E) Average width distribution for the body and tail that was used for further processing. . . . .	207
C.28 Scaling of the chord length with SVL. (A) The maximum chord length from the parabolic fit of figure C.27C was too low. (B) The ratio of the slopes of the best fit line resulted in the scaling correction of $1.13\times$ used in figure C.27D,E.	208
C.29 Scaling of wing loading, maximum width, and average density with (A) SVL and (B) mass. The scaling exponents are presented in table C.6. . . . .	209
C.30 Comparison of landing location and snake size from Socha, O’Dempsey, and LaBarbera (2005) and this study. (A) Overhead view of landing locations from all glide of Socha, O’Dempsey, and LaBarbera (2005) from a launch height of 9.8 m. Many individuals covered over 10 m horizontally, with many up to 15 m. (B) Overhead view of landing location locations from the Cube trials, from a launch height of 8.3 m. Many snakes did not surpass 5 m horizontally. (C)-(E) Comparison of animal mass, SVL, and wing loading from Socha, O’Dempsey, and LaBarbera (2005) and the Cube trials. The individuals from the Cube were generally longer and more massive, with higher wing loadings. Glide time should scale with $\sqrt{W_S}$ , and distance covered should scale with $W_S$ . . .	211

C.31 Comparison of landing location and snake size from Socha, O’Dempsey, and LaBarbera (2005) and this study (same as figure C.30, but color coded by mass, SVL, and wing loading. (A) Ranges of mass, SVL, and wing loading from Socha (2005) and the Cube trials, where darker colors indicate lower values and smaller snakes. (B) Glide distance coded by color for different masses, SVLs, and wing loadings. . . . .	212
C.32 Missing data statistics from the Cube trials. (A) Probability of any time series having gaps of different lengths. Over 60% of the recorded time series (each marker from each trial is treated separately) had no gaps, while about 20% of trials had one gap. (B) The probability of having a gap depends on where you are in the time series. Data is more likely to be missing at the beginning of the trial. There are fewer gaps one quarter through the trial, and about a 2% chance a gap will occur over 50% through the trial. (C) The gap length is generally small, but there are instances of very long gaps. . . . .	214
C.33 Effect of missing data on center of mass position, velocity, accelerations, and calculated aerodynamic forces. The complete time series is shown in red, while the 100 degraded time series are shown in gray. (A) Side view of the center of mass position. (B) Velocity polar diagram. (C) Center of mass accelerations and resultant aerodynamic force. (D) Fraction of missing data is similar between the data missing from the Cube trials (blue) and the degraded time series (green). . . . .	215
C.34 Histogram of RMSE for the center of mass position, velocity, and acceleration about the X, Y, and Z axes. Position errors are small, while velocity errors are generally less than 1% and acceleration errors are less than 5%. . . . .	216
C.35 Effect of missing data on the complex orthogonal decomposition analysis. (A) Temporal frequency ratio is not affected, while spatial frequency ratio is. However, of the 100 degraded time series, only three time series show large errors. (B) Lateral wave amplitude vs. number of spatial periods. (C) Vertical wave amplitude vs. number of spatial periods. (D) Dorsoventral bending angle vs. number of spatial periods. Missing data generally does not have an affect, except for the few trials. . . . .	217

D.1	Schematic of the dynamic model and equations of motion. . . . .	221
D.2	Effect of dorsoventral bending angle, $d_\psi$ , and vertical wave amplitude, $\psi_m$ , on center of mass motion. The three rows are combinations of number of body waves, $\nu_\theta$ , and horizontal wave amplitude, $\theta_m$ , along the observed diagonal of the horizontal wave shape space. The top row within each horizontal wave shape is the side view of $Zvs. Y$ motion of the center of mass, and the bottom row is the top view of $X$ vs. $Y$ . . . . .	231
D.3	Effect of dorsoventral bending angle, $d_\psi$ , and vertical wave amplitude, $\psi_m$ , on yaw, pitch, and roll Euler angles. This is for $\nu_\theta=1.25$ and $\theta_m = 105^\circ$ . . . . .	232
D.4	Effect of snake length and dorsoventral bending angle on center of mass motion.	233
D.5	Effect of undulation frequency and dorsoventral bending angle on center of mass motion. . . . .	234
D.6	Effect of undulation frequency and dorsoventral bending angle on pitch, roll, and yaw Euler angles. . . . .	235
D.7	Effect of corrected forces on glide distance and glide distance. . . . .	237
D.8	Effect of corrected forces and dorsoventral bending on glide performance and pitch dynamics for a vertical wave amplitude of $\psi_m=20^\circ$ . . . . .	238
D.9	Effect of corrected forces and dorsoventral bending on glide performance and pitch dynamics for a vertical wave amplitude of $\psi_m=10^\circ$ . . . . .	239
D.10	Effect of corrected forces and dorsoventral bending on glide performance and pitch dynamics for a vertical wave amplitude of $\psi_m=0^\circ$ . . . . .	240

# List of Tables

2.1	Types of force coefficient data used in this study. Details describing the derivation of the kinematic squirrel coefficients are presented in the Supplemental Information. . . . .	19
3.1	Overview of flying snake simulations shown in figure 3.3 and figure B.2, demarcated by the different shape space regions. . . . .	52
4.1	Summary of gap and stagger changes during different phases of gliding (figure 4.9A). The median and interquartile range (IQR) of gap (G) and stagger (S) are displayed in units of maximum chord length of the animal, denoted by “c”. . . . .	93
C.1	Overview of <i>C. paradisi</i> and <i>C. ornata</i> glides analyzed and animal sizes. Of 131 recorded glides, 51 were analyzed in detail, with 42 from <i>C. paradisi</i> and 9 from <i>C. ornana</i> . . . . .	172
C.2	Overview of <i>C. paradisi</i> specimens used for the mass distribution measurements. . . . .	200
C.3	Parabolic fits to the linear mass density data. . . . .	203
C.4	Snake and image meta data used along side image processing to measure the width of the snake mid-glide. The snakes used for this analysis are from Socha and LaBarbera (2005) [9]. . . . .	204
C.5	Parabolic fits to the width distribution. . . . .	208
C.6	Scaling exponents for flying snake morphometrics (figure C.29. Regressions were performed as per [110]). . . . .	209

# Chapter 1

## Introduction

Comparative biomechanics is the study of animals and plants through the quantitative lens of engineering and mathematics. Animal locomotion is a subset of comparative biomechanics concerned with how animals interact with and move through their environment. This includes describing the motion of the body and its constituent parts through space (kinematics), how the animal produces and controls locomotor forces, and how these forces act to affect the motion and locomotor stability of the animal (dynamics). We study how animals move for two main reasons. First is to answer basic scientific questions about their biology. These include how the animal acquires food, finds mates, progresses through the life cycle, or escapes predation. Some of the most tantalizing questions include transitions from one environment to the next: how did animals transition from water to land? How did flapping flight evolve?

The second motivation to study how animals move is to distill the salient physics that can be used in engineered systems to the benefit of humans. Millions of years of evolution have produced a plethora of animals capable of not only surviving, but thriving, in nearly all environments on Earth. This includes land, air, water, and the interfaces between them. If we want to employ machines that effectively move through these environments, designs based off of time-proven methods should work best.

This dissertation addresses flying snake locomotion from the basic science perspective. It is motivated by the question, how and why do flying snakes undulate while airborne? Flying snakes of the genus *Chrysopelea* comprise five species of snakes found in southeast Asia, and are the only known animals capable of limbless flight. They glide, moving horizontally downward through the air by converting gravitational potential energy into lift and drag forces,

by jumping, flattening their bodies, and undulating through the air. The key components of snake flight are aerial undulation (the changing body position as the snake undulates through the air) and the aerodynamic forces distributed over the body. Previously, aerial undulation had been hypothesized to increase the dynamic stability of snake flight, although the experimental data was too limited to directly test this. This dissertation provides new kinematic data, dynamic modeling, and a non-equilibrium gliding framework to understand how a limbless animal can glide to the ground.

## 1.1 Overview of flying snakes

The first literature accounts of flying snakes appeared nearly 100 years ago. These field observations described sightings of “a flying snake”, almost as in disbelief that such an animal exists [1–4]. Early accounts were unclear as to what the animal was doing in the air. Some described a static body, others a double ‘S’-shape, with the tail whipping vigorously around. The prominent dorsoventral body flattening was noted early on [2], describing the concave surface of the snake like “a piece of bamboo bisected longitudinally”. Shelford (1906) noted that the flattened body likely slows the animal’s descent and lessens its impact force. A fuller understanding of the functional significance of the snake’s body cross-section would have to wait another 108 years. The first quantitative study of flying snake glide performance occurred in 1970. Heyer and Pongsapipatana (1970) launched six specimens of *C. ornata* from a 41 m meteorological tower in Thailand, recording glide distances and time aloft. They described aerial undulation as “swimming through the air,” prompting them to release, among other snakes, sea snakes, to see how they fared. Not only did *Chrysopela* glide farther, but some turned mid-glide and landed on the launch tower.

The first rigorous study of flying snakes occurred in the late 1990’s and early 2000’s [6, 7]. Motivated by the simple question of what are the aerodynamics of snake flight, this work provided the first photographic evidence and quantitative kinematic measurements of snake flight. The kinematic data consisted of three landmark points placed along the snake’s body, reconstructed in 3D, of 14 glides from a height of 9.3 m. The main conclusions were: flying snakes do not simply fall to the ground, but their glides shallow, indicating lift production; the glide performance depends on body size, with smaller individuals performing better; flying snakes always undulate, with an undulation frequency of 1–2 Hz; they use aerial undulation, which consists of a pronounced lateral wave, with significant out-of-plane motion, and which

is distinct from lateral undulation on the ground and in the water; and that *C. paradisi* are the best gliders within the genus [8]. Subsequent studies investigated the effects of animal size on glide performance [9], as well as jump kinematics [10]. Socha et al. (2010) investigated the late-phase glide kinematics, testing whether flying snakes reach equilibrium when gliding from a height of 15 m [11]. Using five landmarks along the body, they found no equilibrium glides from eight trials.

The aerodynamics of flying snakes were first investigated using relatively crude physical models of the concave ventral surface. The models were used to determine which aspects of the snake's unique shape contributed to its aerodynamic performance [12]. They varied the filled volume of the ventral surface, sharpness of the keel edges, and the presence of a backbone bump. They found that the roughly triangular body is robust to shape changes, with relatively high lift-to-drag ratios of 2.7–2.9 and gradual stall as the angle of attack increases. They also tested wake interaction effects by placing two airfoils in tandem, finding some configurations with a 50% increase in the lift-to-drag ratio.

A more rigorous analysis of flying snake aerodynamics, based on the snake's 2D cross-section from stereophotos [13], included force measurements and particle image velocimetry measurements of the wake structure [14]. They determined that the cross-section of the snake's body acts as a lifting bluff body, producing a lift-to-drag ratio of 2.7 at an angle of attack of 35°, with gentle stall characteristics. The cross-section produces appreciable forces over a large angle-of-attack range experienced during gliding. A later 2D computational study found a possible lift enhancement mechanism due to the boundary layer separating near the leading edge along the dorsal surface [15]. A more recent experimental study focused on possible tandem effects due to wake interaction at different gaps (horizontal spacing), staggers (vertical spacing), and angles of attack estimated from the five-point study [16]. They found tandem effects are possible, but strong wake interactions are limited to few configurations of gap, stagger, and angle of attack, some of which may be observed during glides.

## 1.2 Dissertation overview

The major goal of this dissertation is to understand how flying snakes maintain stability while airborne. To that end, this dissertation combines new kinematic measurements of flying snakes, detailed dynamic modeling using the newly discovered components of aerial

undulation, and reduced-order modeling to understand non-equilibrium gliding in animals.

In Chapter 2, I start with a reduced-order modeling framework to understanding non-equilibrium gliding in animals. This work began as a way to better understand a previous modeling study and how the initial pitch angle and initial pitch rate determine the ultimate glide performance [17]. By chance, my advisor Shane Ross, plotted the velocity phase space instead of simply the position of the center of mass in physical space. The velocity phase space showed interesting structure, including an apparent manifold and equilibrium points, that changed as the pitch angle changed. In this chapter, we address the question, what is the effect of angle-of-attack dependent lift and drag coefficients on a glider's trajectory dynamics? This chapter is a detailed investigation into the structure of the velocity phase space and how this structure is related to the lift and drag curves and pitch angle of the glider. The concepts derived here form the foundation for a deeper understanding of glider trajectory dynamics, and provide a foundation for studying pitch-mediated gliding behavior.

In Chapter 3, I present the first of the kinematic results, describing a fuller picture of aerial undulation. This chapter is motivated by the question, how does undulation and body shape affect glide performance and stability? Using an infrared motion-capture system, we recorded 11–17 landmark points on the snake's body. From this increased resolution, we are able to construct the time-vary backbone motion of 36 glide trials from jump heights of 8.3 m. From the kinematic data, we find that aerial undulation consists of two waves of bending. The large-amplitude horizontal wave is easily recognized from video footage, but there is an additional vertical wave that has twice the spatial and temporal frequency as the horizontal wave, and is phase shifted by  $90^\circ$ . There is a third component we term dorsoventral bending, which is the up-down vertical motion of the posterior body. I then show the effects of aerial undulation on the stability of flying snakes by developing a dynamic model of snake flight. By systematically varying the aerial undulation waveform, we find that undulation increases the rotational stability of modeled snake flight, and that dorsoventral bending can control the aerodynamic pitching moment on the modeled snake's body.

In Chapter 4, I provide a further kinematic analysis of the data presented in Chapter 3, and calculate the first estimates of the time-varying lift and drag distributions over the body. This chapter is motivated by the question, can quasi-steady theory predict the lift and drag forces acting on the snake's body? Previously, it was found that undulation frequency was not associated with trajectory performance variables, suggesting that undulation plays a minor role in force production and that quasi-steady theory may be applicable [9]. However,

previous measurements under resolved the body, making it impossible to calculate forces. Quasi-steady theory assumes the forces acting on a body are a function of the instantaneous speed and orientation of the airflow to the body; the time-history of the airflow is not considered. Although quasi-steady theory is insufficient for flapping flyers, it has not been tested explicitly for gliding animals. We test this assumption here and find that quasi-steady over predicts the drag force and under predicts the lift force. I then provide a kinematic analysis of the observed gap and staggers, and test if the body is in a configuration to leverage wake interaction effects.

This dissertation provides a launching point for several future modeling and experimental studies. For example, the non-equilibrium gliding framework presented in Chapter 2 can be extended by adding control with various control objective and comparing the predicted pitch angle history with recorded animal trajectories. Such an analysis may provide insight into the control objectives used by gliding animals. The modeling work in Chapter 3 suggests that we have the basic control template (*sensu* Full (1999)[18]) to control a limbless flying robot. The use of biological waveforms as templates has been recently demonstrated to simplify control in snake robots [19, 20]. While much work is needed to build such a machine, we likely have the key kinematic components and their likely effect on the robot's motion. In fact, building and testing a robophysical model will likely provide new information on control of snake gliding [21]. Lastly, the morphing wing-body kinematics and orientation described in Chapter 4 can be used in computational fluid dynamics simulations. These simulations should provide the physical understanding of the fluid forcing on the animal's body, and how those change as the glide progresses. Additionally, fluid simulations may point to lift-enhancement and drag-reduction mechanisms that enable snake flight, as well as establishing the role of unsteady aerodynamic mechanisms for gliding animals.

## References

- [1] W. M. Daly. A flying snake. *J Bombay Nat Hist Soc* 12.3 (1899), p. 589.
- [2] R. Shelford. A Note on "Flying" Snakes. *Proc. Zoological Soc.* I.XVI (1906), p. 227–230.

- [3] S. S. Flower. Notes on a Second collection of Reptiles made in the Malay Peninsula and Siam, from November 1896 to September 1898, with a List of the Species recorded from those Countries. *Proc Zool Soc L.* 16 (1899).
- [4] H. M. Pendlebury. A "Flying" Snake. *Bull Raffles Mus* 5 (1931), p. 75.
- [5] W. R. Heyer and S. Pongsapipatana. Gliding Speeds of *Ptychozoon lionatum* (Reptilia: Gekkonidae) and *Chrysopelea ornata* (Reptilia: Colubridae). *Herpetologica* 26.3 (1970), p. 317–319.
- [6] J. J. Socha. The biomechanics of flight in snakes. PhD thesis. University of Chicago, 2002.
- [7] J. J. Socha. Gliding flight in the paradise tree snake. *Nature* 418 (2002), p. 603–604. DOI: 10.1038/418603a.
- [8] J. J. Socha, T. O'Dempsey, and M. LaBarbera. A 3-D kinematic analysis of gliding in a flying snake, *Chrysopelea paradisi*. *J. Exp. Biol.* 208 (2005), p. 1817–1833. DOI: 10.1242/jeb.01579.
- [9] J. J. Socha and M. LaBarbera. Effects of size and behavior on aerial performance of two species of flying snakes (*Chrysopelea*). *J. Exp. Biol.* 208 (2005), p. 1835–1847. DOI: 10.1242/jeb.01580.
- [10] J. J. Socha. Becoming airborne without legs: the kinematics of take-off in a flying snake, *Chrysopelea paradisi*. *J Exp Biol* 209 (2006), p. 3358–3369. DOI: 10.1242/jeb.02381.
- [11] J. J. Socha, K. Miklasz, F. Jafari, and P. P. Vlachos. Non-equilibrium trajectory dynamics and the kinematics of gliding in a flying snake. *Bioinspir. Biomim.* 5.045002 (2010). DOI: 10.1088/1748-3182/6/1/019501.
- [12] K. Miklasz, M. LaBarbera, X. Chen, and J. J. Socha. Effects of body cross-sectional shape on flying snake aerodynamics. *Exp. Mech.* 50 (2010), p. 1335–1348. DOI: 10.1007/s11340-010-9351-5.
- [13] J. J. Socha. Gliding flight in *Chrysopelea*: turning a snake into a wing. *Integ. Comp. Biol.* 51 (2011), p. 969–982. DOI: 10.1093/icb/icr092.
- [14] D. Holden, J. J. Socha, N. D. Cardwell, and P. P. Vlachos. Aerodynamics of the flying snake *Chrysopelea paradisi*: how a bluff body cross-sectional shape contributes to gliding performance. *J. Exp. Biol.* 217 (2014), p. 382–394. DOI: 10.1242/jeb.090902.

- [15] A. Krishnan, J. J. Socha, P. P. Vlachos, and L. A. Barba. Lift and wakes of flying snakes. *Phys. Fluids* 26.031901 (2014). DOI: 10.1063/1.4866444.
- [16] F. Jafari. Physical mechanisms of control of gliding in flying snakes. PhD thesis. Virginia Tech, 2016.
- [17] F. Jafari, S. D. Ross, P. P. Vlachos, and J. J. Socha. A theoretical analysis of pitch stability during gliding in flying snakes. *Bioinspir. Biomim.* 9.025014 (2014). DOI: 10.1088/1748-3182/9/2/025014.
- [18] R. J. Full and D. E. Koditschek. Templates and anchors: neuromechanical hypotheses of legged locomotion on land. *J Exp Biol* 202 (1999), p. 3325–3332.
- [19] H. Marvi, C. Gong, N. Gravish, H. Astley, M. Travers, R. L. Hatton, J. R. Mendelson III, H. Choset, D. L. Hu, and D. I. Goldman. Sidewinding with minimal slip: Snake and robot ascent of sandy slopes. *Science* 346.6206 (2014), p. 224–229. DOI: 10.1126/science.1255718. arXiv: arXiv:1410.2945v1.
- [20] H. C. Astley, C. Gong, J. Dai, M. Travers, M. M. Serrano, P. A. Vela, H. Choset, J. R. Mendelson III, D. L. Hu, and D. I. Goldman. Modulation of orthogonal body waves enables high maneuverability in sidewinding locomotion. *Proc Natl Acad Sci* 112 (2015), p. 6200–6205. DOI: 10.1073/pnas.1418965112.
- [21] J. Aguilar, T. Zhang, F. Qian, M. Kingsbury, B. McInroe, N. Mazouchova, C. Li, R. Maladen, C. Gong, M. Travers, R. L. Hatton, H. Choset, P. B. Umbanhowar, and D. I. Goldman. A review on locomotion robophysics: the study of movement at the intersection of robotics, soft matter and dynamical systems. *Rep Prog Phys* 79.110001 (2016), p. 35. DOI: 10.1088/0034-4885/79/11/110001.

# Chapter 2

## Global dynamics of non-equilibrium gliding in animals

MANUSCRIPT AUTHORS: Isaac J. Yeaton, John J. Socha, and Shane D. Ross

**Citation:** Yeaton, I. J., Socha, J. J., & Ross, S. D. (2017). Global dynamics of non-equilibrium gliding in animals. *Bioinspiration & Biomimetics*, **12**(2), 026013.  
doi: 10.1088/1748-3190/aa60e2.

### Abstract

Gliding flight — moving horizontally downward through the air without power — has evolved in a broad diversity of taxa and serves numerous ecologically relevant functions such as predator escape, expanding foraging locations, and finding mates, and has been suggested as an evolutionary pathway to powered flight. Historically, gliding has been conceptualized using the idealized conditions of equilibrium, in which the net aerodynamic force on the glider balances its weight. While this assumption is appealing for its simplicity, recent studies of glide trajectories have shown that equilibrium gliding is not the norm for most species. Furthermore, equilibrium theory neglects the aerodynamic differences between species, as well as how a glider can modify its glide path using control. To investigate non-equilibrium glide behavior, we developed a reduced-order model of gliding that accounts for self-similarity in the equations of motion, such that the lift and drag characteristics alone determine the glide

trajectory. From analysis of velocity polar diagrams of horizontal and vertical velocity from several gliding species, we find that pitch angle, the angle between the horizontal and chord line, is a control parameter that can be exploited to modulate glide angle and glide speed. Varying pitch results in changing locations of equilibrium glide configurations in the velocity polar diagram that govern passive glide dynamics. Such analyses provide a new mechanism of interspecies comparison and tools to understand experimentally-measured kinematics data and theory. In addition, this analysis suggests that the lift and drag characteristics of aerial and aquatic autonomous gliders can be engineered to passively alter glide trajectories with minimal control effort.

**Keywords:** gliding, equilibrium, control

## 2.1 Introduction

Animal gliders move horizontally through the air by exchanging potential energy for kinetic energy and by producing and controlling aerodynamic forces [22, 23]. To meet ecologically relevant goals, including predator escape, moving to new foraging locations, searching for mates, or avoiding the forest floor, the glider must control lift and drag forces to dynamically change the glide path and landing location. Glide dynamics have generally been studied using the limited theoretical framework of equilibrium, in which the glide path is straight and performance only depends on a constant lift-to-drag ratio. However, real glide paths are not straight, and lift-to-drag ratio can vary continuously with angle of attack. How animal gliders use their unique morphologies to achieve ecological goals cannot be answered from the equilibrium framework, as it neglects transient dynamics and angle of attack-dependent force coefficients. Furthermore, the evolution of lift-producing wing-like structures, which has occurred over thirty times in arboreal vertebrates [23], suggests that producing and controlling aerodynamic forces is selectively advantageous. To truly understand the gliding behavior of animals, then, suggests that a non-equilibrium framework is required. Here, we conceptualize glide dynamics using lift and drag coefficients that depend on angle of attack and control, which allows the angle of attack to actively vary. These refinements to previous modeling enables a more realistic view of gliding.

The equilibrium gliding assumption states that the resultant aerodynamic force balances the gravitational force. In this condition, the velocity is constant, the glide path is straight and

angled down from the horizontal at a constant glide angle, and the glide angle and the lift-to-drag ratio are related by  $\cot \gamma = F_L/F_D$  [24]. This assumption has been used to compare gliders and make predictions of performance. For example, heavier individuals with higher wing loading should glide faster than lighter individuals, but both should have the same equilibrium glide angle [24]. Equilibrium theory also predicts that glide range and energy conversion efficiency will be maximized when the lift-to-drag ratio is maximized [25]. These predictions should be valid for any glider, even though species vary greatly in their size, morphology, and diversity of aerodynamic structures. Examples of this diversity include the dorsoventrally flattened body of gliding snakes [11–15], the inter-limb patagial membrane of gliding mammals [26, 27], the rib-wings of gliding lizards [28, 29], the webbed feet of gliding frogs [30], and body/limbs in wingless hexapods [31, 32] and arachnids [33].

However, there is limited evidence of equilibrium gliding in experimental studies. In one study, 52% of *Draco* glides did not reach equilibrium [29]. In experiments with the flying snake *Chrysopelea paradisi*, only one of 14 glide trials originating from a height of 9.6 m appeared to reach equilibrium [8], and no equilibrium glides were found in eight glide trials beginning from a height of 15 m [11]. Two studies of gliders recorded in the wild found similar results. Body-mounted accelerometers attached to gliding colugos generally indicated greater vertical forces than required for equilibrium [27], and no equilibrium glides were found in long horizontal distance (18 m) glides of northern flying squirrels, *Glaucomys sabrinus*. Simulated glides of *G. sabrinus* required time-varying force coefficients to reproduce the observed trajectories in this species [26]. These studies show that non-equilibrium gliding is dominant in real trajectories.

Observations of non-equilibrium gliding are not unexpected given the coupled effects of animal behavior and aerodynamic force production on glide trajectories. All gliders must accelerate to sufficient velocities to produce appreciable aerodynamic forces, so there is always some non-equilibrium portion at the start of any glide. Similarly, slowing the glide before landing and controlling contact with the substrate requires aerodynamic and postural changes [34]. An animal can also modify force production by changing the wing itself, by varying the camber or aspect ratio with relative limb position [35, 36]. Furthermore, gliders can maneuver volitionally, or make small adjustments to the trajectory to achieve a goal such as landing on a targeted tree [37].

The other source of complexity that can affect glide dynamics is the local airflow interaction with the body. During the ballistic and shallowing phases of gliding that precede equilibrium,

the relative air velocity changes continuously in magnitude and in direction. Lift and drag forces scale as the velocity squared, and their lines-of-action depend on the instantaneous flow direction. Additionally, lift and drag coefficients depend strongly on the animal's angle of attack, which changes passively as the glide angle changes, and actively if the animal changes its pitch angle using control. Understanding this coupling of animal behavior and force production requires not only kinematics and force coefficient data, but also modeling to unify experimental observations with physical theory.

Theoretical models have been used to study the effects of force coefficients, wing loading, and initial conditions on glider performance and stability. Models from the late 1800's were developed to understand bird flight [38, 39], but more recent modeling work can be categorized as either particle models or rigid-body models. Particle models consider the glider as a point mass moving in the vertical plane under the influence of lift, drag, and gravity [11, 25, 26, 40]. These models decouple the instantaneous lift and drag coefficients from the glide dynamics, by assuming that the coefficients are either constants or arbitrary functions of time, but not functions of angle of attack. A dominant feature revealed from particle models is damped oscillations in velocity, acceleration, and glide angle time series before the glider reaches equilibrium [11, 25, 39, 40]. Rigid-body models couple both the translational and rotational pitch dynamics of the glider. Jafari *et al.* (2014) developed two tandem-wing rigid-body models to investigate the passive stability characteristics of flying snakes [17], finding that stable glides are possible, but depend on the initial conditions of pitch and pitch rate. Certain combinations of initial conditions lead to equilibrium glides, whereas other combinations lead to falling with a negligible horizontal velocity.

Here, we used theoretical modeling and a new analysis of the velocity polar diagram (*sensu* Tucker [41]) of horizontal vs. vertical velocity to develop a non-equilibrium theoretical framework to understand the mechanics of gliding. This work was specifically motivated by the question, what is the effect of angle-of-attack-dependent lift and drag coefficients on a glider's trajectory dynamics? We developed a rigid-body model using a new rescaling to isolate the effects of the lift and drag coefficients. This rescaling enabled us to test the effect of lift and drag coefficients using simulated glides, with angle-of-attack-dependent force coefficients taken from previous studies. In particular, we used force coefficients from studies of flying squirrels [26, 35], flying snakes [14], sugar gliders [42], flying fish [43], chukar partridge [44] and dragonflies [45]. This broad sampling of animals helps to elucidate commonalities of non-equilibrium gliding, demonstrating the utility of this non-equilibrium framework across

phylogenetically diverse species. As future kinematics studies reveal more detailed glide information, this framework can be used to answer questions about how gliders control the trajectory by varying body posture.

## 2.2 Methods

We formulate the equations of motion for a glider translating in the vertical  $x$ - $z$  plane (figure 2.1e) under the influence of lift, drag, and gravity. We analyze the glider as a rigid body in which angle of attack changes with glide angle and a specified body pitch angle. That is, we do not write an equation of motion for the rotational dynamics, but instead use the pitch angle to elicit different system responses. To encapsulate a glider's motion in an intuitive and informative manner, we use the velocity polar diagram (figure 2.1g) instead of time series of position, velocity, acceleration, and glide angle (figure 2.1a-d). The velocity, acceleration, and glide angle information is embedded in the diagram, and equilibrium gliding can be clearly identified as points where the acceleration vector goes to zero and to which velocity trajectories are attracted to or repelled from.

### 2.2.1 Rigid-body model equations of motion

Using the free-body diagram in figure 2.1f for a glider of mass  $m$  in an inertial reference frame defined by  $x$  and  $z$ , we write the equations of motion in the horizontal and vertical directions as

$$\begin{aligned} m\dot{v}_x &= F_L \sin \gamma - F_D \cos \gamma \\ m\dot{v}_z &= F_L \cos \gamma + F_D \sin \gamma - mg, \end{aligned} \tag{2.2.1}$$

where the overdot signifies the time derivative,  $F_L$  and  $F_D$  are the lift and drag forces,  $v_x$  and  $v_z$  are the velocities in the horizontal and vertical directions, and  $a_x = \dot{v}_x$  and  $a_z = \dot{v}_z$  are the accelerations in the horizontal and vertical directions. The instantaneous glide angle,  $\gamma = -\tan^{-1} v_z/v_x$ , is defined as positive for a clockwise rotation from the horizontal axis (i.e., the glide angle will be positive when the animal glides downward). By definition, the drag force acts counter to the local direction of forward travel along the glide trajectory, lift

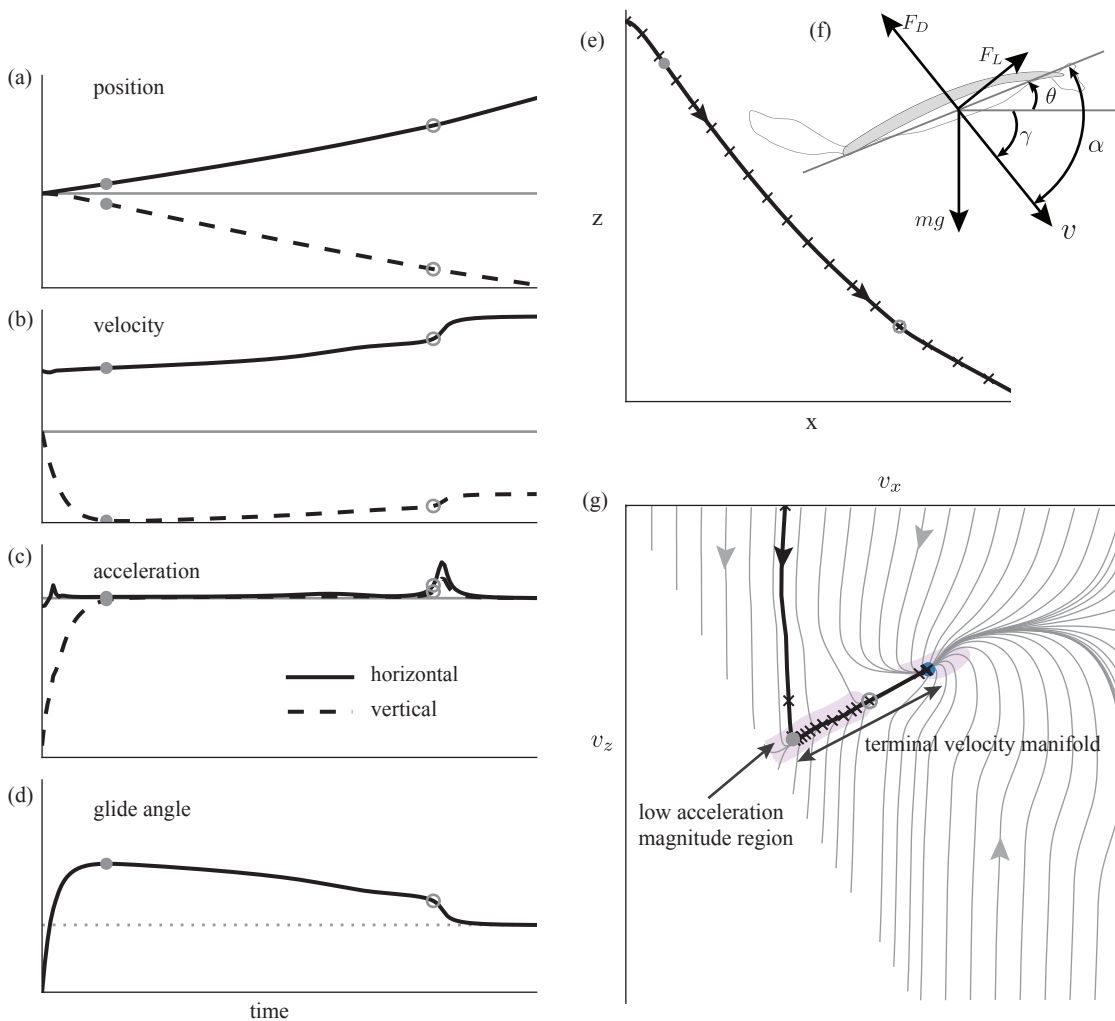


Figure 2.1: Construction of the velocity polar diagram. (a)–(d) Time histories of position, velocity, acceleration, and glide angle from one simulated glide. The solid circle denotes the location of maximum glide angle, marking the end of the ballistic phase. The open circle denotes an increase in acceleration near the end of the trajectory. The dashed line in (d) indicates the equilibrium glide angle,  $\gamma^*$ . (e) Horizontal ( $x$ ) and vertical ( $z$ ) glide path of the simulated glider, where equally spaced points in time are indicated by the ‘x’ markers, and arrows indicate the direction of forward travel. (f) Schematic of the rigid-body glider model with pitch control analyzed and simulated in this study. (g) Velocity polar diagram, with the simulated trajectory overlaid in black and motion in forward time indicated by the arrow on the trajectory. Gray lines indicate trajectories with different initial conditions of velocity. The end of the ballistic phase occurs when the velocity trajectory transitions onto the terminal velocity manifold. The terminal velocity manifold is surrounded by a low acceleration magnitude region,  $\sqrt{a_x^2 + a_z^2} < 0.1$  g, indicated by the purple shading. The animal accelerates along the manifold, indicated by loss of shading and denoted with the open circle. The stable equilibrium is denoted by the blue circle; the equilibrium glide angle is the angle subtended between the horizontal axis and a line from the origin to the equilibrium point. The empty wedge-shaped area results from the angle of attack limitations of the experimentally measured lift and drag coefficients (see Supplemental Information).

force acts normal to it, and both are written as

$$F_L = \frac{\rho v^2}{2} S C_L(\alpha), \quad F_D = \frac{\rho v^2}{2} S C_D(\alpha), \quad (2.2.2)$$

where  $\rho$  is air density,  $v = \sqrt{v_x^2 + v_z^2}$  is airspeed,  $S$  is projected surface area of the glider,  $\alpha = \gamma + \theta$  is angle of attack, and  $\theta$  is pitch angle, which specifies the angle between the mean chord line and the horizontal axis (positive counter-clockwise from the horizontal). Pitch angle is a free parameter in the model, whereas glide angle is not.

The lift and drag coefficients,  $C_L(\alpha)$  and  $C_D(\alpha)$ , are functions of angle of attack in this model, as determined from lift and drag curves specific to each glider. In general, these curves depend on airfoil shape and Reynolds number [46], and must be determined experimentally. For this analysis, we chose characteristic lift and drag curves for a particular Reynolds number and wing shape, using angle of attack as the only free parameter that determines the instantaneous lift and drag coefficients. Although the lift and drag coefficients are velocity-independent, the lift and drag forces are not. Combining equations (2.2.1) and (2.2.2), we arrive at the following expression for the glider's accelerations,

$$\dot{v}_x = \frac{\rho v^2}{2} \frac{S}{m} [C_L(\alpha) \sin \gamma - C_D(\alpha) \cos \gamma] \quad (2.2.3)$$

$$\dot{v}_z = \frac{\rho v^2}{2} \frac{S}{m} [C_L(\alpha) \cos \gamma + C_D(\alpha) \sin \gamma] - g \quad (2.2.4)$$

### 2.2.2 Dimensional analysis

We non-dimensionalize the equations of motion using the chord length  $c$  as the characteristic length scale. For a flying snake, the chord length is nominally the flattened aerial width of the animal [11, 14], and for a gliding mammal, it is the distance between the wrist and the ankle along the stretched patagium [36, 47]. The non-dimensional time scale,  $T = \sqrt{c/g}$ , is found by normalizing by the gravitational acceleration  $g$ ; it follows that the characteristic velocity scale is  $c/T = \sqrt{cg}$ . We define the non-dimensional time, velocity, and positions as

$$\bar{t} = \frac{t}{\sqrt{c/g}}, \quad \bar{v} = \frac{v}{\sqrt{cg}}, \quad \bar{p} = \frac{p}{c}.$$

where  $v$  is either  $v_x$  or  $v_z$  and  $p$  is either  $x$  or  $z$ . After substituting the non-dimensional groups into the equations of motion (2.2.3) and (2.2.4), we find

$$\begin{aligned}\frac{d\bar{v}_x}{d\bar{t}} &= \epsilon \bar{v}^2 [C_L(\alpha) \sin \gamma - C_D(\alpha) \cos \gamma] \\ \frac{d\bar{v}_z}{d\bar{t}} &= \epsilon \bar{v}^2 [C_L(\alpha) \cos \gamma + C_D(\alpha) \sin \gamma] - 1\end{aligned}$$

where the non-dimensional parameter  $\epsilon$  can be cast in terms of wing loading,  $W_S = mg/S$ , as

$$\epsilon = \frac{\rho c S}{2 m} = \frac{\rho g c}{2 W_S}$$

We define  $\epsilon$  as the universal glide scaling parameter and discuss its significance in §2.4.2.

### 2.2.3 Rescaling and final equation form

The non-dimensional equations can be further simplified by rescaling velocity and time as  $\hat{v} = \sqrt{\epsilon} \bar{v}$  and  $\hat{t} = \sqrt{\epsilon} \bar{t}$ . Writing completely in terms of  $\hat{v}_x = \hat{v} \cos \gamma$  and  $\hat{v}_z = -\hat{v} \sin \gamma$ , the Cartesian form of the equations of motion is

$$\hat{v}'_x = -\sqrt{\hat{v}_x^2 + \hat{v}_z^2} [C_L(\alpha) \hat{v}_z + C_D(\alpha) \hat{v}_x] \quad (2.2.5)$$

$$\hat{v}'_z = \sqrt{\hat{v}_x^2 + \hat{v}_z^2} [C_L(\alpha) \hat{v}_x - C_D(\alpha) \hat{v}_z] - 1 \quad (2.2.6)$$

where prime notation is used as a shorthand for rescaled time derivatives  $d/d\hat{t}$ . These equations are integrated to construct the velocity polar diagram trajectories. The polar form of the equations, written in terms of the airspeed  $\hat{v} = \sqrt{\hat{v}_x^2 + \hat{v}_z^2}$  and glide angle  $\gamma = -\tan^{-1} \hat{v}_z/\hat{v}_x$ , is

$$\gamma' = -\hat{v} C_L(\alpha) + \frac{\cos \gamma}{\hat{v}} \quad (2.2.7)$$

$$\hat{v}' = -\hat{v}^2 C_D(\alpha) + \sin \gamma \quad (2.2.8)$$

Note that the rescaled equations do not depend on body size or wing loading, but only on the lift and drag coefficients. Therefore, any differences in glide performance must result from differences in the lift and drag curves.

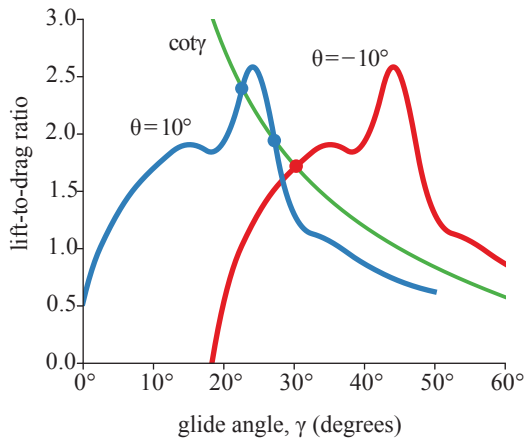


Figure 2.2: Pitch as a bifurcation parameter. Increasing the body pitch angle  $\theta$  shifts the lift-to-drag ratio curves horizontally to the left, which changes the number of intersections with  $\cot \gamma$ . Each intersection is an equilibrium point, which are indicated by round markers at the intersection points for varying pitch angles. Force coefficient data are for a flying snake cross-sectional shape [14] at  $Re=11,000$ .

## 2.2.4 Equilibrium gliding

Equilibrium gliding occurs when the resultant aerodynamic force balances the gravitational force on the glider, producing a constant glide angle and speed. This condition requires that the left-hand sides of expressions (2.2.5) to (2.2.8) are zero, resulting in the equilibrium states  $(\hat{v}_x^*, \hat{v}_z^*)$  and  $(\gamma^*, \hat{v}^*)$ . Once the equilibrium glide angle  $\gamma^*$  is known, the equilibrium airspeed  $\hat{v}^*$  is determined from equations (2.2.7) or (2.2.8), and the equilibrium horizontal and vertical velocities are found using  $\hat{v}_x^* = \hat{v}^* \cos \gamma^*$  and  $\hat{v}_z^* = -\hat{v}^* \sin \gamma^*$ . Simple algebraic manipulation of the equilibrium equations of motion results in the well-known expression for the equilibrium glide angle

$$\frac{F_L}{F_D} = \frac{C_L(\alpha^*)}{C_D(\alpha^*)} = \frac{C_L(\gamma^* + \theta)}{C_D(\gamma^* + \theta)} = \cot \gamma^*, \quad (2.2.9)$$

where  $\alpha^* = \gamma^* + \theta$ . This transcendental equation for the equilibrium glide angle  $\gamma^*$  can have multiple solutions, which depend on the number of times the lift-to-drag ratio curve ( $C_L/C_D$ ) intersects the  $\cot \gamma^*$  curve. Furthermore, the location and number of equilibria depend on the pitch angle  $\theta$ . Because lift and drag are not analytical expressions of angle of attack, the equilibrium glide angle is found numerically. From equation (2.2.9), changing the pitch angle shifts the equilibrium glide angle, and to find these values, we consecutively shifted the lift-to-drag ratio curve over a range of specified pitch angles and used the Newton-Raphson root-finding method to locate the intersections. This technique is shown in figure 2.2, where two equilibrium glide states exist for a pitch of  $10^\circ$  and only one equilibrium for a pitch of  $-10^\circ$ .

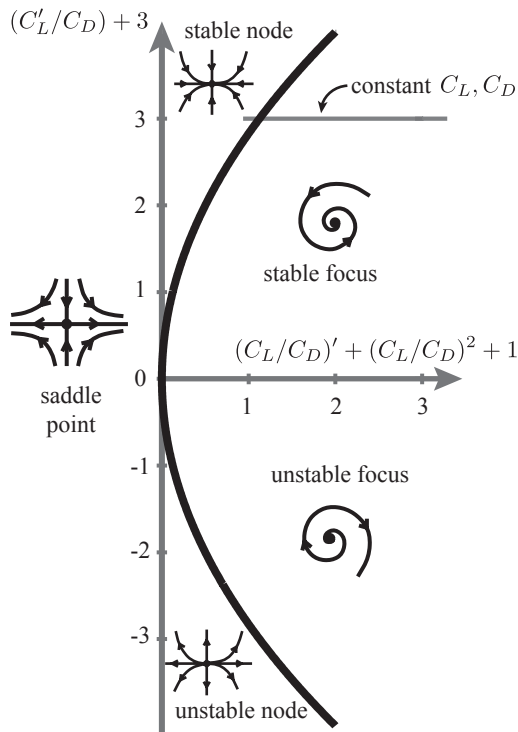


Figure 2.3: Summary of equilibrium type as a function of lift and drag curves. The equilibrium type is uniquely determined by the lift and drag curves and their slopes evaluated at the equilibrium angle of attack. Previous models of animal gliding, which assumed constant lift and drag coefficients, only observed stable node and stable focus type equilibrium points, as indicated by the horizontal gray line.

### 2.2.5 Equilibria type and stability analysis

To determine the stability type and location of equilibrium points in the velocity polar diagram, we use linear stability analysis [48] by classifying the eigenvalues of the Jacobian matrix of partial derivatives for the polar coordinate equations (2.2.7) and (2.2.8) evaluated at equilibrium. For this system of two equations, the eigenvalues  $\lambda_{1,2}$  are

$$\lambda_{1,2} = \frac{C_D}{2(C_L^2 + C_D^2)^{1/4}} \left( -\tau \pm \sqrt{\tau^2 - 8\Delta} \right), \quad (2.2.10)$$

$$\tau = (C_L/C_D) + 3 \quad (2.2.11)$$

$$\Delta = (C_L/C_D)' + (C_L/C_D)^2 + 1 \quad (2.2.12)$$

where  $(C_L/C_D)'$  denotes the slope of the lift-to-drag ratio curve. The stability type depends on both the magnitude and slope of the lift and drag curves at equilibrium. This system permits five common types of equilibrium points, based on the signs and magnitudes of  $\tau$  and  $\Delta$ : stable and unstable foci, stable and unstable nodes, and saddle points. A summary of these equilibrium types is shown in figure 2.3.

If lift and drag coefficients are independent of angle of attack, then the primed terms in equations (2.2.11) and (2.2.12) are zero, and only stable equilibria are possible. That is, the simulated glider will never have a horizontal velocity of zero and will always reach an equilibrium with some horizontal velocity. Additionally, that equilibrium will be a stable focus if lift-to-drag ratio exceeds the low value of  $1/2\sqrt{2} \approx 0.354$  ( $\gamma^* > 70.53^\circ$ ), and otherwise will be a stable node. If lift and drag coefficients are dependent on angle of attack, more dynamical behavior is possible.

### 2.2.6 Model input from experimentally measured lift and drag curves

To test the effect of angle-of-attack-dependent force coefficients and the applicability of the non-equilibrium gliding framework, we use aerodynamic coefficient curves (figure 2.4) from a range of animal gliders, including flying squirrel [35], flying snake [14], sugar glider [42], and flying fish [43], as well as two active flyers, juvenile chukar partridge at 20 days post hatch (d.p.h.) [44], and dragonfly [45]. These species vary in size, Reynolds number, and aerodynamic force-producing structure. The chukar at 20 d.p.h can sustain level flight, but lacks the locomotor capacity of adults, as the wing is still developing and produces only small amounts of lift. Dragonflies use brief periods of gliding, lasting up to 0.5 seconds and covering 1 m. However, gliding is often interrupted by wingbeats, so glide durations are short (less than 0.2 s, mean of 0.13 s [45]). Coefficient curves are classified in three ways, based on data from previous studies (table 2.1). The ‘airfoil’ curves are from wind tunnel experiments of a representative airfoil model. The ‘whole animal’ curves are from wind tunnel measurements of a deceased and taxidermically-prepared animal. The ‘kinematics curves’ are reconstructed from recorded glide trials of flying squirrels, and are further discussed below. The coefficient values were smoothed with third-order B-splines to provide a continuous representation for simulations and stability calculations.

Because the aerodynamic coefficients for the entire animal will be different from those of the airfoil alone [49], we also analyzed force coefficient curves (figure 2.7a) derived from kinematics measurements of flying squirrels gliding to a tree located 18 m from the launch platform [26]. These ‘kinematics’ coefficient curves were back-calculated from individual glides, as well as from an ensemble of all glides (see Supplemental Information). To reconstruct the angle-of-attack-dependent coefficients, first the force coefficients were calculated

by rearranging equation (2.2.2). Second, the time-varying angle of attack was approximated as the sum of the calculated glide angle and an assumed pitch angle of zero degrees. We had to approximate the pitch angle because it was not available from the kinematics data. In general, the force coefficient curves measured from wind tunnel tests are of higher quality because 1) the velocities and angles of attack are precisely known, 2) they cover a wider angle of attack range, and 3) noise-magnifying numerical derivatives [50] are not present. Nonetheless, these coefficient curves were included to help synthesize theoretical predictions with observed glides.

Table 2.1: Types of force coefficient data used in this study. Details describing the derivation of the kinematic squirrel coefficients are presented in the Supplemental Information.

Animal	Data source	Description	Source
Flying squirrel	airfoil	Latex membrane in a wind tunnel	[35]
Flying snake	airfoil	Printed cross-section of <i>Chrysopelea paradisi</i> body	[14]
Chukar 20 d.p.h.	airfoil	Juvenile <i>Alectoris chukar</i> wing	[44]
Sugar glider	whole animal	<i>Petaurus breviceps papuanus</i> placed in wind tunnel	[42]
Dragonfly	whole animal	<i>Calopteryx splendens</i> placed in wind tunnel	[45]
Flying fish	whole animal	<i>Cypselurus hiraii</i> placed in wind tunnel, model L2	[43]
Kinematic squirrel	kinematics	Ensemble of <i>Glaucomys sabrinus</i> glides	[26]
Individual squirrel	kinematics	Individual <i>Glaucomys sabrinus</i> glides	[26]

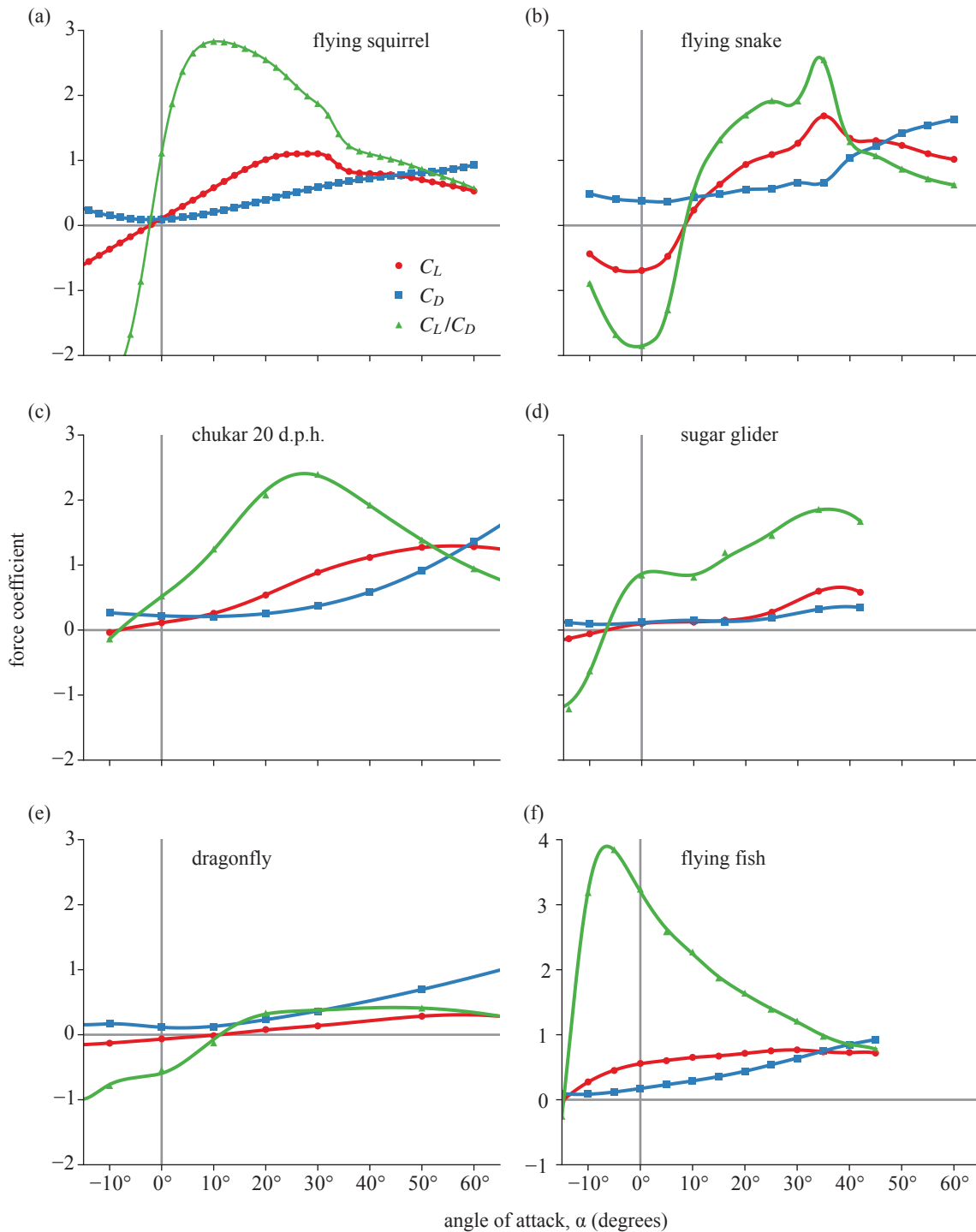


Figure 2.4: Lift, drag, and lift-to-drag ratio coefficient curves used in this study. Airfoil-based curves for (a) flying squirrels [35], (b) flying snakes [14], and (c) chukar partridge [44], and whole-animal curves for (d) sugar gliders [42], (e) dragonflies [45], and (f) flying fish [43]. Measured values are indicated with markers, and spline-fit values are indicated with solid lines.

## 2.2.7 Model assumptions

The complete non-equilibrium glide framework consists of the equations of motion, equations (2.2.5) to (2.2.8), and lift and drag coefficients determined from experiments. The model assumes angle-of-attack dependent, but velocity independent, quasi-steady lift and drag coefficients that are representative of the animal mid-glide. Although lift and drag coefficients are velocity independent, the lift and drag forces depend on the instantaneous velocity. Additionally, we do not explicitly model the rotational motion of the glider, but instead treat only one rotational direction, pitch, as a parameter that is systematically varied to elicit different glide performance. Finally, we treat motion in the vertical  $x$ - $z$  plane only, ignoring side forces and full three-dimensional glide trajectories resulting from yaw and roll rotations. The above assumptions provide the simplest model to explore the effect of angle-of-attack dependent lift and drag coefficients on a glider's trajectory dynamics.

## 2.3 Results

### 2.3.1 Structure of the velocity polar diagrams

Velocity polar diagrams for the airfoil and whole-animal-based lift and drag curves are shown in figure 2.5 for two different pitch angles. In these plots, initial conditions from the animal gliders originate near the origin of the diagram, with a near-zero vertical velocity and low horizontal velocity. These plots show that only certain equilibrium glides can be reached for the initial conditions typically observed in real glides. The velocity polar diagrams generally have multiple equilibria including stable nodes and saddle points. The stable and unstable manifolds of the saddle point delineate the basins of stability of stable glides. The upper stable branch of the saddle point, which runs vertically through the diagrams, acts as a separatrix (*sensu* Strogatz [48]) and can block accessibility to low glide angle equilibrium points. Additionally, saddles show that there are stable and unstable directions in the velocity polar diagram; these directions determine the glider's trend toward equilibrium.

Nearly all velocity trajectories in figure 2.5 (except for figure 2.5dii) fall quickly onto a one-dimensional manifold. If the trajectory originates in the basin of stability of the equilibrium point, the trajectory moves along the manifold and stable gliding is achieved. Otherwise, the trajectory is pushed to a steep glide where the horizontal velocity is low and the animal is

in effect falling. The initial quick descent of the glider to the manifold corresponds to the ballistic phase of gliding (figure 1d and 1g), and movement along the manifold corresponds to the shallowing phase of gliding. We designate this one-dimensional manifold as the ‘terminal velocity manifold’ as it is a higher-dimensional analog of the terminal velocity, and dynamics along it are a relatively slow evolution toward stable equilibrium. The terminal velocity manifold is approximated by the curve of zero vertical acceleration, the  $v_z$  nullcline, along which equation (2.2.6) is zero. A trajectory in the vicinity of the nullcline would be in a near-vertical force balance, with the vertical component of the total aerodynamic force balancing the weight of the glider. Nullclines are shown on the flying snake and chukar velocity polar diagrams (figures 2.5bi, ci, and cii). These curves pass through any equilibrium points present in the velocity polar diagram, and best approximate the terminal velocity manifold locally around the stable node. If a saddle point exists (e.g., figure 2.5ai, aii, bii, cii, and fi), then the terminal velocity manifold is also approximated by the unstable branch of a saddle point and the less-stable manifold of a stable node. Furthermore, we can approximate the terminal velocity manifold analytically (see Supplemental Information), as shown in the inset of figure 2.5bii.

Low-acceleration regions ( $a \leq 0.1$  g where  $a = \sqrt{a_x^2 + a_z^2}$ ) are identified by shading in all velocity polar diagrams in figure 2.5. These regions are located around the equilibrium points and along terminal velocity manifolds, which indicates that the glider will exhibit little change in velocity while far from equilibrium, with glide dynamics dictated by the direction of the manifold. Trajectories can also leave the low-acceleration region (figures 2.5bi and 2.5bii) while moving along the terminal velocity manifold towards equilibrium. In these velocity polar diagrams, this results from the peak in the lift-to-drag ratio of the flying snake coefficients near an angle of attack  $35^\circ$  (figure 2.4b).

### 2.3.2 Pitch bifurcation diagrams

The equilibrium points and corresponding equilibrium glide angles shown in figure 2.5 are summarized in a single bifurcation diagram for each glider in figure 2.6. For a given pitch angle, these diagrams show the stability type and glide angle of all possible equilibrium glides.

The bifurcation diagrams show multiple co-existing equilibrium points at high and low angles of attack, which persist over a range of pitch angles. The flying squirrel bifurcation diagram (figure 2.6a) shows that upwards of four co-existing equilibrium points are possible. In general, only a single stable equilibrium exists when pitch is negative, with equilibrium glide angles relatively insensitive to pitch. We refer to the slope of the pitch bifurcation curve along the branch of stable equilibrium points as the ‘pitch sensitivity’, calculated as  $d\gamma^*/d\theta$ . For the flying squirrel bifurcation diagram, a saddle-node bifurcation occurs at a maximum pitch of  $2^\circ$ . Beyond this pitch angle, no shallow equilibrium glides are observed, and the glider is essentially falling. The flying snake bifurcation diagram (figure 2.6b) is similar to the flying squirrel bifurcation diagram, except that more than four equilibria are possible at select pitch angles around  $1^\circ$ . The stable node and saddle point are much closer, and no equilibrium glides are found beyond the saddle-node bifurcation at a pitch angle of  $12^\circ$ .

The chukar, sugar glider, and dragonfly bifurcation diagrams (figure 2.6c, d, and e) show a flat equilibrium glide angle region over a large range of pitch angles. Due to the low lift-to-drag ratio of the dragonfly, equilibrium glides are steep, being nominally  $70^\circ$  in glide angle. The flying fish and dragonfly bifurcation diagrams show that only negative pitch angles allow stable equilibria; in this condition, a flying fish or dragonfly would be nose-down at equilibrium.

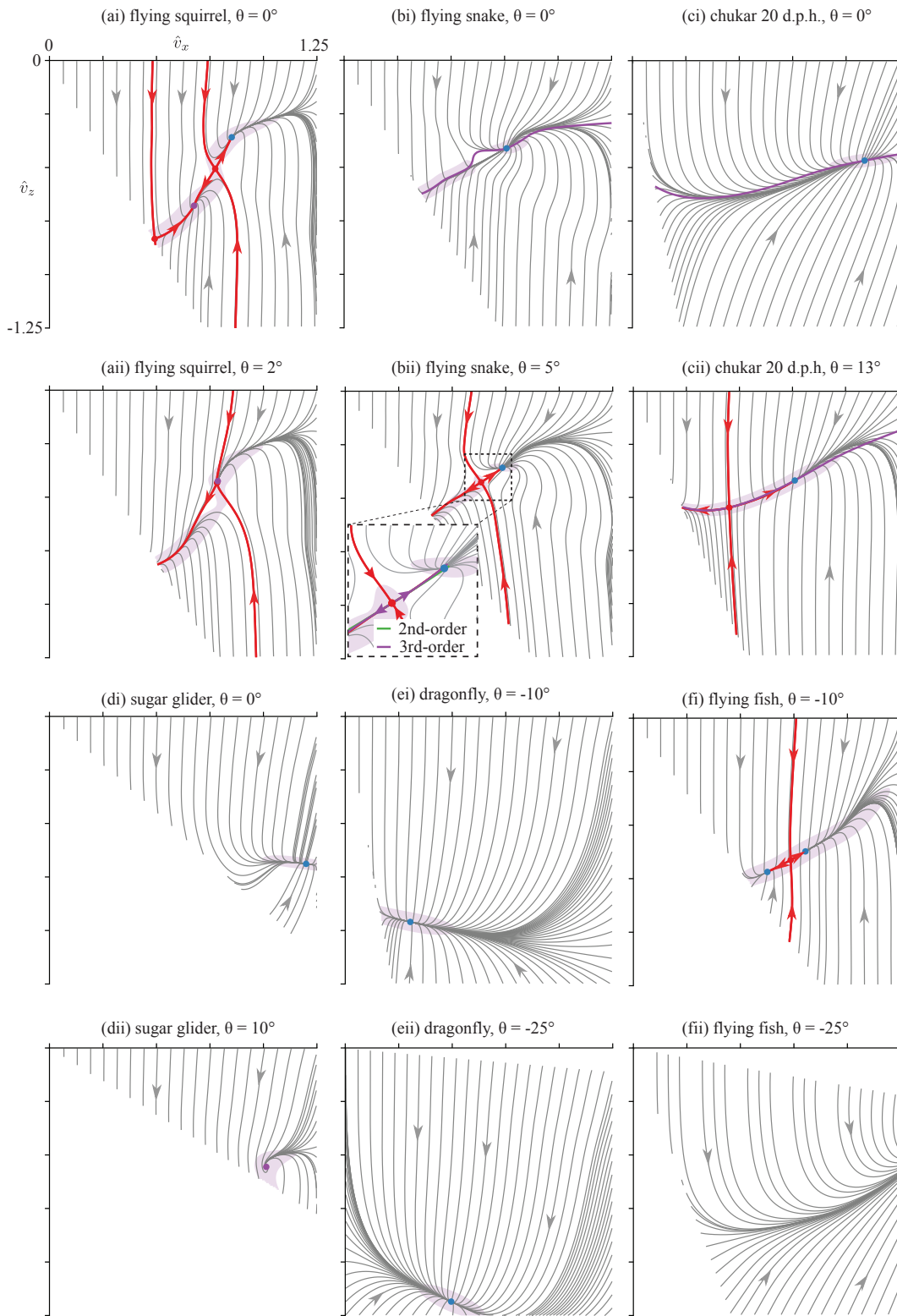


Figure 2.5: Caption on next page.

Figure 2.5: (Previous page.) Velocity polar diagrams. Two different pitch values, indicated by (i) and (ii), are shown for (a) flying squirrels, (b) flying snakes, (c) chukar partridge, (d) sugar gliders, (e) dragonflies, and (f) flying fish. Pitch values are specified by vertical lines in figure 2.6. Gray lines are simulated glide trajectories, and arrows indicate motion along the trajectory through time. Equilibrium gliding is indicated by circle markers, and the glide angle is read as the angle subtended from the horizontal axis as before to the equilibrium point(s). Saddle points and their stable and unstable branches are indicated in red, with separatrices running vertically to the saddle points. The inset in (bii) shows 2<sup>nd</sup> and 3<sup>rd</sup>-order accurate analytical approximations of the terminal velocity manifold in the vicinity of the saddle point equilibrium. Vertical velocity nullclines, where the vertical acceleration is zero, are shown in (bi), (ci), and (cii), as the solid purple line passing through the equilibrium points and near the terminal velocity manifold.

### 2.3.3 Velocity polar diagrams from kinematics data

To demonstrate how these analytical methods can be applied to experimental data, we used mean force coefficients from a flying squirrel glide experiment (figure 2.7a) as model inputs to construct both a bifurcation diagram (figure 2.7b) and velocity polar diagrams at zero and positive pitch values (figures 2.7ci and cii). The kinematic squirrel velocity trajectories show spiraling behaviors around both stable or unstable foci. This spiraling is also present in the velocity polar diagrams derived from individual glide trials (figure 2.7d and e), with the experimental velocity trajectory overlaid.

The kinematic squirrel bifurcation diagram (figure 2.7b) shows foci at low equilibrium glide angles that are insensitive to pitch; in particular, the equilibrium glide angle is almost constant from  $-5^\circ$  to  $4^\circ$ . The two solid lines in this figure indicate the maximum and minimum glide angles of an unstable periodic orbit, which exists between Hopf bifurcation points at  $\theta \approx -1^\circ$  and  $\theta \approx 5.6^\circ$ . This corresponds to the unstable periodic orbit in figure 2.7ci and the only closed contour in the velocity polar diagram. This Hopf bifurcation occurs any time the equilibrium changes from an unstable to a stable focus (and vice versa), and the characteristics of the resulting periodic orbit can be computed analytically given the lift and drag curves (see Supplemental Information).

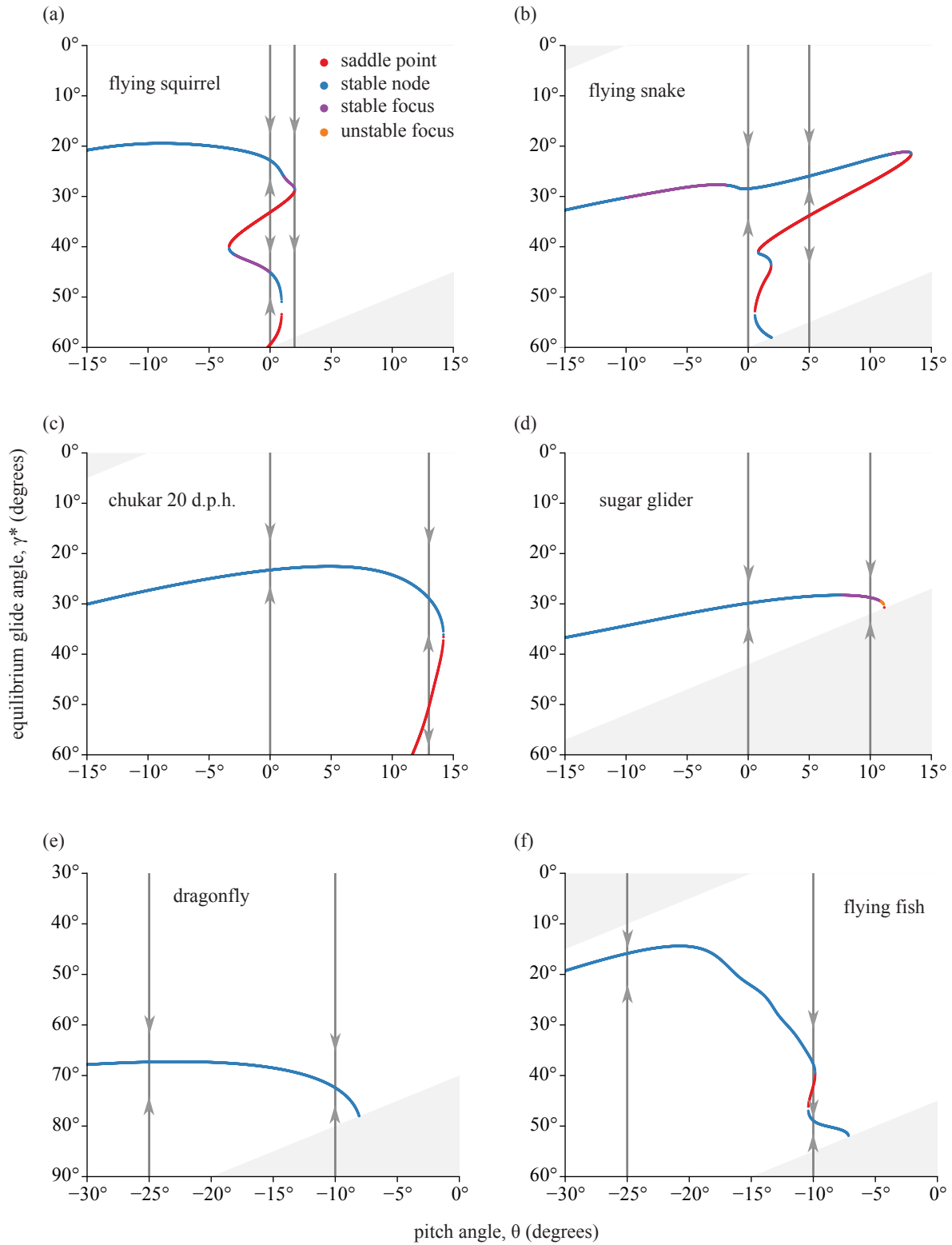


Figure 2.6: Caption on next page.

Figure 2.6: (Previous page.) Pitch bifurcation diagrams for equilibrium glide angle  $\gamma^*$  as pitch angle  $\theta$  varies. Diagrams correspond to (a) flying squirrels, (b) flying snakes, (c) chukar partridge, (d) sugar gliders, (e) dragonflies, and (f) flying fish. Equilibrium glide angles are found as intersection(s) of the bifurcation curve with vertical lines at a specified pitch angle, with multiple intersections indicating multiple equilibrium points. Colors correspond to different equilibrium types; cool colors are locally attracting and warm colors are locally repelling. Vertical lines indicate pitch angles used in the velocity polar diagrams in figure 2.5, and the arrows on these lines indicate the passive direction change of glide angle. Not all angles of attack were available in the original data; these regions are indicated with gray shading.

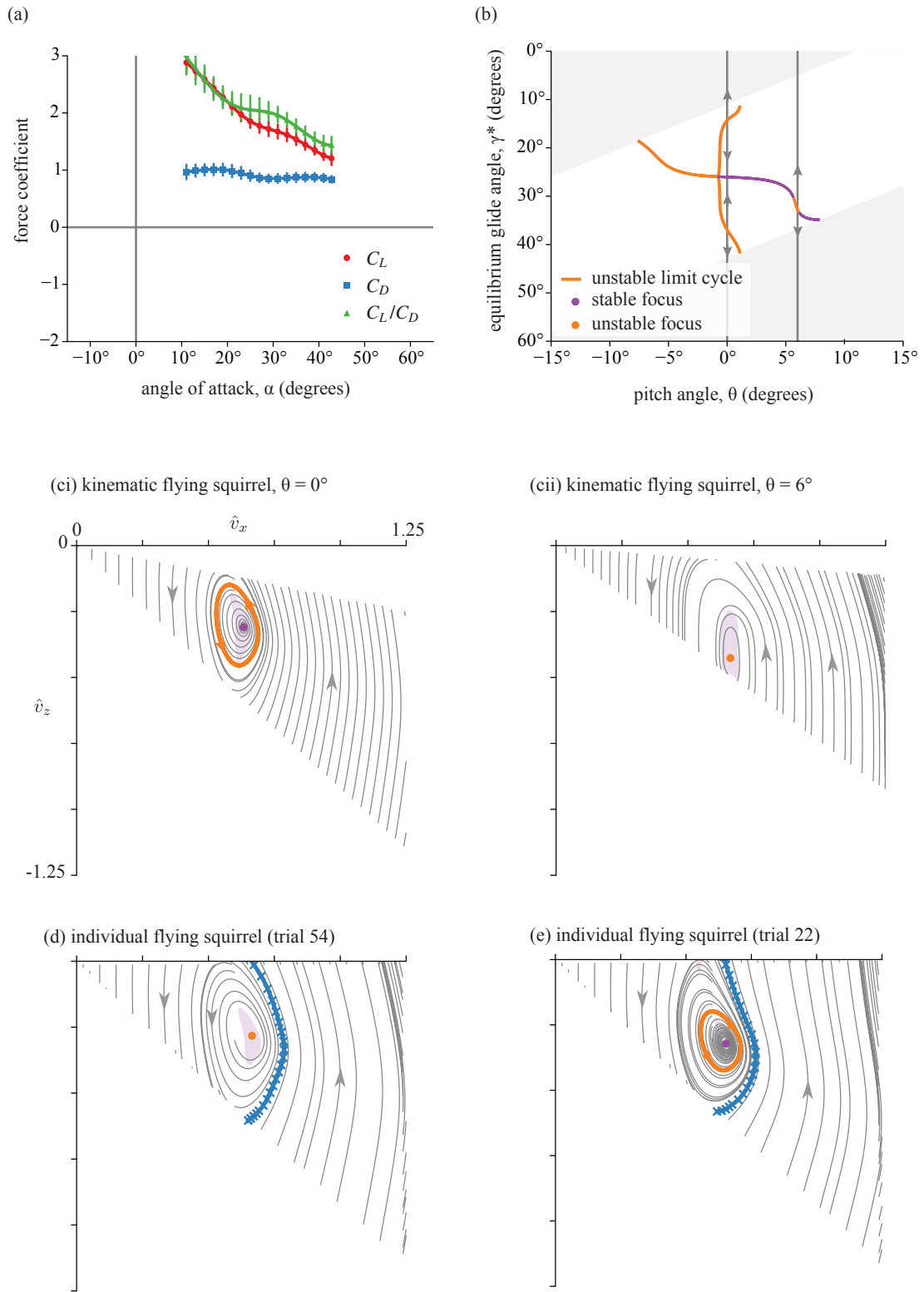


Figure 2.7: Caption on next page.

Figure 2.7: (Previous page.) Non-equilibrium glide framework applied to kinematics data of flying squirrels from ref. [26]. (a) Aerodynamic coefficients derived from an ensemble of kinematics measurements. Solid points are mean  $\pm$  s.e.m. (b) Pitch bifurcation diagram. (ci, cii) Velocity polar diagrams at zero and positive pitch angles, respectively. The closed contour in (ci) is a periodic orbit due to a Hopf bifurcation. (d, e) Velocity polar diagrams derived from individual glide trials. The calculated velocity trajectory is indicated in blue and equal time points are indicated at 0.08 s intervals. Note that all velocity polar diagrams have the same limits because the kinematics data have been non-dimensionalized and rescaled.

## 2.4 Discussion

We have developed a dynamical systems framework to understand non-equilibrium animal gliding based only on the lift and drag coefficients. In this conceptualization of gliding, equilibrium is represented as a point in the velocity polar diagram where the accelerations are zero; trajectories will progress towards or away from equilibrium depending on the initial conditions and the equilibrium type. Analysis of the velocity polar diagram indicates that pitch angle has a large effect on the glide trajectory and that animal gliding has more complicated dynamics than previously realized. However, these dynamics can be systematically explored using the velocity polar diagram and by incorporating the lift and drag coefficient curves into the equation of motion.

### 2.4.1 Effect of lift and drag coefficients

Because lift and drag coefficients are the only model inputs, the analysis presented here can be viewed as a parametric study of representative lift and drag curves and how the structure of these curves affects non-equilibrium gliding. The analytically-derived expressions for equilibrium type (figure 2.3) and the general topology of the velocity polar diagrams (figure 2.5) indicate commonalities in how glide trajectories proceed based solely on the lift and drag curves. First, multiple equilibria are possible, and these generally occur for slightly negative to positive pitch values. Second, unstable equilibria are possible, particularly saddle points which appear along a terminal velocity manifold. Third, spiraling motion in the velocity polar diagram is seen in several of the diagrams, particularly from the kinematics curves, but also when lift and drag coefficients are constants.

The difference in velocity polar diagram structure when there is a terminal manifold or when there is a focus-type equilibrium suggests future extensions of this work to investigate if gliders switch between different glide motifs. The motion around a focus-type equilibrium in the kinematics-based flying squirrel velocity polar diagrams (figure 2.7c, d, e), with a decrease in vertical velocity throughout the trajectory, is not seen in the airfoil-based velocity polar diagrams (figure 2.5). These different gliding motifs could provide complementary means to modify the glide path, but how the animal switches between them is unknown. For example, the focus-based motif should lessen landing forces, because the vertical velocity is near zero or merely slightly positive at the end of the glide. However, the animal would have higher

accelerations throughout the glide, which in theory would require more control authority to maintain stability. In the terminal velocity manifold motif, accelerations are lower for the majority of the glide, but a large pitch-up maneuver would be required for landing to lower the airspeed. How the animal switches between these motifs with changes to lift and drag coefficients, or with unsteady aerodynamic and/or fluid-structure interaction effects [51–53], are important considerations for future work.

Calculating the kinematics-based lift and drag coefficient curves was done as a way to compare measured animal trajectories to model predictions. The velocity polar diagrams derived from wind tunnel measurements (figures 2.5ai, aii, di, and dii) are substantially different from the kinematics-based ones (figures 2.7c, d, e). There are several possible reasons for this. One possibility is that the kinematics data are insufficient (due to undersampling, noise, or experimental error) to derive force coefficient curves. The kinematics data lack the ballistic phase of the glide, and the assumption of zero pitch angle used to derive the kinematics-based curves is likely to be invalid over part of the glide. Another possibility is that wind tunnel coefficient curves do not accurately represent the whole-animal aerodynamics in flight. This is most likely true for the artificial membrane curves, in which a thin latex sheet represents the patagial membrane, but does not include the limbs and tail of the flying squirrel. The sugar glider coefficient curves provide an intermediary to understand whole-animal lift and drag characteristics, as it is of a taxidermically prepared mammal in a likely flight configuration. In fact, these curves show spiraling in the velocity polar diagram (figure 2.5dii) for certain positive pitch angles, which is a likely flight posture used by flying squirrels [34]. Spiraling is also seen in the kinematics-based velocity polar diagrams in figures 2.7c, 2.7d, and 2.7e.

## 2.4.2 Comparison to other modeling studies of gliding

In the model presented here, the magnitude and orientation of the aerodynamic force vectors are modulated by pitch angle. Previous particle models were not directional, with the aerodynamic force vectors evolving under passive dynamics only [11, 25, 26, 40]. However, both types of models neglect rotational stability and consider translational motion assuming quasi-steady aerodynamics.

A significant difference between previous models and the model presented here is that lift and drag coefficients are not constants, but instead are angle of attack dependent. This difference

results in drastically different simulated glide trajectories in both position and velocity space. When lift and drag coefficients are constants, only stable equilibria are possible, meaning that there are no physically realistic values of initial velocity or wing loading that result in falling directly downward. Additionally, these equilibria are predominantly of the focus type — the oscillatory behavior observed in previous models was a consequence of the lift-to-drag ratio only. This oscillatory behavior is very evident when viewed in the velocity polar diagram (see figure 1 in the Supplemental Information). The glider does not smoothly transition from the ballistic phase to motion along the terminal velocity manifold, but instead oscillates towards an equilibrium glide.

When aerodynamic force coefficients depend on angle of attack, coexisting stable and unstable equilibrium points are possible. These equilibrium points organize the global topology of the velocity polar diagram and segregate regions that are reachable from typically low take-off velocities, rendering certain stable glide trajectories infeasible. Certain equilibria become inaccessible when a saddle point appears along the terminal velocity manifold. Because glides originate in the upper left quadrant of the velocity polar diagram, with near-zero vertical velocity and small horizontal velocity, the upper branch of the saddle point’s stable manifold acts as a separatrix, which blocks low glide angle equilibrium points. The appearance of a saddle point explains the basin of stability observations in the  $\theta_0 - \dot{\theta}_0$  space in previous snake modeling work [17], as certain initial condition combinations can lead to unsuccessful glides. In that previous study, the pitch rate affects the traversal of the non-autonomous velocity space, where this separatrix appears and blocks stable glides. This effect can also be understood as sweeping through pitch angle in the pitch bifurcation diagram in figure 2.6b, where moving from negative to slightly positive pitch leads to a saddle-node bifurcation.

The newly presented non-dimensionalization and rescaling of the equations of motion is a significant difference from previous studies. This rescaling reduces the difference between species to their lift and drag coefficient curves only. The universal glide scaling parameter ( $\epsilon \propto c/W_S$ ) not only facilitates modeling and normalization of experimental trajectories, but provides a metric to compare gliders based on their chord length and wing loading. Under geometric scaling of isometry, and assuming  $c \propto L$  and  $m \propto L^3$ , one would expect chord length to scale as  $c \propto m^{1/3}$ . Experimental data suggest that wing loading scales isometrically,  $W_S \propto m^{1/3}$  [22], so one would therefore expect  $\epsilon = \text{constant}$  for a given species. The universal glide scaling parameter is shown in figure 2.8 for a variety of animal gliders across several orders of magnitude of mass. The scaling of  $\epsilon$  with mass is not as evident as with wing

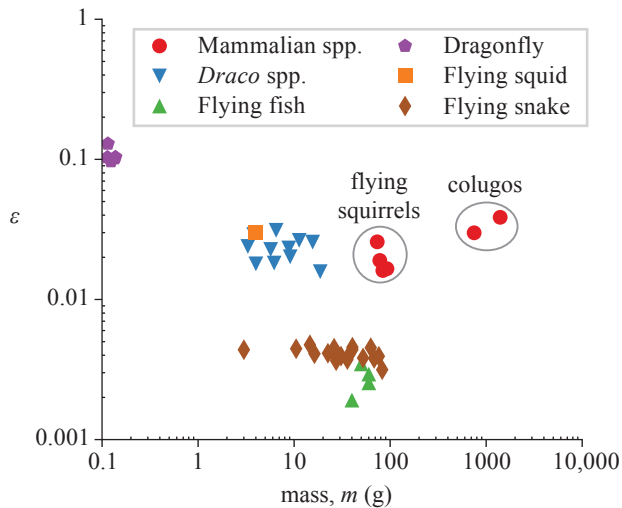


Figure 2.8: Universal glide scaling parameter  $\epsilon$  for gliding animals. Mammalian data for flying squirrels, sugar gliders, and colugos are from refs. [26, 27, 36, 47, 54], *Draco* data are from refs. [28, 29], flying fish (*Cypselurus hiraii*) data are from ref. [43], dragonfly (*Sympetrum sanguine*) data are from ref. [45], flying squid (*Sthenoteuthis ptepus*) data are from ref. [22, 55], and flying snake (*Chrysopelea paradisi*) data are from refs. [8, 9, 22].

loading [22], but there appear to be three distinct groupings. The first grouping has an  $\epsilon$  value of 0.1 and includes dragonflies only. The next grouping has an  $\epsilon$  of 0.04 and includes *Draco*, squid, and mammals. The third grouping, with an  $\epsilon$  of 0.003, includes flying snakes and flying fish. For flying snakes,  $\epsilon$  is nearly constant over two orders of magnitude in mass, and for *Draco*,  $\epsilon$  is nearly constant over one order of magnitude in mass. These different scaling groups suggest that the chord length used to non-dimensionalize the equations of motion has a large effect on  $\epsilon$  for different gliding species.

The universal glide scaling parameter also helps to explain why smaller individuals with lower wing loading are generally better gliders, covering more horizontal distance from a given take-off height. The framework presented here identifies equilibrium points in the velocity polar diagram, but it does not specify the time required to reach equilibrium. By converting both time and velocity back to physical units using  $\epsilon$ ,

$$t = \sqrt{\frac{2W_S}{\rho g^2} \hat{t}}, \quad v = \sqrt{\frac{2W_S}{\rho} \hat{v}} \quad (2.4.1)$$

we see that both dimensional time and velocity are proportional to the square root of wing loading. Because the time to equilibrium  $\hat{t}$  is fixed in (2.4.1), the glider with lower wing loading will reach equilibrium sooner. If a large and a small individual were to take off from the same physical height and with the same initial conditions in the velocity polar diagram, the smaller individual would traverse more of the velocity space before landing. This would correspond with a higher shallowing rate, lower velocity, and greater horizontal distance

traveled.

### 2.4.3 Implications for animals that glide

The global view of gliding developed here provides insight into how a glider's translational motion changes with pitch. The results of this work show that once the glider is at equilibrium, changing pitch angle has only a small effect on glide angle. For example, for the sugar glider (figure 2.6d), the equilibrium glide angles change only  $10^\circ$  over a pitch range of  $25^\circ$ . A similar trend holds for the other wind-tunnel based bifurcation diagrams, in which the low glide angle equilibrium is relatively insensitive to pitch. The initial launch parameters and the ballistic glide phase are therefore important because they determine how close to the basin of stability the glider is, and if control is needed to select a stable equilibrium. This analysis suggests that animals could select pitch values to avoid unstable features in the velocity polar diagram, with a worst-case scenario resulting in a fall with negligible horizontal velocity. A negative pitch angle shortly after launch and through the ballistic phase will confer greater translational stability, and will also act to direct the lift vector horizontally.

Additionally, hysteresis effects are possible as the pitch angle changes. The equilibrium glide angle can increase rapidly if the pitch angle increases above a critical threshold (figures 2.6a and b). To re-establish a low glide angle equilibrium glide, a glider would have to decrease its pitch to a negative value so that only the upper stable branch of equilibria are possible. Therefore, a pitch-up maneuver prior to landing would not only slow the animal, but may remove all equilibria from the velocity polar diagram, so the animal would begin to fall. Only very steep glides are possible for some animals, such as dragonflies (figure 2.6e) and gliding arthropods. Arthropod glide trajectories consist of large glide angles between  $70^\circ$ – $75^\circ$  and small lift-to-drag ratio of approximately 0.3 [31–33]. Although lift and drag coefficient data are not available, these steep trajectories suggest velocity polar diagram structure similar to figure 2.5e, with steep glides to a stable equilibrium.

The framework presented here also helps to address the question of if and when equilibrium is reached in gliding, as it clearly distinguishes true equilibrium where accelerations are zero, from equilibrium-like gliding in the shallowing phase and along the terminal velocity manifold where accelerations are small. Measured fluctuations of the glide path, which indicate non-equilibrium gliding, can occur for several reasons. One possibility is the animal in such a trajectory is using small postural changes to maintain a particular pitch angle or to slightly

alter the glide path. Another possibility is that experimental errors, from digitization and numerical derivatives of position data, give the appearance of spurious fluctuations. In either case, although its velocities and accelerations are changing, the glider is in effect confined to a region around equilibrium as it moves along the  $v_z$  nullcline and the terminal velocity manifold. The animal's trajectory in the velocity polar diagram, or its pitch angle history when viewing the pitch bifurcation diagram, can then be used to quantify the amount of non-equilibrium gliding and possibly control effort to maintain stability.

Lastly, the non-equilibrium gliding framework helps to elucidate the role of aerodynamic coefficients and airfoil performance on the evolution of flight. It has been previously suggested that phugoid gliding (long-wavelength oscillation of the glide trajectory) was used by the feathered dinosaur *Microraptor gui* [56]. These phugoid oscillations can be viewed as the position-space representation of a stable focus in the velocity polar diagram. Other phase-space structures, such as the terminal velocity manifold and the acceleration along it, likely confer other stability or energetic advantages. Detailed wind tunnel measurements of aerodynamic coefficients of *Microraptor gui* [57] can be used in the framework presented here to quantify how phase-space structures lead to variable glide performance between prehistoric and modern gliders.

## 2.5 Conclusions

We have presented a non-equilibrium framework of animal gliding based on the underlying structure in the equations of motion and empirically measured lift and drag coefficient curves. We find several structures in the velocity polar diagram relevant to gliders, including a terminal velocity manifold surrounded by low acceleration magnitude regions, saddle points that define the basin of stability of low glide angle equilibrium points, and equilibrium points of varying type and stability that affect glide performance. This framework not only clarifies previous modeling studies which assumed constant lift-to-drag ratio, but indicates how an animal can actively control its glide trajectory using pitch angle. New pitch bifurcation diagrams show how the equilibrium points change with pitch angle, and how the equilibrium points alter the structure of the velocity polar diagram during all phases of gliding. As more detailed kinematics data become available, this framework can be used to understand how experimentally recorded gliders alter their trajectory through control of body orientation and the likely drivers of this control. This framework also suggests that the glide dynamics

of engineered aerial and aquatic autonomous gliders can be designed to exploit the structure of the velocity polar diagram. To exploit the structure of the velocity polar diagram would require designing angle-of-attack dependent lift and drag coefficients such that equilibria of known type, stability, and equilibrium glide angle are placed in the velocity polar diagram. The autonomous glider would then only need small actuations in pitch angle to passively switch to different glide states.

## References

- [8] J. J. Socha, T. O'Dempsey, and M. LaBarbera. A 3-D kinematic analysis of gliding in a flying snake, *Chrysopelea paradisi*. *J. Exp. Biol.* 208 (2005), p. 1817–1833. DOI: 10.1242/jeb.01579.
- [9] J. J. Socha and M. LaBarbera. Effects of size and behavior on aerial performance of two species of flying snakes (*Chrysopelea*). *J. Exp. Biol.* 208 (2005), p. 1835–1847. DOI: 10.1242/jeb.01580.
- [11] J. J. Socha, K. Miklasz, F. Jafari, and P. P. Vlachos. Non-equilibrium trajectory dynamics and the kinematics of gliding in a flying snake. *Bioinspir. Biomim.* 5.045002 (2010). DOI: 10.1088/1748-3182/6/1/019501.
- [12] K. Miklasz, M. LaBarbera, X. Chen, and J. J. Socha. Effects of body cross-sectional shape on flying snake aerodynamics. *Exp. Mech.* 50 (2010), p. 1335–1348. DOI: 10.1007/s11340-010-9351-5.
- [13] J. J. Socha. Gliding flight in *Chrysopelea*: turning a snake into a wing. *Integ. Comp. Biol.* 51 (2011), p. 969–982. DOI: 10.1093/icb/icr092.
- [14] D. Holden, J. J. Socha, N. D. Cardwell, and P. P. Vlachos. Aerodynamics of the flying snake *Chrysopelea paradisi*: how a bluff body cross-sectional shape contributes to gliding performance. *J. Exp. Biol.* 217 (2014), p. 382–394. DOI: 10.1242/jeb.090902.
- [15] A. Krishnan, J. J. Socha, P. P. Vlachos, and L. A. Barba. Lift and wakes of flying snakes. *Phys. Fluids* 26.031901 (2014). DOI: 10.1063/1.4866444.
- [17] F. Jafari, S. D. Ross, P. P. Vlachos, and J. J. Socha. A theoretical analysis of pitch stability during gliding in flying snakes. *Bioinspir. Biomim.* 9.025014 (2014). DOI: 10.1088/1748-3182/9/2/025014.

- [22] J. J. Socha, F. Jafari, Y. Munk, and G. Byrnes. How animals glide: from trajectory to morphology. *Can. J. Zool.* 93 (2015), p. 901–924. DOI: 10.1139/cjz-2014-0013.
- [23] R. Dudley, G. Byrnes, S. P. Yanoviak, B. Borrell, R. M. Brown, and J. A. McGuire. Gliding and the functional origins of flight: biomechanical novelty or necessity? *Annu. Rev. Ecol. Evol. Syst.* 38 (2007), p. 179–201. DOI: 10.1146/annurev.ecolsys.37.091305.110014.
- [24] S. Vogel. *Glimpses of Creatures in Their Physical Worlds*. Princeton University Press, 2009.
- [25] D. Willis, J. Bahlman, K. Breuer, and S. Swartz. Energetically optimal short-range gliding trajectories for gliding animals. *AIAA J.* 49 (2011), p. 2650–2657. DOI: 10.2514/1.J051070.
- [26] J. W. Bahlman, S. M. Swartz, D. K. Riskin, and K. S. Breuer. Glide performance and aerodynamics of non-equilibrium glides in northern flying squirrels (*Glaucomys sabrinus*). *J. R. Soc. Interface* 10.20120794 (2013). DOI: 10.1098/rsif.2012.0794.
- [27] G. Byrnes, N. T.-L. Lim, and A. J. Spence. Take-off and landing kinetics of a free-ranging gliding mammal, the Malayan colugo (*Galeopterus variegatus*). *Proc. R. Soc. B* 275 (2008), p. 1007–1013. DOI: 10.1098/rspb.2007.1684.
- [28] J. A. McGuire. Allometric prediction of locomotor performance: an example from southeast Asian flying lizards. *Am. Nat.* 161 (2003), p. 337–349. DOI: 10.1086/346085.
- [29] J. A. McGuire and R. Dudley. The cost of living large: comparative gliding performance in flying lizards (Agamidae: *Draco*). *Am. Nat.* 166 (2005), p. 93–106. DOI: 10.1086/430725.
- [30] M. G. McCay. Aerodynamic stability and maneuverability of the gliding frog *Polypedates dennysi*. *J. Exp. Biol.* 204 (2001), p. 2817–2826.
- [31] S. P. Yanoviak, R. Dudley, and M. Kaspari. Directed aerial descent in canopy ants. *Nature* 433 (2005), p. 624–626. DOI: 10.1038/nature03254.
- [32] Y. Munk, S. P. Yanoviak, M. A. R. Koehl, and R. Dudley. The descent of ant: field-measured performance of gliding ants. *J. Exp. Biol.* 218 (2015), p. 1393–1401. DOI: 10.1242/jeb.106914.

- [33] S. P. Yanoviak, Y. Munk, and R. Dudley. Arachnid aloft: directed aerial descent in neotropical canopy spiders. *J. R. Soc. Interface* 12.20150534 (2015). DOI: 10.1098/rsif.2015.0534.
- [34] K. E. Paskins, A. Bowyer, W. M. Megill, and J. S. Scheibe. Take-off and landing forces and the evolution of controlled gliding in northern flying squirrels *Glaucomys sabrinus*. *J. Exp. Biol.* 210 (2007), p. 1413–1423. DOI: 10.1242/jeb.02747.
- [35] A. Song, X. Tian, E. Israeli, R. Galvao, K. Bishop, S. Swartz, and K. Breuer. Aeromechanics of membrane wings with implications for animal flight. *AIAA J.* 46 (2008), p. 2096–2106. DOI: 10.2514/1.36694.
- [36] K. L. Bishop. The relationship between 3-D kinematics and gliding performance in the southern flying squirrel, *Glaucomys volans*. *J. Exp. Biol.* 209 (2006), p. 689–701. DOI: 10.1242/jeb.02062.
- [37] K. Vernes. Gliding performance of the Northern flying squirrel (*Glaucomys sabrinus*) in mature mixed forest of Eastern Canada. *J. Mammal.* 82.4 (2001), p. 1026–1033. DOI: 10.1644/1545-1542(2001)082%3C1026:GPOTNF%3E2.0.CO;2.
- [38] N. Y. Zhukovskii. On soaring of birds. *Tr. Otd. fiz. Nauk Obs. lyubit. yestestvz.* 4.2 (1891).
- [39] A. A. Andronov, A. A. Vitt, and S. E. Khaikin. *Theory of Oscillators*. Addison-Wesley Publishing Company, Inc., 1966.
- [40] G. Dyke, R. de Kat, C. Palmer, J. van der Kindere, D. Naish, and B. Ganapathisubramani. Aerodynamic performance of the feathered dinosaur *Microraptor* and the evolution of feathered flight. *Nat. Commun.* 4.2489 (2013). DOI: 10.1038/ncomms3489.
- [41] V. A. Tucker. Gliding flight: speed and acceleration of ideal falcons during diving and pull out. *J. Exp. Biol.* 201 (1998), p. 403–414.
- [42] W. Nachtigall, R. Grosch, and T. Schultze-Westrum. Gleitflug des Flugbeutlers *Petaurus breviceps papuanus* (Thomas) I. *J. Comp. Physiol.* 92 (1974), p. 105–115. DOI: 10.1007/BF00661136.
- [43] H. Park and H. Choi. Aerodynamic characteristics of flying fish in gliding flight. *J. Exp. Biol.* 213 (2010), p. 3269–3279. DOI: 10.1007/978-1-4020-9898-7\_3.
- [44] A. M. Heers, B. W. Tobalske, and K. P. Dial. Ontogeny of lift and drag production in ground birds. *J. Exp. Biol.* 214 (2011), p. 717–725. DOI: 10.1242/jeb.051177.

- [45] J. M. Wakeling and C. P. Ellington. Dragonfly flight I. Gliding flight and steady-state aerodynamic forces. *J. Exp. Biol.* 200 (1997), p. 543–556.
- [46] S. Sunada, A. Sakaguchi, and K. Kawachi. Airfoil section characteristics at a low Reynolds number. *J. Fluids Eng.* 119 (1997), p. 129–135. DOI: 10.1115/1.2819098.
- [47] K. L. Bishop. Aerodynamic force generation, performance and control of body orientation during gliding in sugar gliders (*Petaurus breviceps*). *J. Exp. Biol.* 210 (2007), p. 2593–2606. DOI: 10.1242/jeb.002071.
- [48] S. H. Strogatz. *Nonlinear Dynamics and Chaos: With Applications to Physics, Biology, Chemistry, and Engineering*. Perseus Books Publishing, LLC, 2001.
- [49] L. M. Milne-Thomson. *Theoretical Aerodynamics*. Courier Dover Publications, 1966.
- [50] J. A. Walker. Estimating velocities and accelerations of animal locomotion: a simulation experiment comparing numerical differentiation algorithms. *J. Exp. Biol.* 201 (1998), p. 981–995.
- [51] P. Ern, F. Risso, D. Fabre, and J. Magnaudet. Wake-induced oscillatory paths of bodies freely rising or falling in fluids. *Annu. Rev. Fluid Mech.* 44 (2012), p. 97–121. DOI: 10.1146/annurev-fluid-120710-101250.
- [52] L. Heisinger, P. Newton, and E. Kanso. Coins falling in water. *J. Fluid Mech.* 742 (2014), p. 243–253. DOI: 10.1017/jfm.2014.6. arXiv: arXiv:1312.2278v1.
- [53] L. Vincent, W. S. Shambaugh, and E. Kanso. Holes stabilize freely falling coins. *J. Fluid Mech.* 801 (2016), p. 250–259. DOI: 10.1017/jfm.2016.432.
- [54] B. J. Stafford, R. W. J. Thorington, and T. Kawamichi. Gliding behavior of Japanese giant flying squirrels (*Petaurista leucogenys*). *J. Mammal.* 83 (2002), p. 553–562. DOI: 10.1126/science.95.2469.427-b.
- [55] R. O’Dor, J. Stewart, W. Gilly, J. Payne, T. C. Borges, and T. Thys. Squid rocket science: how squid launch into air. *Deep Sea Res. Part II Top. Stud. Ocean.* 95 (2013), p. 113–118. DOI: 10.1016/j.dsr2.2012.07.002.
- [56] S. Chatterjee and R. J. Templin. Biplane wing planform and flight performance of the feathered dinosaur *Microraptor gui*. *Proc. Natl. Acad. Sci. USA* 104 (2007), p. 1576–1580. DOI: 10.1073/pnas.0609975104.

- [57] D. Evangelista, G. Cardona, E. Guenther-Gleason, T. Huynh, A. Kwong, D. Marks, N. Ray, A. Tisbe, K. Tse, and M. Koehl. Aerodynamic characteristics of a feathered dinosaur measured using physical models. Effects of form on static stability and control effectiveness. *PLoS One* 9.e85203 (2014). DOI: 10.1371/journal.pone.0085203.

# Chapter 3

## Undulation enhances stability, enabling gliding in flying snakes

MANUSCRIPT AUTHORS: Isaac J. Yeaton, Shane D. Ross, and John J. Socha

**Citation:** Yeaton, I. J., Ross, S. D., & Socha, J. J. (2018). Undulation enhances stability, enabling gliding in flying snakes. *Manuscript in preparation*.

### Abstract

Aerial undulation is an evolved pattern of body bending used by flying snakes during gliding. The primary role of aerial undulation is ostensibly the same as in terrestrial and aquatic undulation: to generate propulsive thrust. However, flying snakes generate locomotor forces by falling through the air, which does not necessarily require undulation. Here we ask, is aerial undulation a non-functional behavioral vestige of lateral undulation, or is it a novel aerial control strategy? We used high-speed motion capture of flying snakes to quantify the aerial undulation waveform for the full body for the first time. The three-dimensional body motion consists of two waves of horizontal and vertical bending and a net out-of-plane displacement. The newly discovered vertical wave has twice the spatial and temporal frequencies as the horizontal wave and is phase-shifted by  $90^\circ$ . We then tested the effects of aerial undulation on flight dynamics by developing an anatomically-accurate mathematical model of snake flight. Simulated glides without undulation covered significant horizontal and vertical distances,

indicating that undulation is not a strict requirement for snake flight. However, the addition of undulation stabilized the rotational motion, which drastically increased glide performance. Additionally, the model results show that out-of-plane displacement can control pitching dynamics and that inertial yaw torques can be used for maneuvering. This work demonstrates that aerial undulation serves a different function than other known uses of undulation, and suggests that limbless flying robots can be controlled using aerial undulation as a template.

**Keywords:** gliding, biomechanics, control, snake, undulation

### Significance statement

Flying snakes are the only known limbless flyers. They glide through the air using a unique body waveform termed aerial undulation. We measured aerial undulation in flying snakes gliding through a large indoor arena, and then simulated glides using an anatomically-accurate model of snake flight. Aerial undulation enables gliding by inducing rotational stability, which in turn induces stable forward flight, serving an analogous role as the spin of a thrown frisbee. Flying snakes therefore use undulation for a fundamentally different function than in other terrestrial and aquatic undulating animals. This work suggests that a bioinspired limbless flying robot can be controlled using aerial undulation as a control template.

## 3.1 Introduction

Undulation is an evolutionarily ancient locomotor pattern used by a diverse range of long-bodied animals for propulsion in fluids and in terrestrial environments. Animals use environment-dependent patterns of axial bending that enable the body to push against the surrounding medium in a stable and efficient manner [58, 59]. Common wave patterns include lateral undulation on flat and rough surfaces [60–63], sidewinding on sand [19, 20], viscous swimming at low Reynolds number [64–66], and inertial swimming at high Reynolds numbers [67–70]. In contrast to the well understood role of aquatic and terrestrial undulation, the role of aerial undulation on limbless flight dynamics is unknown.

Flying snakes (*Chrysopelea*) are the only known animals capable of limbless flight. These animals glide using aerial undulation, moving horizontally downward through air by converting

gravitational potential energy into aerodynamic lift and drag. Their undulation is characterized by an ‘S’-shape body planform (figure 3.1), a relatively low undulation frequency of 1–2 Hz, and a flattened, airfoil-like body cross-section (figure 3.1B) [7–9, 11, 13]. Most glides begin with a jump into the air, during which a wave of dorsoventral flattening passes from the head to the vent [10]. This flattening transforms the snake’s circular cross-section into a roughly triangular airfoil (figure 3.1B), with favorable aerodynamic properties and gentle stall characteristics (figure B.6) [12, 14, 15].

Aerial undulation continuously reconfigures the snake’s body, turning the animal into a morphing wing (figure 3.1D). Previous studies of snake glides determined that flying snakes always undulate while airborne, but it is unclear if undulation is a functional requirement, or is simply a behavioral remnant of snake locomotion. Prior measurements under-resolved the animal’s body, making it difficult to precisely quantify the time-varying body configuration, which is necessary to test how aerial undulation affects flight dynamics and reveal the mechanical function of aerial undulation [7, 9, 11].

One might expect from analogy with terrestrial and aquatic undulation that aerial undulation is used to generate propulsive thrust. On solid media, undulatory locomotion occurs due to distributed contact forces over ventral and lateral regions of the body, and in water, fluid displacement or suction along the body causes forward motion [71]. In both cases, the net propulsive thrust acts predominantly within the plane of undulation. Modulation of the body in the vertical direction may be used for secondary purposes, such as reducing drag or increasing the normal force [20, 61]. Forward motion stops when undulation stops, and because of the body’s distributed contact area and neutral buoyancy, rotational stability is not a primary concern.

For snakes, a successful glide with horizontal motion over the ground requires generating aerodynamic forces to offset the animal’s weight. Lift and drag forces are produced by air flowing over the flattened body as it accelerates downward under gravity, with the reciprocating motion produced by muscular contractions likely not enhancing force production [9]. The resulting aerodynamic forces act out of the plane of horizontal undulation, and undulation will continuously change the distribution of the forces on the body. Time-varying forces should affect the rotational behavior of the body [72], as flying snakes have two additional rotational degrees of freedom (about the pitch and roll axes) compared to terrestrial undulators [73]. These physical challenges of flight without wings, and the unique body kinematics of flying snakes, suggest that aerial undulation has a functional role during limbless flight.

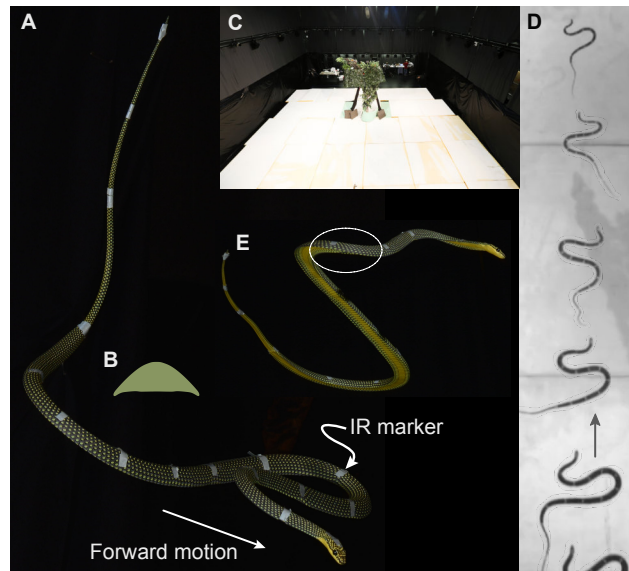


Figure 3.1: Measurements of gliding in snakes. (A) The flying snake, *Chrysopelea paradisi*, in the mid-glide posture, with a flattened body and infrared (IR) markers placed along the dorsal surface and tail. (B) The body's flattened cross-sectional shape when gliding [13]. (C) Front view of the glide arena from the top of the launch platform. The floor is covered with white foam padding and a tree is placed in the center to encourage jumps. Motion capture cameras are placed around the perimeter. Photo courtesy of Mike Diersing. (D) Morphing wing-body seen from snapshots of an overhead view of aerial undulation as the snake glides through the indoor glide arena. Motion is from bottom to top, with the snake appearing smaller as it moves away from the camera. (E) Side view of a *C. paradisi* glide showing the out-of-plane twisting at the 'U'-bends due to the vertical wave, indicated by the white oval.

Here, we address whether aerial undulation is a requirement for snake gliding flight by assessing its effects on flight dynamics. Using high-speed motion capture and a large indoor glide arena, we quantify aerial undulation to provide the first understanding of the entire morphing wing-body. We then synthesize these observations with aerodynamic force production by developing the first anatomically accurate theoretical model of snake flight, which we use to test the performance and stability properties of aerial undulation on limbless flight. Our results provide a foundation for designing snake-inspired robots that use aerial undulation to glide through the air, adding to the growing library of robotic snake locomotion on variable substrates including on sand, in water, and in trees.

## 3.2 Results and Discussion

### 3.2.1 Flying snakes use orthogonal bending waves when gliding

Aerial undulation consists of coupled waves of horizontal and vertical bending. We measured the position of 11-17 landmarks placed along the body from seven snakes gliding from a height of 8.3 m in an indoor glide arena (figure 3.1). We used spline fits to the landmark points on the body in 36 trials to create the first continuous and three-dimensionally accurate representation of the snake,  $\mathbf{r}$ . Using the unit tangent vector of the spline,  $\hat{t} = \partial\mathbf{r}/\partial s$ , we simplify the complex motion of aerial undulation into two bending angle waves that travel down the body. The horizontal and vertical waves are given by

$$\bar{\theta}(s, t) = -\tan^{-1} \hat{t}_x/\hat{t}_y \quad \text{and} \quad \bar{\psi}(s, t) = \sin^{-1} \hat{t}_z \quad (3.2.1)$$

where  $\bar{\theta}(s, t)$  and  $\bar{\psi}(s, t)$  are local angles the body makes relative to the horizontal and vertical directions, respectively, as functions of arc length  $s$  and time  $t$  (figure 3.2I,J). We define bending waves from the angle data because periodic angle changes more closely resemble the underlying muscle activation pattern known to produce undulation in snakes [74, 75] and enables more accurate kinematic modeling [63].

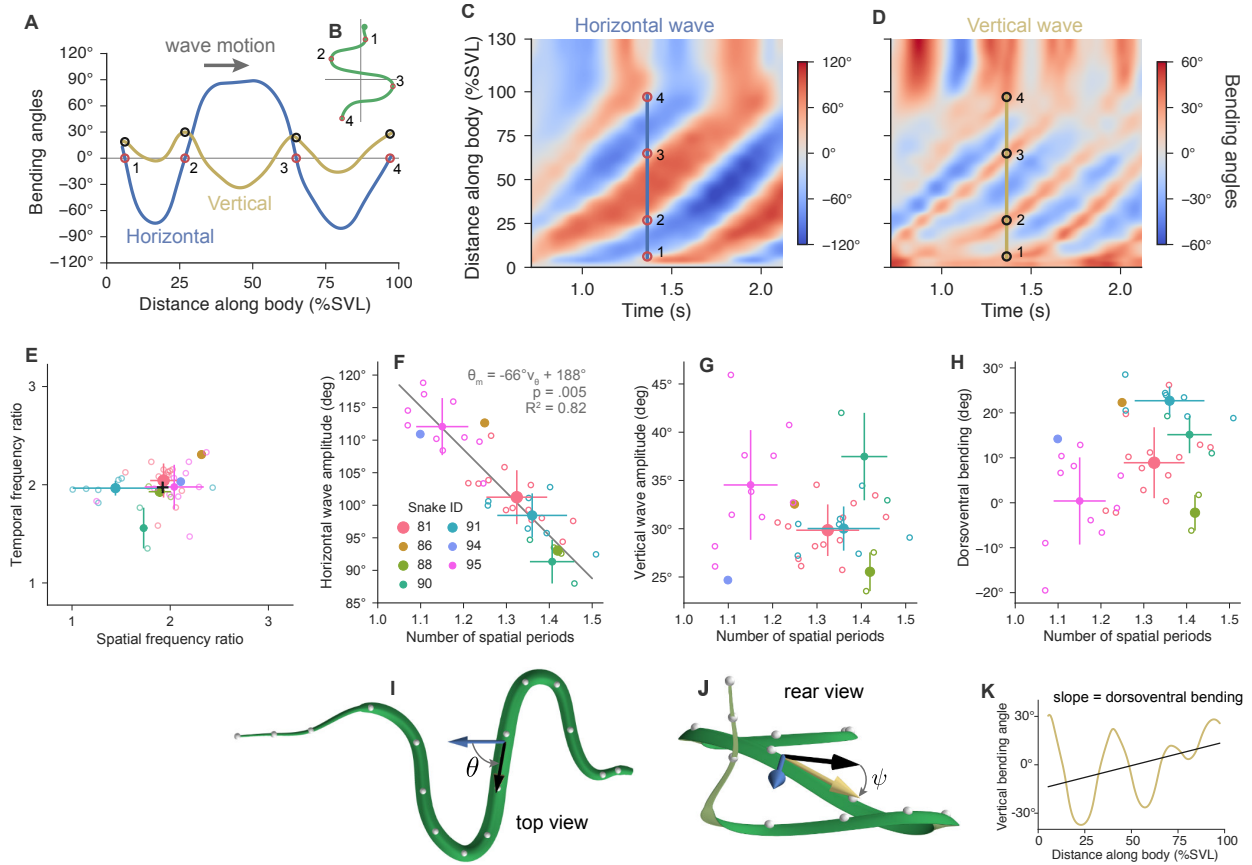


Figure 3.2: Caption on next page.

Figure 3.2: (Previous page.) Measured body kinematics in flying snakes. (A) Horizontal and vertical bending waves with the overhead view of snake's backbone (B) near halfway through a glide. The large-amplitude flat-top horizontal wave and the small-amplitude vertical wave travel together down the body. The vertical wave has twice the spatial and temporal frequencies as the horizontal wave. Zero crossings of the horizontal wave (red markers) correspond to 'U'-bend of the snake, as well as peaks in the vertical wave (black markers). (C and D) Space-time bending plots showing the traveling waves of bending. The time-point indicated in (A) and (B) is denoted by the vertical lines. (E-H) Results of the complex orthogonal decomposition analysis to quantify the spatial and temporal characteristics of aerial undulation. (E) Ratios of temporal and spatial frequencies of the horizontal and vertical waves. The black '+' is the overall average, indicating that the vertical wave has twice the spatial and temporal frequencies as the horizontal wave. (F) The average horizontal wave amplitude is tightly coupled with the number of spatial periods of the horizontal wave (gray line). Individual glides from seven different animals are shown with small colored markers and individual averages are shown with large markers and one standard deviation bars. The size of the average marker indicates the snake's mass. (G) Average vertical wave amplitude vs. number of spatial periods of the horizontal wave. (H) Average dorsoventral bending angle (out-of-plane gross body bending) is not coupled with the number of spatial periods of the horizontal wave, but is non-zero, indicating that the flying snakes body is not always parallel to the ground while gliding. (I and J) Definition of the local horizontal and vertical bending angles shown from the top and side view of the snake. The horizontal angle,  $\theta$ , is defined as the angle between the blue unit vector in the  $-\hat{y}$  direction and the projection of the yellow tangent vector into the horizontal plane (black vector). The local vertical bending angle,  $\psi$ , is the angle between the yellow tangent vector and the horizontal projection. On the snake images, the gray markers indicate the location of the IR markers, dark green is the dorsal surface, and yellow-green is the ventral surface. (K) Definition of the dorsoventral bending angle as the slope of the best-fit line (black) to the vertical wave amplitude (yellow) as a function of distance along the body.

Previous kinematic measurements were insufficient to uncover the fine-scale vertical motion of the body [7, 8, 11]. However, our data reveal that flying snakes employ two waves: a large-amplitude horizontal wave and a newly discovered smaller amplitude vertical wave, both of which travel down the body from the head to the vent in a consistent manner (figure 3.2A,C,D). These waves form after an initial transient as the snake jumps into a relatively straight posture and then forms the characteristic ‘S’-shape glide posture.

There are four kinematic features of aerial undulation relating the newly discovered vertical wave to the horizontal wave (figure 3.2A). First, the vertical wave has twice the spatial and temporal frequencies as the horizontal wave, indicating that the body has twice as many vertical bends as lateral bends (figure 3.2A,E). Second, the ‘U’-bends on the flying snake’s body can be identified as the zero crossings on the bending angle plot (figure 3.2B). Third, these zero crossings are maxima of the vertical wave, indicating that the horizontal and vertical waves are phase-shifted by  $90^\circ$  and are therefore orthogonal. Fourth, the maximum out-of-plane bending occurs at the ‘U’-bends and halfway along the straight segments. At the ‘U’-bends, the snake’s airfoil cross-section twists due to the body’s out-of-plane motion (figure 3.1E).

The instantaneous shape of the traveling waves vary with time as the animal accelerates and produces aerodynamic forces, but several features remain common. The horizontal wave is a flat-top sinusoid with an amplitude of  $80^\circ$  to  $120^\circ$  (figure 3.2A,C). The amplitude itself depends on the number of spatial periods, with fewer spatial periods resulting in higher horizontal bending angles (figure 3.2F, 3.3A). The vertical wave is a narrow-peaked sinusoid with broad troughs (figure 3.2A,D), with amplitudes ranging from  $20^\circ$  to  $45^\circ$  (figure 3.2G).

We quantified the spatial and temporal characteristics of the two waves using complex orthogonal decomposition, which decomposes the ensemble of bending angle data into time-varying modal shapes sorted by the observed variance; when the modes are linearly combined, the full waveform is recovered [76, 77]. Flying snakes use horizontal wave shapes with 1–1.5 spatial periods that undulate at 1–1.7 Hz, and vertical wave shapes with 2–3 spatial periods that undulate at 2–3.4 Hz. The vertical-to-horizontal spatial and temporal frequency ratios are close to two: the spatial frequency ratio is  $1.87 \pm 0.35$  and temporal frequency ratio is  $1.98 \pm 0.21$  (figure 3.2E). The horizontal wave is more organized than the vertical wave, with only one or two modes required to describe 95% of the observed variance, and the first mode accounting for 88% of the variance. The vertical wave requires four modes to explain 95% of the variance, with the first mode contributing only 66% of the variance (figure B.1).

There is an additional third component to aerial undulation that we term ‘dorsoventral bending’ (figure 3.2H). Relative to the horizontal direction (parallel to the ground), dorsoventral bending is the up and down motion of the posterior body relative to the head (figure 3.2K). We quantified dorsoventral bending as the average slope of a linear regression to the vertical bending angles, with values ranging from  $-20^\circ$  to  $30^\circ$  (figure 3.2H). Dorsoventral bending was always present in the recorded glides, but was not significantly related to the number of spatial periods.

### 3.2.2 A new model of limbless flight

We tested the effects of orthogonal horizontal and vertical waves, as well as dorsoventral bending, on glide dynamics using a new, anatomically-accurate model of snake flight. Manipulation of the model allows us to systematically test how the components of aerial undulation (horizontal wave amplitude, number of spatial periods, and undulation frequency) effect short-term and long-term glide dynamics.

In the model, we prescribe traveling waves of horizontal and vertical bending that capture the observed kinematic features of the measured bending waves (figure 3.2A, 3.3A). The horizontal wave is modeled as a large-amplitude, flat-topped sinusoid, and the vertical wave as a small-amplitude sinusoid (figure B.2C). The horizontal and vertical waves are parameterized as

$$\bar{\theta}(s, t) = \theta_m \sin \left[ \frac{\pi}{2} \cos \left( \frac{2\pi\nu_\theta}{L} s - 2\pi f_\theta t + \phi_\theta \right) \right] \quad (3.2.2)$$

$$\bar{\psi}(s, t) = \psi_m \cos \left( \frac{2\pi\nu_\psi}{L} s - 2\pi f_\psi t + \phi_\psi \right) + \frac{d_\psi}{L} s \quad (3.2.3)$$

where  $\theta_m$  and  $\psi_m$  are the maximum horizontal and vertical bending angles (figure 3.2F,G),  $\nu$  is the number of spatial periods (figure 3.2F),  $f$  is the undulation frequency,  $\phi$  is the phase shift, and  $d_\psi$  is the dorsoventral bending angle (figure 3.2H). The horizontal and vertical waves are coupled as in the kinematic data, with  $\nu_\psi = 2\nu_\theta$ ,  $f_\psi = 2f_\theta$ , and  $\phi_\psi = 2(\phi_\theta - \pi/2)$  (figure 3.2E), reducing the kinematics model to five variables that define the body shape:  $\theta_m$ ,  $\psi_m$ ,  $\nu_\theta$ ,  $f_\theta$ , and  $d_\psi$ . The position  $\mathbf{r} = [x, y, z]$  of the body relative to the center of mass is calculated by integrating  $\partial_s x = \cos \bar{\psi} \sin \bar{\theta}$ ,  $\partial_s y = -\cos \bar{\psi} \cos \bar{\theta}$ , and  $\partial_s z = \sin \bar{\psi}$ .

The center of mass position,  $\vec{R}_o$ , and orientation of the body (yaw, pitch, and roll angles)

are found by integrating the translational and rotational equations of motion

$$\int_0^L (\vec{f}_L + \vec{f}_D) ds - m\vec{g} = m\ddot{\vec{R}}_o \quad (3.2.4)$$

$$\vec{M}_A = \underbrace{\mathbf{I}_o \cdot \dot{\vec{\omega}} + \vec{\omega} \times (\mathbf{I}_o \cdot \vec{\omega})}_{\text{rigid-body terms}} + \underbrace{[\dot{\mathbf{I}}_o] \cdot \vec{\omega} + \vec{\omega} \times \vec{h}_o + [\dot{\vec{h}}_o]}_{\text{inertial moments}} \quad (3.2.5)$$

where  $\vec{f}_L$  and  $\vec{f}_D$  are the infinitesimal lift and drag forces calculated from the local velocity using previously measured quasi-steady lift and drag coefficients [14] and simple sweep theory to account for the curved segments [72, 78],  $\vec{M}_A$  is the resultant aerodynamic moment, and  $m$  is the mass of the animal. Because the snake continuously reconfigures its body relative to the center of mass, we decompose the non-aerodynamic contributions to rotational motion into rigid-body terms and variable-geometry inertial moments. We use the standard aircraft angle convention: positive pitch indicates tipping backwards, positive roll indicates banking to right, and positive yaw indicates rotating left about the vertical axis.

### 3.2.3 Undulation enhances rotational stability, increasing glide performance

To test the effects of aerial undulation on glide performance, we simulated glides with  $f_\theta = 0$  Hz (no undulation) and  $f_\theta = 1.2$  Hz (the observed mean undulation frequency), while varying over the number of spatial periods,  $\nu_\theta$ , and horizontal wave amplitude,  $\theta_m$  (figure 3.3A). Based on the observed ranges from the kinematic data, we discretized the shape space into 121 shapes, with the number of body waves ranging from  $1 \leq \nu_\theta \leq 1.5$  and the horizontal wave amplitudes from  $90^\circ \leq \theta_m \leq 119^\circ$  (figure 3.3A). We segregated the shape space along the diagonal of observed shapes to enable a finer analysis (figure B.2B). The lower left portion contains visibly “open” shapes and the upper right visibly “closed” shapes. The vertical wave amplitude and the dorsoventral bending angle were kept constant at  $\psi_m = 20^\circ$  and  $d_\psi = 10^\circ$ , respectively. Their combined effect is tested later. We then simulated glides until the snake’s center of mass contacted the ground or until any of the yaw, pitch, or roll angles went unstable by exceeding a generous threshold of  $85^\circ$  [72]. If any angle exceed the threshold, we deemed the glide to be unstable. We tested both short-term glide dynamics with a launch height of 10m, and long-term glide dynamics with a launch height of 75m, both with and without undulation. The 10m height is consistent with this and other

flying snake experimental studies [8], and the 75m height guaranteed that all glides became rotationally unstable and is also congruent with the maximum height of Dipterocarpaceae trees in the snake’s native Indo-Malayan forest habitat [79].

The model shows that aerial undulation produces positive effects on glide performance, generally increasing the height fallen and the horizontal distance travelled before the simulated snake becomes unstable (figure 3.3B-E, table 3.1). For short glides, 94% of glides with undulation were stable, whereas only 50% of glides without undulation were stable (figure 3.3B,C). Among the observed body shapes, all glides with undulation were stable, whereas only 35% of static posture snakes were stable. The effect of undulation on increasing the horizontal glide distance is less pronounced, with the average distance increasing from 4 m to 4.3 m. With the observed shapes (indicated in the diagonal region of figure 3.3A), the average glide distance increases from 4 m to 4.9 m (figure 3.3D,E).

Undulation has a larger effect during long glides starting from 75m (figure B.2H,K, table 3.1). Undulation increased both the height fallen before becoming unstable and the horizontal distance travelled in 86% of glides. For observed shapes with undulation, all glides covered greater vertical distance, and 92% of glides travelled farther. Of the 8% of glides without undulation that did travel farther, they only did so by an average of 0.16 m. Conversely, undulation increased the average height fallen by 12.5 m and the average horizontal distance travelled by 6.9 m.

Table 3.1: Overview of flying snake simulations shown in figure 3.3 and figure B.2, demarcated by the different shape space regions.

Metric	Fig.	All	Obs.	Open	Closed
Frac. stable (0 Hz)	3.3B	49.6%	34.7%	83.3%	36%
Frac. stable (1.2 Hz)	3.3C	94.2%	100%	100%	80.6%
Glide dist. (0 Hz)	3.3D	4 m	4 m	4.2 m	3.7 m
Glide dist. (1.2 Hz)	3.3E	4.3 m	4.9 m	3.4 m	4.2 m
Vert. increase (75 m)	B.2H	10.5 m	12.5 m	13.8 m	4.5 m
Dist. increase (75 m)	B.2K	5 m	6.9 m	5.9 m	1.8 m

The modeling results indicate that undulation increases the rotational stability of flying snake glides, but without undulation, the static body will still produce aerodynamic forces and experience net horizontal travel (figure B.2D). Undulation is therefore not a strict requirement for gliding. However, the static body postures are generally unstable (figure 3.3B). Such instability can manifest itself over short glides, with the simulated snake becoming unsta-

ble before falling 10 m vertically. For glides without undulation, some shapes are inherently more stable than others and thus performed better. The ‘open’ shapes are generally more stable than the ‘closed’ shapes. Stability without undulation is generally poor in the observed diagonal region, with shapes with lower horizontal wave amplitudes performing worst.

The addition of undulation enables the simulated snakes to glide longer and farther over the ground (figure 3.3D,E). This indicates that undulation is functionally important for gliding by increasing the stability of the system. The model results suggest that aerial undulation is used for a different mechanical function than in all other animals that undulate.

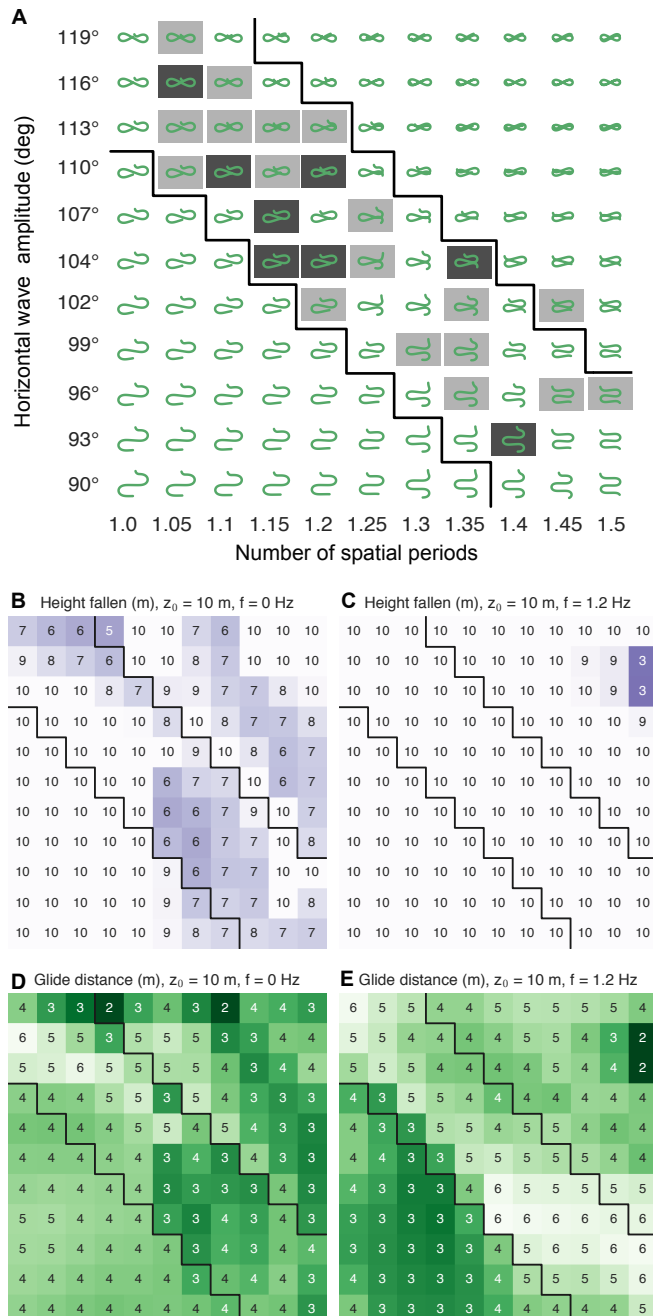


Figure 3.3: Simulated flying snake glides. (A) Horizontal wave shape space used for simulated glides. Gray and black boxes indicate counts (one or two, respectively) of experimentally observed body shapes (figure 3.2F). The shape space is naturally demarcated along the diagonal of observed body shape, “open” shapes in the lower left, and “closed” shapes in the upper right. The different regions are separated by the black boarders. (B) Height fallen during short glides before becoming unstable with no undulation. A ‘10’ denotes a stable glide, and the black boarders demarcate the observed body shapes observed in the kinematic measurements. Many shapes within the observed diagonal are unstable. (C) Height fallen during short glides before becoming unstable with undulation. Undulation improves the stability properties of shapes within the observed region. (D) Horizontal glide distance without undulation. (E) Horizontal glide distance with undulation. Undulation generally increases the glide distance, especially within the observed region.

### 3.2.4 Dorsoventral bending controls pitching motion in flying snakes

To elucidate the effects of the vertical wave amplitude and dorsoventral bending on glide dynamics, we systematically varied these parameters over the range observed from the measured kinematics (figure 3.2G,H). We simulated glides with vertical wave amplitudes of  $\psi_m = 0^\circ$ ,  $10^\circ$ , and  $20^\circ$  (i.e., planar undulation, to increasing levels of out-of-plane motion), and dorsoventral bending of  $-20^\circ$  to  $20^\circ$  in  $10^\circ$  increments (figure 3.4A), for 11 different body shapes along the the best-fit line of body shapes in figures 3.2F and figure 3.3A. Variations of the vertical wave have a small effect on the glide trajectory (figure B.3), whereas dorsoventral bending has a larger effect. However, a perfectly planar snake ( $\psi_m = 0^\circ$ ), which was never observed in the experimental glide trials, performed worst. Increasing levels of vertical wave amplitude increased glide performance, due to the out-of-plane twisting of the cross section to a more advantageous angle of attack for force production (figure 3.1E, 3.2J).

In contrast to the vertical wave amplitude, dorsoventral bending had a marked effect on the glide performance by affecting the pitch dynamics (figure 3.4). At a dorsoventral bending angle of  $-20^\circ$ , with the posterior body beneath the head, the glides did not shallow, but instead became unstable in pitch before falling 10 m (figure 3.4C). At a dorsoventral bending angle of  $20^\circ$ , with the posterior body above the head, the center of mass trajectory curved backward, with some shapes landing behind the jump location. This poor glide performance is due to upward pitching of the body (figure 3.4C). Although the performance was poor, these glides were rotationally stable. At intermediate values of dorsoventral bending, all glides were stable, and performance was best at a dorsoventral bending angle of  $10^\circ$ . At this dorsoventral bending angle, the pitch angle is closest to the starting value near  $0^\circ$ .

To understand the coupling of dorsoventral bending, pitching motion, and glide performance, we also simulated glides with the rotational equations of motion disabled. Instead of solving the coupled non-linear system of equations together, (3.2.4) and (3.2.5), we sampled the aerodynamic forces on the body at different phases through the undulation cycle and integrated (3.2.4) to calculate the position and speed of the center of mass; at each phase of undulation, we then calculated the resulting moments acting on the body by evaluating (3.2.5), with the orientation kept constant. In effect, this is a virtual wind tunnel experiment in which we use the dynamic model to calculate the distributed forces acting on the body as it accelerates. This technique also allows us to remove the highly non-linear coupling of the translational and rotational motion to quantify the aerodynamic and inertial contributions

to the rotational motion. For this analysis, we report the phase-averaged pitch moment at the end of the trajectory, where speeds are greatest and forces are largest.

In figure 3.4D, as the dorsoventral bending increases from  $-20^\circ$  to  $10^\circ$ , we see the landing position of the simulated snake increase as the average pitch moment increases toward zero. At a dorsoventral bending of  $20^\circ$ , the phase-averaged pitch moment becomes positive, and the glide performance decreases. For each dorsoventral bending angle, the glide performance and average pitch moment also depend on the shape used, specifically the number of spatial periods and the horizontal wave amplitude. For a given shape, dorsoventral bending has a large effect on the average pitch moment (figure 3.4E), and as the number of spatial periods increases, the moments diverge, becoming more positive or negative depending on the dorsoventral bending angle. Large negative pitch moments are associated with dorsoventral bending angles of  $-20^\circ$  to  $0^\circ$ , near zero pitch moments for a dorsoventral bending angle of  $10^\circ$ , and large positive pitch moments for a dorsoventral bending angle of  $20^\circ$ . The sign of the phase-averaged pitch moments in figure 3.4E correspond to the pitching-up or pitching-down in figure 3.4C and the resulting glide performance in figure 3.4B. Figure 3.4F provides an alternative view of figure 3.4E, which highlights how the the average pitch moment is smallest for shapes with fewer spatial periods (and higher horizontal wave amplitudes). The point of zero pitch moment varies for each shape, but occurs for a positive dorsoventral bending angle. The slope provides a measure of the sensitivity of a particular shape to changes in pitch moment due to changes in dorsoventral bending during a glide. Shapes in the lower right of the horizontal wave shape space are more sensitive to the out-of-plane motion of the body, whereas shapes in the upper left are less affected by pitching motion.

Our parametric study of vertical wave amplitude and dorsoventral bending provides insight into the observed flying snake kinematics, and also points to a pitch control strategy for a flying snake-inspired robot. The vertical wave causes the body to twist out-of-plane, modifying the local orientation of the flattened airfoil with the free-stream airflow. Dorsoventral bending controls the magnitude and sign of the aerodynamic pitch moment that acts on the body. Net non-zero pitch moments were associated with the snake becoming unstable in pitch and/or overall poor glide performance. A flying snake can control the pitch moment by mid-flight variations of the dorsoventral bending angle or the horizontal wave shape. Correcting a pitch instability requires changing the sign of the pitch moment (figure 3.4F), which only occurs as dorsoventral bending changes.

The model results suggest a pitch control strategy that involves varying the dorsoventral

bending (moving the posterior body above or below the head) in a time-varying manner to change the net pitch moment acting on the animal or robot. Because the pitch moment is sensitive to dorsoventral bending, a semi-periodic change in dorsoventral bending should be able to correct for any inherent pitch instability or disturbance during a glide. The time-varying motion of the posterior body up and down is seen in footage of flying snakes, and is likely constrained by the zygapophyses, which are bony protrusions from the vertebra that limit dorsiflexion.

In the mathematical formulation of flying snake kinematics, (3.2.3), dorsoventral bending has the same form as a steering parameter in traditional planar snake-inspired robots [80]. In these other formulations, the horizontal wave is biased laterally, changing the distribution of forces and causing the robot to move in circular arcs. In flying snakes, this biased undulation is present in the vertical wave, not in the horizontal wave. Instead of being used for steering, the bias is used to control the rotational stability of the model by modifying the aerodynamic force distribution.

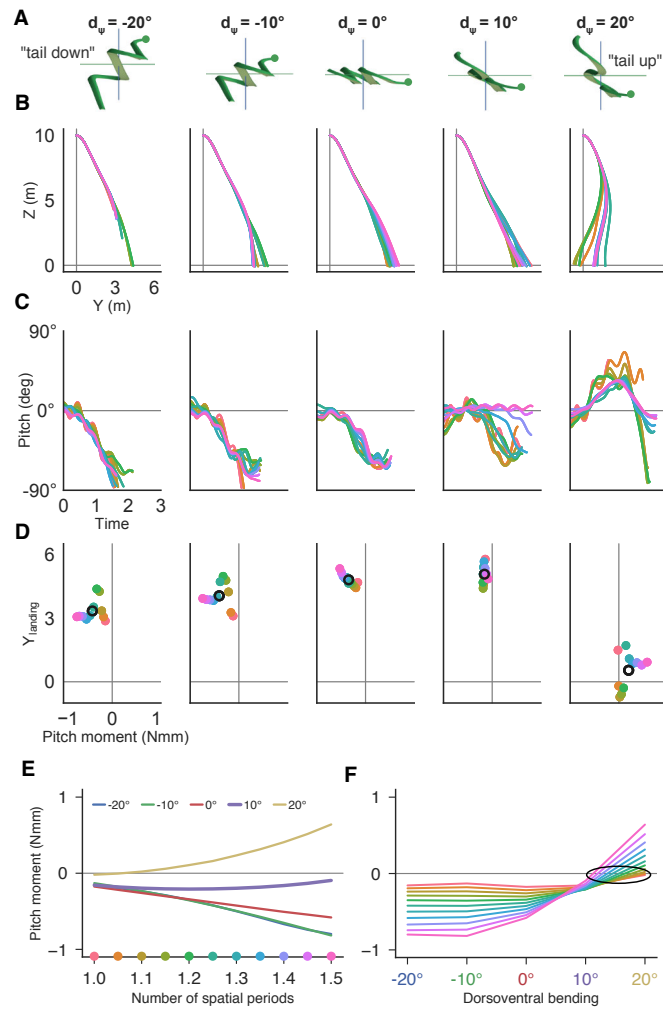


Figure 3.4: Caption on next page.

Figure 3.4: (Previous page.) Effect of dorsoventral bending,  $d_\psi$ , on glide dynamics and controlling pitching motion. (A) Side views of simulated snake kinematics, where motion would be from left to right, for  $d_\psi$  ranging from  $-20^\circ$  to  $20^\circ$  and a vertical wave amplitude  $\psi_m=20^\circ$  (same as for glides in figure 3.3). The head of the snake is indicated with the green circle. Negative  $d_\psi$  causes the posterior body to fall below the head (“tail down”); both negative and positive values are seen in snake glides. (B) Side view of the center of mass trajectory, where colors indicate different  $\nu_\theta$  and  $\theta_m$  combinations (see (E) for the color key). The performance peaks at  $d_\psi=10^\circ$ , and is worst at  $d_\psi=20^\circ$ . The stability is worst for  $-20^\circ$ , as some glides do not reach the ground. (C) Pitch angle during full simulations vs. normalized time (physical time multiplied by the undulation frequency). Most glides pitch down, especially for negative dorsoventral bending. Best performing glides occur for  $d_\psi$  of  $10^\circ$ , where the pitch angle is near zero. (D) Terminal landing position vs. phased-averaged pitch moment for different dorsoventral bending angles and number of spatial periods. Dorsoventral bending has a large effect on the glide performance by affecting the pitch moment. (E and F) The effect of the number of spatial periods and dorsoventral bending on the phase-averaged pitch moment. (E) Different colored lines indicate different  $d_\psi$  combinations, while colored points indicate different  $\nu_\theta$  and  $\theta_m$  combinations along the best-fit line of figure 3.2F. The sign of the pitch moment depends on the dorsoventral bending angle, while the magnitude depends on the number of spatial periods. (F) Alternative view of (E), where lines indicate different  $\nu_\theta$  and  $\theta_m$  combinations. The point of zero pitch moment occurs for positive  $d_\psi$  and is indicated by the black oval. Varying  $d_\psi$  is more effective than varying  $\nu_\theta$  to change the sign and amplitude of the pitch moment.

### 3.2.5 Inertial maneuvering in flying snakes

The phase-averaging analysis also enables us to quantify the relative contribution of aerodynamic and inertial moments on the dynamics of snake flight. From the rotational equations of motion, (3.2.5), the orientation of the body is affected by both external aerodynamic forces and the changing of the mass distribution about the center of mass. The aerodynamic contribution (figure 3.5A) increases with time as the velocity increases, whereas the inertial contribution (figure 3.5B) stays constant. Both moments are periodic, with only the pitch moment (figure 3.5A) showing a non-zero phase average.

We take the relative contribution of inertial-to-aerodynamic moments as the ratio of the peak-to-peak amplitude from the respective time series (figure 3.5C) about the pitch, roll, and yaw axes for different dorsoventral bending angles and number of spatial periods. About the pitch and roll axes, inertial moments initially dominate, but within one undulation cycle, their contribution rapidly decreases. Inertial yaw moments are generally an order of magnitude greater than both aerodynamic yaw moments and inertial moments about the other axes. Inertial yaw moments arise from the large-amplitude horizontal wave and the broad ‘S’-shape of flying snakes. This result suggests that flying snakes could employ inertial yaw turning as a mechanism for maneuvering. Such maneuvers would be initiated by timing a bias to the horizontal wave during part of the undulation phase when inertial yaw moments are large, which would result in a net reorientation in under one undulation cycle.

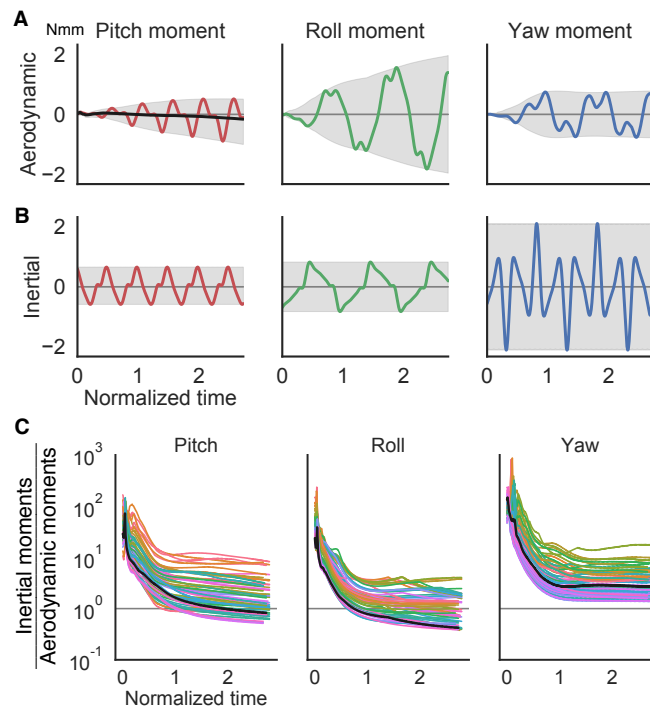


Figure 3.5: Inertial maneuverability in flying snakes. (A) Aerodynamic pitch, roll, and yaw moments from the phase averaging analysis (Eq. 3.2.5). Periodic traces indicate the moment time series for one phase, while gray bands indicate the extrema for all phases. The magnitude increases with time because the speed increases as the simulated snake falls due to gravity. The black line is the phase-averaged pitch moment (used in figure 3.4D-F), which is non-zero. The phase-averaged roll and yaw moments are always zero. (B) Inertial moments from the phase averaging analysis. The extrema do not change with time because inertial moments are independent of the animal's speed. (C) Relative contribution of inertial-to-aerodynamic moments (the peak-to-peak ratio of the moment time series) throughout a glide for different dorsoventral bending angles and number of spatial periods, with the vertical wave amplitude constant at  $20^\circ$ . Colors indicate different  $\nu_\theta$  combinations and are the same as in figure 3.4. The black line is the parameter combination of  $\nu_\theta$  and  $d_\psi$  shown in (A) and (B). Inertial moments always dominate at the beginning of the glide. Inertial yaw moments always dominate, suggesting a mechanism of maneuvering.

### 3.3 Conclusions

Flying snakes use undulation differently than all other known undulating animals: to increase their rotational stability. The increased rotational stability results in translational stability and an increase in glide performance. The newly discovered kinematic components of aerial undulation, and their effects on flight dynamics, suggest that a bioinspired flying snake robot can glide using aerial undulation as a control template [18]. The robot would require the following: first, observed horizontal wave shapes should be used, as they result in better rotational stability and performance. Second, the robot should employ a vertical wave, as this orients the local body cross section to be more aerodynamically advantageous. Third, the robot will likely be unstable in pitch, and should therefore use out-of-plane movement (with the posterior section alternating above and below the anterior section) to stay roughly horizontal with the ground. Fourth, biasing the horizontal wave will result in inertial yaw reorientations in under one undulation cycle. Ultimately, using the aerial undulation template should drastically simplify controlling a limbless flying robot.

### References

- [7] J. J. Socha. Gliding flight in the paradise tree snake. *Nature* 418 (2002), p. 603–604. DOI: 10.1038/418603a.
- [8] J. J. Socha, T. O’Dempsey, and M. LaBarbera. A 3-D kinematic analysis of gliding in a flying snake, *Chrysopelea paradisi*. *J. Exp. Biol.* 208 (2005), p. 1817–1833. DOI: 10.1242/jeb.01579.
- [9] J. J. Socha and M. LaBarbera. Effects of size and behavior on aerial performance of two species of flying snakes (*Chrysopelea*). *J. Exp. Biol.* 208 (2005), p. 1835–1847. DOI: 10.1242/jeb.01580.
- [10] J. J. Socha. Becoming airborne without legs: the kinematics of take-off in a flying snake, *Chrysopelea paradisi*. *J Exp Biol* 209 (2006), p. 3358–3369. DOI: 10.1242/jeb.02381.
- [11] J. J. Socha, K. Miklasz, F. Jafari, and P. P. Vlachos. Non-equilibrium trajectory dynamics and the kinematics of gliding in a flying snake. *Bioinspir. Biomim.* 5.045002 (2010). DOI: 10.1088/1748-3182/6/1/019501.

- [12] K. Miklasz, M. LaBarbera, X. Chen, and J. J. Socha. Effects of body cross-sectional shape on flying snake aerodynamics. *Exp. Mech.* 50 (2010), p. 1335–1348. DOI: 10.1007/s11340-010-9351-5.
- [13] J. J. Socha. Gliding flight in *Chrysopelea*: turning a snake into a wing. *Integ. Comp. Biol.* 51 (2011), p. 969–982. DOI: 10.1093/icb/icr092.
- [14] D. Holden, J. J. Socha, N. D. Cardwell, and P. P. Vlachos. Aerodynamics of the flying snake *Chrysopelea paradisi*: how a bluff body cross-sectional shape contributes to gliding performance. *J. Exp. Biol.* 217 (2014), p. 382–394. DOI: 10.1242/jeb.090902.
- [15] A. Krishnan, J. J. Socha, P. P. Vlachos, and L. A. Barba. Lift and wakes of flying snakes. *Phys. Fluids* 26.031901 (2014). DOI: 10.1063/1.4866444.
- [18] R. J. Full and D. E. Koditschek. Templates and anchors: neuromechanical hypotheses of legged locomotion on land. *J Exp Biol* 202 (1999), p. 3325–3332.
- [19] H. Marvi, C. Gong, N. Gravish, H. Astley, M. Travers, R. L. Hatton, J. R. Mendelson III, H. Choset, D. L. Hu, and D. I. Goldman. Sidewinding with minimal slip: Snake and robot ascent of sandy slopes. *Science* 346.6206 (2014), p. 224–229. DOI: 10.1126/science.1255718. arXiv: arXiv:1410.2945v1.
- [20] H. C. Astley, C. Gong, J. Dai, M. Travers, M. M. Serrano, P. A. Vela, H. Choset, J. R. Mendelson III, D. L. Hu, and D. I. Goldman. Modulation of orthogonal body waves enables high maneuverability in sidewinding locomotion. *Proc Natl Acad Sci* 112 (2015), p. 6200–6205. DOI: 10.1073/pnas.1418965112.
- [58] M. Walton, B. C. Jayne, and A. F. Bennet. The energetic cost of limbless locomotion. *Science* 249 (1990), p. 524–527. DOI: 10.1126/science.249.4968.524.
- [59] J. K. Hopkins, B. W. Spranklin, and S. K. Gupta. A survey of snake-inspired robot designs. *Bioinspir Biomim* 4 (2009), p. 021001. DOI: 10.1088/1748-3182/4/2/021001.
- [60] Z. V. Guo and L Mahadevan. Limbless undulatory propulsion on land. *Proc Natl Acad Sci* 105 (2008), p. 3179–3184. DOI: 10.1073/pnas.0705442105.
- [61] D. L. Hu, J. Nirody, T. Scott, and M. J. Shelley. The mechanics of slithering locomotion. *Proc Natl Acad Sci* 106 (2009), p. 10081–10085. DOI: 10.1073/pnas.0812533106.
- [62] S. Alben. Optimizing snake locomotion in the plane. *Proc R Soc A* 469 (2013), p. 20130236. DOI: 10.1098/rspa.2013.0236. arXiv: arXiv:1304.4479v1.

- [63] S. Hirose. *Biologically Inspired Robot*. Oxford University Press, 1993.
- [64] J. T. Pierce-Shimomura, B. L. Chen, J. J. Mun, R. Ho, R. Sarkis, and S. L. McIntire. Genetic analysis of crawling and swimming locomotory patterns in *C. elegans*. *Proc Natl Acad Sci* 105 (2008), p. 20982–20987. DOI: 10.1073/pnas.0810359105.
- [65] C. Fang-Yen, M. Wyart, J. Xie, R. Kawai, T. Kodger, S. Chen, Q. Wen, A. D. T. Samuel, and A. D. Samuel. Biomechanical analysis of gait adaptation in the nematode *Caenorhabditis elegans*. *Proc Natl Acad Sci* 107 (2010), p. 20323–20328. DOI: 10.1073/pnas.1003016107.
- [66] I. Hums, J. Riedl, F. Mende, S. Kato, H. S. Kaplan, R. Latham, M. Sonntag, L. Traunmüller, and M. Zimmer. Regulation of two motor patterns enables the gradual adjustment of locomotion strategy in *Caenorhabditis elegans*. *Elife* 5.e14116 (2016). DOI: 10.7554/eLife.14116.
- [67] S. G. Taylor. Analysis of the swimming of long and narrow animals. *Proc R Soc L. A Math Phys Sci* 214 (1952), p. 158–183. DOI: 10.1098/rspa.1952.0159.
- [68] M. Gazzola, M. Argentina, and L. Mahadevan. Gait and speed selection in slender inertial swimmers. *Proc Natl Acad Sci USA* 112 (2015), p. 3874–3879. DOI: 10.1073/pnas.1419335112.
- [69] A. J. Ijspeert. Central pattern generators for locomotion control in animals and robots: a review. *Neural Networks* 21 (2008), p. 642–653. DOI: 10.1016/j.neunet.2008.03.014.
- [70] A. J. Ijspeert, A. Crespi, D. Ryczko, and J.-M. Cabelguen. From swimming to walking with a salamander robot driven by a spinal cord model. *Science* 315 (2007), p. 1416–1420. DOI: 10.1126/science.1138353.
- [71] B. J. Gemmell, S. P. Colin, J. H. Costello, and J. O. Dabiri. Suction-based propulsion as a basis for efficient animal swimming. *Nat Commun* 6 (2015), p. 1–8. DOI: 10.1038/ncomms9790.
- [72] F. Jafari, S. Tahmasian, S. D. Ross, and J. J. Socha. Control of gliding in a flying snake-inspired n-chain model. *Bioinspir Biomim* 12 (2017), p. 066002. DOI: 10.1088/1748-3190/aa8c2f.
- [73] R. Dudley. Mechanisms and implications of animal flight maneuverability. *Integ Comp Biol* 42 (2002), p. 135–140. DOI: 10.1093/icb/42.1.135.

- [74] B. C. Jayne. Muscular mechanisms of snake locomotion: An electromyographic study of lateral undulation of the Florida banded water snake (*Nerodia fasciata*) and the yellow rat snake (*Elaphe obsoleta*). *J. Morphol.* 197 (1988), p. 159–181. DOI: 10.1002/jmor.1051970204.
- [75] G. B. Gillis. Neuromuscular control of anguilliform locomotion: patterns of red and white muscle activity during swimming in the American eel *Anguilla rostrata*. *J. Exp. Biol.* 201 (1998), p. 3245–3256.
- [76] B. F. Feeny and A. K. Feeny. Complex modal analysis of the swimming motion of a whiting. *J Vib Acoust.* 135.021004 (2013). DOI: 10.1115/DETC2011-48204.
- [77] B. F. Feeny, P. W. Sternberg, C. J. Cronin, and C. A. Coppola. Complex orthogonal decomposition applied to nematode posturing. *J Comput Nonlinear Dyn* 8.041010 (2013). DOI: 10.1115/1.4023548.
- [78] C. P. Ellington. The aerodynamics of hovering insect flight. I. The quasi-steady analysis. *Phil Trans R Soc L. B* 305.1122 (1984).
- [79] R. Dudley and P. DeVries. Tropical rain forest structure and the geographical distribution of gliding vertebrates. *Biotropica* 22 (1990), p. 432–434. DOI: 10.2307/2388564.
- [80] M. Saito, M. Fukaya, and T. Iwasaki. Modeling, analysis, and synthesis of serpentine locomotion with a multilink robotic snake. *IEEE Control Syst Mag* 22 (2002), p. 64–81.

# Chapter 4

## Body configuration and force production in flying snakes

MANUSCRIPT AUTHORS: Isaac J. Yeaton, Shane D. Ross, and John J. Socha

**Citation:** Yeaton, I. J., Ross, S. D., & Socha, J. J. (2018). Body configuration and force production in flying snakes. *Manuscript in preparation*.

### Abstract

Flying snakes (genus *Chrysopelea*) are the only known animals to fly without pairs of symmetric wings. Instead, the snakes jump, splay their ribs, and undulate through the air as they glide to the ground. The snake's ability to glide depends on how well its morphing wing-body produces lift and drag forces. Previous studies showed that the snake's roughly triangular body cross-section acts as a symmetric lifting bluff body, producing high lift over a large angle of attack range. However, previous kinematics experiments under-resolved the body, making it impossible to estimate the aerodynamic load on the animal or to quantify the different wing configurations throughout the glide. Here, we combine new glide experiments and previously measured lift and drag coefficients to estimate the aerodynamic forces acting on flying snakes during short glides. This analysis is enabled by new kinematic measurements of the center of mass motion. We find that quasi-steady theory under-predicts lift by 35% and over-predicts drag by 40%. With the increased resolution along the body,

we are also able to quantify the relative spacing of the body as it translates through the air. In steep glides, the body is generally not positioned to experience appreciable tandem effects from wake interaction during the glide. These results suggest unsteady 3D effects, with appreciable force enhancement, are important for snake flight. Future work can use the kinematics data presented herein to form test conditions for physical modeling, as well as computational studies to understand unsteady fluid dynamic effects on snake flight.

**Keywords:** gliding, snake, undulation, aerodynamics

## 4.1 Introduction

Flying snakes (*Chrysopelea*) are the only known animals to fly without bilaterally-symmetric wings. Animal flight requires producing and controlling aerodynamic lift and drag forces via neuromuscular control and/or specialized morphology. Flapping fliers use paired beating wings, while gliders deploy pairs of stretched skin between limbs [26, 27], extendable ribs [28, 29], webbed feet [30], or modified fins [43, 55]. In contrast, flying snakes flatten their bodies and undulate through the air, turning the whole animal into an ‘S’-shaped morphing wing [7]. The wing-body changes configuration continuously throughout the glide as the body forms straight segments connected by tight lateral bends that travel posteriorly (figure 4.1D) [8]. While airborne, the posture of the body is never symmetric about any axis.

A fundamental component to snake flight is how effective the wing-body is at producing lift and drag forces, and how these forces change as the animal accelerates and the glide shallows [22]. Understanding lift and drag production requires knowing the detailed kinematics of the morphing wing, as well as the lift and drag characteristics of the wing at each configuration. Given the orientation of the wing-body and the lift and drag coefficients of the cross-section, first-order approximations of the lift and drag forces can be calculated using the quasi-steady assumption [78].

The quasi-steady assumption states that the forces acting on a wing are a function of its instantaneous speed and orientation to the flow; the time history of the flow is not considered. The validity of quasi-steady theory is easily checked if the resultant aerodynamic force matches the center of mass acceleration of the animal. Although the quasi-steady assumption has proved insufficient to explain force production during flapping flight of insects and vertebrates [79, 81–88], it has not been tested explicitly for gliding animals with their nominally

static body postures [13, 22]. Despite flying snakes displaying large postural changes due to undulation, a previous study found that undulation frequency was not significantly correlated to any glide performance variables, suggesting that undulation itself has a minor role in aerodynamic force production and that quasi-steady theory is applicable [9]. Additionally, the fast forward speed compared to the relatively slow speed of undulation, quantified as the advance ratio, suggests that quasi-steady theory is applicable [14]. However, the aerodynamic forces produced during snake flight have never been calculated because the detailed wing-body kinematics and the center of mass trajectory were unknown.

A quasi-steady analysis requires that the lift and drag coefficients to be known. The lift and drag characteristics of the 2D cross-sectional shape of *C. paradisi* have been studied previously using load cell measurements, particle image velocimetry, and computational fluid dynamics [12, 14, 15]. The roughly triangular cross-section acts as a lifting bluff body (figure 4.1D, 4.2F, 4.3A), with the concave ventral surface and protruding lips serving to improve force production. The shape produces appreciable lift over a large range of angle-of-attack, with the lift-to-drag ratio peaking at an angle of attack of  $35^\circ$  (figure 4.3A). The profile has gentle stall characteristics, with drag increasing slowly after  $35^\circ$ . The cross-section is also effective at producing lift at high angles of attack, as the lift coefficient at  $60^\circ$  is roughly the same as at  $15^\circ$ . Additional physical modeling also determined that when two snake-like profiles are offset, there is a modification of the lift and drag through wake interaction effects [12]. More recent physical modeling investigated these tandem effects, finding appreciable lift-to-drag ratio changes for particular wing configurations that may be realizable during gliding [16].

In addition to the lift and drag characteristics, quasi-steady theory requires knowledge of the wing body kinematics: the instantaneous wing configuration, its orientation to the flow, and the animal's center of mass motion. Previous kinematic measurements of snake flight recorded either three or five landmarks on the body [7, 8, 11]. Although these data enabled a detailed trajectory analysis, the time-varying body posture and its orientation to the airflow had to be estimated from the horizontal body posture and glide angle. However, different sections of the body will experience different angles of attack, and portions of the body are swept relative to the airflow, which will affect the forces and moments acting on the body. Additionally, the out-of-plane bending of the body causes the snake's wing body to twist, thereby changing the angle of attack (see Chapter 3). This coarse understanding of the body made it impossible to estimate the locomotor forces and difficult to guide physical

and computational modeling studies. Additionally, the center of mass position, velocity, and acceleration could only be estimated, as the true configuration of the body was not known.

Here, we test the effectiveness of quasi-steady theory at approximating lift and drag forces at different times and locations along the snake’s body. We used a new kinematic analysis of between 11–17 landmark points along the snake’s body (described previously in Chapter 3), sufficient to recover the time-varying body posture of seven flying snakes. This new analysis enabled us to calculate, for the first time, the true center of mass position, velocity, and acceleration, as well as the morphing wing-body. Then, using as few assumptions as possible, we define the wing orientation and calculate quasi-steady lift and drag forces using the previously measured force coefficients, the blade element method, and simple sweep theory. We tested the quasi-steady assumption by comparing absolute errors between the resultant aerodynamic force and the calculated center of mass acceleration about the lateral, forward, and vertical directions, as well as corrections to the quasi-steady lift and drag forces such that this error is zero. This study provides the first analysis of the total aerodynamic load on flying snakes during gliding, as well as which portions of the body contribute most to force production. Additionally, we use the kinematics data to provide experimentally-observed test configurations for Reynolds number, angles of attack, and sweep angles, to guide future physical and computational modeling of snake flight.

## 4.2 Methods

### 4.2.1 Measurements of snake kinematics

A portion of the kinematics data presented here have been presented previously in Chapter 3, so we only highlight the experimental procedure here. We recorded the position of between 11 and 17 infrared tape markers placed along the dorsal surface of flying snakes using a 23-camera motion capture system with a sampling rate of 179 Hz. Experiments were conducted in the “Cube”, a three story tall blackbox theatre (a large indoor glide arena) located in the Moss Arts Center at Virginia Tech, under IACUC approval #15-034 (figure 4.1A-C). Snakes were allowed to jump and glide under their own volition from a height of 8.3 m. From the landmark points, we exported the marker trajectories and filled gaps using Kalman filters. We then smoothed the marker time series using two passes of a 2nd-order Butterworth filter, with cutoff frequencies selected separately for each coordinate time series for each marker,

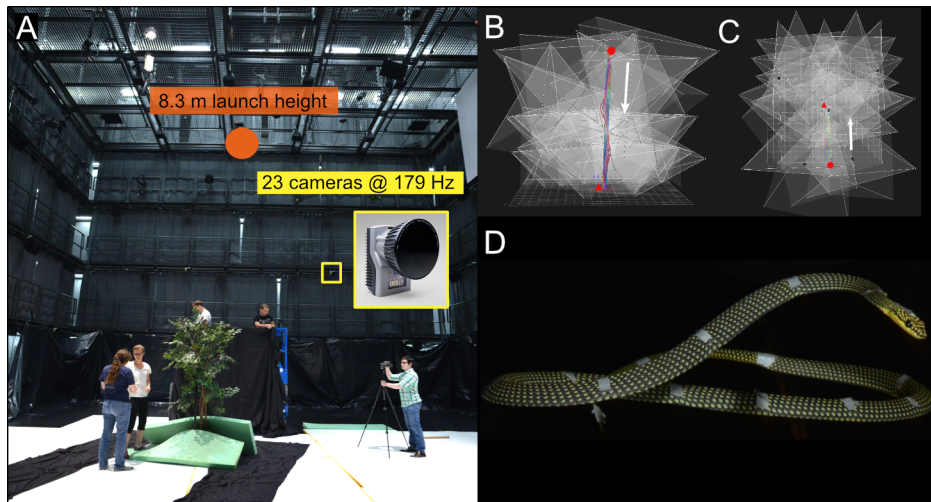


Figure 4.1: Indoor glide arena and glide trial experiments. (A) View of the “Cube”, showing the blackbox theatre equipped with launch platform, high-speed motion capture cameras, and target tree. (B,C) Rear and top views of the motion capture camera coverage cones. The IR marker trajectories for one trial are shown, with the jump and landing locations indicated by the red markers. (D) *C. paradisi* in an ‘S’-shaped glide posture. The flattened body and airfoil cross-sectional shape twist along the body. The infrared markers are shown along the dorsal surface of the animal.

as per Winter [89].

## 4.2.2 Reconstructing the body position

From the filtered marker time series, we fit cubic splines to form a continuous representation of the body at each moment in time (figure 4.2A,B). The spline defines the position of each location of the body,  $\mathbf{r}^I(t) = (x(t), y(t), z(t))$ , relative to the inertial frame. We calculated the velocity and acceleration of each location along the body in the inertial frame using finite differences,

$$\mathbf{v}^I(t) = \frac{\mathbf{r}(t + \Delta t) - \mathbf{r}(t - \Delta t)}{2\Delta t} \quad (4.2.1)$$

$$\mathbf{a}^I(t) = \frac{\mathbf{r}(t + \Delta t) - 2\mathbf{r}(t) + \mathbf{r}(t - \Delta t)}{\Delta t^2} \quad (4.2.2)$$

with second-order accurate forward and backward differences used at the beginning and end of each time series. We then super-imposed the average mass distribution, measured from

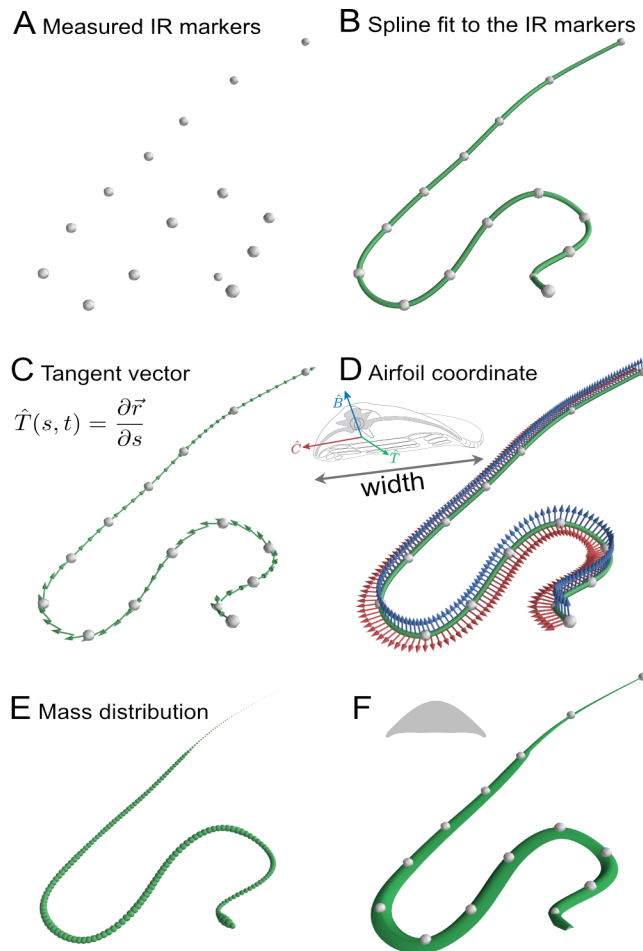


Figure 4.2: Method of reconstructing the morphing wing-body of flying snakes from recorded infrared marker (IR) trajectories. Each image shows the reconstruction step from one trial at the same time instance. (A) The measured IR markers provide a discrete representation of the body. (B) Cubic splines are fit to the IR markers, providing a continuous representation. (C) The tangent vector,  $\hat{T}$ , is used, along with the vertical direction, to define the airfoil coordinate system in (D). The width of the body is taken to define the chord-line,  $\hat{C}$ , and  $\hat{B}$  points upward through the backbone. (E) Mass distribution overlaid on the spline, visualized as spherical markers with radius proportional to the mass. The head and mid-body are relatively more massive; the tail only accounts for  $\approx 9\%$  of the animal mass. (F) Complete reconstruction of the morphing wing-body, showing the *C. paradisi* cross section overlaid on the spline, incorporating the orientation from (D) and the width distribution.

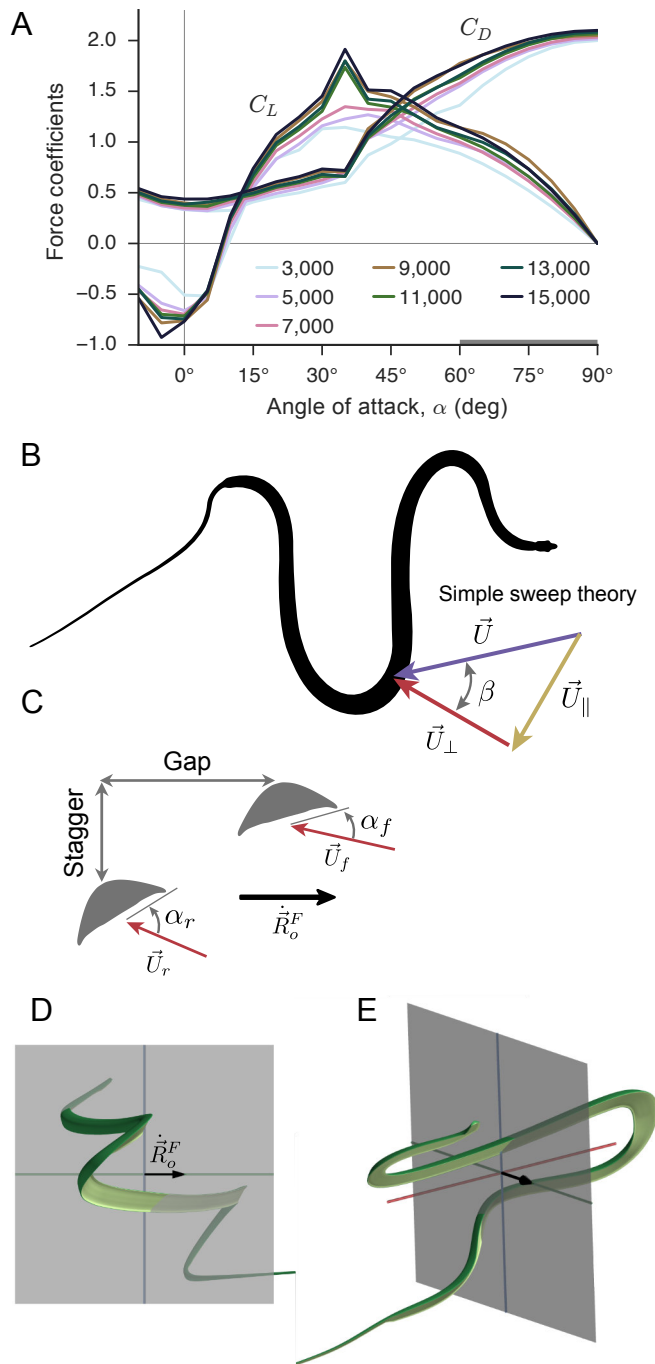


Figure 4.3: Quasi-steady aerodynamics and gap and stagger calculations. (A) Quasi-steady lift and drag coefficients for different angles of attack and Reynolds number, based on Holden et al. (2014). The coefficients for  $\alpha > 60^\circ$  are polynomial extrapolations such that the lift and drag coefficients match a triangular bluff body at  $\alpha = 90^\circ$  [90, 91]. (B) Simple sweep theory and sweep angle calculation. The perpendicular velocity component is used in the force calculations, and is found by removing the velocity component parallel to the local tangent direction. (C) Definition of gap, stagger, and angle of attack of the snake in the trajectory reference frame. Gap is the horizontal spacing and stagger is the vertical spacing. Both the front and rear airfoils have different angles of attack, sweep angles, and different local velocities. (D,E) Two time instances from a glide showing intersections of the body with the plane through the center of mass. The location of these intersections is used to calculate gap and stagger. The body is rotated to the trajectory reference frame, with the center of mass velocity in the  $+y$ -direction, denoted by the black arrow. The time point in (D) is from 53% through the glide, while (E) is from 90%. The dorsal surface is indicated in green and the ventral surface in yellow.

snake sectioning (see Appendix B,C.6), onto the spline and calculated the center of mass as

$$\vec{R}_0^I(t) = \frac{1}{M} \sum m_i \mathbf{r}(t), \quad (4.2.3)$$

where  $\vec{R}_0^I(t)$  is the center of mass,  $m_i$  is the mass of each element of the body (figure 4.2E), and  $M$  is the total mass. The center of mass position was then filtered using a Butterworth filter as above, and the center of mass velocity and acceleration were calculated using finite differences.

The center of mass trajectory was then iteratively rotated from the inertial frame into a straightened frame such that the glide path aligns with the vertical  $YZ$  plane while preserving the total arc-length displacement of the center of mass. The kinematics variables were rotated into the straightened frame by the yaw angle about the  $Z$  axis as

$$\psi = -\tan^{-1} \left( \dot{R}_{0,x} / \dot{R}_{0,y} \right) \quad (4.2.4)$$

The glide angle,  $\gamma$ , was calculated from the straightened frame center of mass velocity as

$$\gamma = -\tan^{-1} \left( \dot{R}_{0,z} / \dot{R}_{0,y} \right) \quad (4.2.5)$$

which is the angle of the center of mass velocity down from the horizontal direction.

### 4.2.3 Center of mass motion

The center of mass motion was analyzed by considering the trajectories from the overhead view in the inertial frame ( $X$  and  $Y$ ), as well as the side view in the straightened trajectory frame ( $Y$  and  $Z$ ). The trajectories were also analyzed using velocity polar diagrams, which encode how the forward and vertical velocity change during the glide. These diagrams also encode the glide angle and different phases of gliding (ballistic, shallowing, etc.), which can be related to the angle-of-attack dependent lift and drag characteristics of the glider [91]. The velocities, and therefore the entire diagram, can be non-dimensionalized and rescaled using an animal-specific characteristic velocity scale,  $v^*$ , given by

$$v^* = \sqrt{\frac{2W_S}{\rho}} \quad (4.2.6)$$

where  $W_S$  is the wing loading and  $\rho$  is the air density. The velocities are scaled as

$$\hat{v} = \frac{v}{v^*} \quad (4.2.7)$$

The non-dimensionalization and rescaling enables us to compare trajectories from different individuals with different sizes.

#### 4.2.4 Reconstructing the wing-body orientation

The wing orientation of the snake's body was reconstructed by overlaying an airfoil coordinate system onto the spline (figure 4.2C,D). The airfoil coordinate system, denoted as  $\{\hat{T}, \hat{C}, \hat{B}\}$ , allows us to calculate the orientation of the body relative to the flow and calculate aerodynamic forces. To define the airfoil coordinate system, we used the unit tangent vector,  $\hat{T}$ , of the spline and the inertial  $\hat{Z}$  direction. The unit tangent vector is locally tangent to the body and points posteriorly down the body from the head to the vent and is defined from the spline only. The width of the animal was taken as the chord-line direction, denoted as  $\hat{C}$ . Lastly, the coordinate system was closed by selecting a direction that locally points up through the backbone of the animal, denoted as  $\hat{B}$ . The airfoil coordinate system is given by

$$\hat{T}(s, t) = \frac{\partial \mathbf{r}^I(s, t)}{\partial s} \quad (4.2.8)$$

$$\hat{C}(s, t) = \frac{\hat{Z} \times \hat{T}(s, t)}{\|\hat{Z} \times \hat{T}(s, t)\|} \quad (4.2.9)$$

$$\hat{B}(s, t) = \hat{T}(s, t) \times \hat{C}(s, t) \quad (4.2.10)$$

where  $s$  is the arc-length coordinate. We defined  $\hat{C}(s, t)$  such that it lies within the horizontal plane of the inertial coordinate system. We tried to define the  $\hat{C}$  direction using other assumptions about minimal twisting of the snake, but visually the results did not match observed photographic and video footage of the glides. We note that the airfoil coordinate system twists depending on the local orientation of the body.

From the airfoil coordinate system, the two-dimensional airfoil shape can be rotated to lie within the  $\hat{C} - \hat{B}$  plane, and scaled to match the measured width based on its distance along the body (figure 4.2F). The resulting body is visually very similar to the observed body while gliding.

### 4.2.5 Lift and drag forces

Lift and drag forces acting on the body were calculated using the blade element method and simple sweep theory, along with previously measured quasi-steady lift and drag coefficients. Each location along the body is treated as aerodynamically independent (i.e. no wake-interaction effects) and the lift and drag forces were calculated as

$$\vec{f}_L = \frac{\rho U_\perp^2}{2} \cdot c(s) \cdot C_L(\alpha, Re) \cdot \hat{L} \quad (4.2.11)$$

$$\vec{f}_D = \frac{\rho U_\perp^2}{2} \cdot c(s) \cdot C_D(\alpha, Re) \cdot \hat{D} \quad (4.2.12)$$

where  $\vec{f}$  is the force per unit length,  $\rho$  is the air density,  $U_\perp$  is the velocity locally perpendicular to the body,  $c(s)$  is the measured chord length as it varies along the body,  $C_L$  and  $C_D$  are the lift and drag coefficients (figure 4.3A) as functions of angle-of-attack  $\alpha$  and Reynolds number  $Re = Uc/\nu$ , where  $U$  is the total velocity magnitude, and  $\hat{L}$  and  $\hat{D}$  are described below. The total aerodynamic force that acts at the center of mass is calculated by integrating the lift and drag forces along the body.

Simple sweep theory was used to calculate forces on the curved sections of the body. Only the velocity component that is locally perpendicular to the body was used to calculate the forces, enabling us to use previously measured lift and drag coefficients for the snake body cross-section with a sweep angle of zero degrees. The local velocity,  $\dot{\mathbf{R}}(s, t)$ , was projected into the  $\hat{C} - \hat{B}$  plane such that it is locally normal to the body as follows,

$$\dot{\mathbf{R}}_T = (\dot{\mathbf{R}} \cdot \hat{T})\hat{T} \quad (4.2.13)$$

$$\dot{\mathbf{R}}_{CB} = \dot{\mathbf{R}} - \dot{\mathbf{R}}_T \quad (4.2.14)$$

$$U_\parallel = \|\dot{\mathbf{R}}_T\| \quad (4.2.15)$$

$$U_\perp = \|\dot{\mathbf{R}}_{CB}\| \quad (4.2.16)$$

where the subscripts indicate along which direction the velocity lies. The angle of attack is the angle between the perpendicular velocity and the chord-line direction, and is given by

$$\alpha(s, t) = \cos^{-1} \left( \frac{\dot{\mathbf{R}}_{CB} \cdot \hat{C}}{U_\perp} \right) \quad (4.2.17)$$

The sweep angle,  $\beta$ , was calculated as the angle between the velocity within the plane of the

bottom of the snake and the total velocity.

$$\beta(s, t) = \cos^{-1} \left( \frac{\dot{\mathbf{R}}_{TC} \cdot \hat{T}}{\|\dot{\mathbf{R}}_{TC}\|} \right) - \frac{\pi}{2} \quad (4.2.18)$$

where  $\dot{\mathbf{R}}_{TC} = \dot{\mathbf{R}} - \dot{\mathbf{R}}_B$  and  $\dot{\mathbf{R}}_B = (\dot{\mathbf{R}} \cdot \hat{B})\hat{B}$ . The shift of  $\pi/2$  accounts for the above dot product as the angle between the tangent vector and the velocity, not the velocity and the chord-line direction.

The lift and drag coefficients are functions of both angle of attack and Reynolds number. The orientation of the drag vectors,  $\hat{D}$ , act along the direction of the perpendicular velocity  $\dot{\mathbf{R}}_{CB}$ ; the orientation of the lift vector,  $\hat{L}$ , acts normal to both the tangent vector and drag vector. The force orientations are given by

$$\hat{D} = -\dot{\mathbf{R}}_{CB}/U_{\perp} \quad (4.2.19)$$

$$\hat{L} = \hat{T} \times \hat{D} \quad (4.2.20)$$

The effect of simple sweep theory is to reduce the velocity in the force equations (4.2.11) and (4.2.12). We quantified this effect by taking the ratio of the forces with and without the simple sweep theory assumption. Because simple sweep theory only affects the velocity, this ratio is the fraction of the dynamic pressure due to the curved sections of the snake body. The dynamic pressure fraction reduces to

$$q_f = \frac{U_{\perp}^2}{U^2} \quad (4.2.21)$$

#### 4.2.6 Aerodynamic force errors

We quantified the error of the quasi-steady force estimates by comparing the total aerodynamic force acting at the center of mass with the acceleration of the center of mass in the straightened frame. The translational equations of motion for the snake are

$$\vec{F}_L + \vec{F}_D + m\vec{g} = m\ddot{\mathbf{R}}_0 \quad (4.2.22)$$

where  $m$  is the animal's mass,  $\vec{g}$  is gravity, and  $\ddot{\vec{R}}_0$  is the center of mass acceleration. The total lift and drag forces acting at the center of mass,  $\vec{F}_L$  and  $\vec{F}_D$ , are

$$\vec{F}_L = \int_0^L \vec{f}_L ds \quad \vec{F}_D = \int_0^L \vec{f}_D ds \quad \vec{F}_A = \vec{F}_L + \vec{F}_D \quad (4.2.23)$$

where  $L$  is the length of the animal and  $\vec{F}_A$  is the total aerodynamic force. The translational equations of motion were normalized by the weight of each animal,  $mg$ , so that errors could be compared across individuals. The weight term was then moved to the righthand side of (4.2.22) to isolate the forces. This manipulation results in the normalized force equation

$$\frac{\vec{F}_A}{mg} = \frac{\ddot{\vec{R}}_0}{g} + \hat{Z} \quad (4.2.24)$$

The absolute force errors are

$$\begin{aligned} \epsilon_x &= \ddot{\vec{R}}_{0,X} - \bar{F}_{A,X} \\ \epsilon_y &= \ddot{\vec{R}}_{0,Y} - \bar{F}_{A,Y} \\ \epsilon_z &= \ddot{\vec{R}}_{0,Z} - \bar{F}_{A,Z} + 1 \\ \epsilon &= (\epsilon_x, \epsilon_y, \epsilon_z) \end{aligned} \quad (4.2.25)$$

where the bar indicates normalized forces and accelerations, and the one in the  $\epsilon_z$  equation results from the gravitational acceleration. Because the errors were calculated in the straightened frame,  $\epsilon_x$  is the lateral error of forces trying to move the center of mass away from the trajectory,  $\epsilon_y$  is the error contributing to forward motion, and  $\epsilon_z$  is the error in offsetting the animal's weight against gravity. Using the straightened frame allows us to compare errors consistently across trials. If instead we used the forces and acceleration in the inertial frame, the  $\epsilon_x$  and  $\epsilon_y$  errors would not directly correlate to moving the animal away from the trajectory or for forward motion, but a less intuitive combination of the two.

For each trial, we compared the force errors against the height of the animal's center of mass above the ground. We chose to use height instead of time since the jump because evaluating when the jump begins is subject to human error. Lastly, linear interpolation was used to interpolate the accelerations and forces such that each glide was sampled on a uniform height grid. This enabled us to calculate the averages and standard deviations of the forces, accelerations, and errors for each individual.

### 4.2.7 Corrections to the lift and drag forces

We found what appear to be constant errors in the force estimates about the forward ( $\epsilon_y$ ) and vertical ( $\epsilon_z$ ) directions. Observations of the error time series suggests that quasi-steady theory overestimated the drag force and underestimated the lift force. To determine how the lift and drag forces needed to be modified to reduce the errors, a numerical minimization procedure was used to modify the force distribution along the snake's body. We calculated the necessary change in the force contributions throughout the glide by minimizing the total error  $\epsilon'$  given by

$$\epsilon' = \|\ddot{\bar{R}}_0 - \bar{F}'_A\| \quad (4.2.26)$$

where the prime denotes the modified and normalized force given by

$$\bar{F}'_L = b_L \bar{F}_L \quad \bar{F}'_D = b_D \bar{F}_D \quad \bar{F}'_A = \bar{F}'_L + \bar{F}'_D \quad (4.2.27)$$

where the two time-varying scalar force modifiers determined numerically are  $b_L$  and  $b_D$  for the lift and drag forces, respectively.

### 4.2.8 Gap and stagger

Gap and stagger are defined as the relative horizontal and vertical position of the downstream body segment relative to the upstream segment. To quantify the relative spacing of the body for possible wake interaction effects, we calculated the time-varying gap and stagger values of the snakes throughout the trajectory. Gap and stagger are calculated in the trajectory reference frame, defined by rotating the body from the straightened frame such that the center of mass velocity is in the forward direction. In the trajectory reference frame, gap is defined as the horizontal distance between the upstream and downstream segments and stagger as the vertical distance (figure 4.3C). Beginning in the straightened frame, the center of mass position was removed to isolate the relative motion of body about the center of mass. Next, the body was rotated about the lateral ( $\hat{X}$ ) axis by the glide angle equation (4.2.5) such that the center of mass velocity was in the forward direction. The rotations of the body

into the different frames are given by

$$\mathbf{R}^S = \mathbf{C}^{I \rightarrow S} \cdot \mathbf{R}^I \quad (4.2.28)$$

$$\mathbf{R}^{S,c} = \mathbf{R}^S - \vec{R}_0^S \quad (4.2.29)$$

$$\mathbf{R}^F = \mathbf{C}^{S \rightarrow F} \cdot \mathbf{R}^{S,c} \quad (4.2.30)$$

where the superscripts denote the inertial ( $I$ ), straightened ( $S$ ), and trajectory reference ( $F$ ) frames, and the rotation matrices are denoted by  $\mathbf{C}$ .

Once in the trajectory reference frame, we found intersections of the body spline with a vertical plane at the center of mass (figure 4.3D,E). The locations of the intersections defined where the gap and stagger values were calculated. For each intersection, we took the relative displacement between the upstream and downstream airfoils as the gap and stagger, respectively. Sometimes, the body intersected the vertical plane multiple times. During these instances, we defined two separate gap and stagger values from the first and second intersections and the second and third intersections.

#### 4.2.9 Gap and stagger from previous kinematic measurements

Analysis of the center of mass trajectory revealed steep glides compared to previous kinematic measurements of snake glides [8, 11]. This prompted us to revisit data from previous studies to extract gap and stagger information. For this analysis, we used data from Socha et al. [11], which was the previous best kinematics data. This experiment recorded late-phase gliding in two individuals, with four trials per snake analyzed, of glides originating from a height of 15 m. The data comprise trajectories of five landmark points (head, 1/4 SVL, 1/2 SVL, 3/4 SVL, and vent), rotated into the trajectory reference frame. Gap and stagger values were estimated from these data as described above, using marker pairs — head–1/2, 1/4–3/4, and 1/2–vent — at time points when the lateral displacement of the marker pairs were the same. Time points with the same lateral displacement are an approximation to intersections of the body with the vertical plane at center of mass; this approximation was made because the center of mass is not precisely known from the five point data.

#### 4.2.10 Assumptions

The analysis presented in this study is based on several layers of assumptions, beginning with the measured infrared marker trajectories. From the marker trajectories, the spline curve was used to represent the body as it moves through space. Next, the mass and width distributions were overlaid on the spline; the mass distribution was measured from anatomical snake sectioning, and the width distribution from photographs. The gap and stagger calculations are based on the spline, while the relative angle-of-attack and sweep angle of the wing segments incorporates assumptions discussed below.

A needed assumption for the quasi-steady force calculations is the orientation of the airfoil coordinate system. The airfoil coordinate system directly affects the aerodynamic force calculations, as it determines the angle of attack. We selected a robust method to calculate the airfoil coordinate system that resulted in a reconstructed wing-body that visually matched photographs of the snakes while airborne. The visual match included the twisting of the body at the ‘U’-bends, the overall orientation of the straight segments, as well as the calculated forces being smooth. The other aerodynamic assumptions are (1) the use of simple sweep theory to account for the non-perpendicular body segments and (2) quasi-steady aerodynamics. The simple sweep theory assumption enabled the use of our current best understanding of flying snake aerodynamics, as no data exists on the relative orientation of the airflow to the body. Likewise, the quasi-steady aerodynamics theory had not been tested on flying snake locomotion given our previously poor understanding of the whole body during a glide. The data presented in this study should help guide future work to address the assumptions used here.

## 4.3 Results

### 4.3.1 Center of mass motion

The center of mass trajectory from the side and overhead views is shown in figure 4.4A,B for a total of seven individuals. For the center of mass analysis, multiple glides from three individuals are shown separately, chosen because these individuals gave the greatest number of useable trials to analyze, and happened to span the observed mass range of animals tested. The side views indicate relatively steep glides compared to previous studies. The largest animal (snake 81, mass: 107.2 g) only covered about 4 m horizontally from an 8.3 m jump height. The lightest animal (snake 95, mass: 37.3 g) has more variation in the horizontal glide distance, but generally performed better and covered horizontal distances up to 5 m. Trial 618 (figure 4.4Ai,Bi) was the best performing glide, as it shallowed fastest and covered the most horizontal distance. However, the snake landed on the target tree placed in the glide arena (figure 4.1A), so the full potential was not recorded; it is estimated that this snake could have glided 7 m horizontally. The overhead view of the center of mass trajectories (figure 4.4B) shows that the glide paths were generally not straight. The center of mass motion has broad arcs, but no discernible turning events were observed. The overhead view shows that there were no oscillations of the center of mass due to undulation.

The dimensional velocity polar diagrams (figure 4.4C) indicate initial forward velocities at or below 2 m/s for all snakes. The velocity trajectories initially move vertically on the diagram as the snakes accelerate downwards while, the horizontal velocity stays constant during the ballistic phase. The glide angle during this phase increases from roughly  $0^\circ$  to  $60^\circ$ – $75^\circ$  before the velocity trajectory arcs upward. The shape of the arc upwards is similar across all glides and is consistent with motion onto the “terminal velocity manifold” in theoretical models of gliding [91]. For the smallest snake (figure 4.4Ci), the trajectory curves upwards the most, indicating it progressed farthest through the glide. The curve upwards is more apparent when viewing the non-dimensional and rescaled velocity polar diagrams (figure 4.4D), as all effects of animal size have been removed. The glides that performed best, trial 618 from snake 95 and trial 505 from snake 88, progressed farthest on the velocity polar diagram and had higher initial horizontal velocities. The higher velocity likely caused the glide to transition more quickly, while slower horizontal velocities took longer to transition.

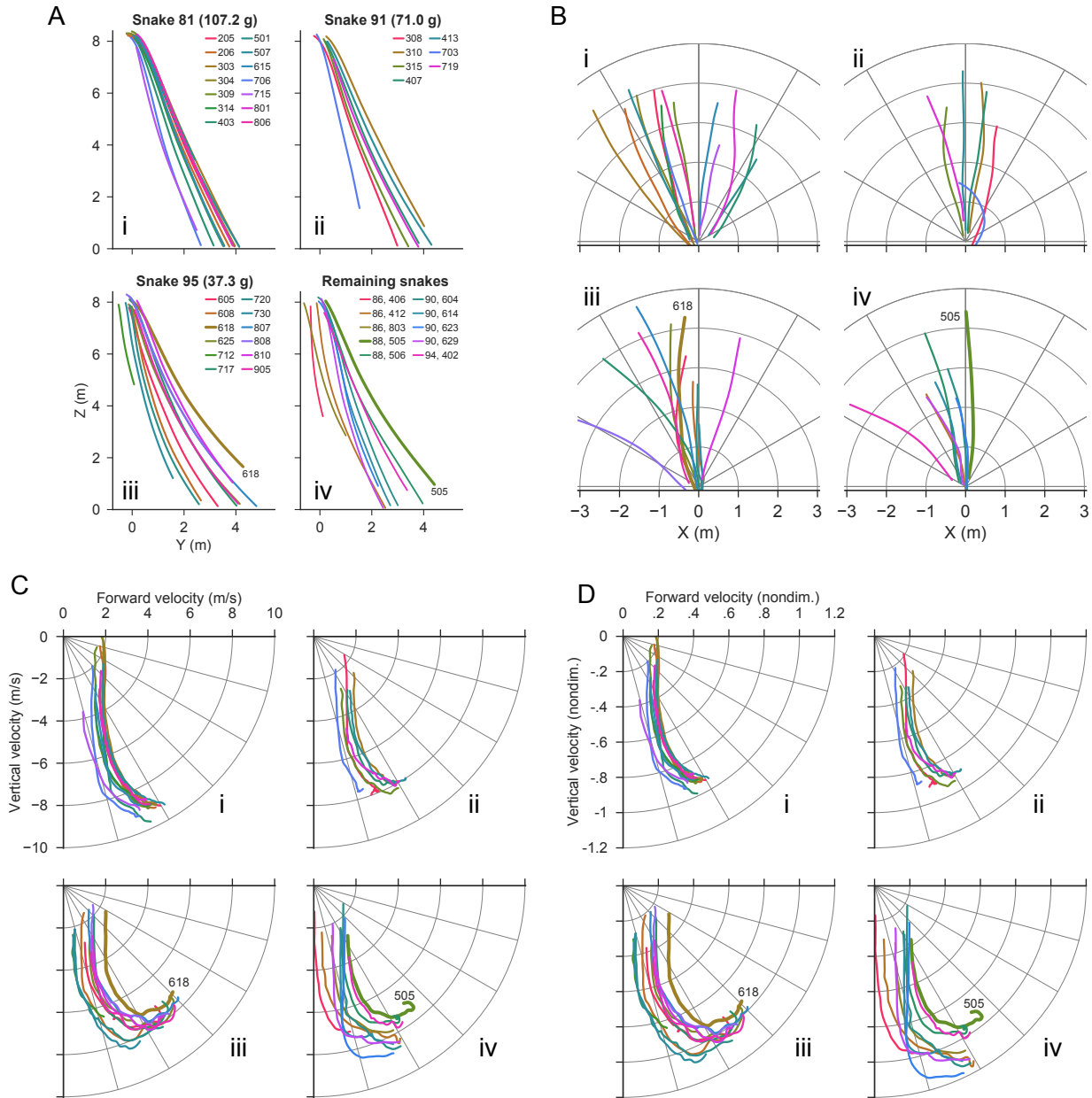


Figure 4.4: Caption on next page.

Figure 4.4: (Previous page.) Overview of trajectory dynamics for 43 trials from seven flying snakes. (A) Side view of the glide path in the straightened frame. Three of the panels are for three individuals that gave the greatest number of usable glides and spanned the entire mass range of snakes used. The last panel shows glides for four additional individuals. Different trials for each snake are indicated by different colors and the trial number is labelled. The first number of the trial identification is the day of testing. The best performing glides are trial 618 from snake 95 and trial 505 from snake 88. (B) Overhead view of the glide path showing the unfiltered center of mass position in the inertial frame. The glides are generally not straight and show broad arcing behavior. (C) Velocity polar diagrams of forward and vertical velocity in the straightened frame. The glide angle is the angle subtended from the horizontal downward. (D) Velocity polar diagrams that has been non-dimensionalized and rescaled to remove the effects of animal size. Velocity trajectories show a characteristic vertical portion during the ballistic phase, followed by an upward hook onto the terminal velocity manifold near a rescaled velocity of 1. The lightest snake (snake 95) progresses farthest on the diagram and had the best glide performance (in trial 618).

### 4.3.2 Lift and drag forces

The quasi-steady forces and center of mass accelerations are shown in figure 4.5 for the three individuals with the greatest number of usable glides. If quasi-steady theory properly accounts for the aerodynamic forces, the left and right plots in figure 4.5 should be the same. We see the same trends across individuals in regards to the forces and accelerations, but quasi-steady theory is insufficient to explain the aerodynamic forces on the snake. In general, the force estimates are smoother than the accelerations, with smaller standard deviations during the trajectory. The lower standard deviation is due to only needing to perform one numerical derivative to calculate velocities, while the center of mass acceleration requires two derivatives, as well as integrating the forces having a filtering effect.

Both the average lateral force and lateral accelerations are near zero, indicating fairly good agreement between the accelerations and quasi-steady theory (figure 4.5A). The deviations are larger about the forward and vertical directions. The forward forces, which are the aerodynamic forces responsible to pull the animal horizontally over the ground, are too low compared to the accelerations. The average accelerations peak at approximately 0.5 body weight (BW), while the forces peak at approximately 0.25 BW (figure 4.5B). In contrast, the vertical forces are higher than the accelerations. The vertical forces are responsible for offsetting the animal's weight against gravity. The force time series indicate that more vertical force is produced than needed to support the weight (forces are above the dashed line in figure 4.5C). The accelerations are lower and only cross the supporting body weight threshold for the lightest snake. Therefore, the quasi-steady force estimates show qualitatively the same trends as the accelerations, but the forces are underestimated in the forward direction and overestimated in the vertical direction.

Across individuals, the accelerations about the lateral direction are similar. However, there is a qualitative difference in the forward and vertical directions between the lightest and heaviest individuals (snake 95, mass: 37.3 g and snake 81, mass: 107.2 g) with a difference in mass of approximately  $2.9\times$ . The forward acceleration of the lighter snake peaks and then decreases near the end of the glide, whereas the heavier snake does not show this behavior. The vertical accelerations show the lighter snake accelerating upward near the end of the trajectory, whereas the heavier snake does not. The medium-heavy snake (snake 91, mass: 71 g, mass ratio of  $1.9\times$  compared to the lighter snake) appears to be accelerating slightly upwards.

### 4.3.3 Aerodynamic force errors and corrections

The absolute force errors, defined as the absolute difference between the calculated center of mass acceleration and the resultant aerodynamic force, are shown in figure 4.6A for all of the seven snakes analyzed. Errors are near zero about the lateral direction. The forward force error is approximately  $0.25 BW$ , while the vertical force error is approximately  $-0.5 BW$ . The physical interpretation of these errors is that quasi-steady theory overestimates drag and underestimates lift, as the drag force acts predominantly in the vertical direction, while the lift force acts predominantly in the forward direction. Decreasing drag and increasing lift will rotate the resultant aerodynamic force vector forward and reduce the error.

The required multipliers to the lift and drag forces to reduce the total error to zero are shown in figure 4.6B. The lift force needs to increase by  $1.35\times$  and the drag force needs to decrease by  $0.6\times$  of the quasi-steady values. The change in drag is constant throughout the glide. The change in lift decreases from approximately  $2\times$  to  $1\times$  as the glide progresses. The force multipliers indicate that quasi-steady theory consistently overestimates the total drag force by approximately 40% and underestimates the total lift force by approximately 35%.

### 4.3.4 Lift and drag distributions

The time-varying lift and drag distributions for the best performing glides are shown in figure 4.7 for different heights as the animals glide. The force distributions have the same orientation as predicted by quasi-steady theory, but have been scaled using the lift and drag multipliers such that the total force errors are near zero. Therefore, the true local lift and drag force may be quite different than shown. By 10% through the glide (the first row in figure 4.7), the snake bodies have already formed the ‘S’-shaped glide posture, and lift and drag forces are being produced. As the glides progress, the smaller animal (snake 95, mass: 37.3 g, SVL: 64.4 cm) forms a tight body posture, with the posterior body dropping below the head. The larger animal (snake 88, mass: 71.9 g, SVL: 88.8 cm) has a more open body posture, with fewer spatial periods of bending, and a more horizontal orientation.

There are commonalities in the force distributions for both animals. The force magnitude increases as the animals accelerate downward. The drag force is continuous along the body, including both the straight segments and the ‘U’-bends. In contrast, the lift force decreases to zero at the ‘U’-bends, and is largest along the straight segments. The transition region to

zero lift is small and does not extend over the entire ‘U’-bend region. The small transition region is likely related to low sweep angles before and after the ‘U’-bends (figure 4.8E,F). The estimated force produced by the tail is small because of its small width. This small width also results in lower Reynolds numbers (figure 4.8A,B). For snake 88, the body is initially highly swept, with the straight segments angled roughly  $45^\circ$  relative to the forward direction. However, the model still indicates that these areas produce appreciable lift force. The side views of the glides indicate that the drag force acts in the vertical direction and against the direction of forward motion. The lift force is angled upwards relative to the horizontal and along the direction of forward motion.

For the glides shown in figure 4.7, the time histories of the Reynolds numbers, angles of attack, sweep angles, and dynamic pressure fraction distributions are shown in figure 4.8. The Reynolds number (figure 4.8A,B) increases throughout the glide as the animal accelerates. The larger animal has higher Reynolds numbers due to its greater width and speed. The Reynolds numbers peak midway along the body, where the animal is widest. The angles of attack are high, ranging from  $60^\circ$  to  $90^\circ$  at various points along the body. The ‘U’-bends have the highest angles of attack (shown as dashed lines in figure 4.8A,B), which results in the locations of zero lift production in figure 4.7. The ‘U’-bends have the highest sweep angles, and locations along the body near the ‘U’-bends have low sweep values. Even along the straight segments, the sweep angle is generally greater than  $30^\circ$ . Lastly, the dynamic pressure fraction due to simple sweep theory is shown in figure 4.8G,H, with the 75% contour highlighted. Values of 100% indicate no decrease in lift or drag due to the swept wing, whereas values of 0% indicate no force being produced because of sweep. The straight segments of the snake maintain the most dynamic pressure, although there are regions where this is not the case (figure 4.8G and figure 4.7 for snake 95 at 0.7 and 0.6 of the height fallen).

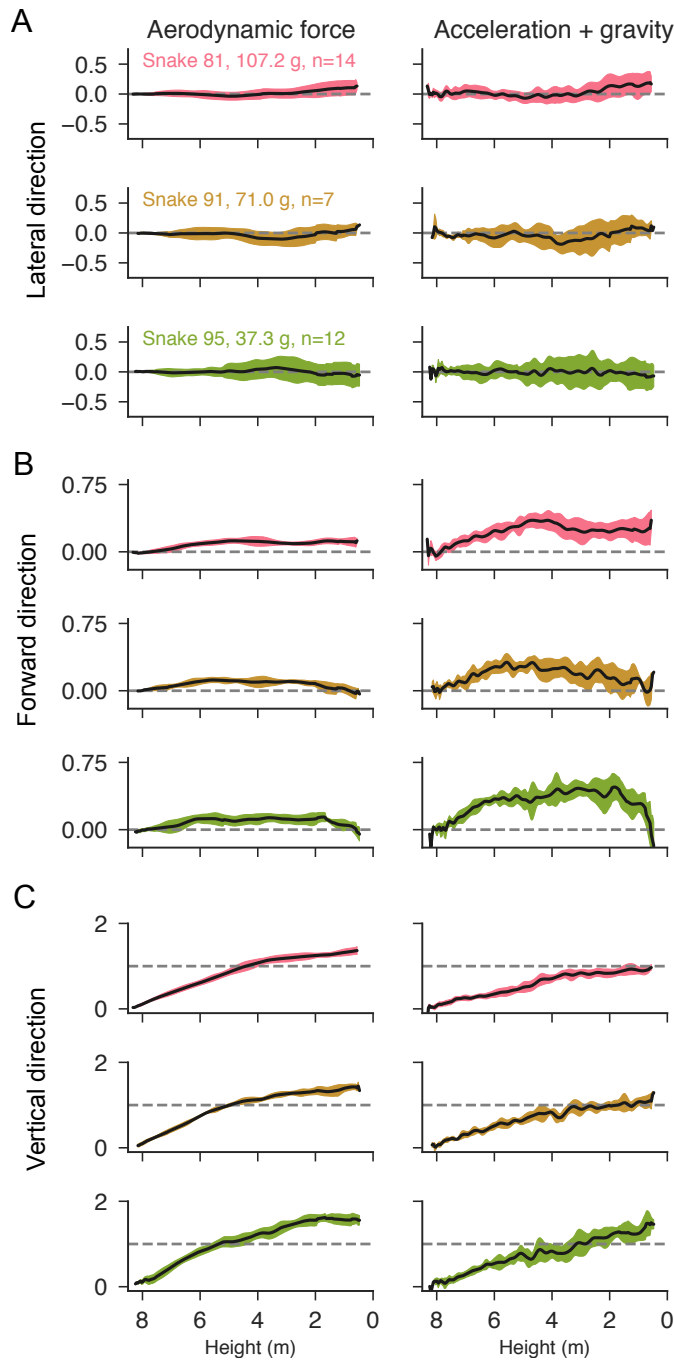


Figure 4.5: Aerodynamic force estimates and center of mass acceleration, normalized by body weight, as functions of height for three snakes. The left column is determined from the left hand side of equation (4.2.24), which consists of the integrated lift and drag forces. The right column is determined from the right-hand side of equation (4.2.24) and consists of the accelerations and gravity. The black line is the average for all trials and the colored band is  $\pm 1$  standard deviation. (A) Lateral direction force and acceleration components are close to zero. (B) Forward forces, responsible for horizontal motion over the ground, are smoother than forward accelerations, but the force estimates are too low. (C) Vertical forces, responsible to offset the animal’s weight, are too high compared to vertical accelerations. The dashed line indicates the equilibrium configuration when the aerodynamic forces balance the weight.

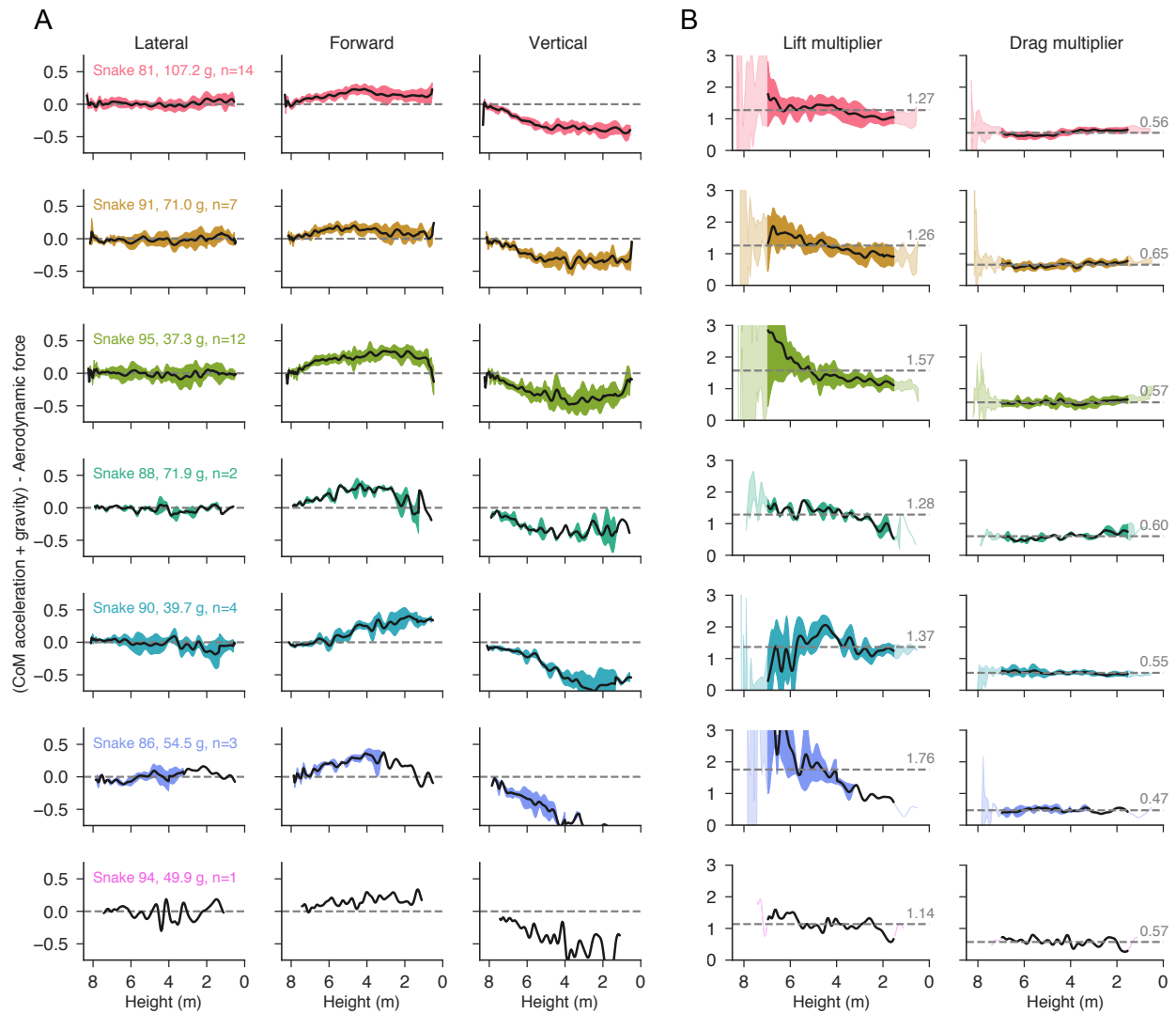


Figure 4.6: Aerodynamic force errors and corrections. (A) Absolute force errors normalized by body weight about the lateral, forward, and vertical directions given by equation (4.2.25) for 43 glide trials from seven snakes. The average errors are shown in black, with the colored bands indicating  $\pm 1$  standard deviation. Lateral errors are near zero. Forward force errors are positive, with a maximum error of 0.25 BW, indicating insufficient forward force. The vertical force error is negative, with a minimum of approximately -0.5 BW, indicating too much vertical force. (B) Corrections to the quasi-steady lift and drag forces to reduce the forward and vertical force errors to zero. The left column is the multiplier needed for the lift force and the right column is the multiplier needed for the drag force. The drag multiplier is constant throughout the glides and is approximately  $0.6\times$ , while the lift multiplier decreases throughout the glide. The average lift multiplier is approximately  $1.35\times$ .

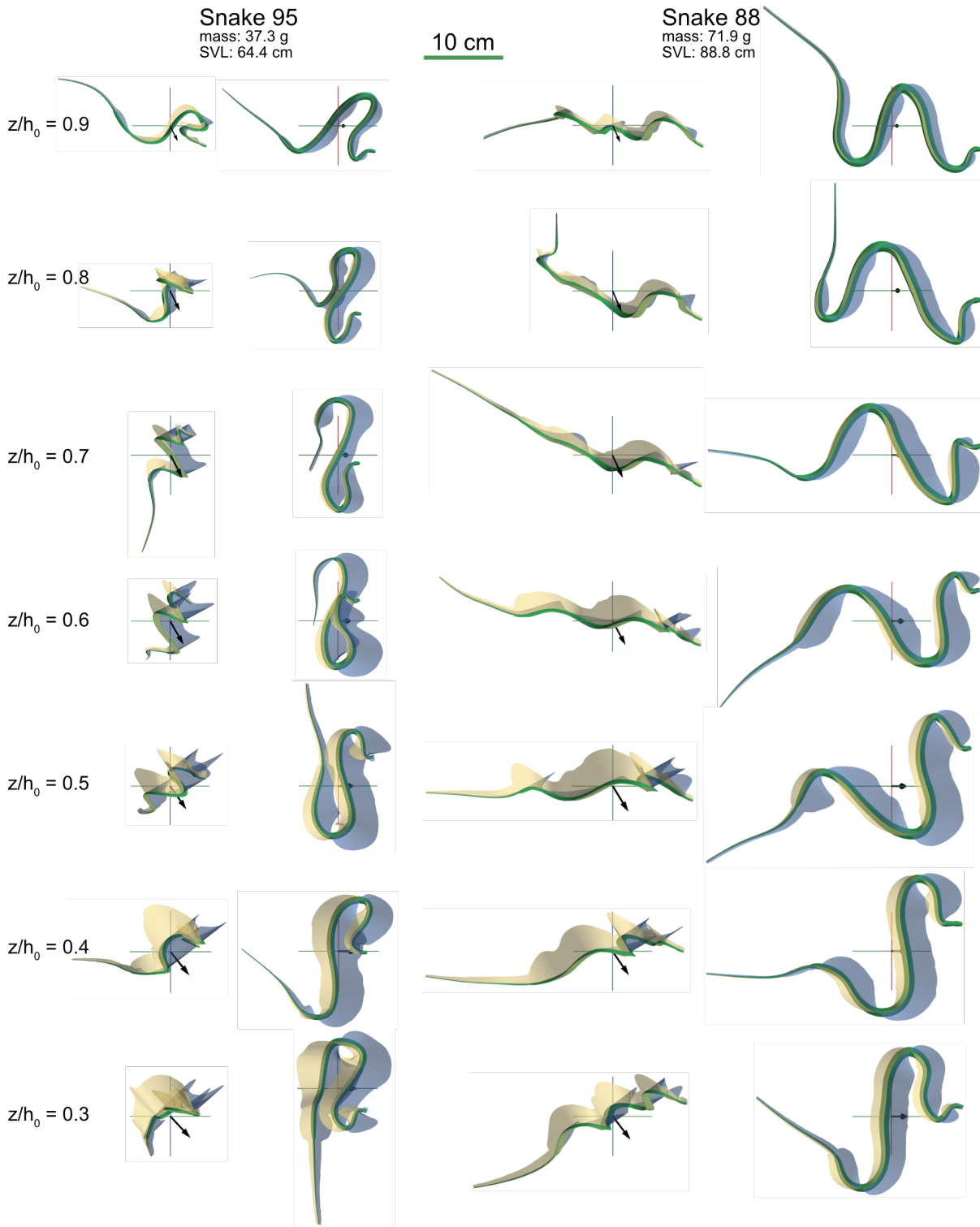


Figure 4.7: Caption on next page.

Figure 4.7: (Previous page.) Corrected quasi-steady lift and drag force distributions for two snakes from the best performing glides. For each snake, lift force distribution (blue) and drag force distribution (yellow) are shown from the side and top view (left and right columns). Progress through the glide (height fraction) is marked by the rows, with 0.9 being closest to the launch branch. The instantaneous forces have been corrected using the force multipliers from figure 4.6B. The instantaneous center of mass velocity is shown with the black arrow, and the center of mass location by the axes. Each image is scaled such that the green coordinate axis is 10 cm. The smaller snake, snake 95, had more out-of-plane motion of the posterior body and a tighter body profile than the larger snake 88. For both animals, the drag force is continuous and large over the whole body, with the straight and ‘U’-bend segments contributing similar amounts. The lift force is lowest at the ‘U’-bends, but the symmetric airfoil produces force along the interior of the bend. The tail produces little force due to its small width.

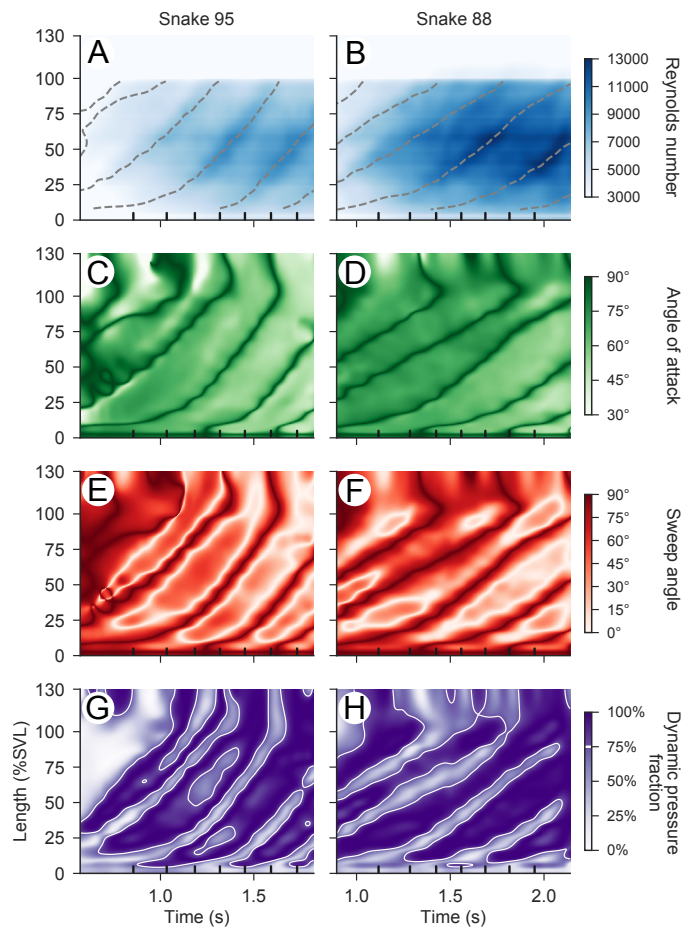


Figure 4.8: Space-time plots of Reynolds number, angle of attack, sweep angle, and dynamic pressure fraction for the glides shown in figure 4.7. The locations of the time points in figure 4.7 are indicated by the vertical black marks. (A,B) Reynolds number distribution, where the gray dotted lines denote the ‘U’-bends, found as zero crossings of the horizontal wave. The Reynolds number increases as the animal accelerates, with snake 88 having higher Reynolds numbers because it is wider than snake 95. The tail has a much lower Reynolds number because of its small width. (C,D) Angle-of-attack distributions, where the ‘U’-bends are ridges of high angle of attack. (E,F) Sweep angle distribution, where ridges of high sweep at the ‘U’-bends are surrounded by sweep angles near 0°. Both the angles of attack and sweep angles generally decrease as the glide shallows. (G,H) Fraction of the dynamic pressure,  $U_{\perp}^2/U^2$ , due to simple sweep theory. Regions where over 75% of the dynamic pressure is maintained are dark and outlined with the white contour; these regions generally occur along the straight segments between the ‘U’-bends.

### 4.3.5 Gap and stagger

The relative spacing of the perpendicular body segments for all glides and at different progressions through the glide are shown in figure 4.9A and summarized in table 4.1. Initially, the distributions of gap (horizontal spacing) and stagger (vertical spacing) show high spread, which decreases later in the glide. During the first quarter of the glides, the median gap is  $3.0c$  (chord) and the median stagger is  $3.7c$ . The second quarter of the glides exhibits the same median stagger of  $3.7c$ , but the median gap decreases to  $1.0c$ . During the third and fourth quarters of the glides, the median gap is effectively  $0c$ , while the median stagger is  $4.2c$ . As a measure of distribution spread, we use the interquartile range (IQR). Initially, the gap and stagger interquartile range is  $(3.8c, 2.4c)$ , which decreases to  $(2.7c, 1.8c)$  during the second quarter of the glide. The interquartile ranges decrease further to  $(2.1c, 1.7c)$  and  $(2.0c, 1.3c)$  during the second half of the glides. The gap and stagger distributions indicate gaps that are near zero and even negative. A gap of zero indicates the forward airflow contacts the anterior and posterior body simultaneously, while a negative gap indicates the rear airfoil leads the front airfoil. Staggers are generally positive, indicating that the rear airfoil is below the front airfoil relative to the airflow.

Overlaid on the joint distributions are the gap and stagger measurement locations for wake interaction effects [16]. Gap and stagger combinations are observed in the aerodynamic interaction region, although these combinations are relatively rare. Wake interaction effects are most prominent along the top row, with the rear airfoil directly behind the front airfoil. There are also wake interaction effects along the second row, but the effect is smaller. The gap and stagger measurement locations initially overlap with the observed gap and stagger distributions, but the overlap is less later in the glide, as the observed distribution moves to a gap of zero chords.

The angles of attack of the front and rear airfoils are shown in figure 4.9B. The angle of attack of the rear airfoil is correlated with the angle of attack of the front airfoil. Initially, angles of attacks are very high, upwards of  $70^\circ$  to  $90^\circ$ , with the median angle of attack being  $74^\circ$  for both the front and rear airfoils. As the glides progress, the spread of the angle of attack distribution decreases, and the median angle of attack ultimately decreases to  $56^\circ$  for the front airfoil and  $65^\circ$  for the rear airfoil. All angles of attack were high, indicating large drag coefficients and small lift coefficients (figure 4.3A). The sweep angles of the front and rear airfoils (figure 4.9C) do not follow a clear trend as do the angle of attacks. Initially, there

is a large cluster of high sweep angles, which may be due to the jump and body formation phase of the glide. Later in the glide, the higher sweep angles are not seen, but there is no clear trend relating the sweep angle of the front and rear airfoils.

Lastly, gaps and staggers from this study and estimated gaps and staggers from a previous study with only five markers on the snake [11] are shown in figure 4.9D. The gaps from the five marker trials are much greater than observed in this study. The steep glides from this study have a gap of approximately  $0c$ , while the shallow glides from Socha et al. (2010) [11] have a gap greater than  $5c$ , although the staggers are similar. The gap and stagger combinations from the five-point trials are generally in the wake interaction region, although few time points from the current study are located in the wake interaction region. The third panel of figure 4.9D indicates that although uncommon, gap and stagger configurations in the wake interaction region are observed in the present study.

Table 4.1: Summary of gap and stagger changes during different phases of gliding (figure 4.9A). The median and interquartile range (IQR) of gap (G) and stagger (S) are displayed in units of maximum chord length of the animal, denoted by “ $c$ ”.

Height fraction	Median (G,S)	Gap IQR (Q1, Q3)	Stagger IQR (Q1, Q3)
$1.00 \geq z/h_0 \geq 0.75$	(3.0 c, 3.7 c)	3.8 c (1.4 c, 5.2 c)	2.4 c (2.6 c, 5.0 c)
$0.75 \geq z/h_0 \geq 0.50$	(1.0 c, 3.7 c)	2.7 c (-0.4 c, 2.4 c)	1.8 c (2.7 c, 4.5 c)
$0.50 \geq z/h_0 \geq 0.25$	(-0.4 c, 4.2 c)	2.1 c (-1.5 c, 0.6 c)	1.7 c (3.3 c, 5.0 c)
$0.25 \geq z/h_0 \geq 0.00$	(0.0 c, 4.2 c)	2.0 c (-1.1 c, 0.9 c)	1.3 c (3.5 c, 4.8 c)

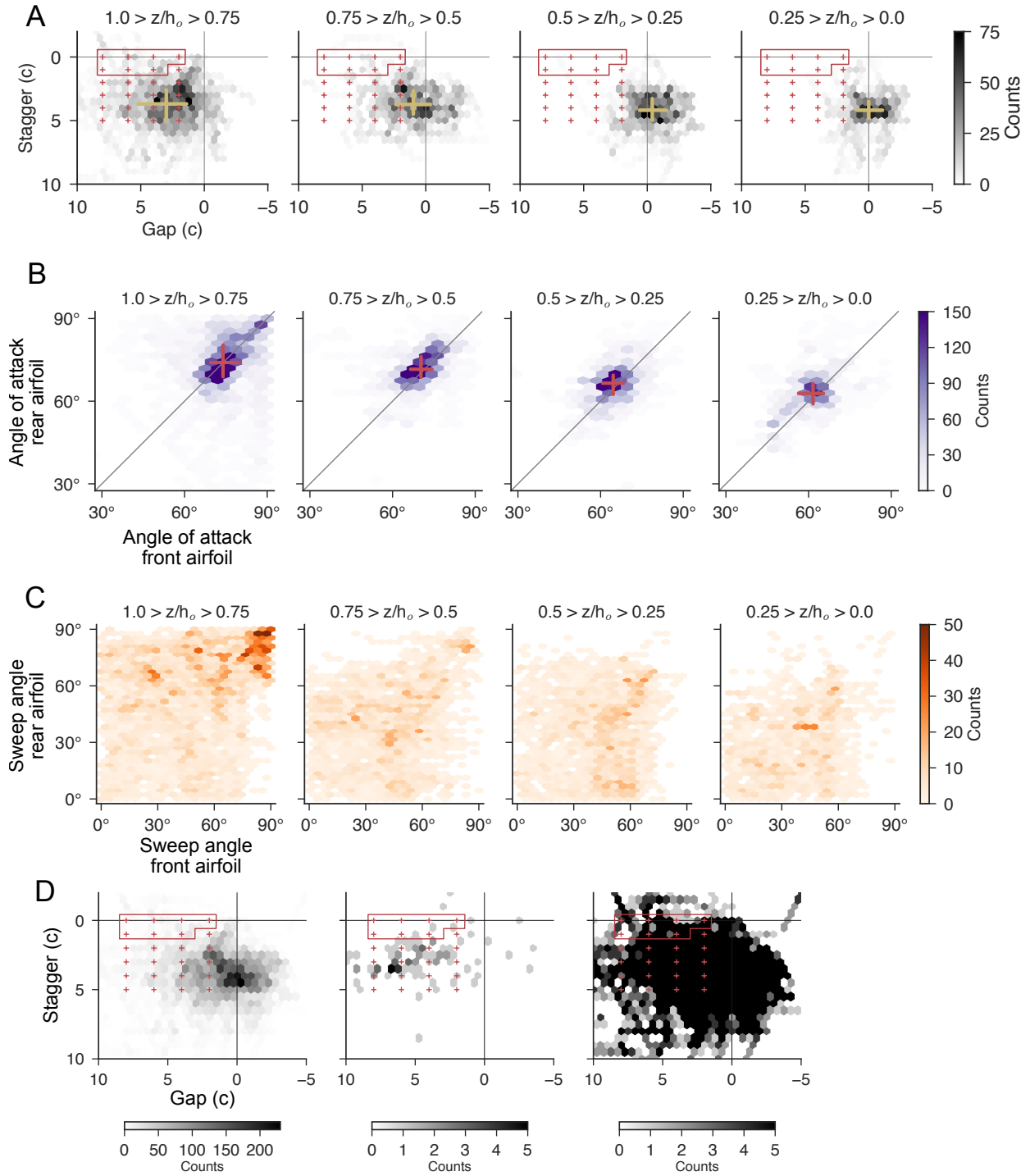


Figure 4.9: Caption on next page.

Figure 4.9: (Previous page.) Distributions of gap, stagger, angle of attack, and sweep angle of the 43 glide trials analyzed. Columns (A)–(C) show the distributions for different height fractions through the glide. (A) Distributions of stagger vs. gap, with the median, first, and third quartiles marked in yellow. The red ‘+’ symbols denote measurement locations for wake interaction effects [16]. Measurement configurations where wake interaction effects are greatest are enclosed in the red box. Initially, the gap and stagger distributions are relatively disperse, but coalesce as the glides progress. (B) Angle of attack of the rear airfoil vs. angle of attack of the front airfoil. The angles of attack are correlated and initially spread along the diagonal. The angles of attack decrease as the glides progress, which results in more lift and less drag. (C) Sweep angle of the front and rear airfoils do not follow a clear trend, indicating the airflow is not usually perpendicular to the body, even along the straight segments. (D) Comparison of gap and stagger from this study (first panel) and from Socha et al. (2010) [11] (second panel). The third panel displays the same information as the first panel, but with the same color bar range as the second panel to highlight the spread of the data. The tandem effects test locations are overlaid on each plot. Each study has measured gaps and staggers in the wake interaction region.

## 4.4 Discussion

### 4.4.1 Center of mass motion

The overhead and side views of the glide trajectory provide our first measurements of the center of mass motion of flying snake glides. The recorded glides were steeper than would be anticipated from previous studies, with the horizontal glide distance of only 4 m from a jump height of 8.3 m, whereas glides from previous experiments travelled between 9 m to 14 m horizontally from a jump height of 9.8 m. There are several possible explanations for this, including the more massive snakes used in the present study, the animal's being conditioned to a sedentary life, physical markers being placed on the body, lack of visual cues from the indoor glide arena, or because wild-caught snakes are more accustomed to gliding. Alternatively, only the best performing glides from previous studies were analyzed in detail, whereas all trials, regardless of performance, were analyzed in the present study. The larger mass directly affects the wing loading of the animal, with predictable results in the velocity polar diagram. To address visual cues, a target tree was placed in the arena, as has been done for previous studies. There was no discernible difference when handling the animals and encouraging them to jump. Additionally, the physical tape markers, as opposed to painted markers, were placed carefully on the animal's dorsal surface to minimize disturbance to their flattening. One snake was left unmarked and did not show noticeably different glide behavior or performance than the marked snakes. Although the glides were steep, the increased spatial and temporal resolution enabled us to fully quantify the position of the body in much greater detail than previous studies. This improved understanding enables us to calculate the center of mass, as well as estimate aerodynamic forces, and measure the gap and stagger of different body segments.

The overhead view of the glide path (figure 4.4B) did not show obvious center of mass deviations related to undulation. These data show the unfiltered center of mass, so the smoothing effects of digital filtering are not present. We do see broad arcing turns, although no distinct turning events were observed during the trials. This arcing motion could be due to the initial jump conditions and a result of stabilizing the rotational motion. There is one trajectory that followed a fairly straight course, trial 413 from snake 91 (figure 4.4Bii), from the launch branch to the target tree. We recorded only a handful glides that landed on the tree.

The velocity polar diagrams (figure 4.4C,D) have been discussed previously from a theoretical modeling perspective [91]. The empirical velocity polar diagrams provided here support several claims from that study. First, the wing loading rescaling enables comparisons between individuals that vary in mass. The theoretical study predicted that smaller individuals would progress further through the diagram and show better glide performance, which was seen in this study with individuals varying by a factor of three in mass. Additionally, a greater initial forward velocity was predicted to more quickly reach a steady state glide and perform better. The best performing glides were found to have greater initial forward velocities. All diagrams show a characteristic turn that signifies the transition from the ballistic to the shallowing phases of gliding. The theoretical model predicted that a trajectory curving upwards in the velocity polar diagram occurs as the trajectory transitions onto the terminal velocity manifold, which is a higher-dimensional analogue to the terminal velocity. This transition point occurs for different airspeeds depending on the animal speed. However, the rescaled diagrams show that the transition occurs for a non-dimensional speed of approximately one.

#### 4.4.2 Lift and drag forces

Quasi-steady theory was insufficient to explain the aerodynamic forces produced during short glides in flying snakes. When compared to the center of mass acceleration, the quasi-steady lift forces were too low by 35% and the quasi-steady drag forces were too high by 40%. We found that the required decrease in drag was constant throughout the glides, while the required increase in lift decreased throughout the glide.

One possibility for the lift multiplier changing with progress through the glide is that initially the angles of attack are high. As the glide progresses, the angles of attack decrease from  $70^\circ$ – $90^\circ$  at the start to  $50^\circ$ – $70^\circ$  at the end of the glide. The lift and drag curves are substantially different at high angles of attack; the lift coefficient is near zero, while the drag coefficient is at a maximum. The relative change in the lift and drag coefficients also varies as the angle of attack is decreased. From  $90^\circ$  to  $60^\circ$ , the extrapolated lift coefficient increases from 0 to 1, while the extrapolated drag coefficient only decreases from the approximately 2 to 1.6. Therefore, the modification to the lift force is more sensitive during the initial portion of the glide as the angle of attack decreases from a high value. However, the true lift and drag values in this region are unknown, as they were not measured in previous experiments.

In light of the assumptions used to calculate forces, the corrected quasi-steady values provide

the first estimates of the time-varying force distributions. A surprising result from the lift and drag distribution in figure 4.7 is that the ‘U’-bends are not as detrimental to lift production as previously thought. There is a transition region near the ‘U’-bend where the lift force is zero, but this region is small. The drag force at the ‘U’-bends is continuous and should help to offset the animal’s weight. However, the force calculations at the ‘U’-bends is highly dependent on the validity of simple sweep theory, as the ‘U’-bends are the most swept portions of the body. Additionally, the force (figure 4.7) and sweep angle distributions (figure 4.8E,F) show the straight segments are not perpendicular to the airflow, reducing their ability to produce lift and drag. An unexpected result from the angle of attack distributions (figure 4.8B,D) is that the angles of attack are high, even along the straight segments. The high angles of attack are likely due to the steepness of the glides. High angle of attack aerodynamics therefore dominate for flying snakes, as the the angles of attack begin high and then decrease slightly as the glide shallows.

### 4.4.3 Gap, stagger, and airflow orientation

The distributions of gap and stagger, and how they change depending on progress through the glide (figure 4.9A), was surprising because of the zero or even negative gap values at the end of the glide. We attribute the low and negative gap values to the steep glide paths compared to other studies. The gap and stagger results indicate that flying snakes use a wide range of body configurations relative to the airflow. All of the configurations may not be advantageous from an aerodynamics and glide performance perspective, but may serve ecologically relevant functions. For example, snakes executing short glides, or falling near vertically, may do so to escape predators. Falling straight downwards still requires controlling aerodynamic and inertial forces to ensure stability, but will not result in meaningful horizontal travel. Steep glides may allow the snakes to fall away from the predator while staying on the same tree, or in the nearby area.

Flying snakes therefore have a large performance envelope within which to operate. Some glides can be viewed as predominantly falling, in which the animal moves vertically downward or only covers a few meters horizontally, whereas other glides cover significant horizontal distance, possibly to escape to a different tree. It is known that other gliding animals, such as flying squirrels and *Draco* lizards, have higher shallowing rates and shallower glides than flying snakes [22], but they may not be able to execute very steep glides. The morphing wing-

body of flying snakes may be uniquely suited to stabilize short glides, as it possibly allows the animal to correct for rotational torques. Additionally, the multi-wing configuration may enable wake interactions that increase glide performance (figure 4.9D), although this may not be volitional and simply an artifact of the shallowing glide.

#### 4.4.4 Future work

Future studies are needed to address the assumptions used in this work. The biggest kinematic assumption is the airfoil coordinate system that is overlaid on the spline fit of the body. This assumption was used because the orientation of the body was not directly available from the marker time series. The airfoil coordinate system directly affects the force estimates, as well as angle of attack and sweep angle estimates. Future experiments, with greater camera coverage, may be able to measure the flattened body orientation. This would provide information on the orientation of the body and define the airfoil coordinate system at discrete points along the body. Splines that preserve the measured orientation information, along with torsion constraints, can then be fit to the body [92].

The next assumptions to be addressed are quasi-steady theory and simple sweep theory. Both assumptions were applied so that previously measured lift and drag coefficients could be used. An alternative to using quasi-steady force coefficients and simple sweep theory would be to perform computational fluid dynamics simulations, with a moving mesh derived from the kinematics analysis. This analysis would account for unsteady fluid phenomena, and provide details about wake interaction, vortex shedding, and flow at the ‘U’-bends of the snake. This analysis should also provide insights into span-wise flow along the straight body segments. Alternatively, physical models can be constructed using our increased understanding of the morphing wing-body. The physical models can be 3D printed and placed in a water tunnel, similar to Holden et al. (2014). Flow and force measurements can then be taken of the whole snake, or of straight segments at different attack and sweep angle combinations (figure 4.8C,D). However, this technique would not capture the unsteady behavior as the snake accelerates, or changes in the flow structure due to undulation.

## 4.5 Conclusions

Using a new kinematics analysis of the center of mass trajectory and body orientation, we tested if quasi-steady theory can predict the time-varying lift and drag forces on flying snakes. Quasi-steady theory was insufficient to explain the forces acting on the body; the drag force was over estimated by approximately 40% and the lift force under estimated by approximately 35%. Using the corrected lift and drag forces, quasi-steady theory predicts that the swept wing-body of flying snakes produces appreciable aerodynamic force over the entire length, including the ‘U’-bends. Our results indicate that unsteady and 3D aerodynamic effects are likely important for snake flight, even during short glides. During some glides, we did find body configurations where the anterior body was located where wake interaction effects are possible, but this is unlikely to explain the failure of quasi-steady theory. However, wake interaction effects may be more prominent during late phase gliding. The time-varying body posture and orientation can be used in future computational dynamics and physical modeling studies to elucidate unsteady and 3D aerodynamic phenomena during snake flight.

## References

- [7] J. J. Socha. Gliding flight in the paradise tree snake. *Nature* 418 (2002), p. 603–604. DOI: 10.1038/418603a.
- [8] J. J. Socha, T. O’Dempsey, and M. LaBarbera. A 3-D kinematic analysis of gliding in a flying snake, *Chrysopelea paradisi*. *J. Exp. Biol.* 208 (2005), p. 1817–1833. DOI: 10.1242/jeb.01579.
- [9] J. J. Socha and M. LaBarbera. Effects of size and behavior on aerial performance of two species of flying snakes (*Chrysopelea*). *J. Exp. Biol.* 208 (2005), p. 1835–1847. DOI: 10.1242/jeb.01580.
- [11] J. J. Socha, K. Miklasz, F. Jafari, and P. P. Vlachos. Non-equilibrium trajectory dynamics and the kinematics of gliding in a flying snake. *Bioinspir. Biomim.* 5.045002 (2010). DOI: 10.1088/1748-3182/6/1/019501.
- [12] K. Miklasz, M. LaBarbera, X. Chen, and J. J. Socha. Effects of body cross-sectional shape on flying snake aerodynamics. *Exp. Mech.* 50 (2010), p. 1335–1348. DOI: 10.1007/s11340-010-9351-5.

- [13] J. J. Socha. Gliding flight in *Chrysopelea*: turning a snake into a wing. *Integ. Comp. Biol.* 51 (2011), p. 969–982. DOI: 10.1093/icb/icr092.
- [14] D. Holden, J. J. Socha, N. D. Cardwell, and P. P. Vlachos. Aerodynamics of the flying snake *Chrysopelea paradisi*: how a bluff body cross-sectional shape contributes to gliding performance. *J. Exp. Biol.* 217 (2014), p. 382–394. DOI: 10.1242/jeb.090902.
- [15] A. Krishnan, J. J. Socha, P. P. Vlachos, and L. A. Barba. Lift and wakes of flying snakes. *Phys. Fluids* 26.031901 (2014). DOI: 10.1063/1.4866444.
- [16] F. Jafari. Physical mechanisms of control of gliding in flying snakes. PhD thesis. Virginia Tech, 2016.
- [22] J. J. Socha, F. Jafari, Y. Munk, and G. Byrnes. How animals glide: from trajectory to morphology. *Can. J. Zool.* 93 (2015), p. 901–924. DOI: 10.1139/cjz-2014-0013.
- [26] J. W. Bahlman, S. M. Swartz, D. K. Riskin, and K. S. Breuer. Glide performance and aerodynamics of non-equilibrium glides in northern flying squirrels (*Glaucomys sabrinus*). *J. R. Soc. Interface* 10.20120794 (2013). DOI: 10.1098/rsif.2012.0794.
- [27] G. Byrnes, N. T.-L. Lim, and A. J. Spence. Take-off and landing kinetics of a free-ranging gliding mammal, the Malayan colugo (*Galeopterus variegatus*). *Proc. R. Soc. B* 275 (2008), p. 1007–1013. DOI: 10.1098/rspb.2007.1684.
- [28] J. A. McGuire. Allometric prediction of locomotor performance: an example from southeast Asian flying lizards. *Am. Nat.* 161 (2003), p. 337–349. DOI: 10.1086/346085.
- [29] J. A. McGuire and R. Dudley. The cost of living large: comparative gliding performance in flying lizards (Agamidae: *Draco*). *Am. Nat.* 166 (2005), p. 93–106. DOI: 10.1086/430725.
- [30] M. G. McCay. Aerodynamic stability and maneuverability of the gliding frog *Polypedates dennysi*. *J. Exp. Biol.* 204 (2001), p. 2817–2826.
- [43] H. Park and H. Choi. Aerodynamic characteristics of flying fish in gliding flight. *J. Exp. Biol.* 213 (2010), p. 3269–3279. DOI: 10.1007/978-1-4020-9898-7\_3.
- [55] R. O’Dor, J. Stewart, W. Gilly, J. Payne, T. C. Borges, and T. Thys. Squid rocket science: how squid launch into air. *Deep Sea Res. Part II Top. Stud. Ocean.* 95 (2013), p. 113–118. DOI: 10.1016/j.dsr2.2012.07.002.

- [78] C. P. Ellington. The aerodynamics of hovering insect flight. I. The quasi-steady analysis. *Phil Trans R Soc L. B* 305.1122 (1984).
- [79] R. Dudley and P. DeVries. Tropical rain forest structure and the geographical distribution of gliding vertebrates. *Biotropica* 22 (1990), p. 432–434. DOI: 10.2307/2388564.
- [81] A. Hedenström, L. C. Johansson, M. Wolf, R. Von Busse, Y. Winter, and G. R. Spedding. Bat flight generates complex aerodynamic tracks. *Science* 316 (2007), p. 894–897. DOI: 10.1126/science.1142281.
- [82] D. R. Warrick, B. W. Tobalske, and D. R. Powers. Aerodynamics of the hovering hummingbird. *Nature* 435 (2005), p. 1094–1097. DOI: 10.1038/nature03647.
- [83] J. J. Videler, E. J. Stamhuis, and G. D. E. Povel. Leading-edge vortex lifts swifts. *Science* 306 (2004), p. 1960–1962. DOI: 10.1126/science.1104682.
- [84] C. P. Ellington, C. van den Berg, A. P. Willmott, and A. L. R. Thomas. Leading-edge vortices in insect flight. *Nature* 384 (1996), p. 626–630. DOI: 10.1038/384626a0.
- [85] F. T. Muijres, L. C. Johansson, R. Barfield, M. Wolf, G. R. Spedding, and A. Hedenstrom. Leading-edge vortex improves lift in slow-flying bats. *Science* 319 (2008), p. 1250–1253. DOI: 10.1126/science.1153019.
- [86] T. Maxworthy. The fluid dynamics of insect flight. *Ann Rev Fluid Mech* 13 (1981), p. 329–350.
- [87] M. H. Dickinson, F.-O. Lehmann, and S. P. Sane. Wing rotation and the aerodynamics basis of insect flight. *Science* 284 (1999), p. 1954–1960. DOI: 10.1126/science.284.5422.1954.
- [88] D. D. Chin and D. Lentink. Flapping wing aerodynamics: from insects to vertebrates. *J Exp Biol* 219 (2016), p. 920–932. DOI: 10.1242/jeb.042317.
- [89] D. A. Winter. *Biomechanics and Motor Control of Human Movement*. John Wiley & Sons, 2009.
- [90] S. F. Hoerner. *Fluid-dynamic drag: practical information on aerodynamic drag and hydrodynamic resistance*. Hoerner Fluid Dynamic, 1965.
- [91] I. J. Yeaton, J. J. Socha, and S. D. Ross. Global dynamics of non-equilibrium gliding in animals. *Bioinspir Biomim* 12 (2017), p. 026013. DOI: 10.1088/1748-3190/aa60e2.

- [92] M. Huard, R. T. Farouki, N. Sprynski, and L. Biard.  $C^2$  interpolation of spatial data subject to arc-length constraints using Pythagorean-hodograph quintic splines. *Graphical Models* 76 (2014), p. 30–42. DOI: 10.1016/j.gmod.2013.10.005.

# Chapter 5

## Conclusions

This dissertation was motivated by the question, how and why do ‘flying snakes’ undulate through the air? Using a combined approach of reduced-order modeling, animal glide experiments, and detailed dynamic modeling, I found strong evidence to support the hypothesis that flying snakes undulate to increase their rotational stability, enabling gliding. Although it is intuitive that an animal without bilaterally symmetric wings would undulate to “average out” the forces acting on its body, this appears to be a unique function of undulation in animals, and had only been previously hypothesized, but never tested, as the primary role of undulation in flying snakes [8, 9]. Instead of producing propulsive thrust, flying snakes appear to use undulation to dynamically stabilize their motion.

In Chapter 2, I proposed a non-equilibrium framework of gliding based on the question, what is the effect of angle-of-attack dependent lift and drag coefficients on glide dynamics? The physics governing the motion of any gliding animal is straightforward: the animal accelerates downward under gravitational acceleration, while producing lift and drag forces as it pushes against the air. The size of the animal determines its speed, while the morphological variations determine the forces produced. It is therefore natural that the complexity associated with size and shape differences can be dealt with in a general way.

The non-equilibrium framework is based on the velocity polar diagram of horizontal vs. vertical velocity, using non-dimensional and rescaled velocities. This rescaling enables us to compare glide performance across individuals and species. The structure of the velocity polar diagram, such as the location and type of equilibrium points for varying pitch angle, the terminal velocity manifold, and the appearance of separatrices, depend on the lift and

drag curves. Previous modeling studies generally ignored the angle of attack dependence, or analyzed the performance based on the static case, in which the lift-to-drag ratio defines the glide angle. The addition of angle-of-attack dependent lift and drag coefficients and the use of the velocity polar diagram indicates that simple gliders can show complex behavior, and that the pitch angle can be varied to elicit different gliding behavior.

In Chapters 3 and 4, I focused specifically on flying snake locomotion. Using a high-speed motion capture system and an increased marker resolution along the body, I was able to reconstruct the morphing wing-body of flying snakes, as documented in Chapter 3. The experimental data revealed that the body has more complex vertical motion than previously realized. The three-dimensional motion of the body can be readily understood as two coupled waves of horizontal and vertical bending and a gross out-of-plane motion. The newly discovered vertical wave has twice the spatial and temporal frequency as the horizontal wave, and is phase shifted by  $90^\circ$ . The amplitude of the horizontal wave is inversely related with number of spatial periods of horizontal bending; fewer periods of bending correspond to tight bends on the animal's body. Lastly, there is a gross out-of-plane motion of the snake, termed dorsoventral bending, with either the posterior body above or below the head.

To uncover the functional role of aerial undulation, I developed a detailed dynamical model of snake flight that incorporates the above components of aerial undulation. By systematically varying the aerial undulation parameters, the model shows that undulation generally increases the rotational stability of flying snake locomotion. This increase in rotational stability allows the simulated snake to fall farther and cover more distance over the ground. We found that there is an inherent pitch instability due to aerodynamic moments that undulation cannot mitigate, but that dorsoventral bending can mitigate. Changing the dorsoventral bending angle can change the sign of the aerodynamic pitch moment, whereas changing the horizontal shape cannot. Lastly, the model shows that large inertial moments about the yaw axis exist due to the large-amplitude horizontal wave. This could be used as a turning mechanism in flying snakes, as they can bias the horizontal wave to reorient about the yaw axis.

In Chapter 4, I provided a kinematic analysis of the center of mass motion and provided the first estimates of the lift and drag distributions over the body. This chapter was motivated by the question, can quasi-steady theory predict the lift and drag forces on the snake's body? We found that quasi-steady theory was unable to predict the required aerodynamic force, under-predicting lift by 30% and over-predicting drag by 40%. Additionally, we determined

that the gap and stagger values of the body likely cannot explain this discrepancy. Overall, this evidence suggests that unsteady aerodynamic effects are likely important and must be investigated.

## 5.1 Future work

This dissertation suggests several lines of future inquiry to understand gliding animals and flying snakes in greater detail.

### 5.1.1 Non-equilibrium framework of gliding

The non-equilibrium framework of gliding can be extended by incorporating a pitch model into the equations of motion and considering the extended phase space of  $(v_x, v_z, \theta)$ . The rotational model can be passive, with the pitch moment determined from a previously measured pitching moment coefficient, or active with the use of control. An optimal control formulation is one possible technique, in which the time-varying pitch angle is selected to achieve a control objective. Possible control objectives include minimizing glide time between two objects, minimizing the height lost between two objects, or maximizing the glide distance from a given jump height. The structure of the (extended) velocity polar diagram, due to the lift and drag curves, will affect the optimal pitch angle. Additionally, the time histories of pitch could be compared with experimentally measured pitch angles to possibly elucidate the control objective for the animal.

### 5.1.2 Dynamic model of snake flight

The dynamical model of snake flight can be extended in several ways to test control of limbless snake flight. The model contains five parameters that can be controlled to meet different objectives: horizontal wave amplitude  $\theta_m$ , number of spatial periods of the horizontal wave  $\nu_\theta$ , undulation frequency  $f_\theta$ , vertical wave amplitude  $\psi_m$ , and dorsoventral bending angle  $d_\psi$ . Possible control objectives and questions that can be asked include: Can the rotational motion be stabilized? What is the most effect parameter to vary to stabilize the rotational motion? How robust is stabilization to differing initial conditions?

In addition to stabilizing the rotational motion, a control objective of steering the simulated snake to land at a particular location, or turning, can also be investigated. From the overhead view of the center of mass trajectory, we observed broad arching turns. One question that can be investigated is if the center of mass can be made to follow a straight line, or are the broad arching turns due to the initial jump orientation? Additionally, the time scales associated with controlling the rotational motion and trajectory can be investigated. As the animal begins to rotate, how quickly must the snake respond to correct the rotation, or alter its trajectory?

The model can be amended to more accurately model flying snake kinematics. For example, the vertical wave shape could be modified to more closely match the observed kinematics, with a sharp peak at the ‘U’-bends, and a broad trough along the straight segments (figure 5.1). This can be accomplished by changing the vertical wave from

$$\bar{\psi}(s, t) = \psi_m \cos \left( \frac{2\pi\nu_\psi}{L} s - 2\pi f_\psi t + \phi_\psi \right) + \frac{d_\psi}{L} s \quad (5.1.1)$$

to a form of

$$\bar{\psi}(s, t) = \psi_m \sin \left( -\beta \cos(s + \phi_\psi) + \phi_\psi \right) + \frac{d_\psi}{L} s \quad (5.1.2)$$

where  $\beta < 1$  controls the flatness of the valleys and the appropriate arguments to the periodic functions must be determined.

Another possibility is to add a tail to simulate its aerodynamic and inertial effects on stability. The tail can be modeled as a passive, but forced beaded string, where one end is forced due to the prescribed body kinematics of the vent, and all all beads experience forces between neighbors, and the lift and drag forces as the body accelerates.

An alternative approach to model flying snake kinematics is to prescribe traveling waves of muscle contraction instead of traveling waves of bending. The serpenoid curve model of snake kinematics is based on the assumption that sinusoidal waves of muscle activation lead to sinusoidal curvature and the observed body shape of snakes. However, this does not account for the flat regions of the horizontal wave. These flat regions may result from inertial effects of undulation without ground reaction forces. This could be tested by modeling the snake as a kinematic chain with periodic torques acting at the joints, undulating in the air.

Lastly, the aerodynamic model can be improved as better data becomes available. This includes the lift and drag coefficients at greater angles of attack, at different sweep angles,

as well as different body cross-sectional shapes. The posterior section of the snake's body appears to have less pronounced ventral lips, resulting in the ventral surface being less concave. The cross-sectional shape of the snake can therefore be considered as a variable that changes with distance along the body, similar to the width and mass distributions. The force coefficients of the representative cross-sectional shapes at different positions along the body could be easily incorporated into the existing model. However, many more fluid dynamics experiments must be conducted to fully map this parameter space.

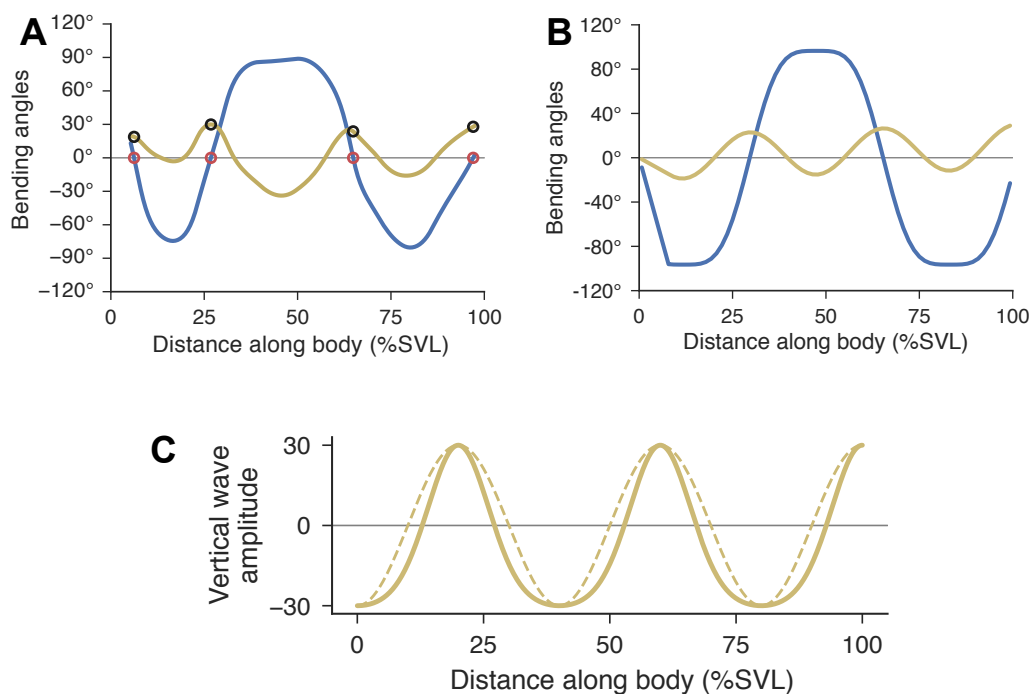


Figure 5.1: Modifying the vertical wave to more closely resemble the observed kinematics. (A) Horizontal (blue) and vertical wave (yellow) from one trial at one time point. Notice the peaked vertical wave with broad troughs. (B) Modeled horizontal and vertical waves. The horizontal wave is a flat-topped sinusoid, while the vertical wave is a standard sinusoid. (C) Proposed modification of the vertical wave (solid line) compared to the current sinusoidal model (dashed line). The proposed model has sharper peaks and broad troughs. The flatness of the valleys can be tuned with one parameter ( $\beta$  in equation 5.1.2). The dashed line is for  $\beta = 0$  (standard sine curve) and the solid line is for  $\beta = 0.5$ .

### 5.1.3 Flying snake kinematic experiments

The kinematic experiments in the Cube provided an unprecedented level of detail of the snake's body in the air. However, the performance was less than we expected from previous measurements. Trials from the Cube only covered roughly 4 m horizontally, while we expected upwards of 8 to 10 m for maximal performances. It was therefore difficult to answer questions of control and performance from the Cube data because only a few undulation periods were recorded and the performance spread was quite small.

By increasing the glide height and time aloft, and by using smaller snakes, there will be more data available to answer questions such as: Which aspects of aerial undulation are associated with better glide performance, for example, number of horizontal spatial wave periods or vertical wave amplitude? Does location in the horizontal wave shape space change with time? How does the dorsoventral bending angle change with time? Is this change associated with the body orientation? How do the bending waves change during turns?

To address these questions, I suggest further glide experiments outside, with the use of an articulating aerial lift. A trial run of this experiment was conducted in September 2017 at the German Club at Virginia Tech. From these experiments, we recorded similar glide performance from 8.3 m as in the Cube two years prior (Appendix C.8). We also released the snakes from a height of 20 m and recorded much better glide performance. To answer the questions above will require marking the snake's with a similar density of landmark points along the body. The time-consuming component will be the 3D reconstruction of the landmark points. However, a similar analysis pipeline as developed for the Cube data can be used.

### 5.1.4 Additional flying snake measurements

There are other aspects of flying snake locomotion that can be investigated: landing and perturbations. We currently have many high speed videos of flying snakes landing on a horizontal bar from short jumps. The kinematics of snake landing depended on the location(s) along the body where the bar contact occurs. Head, mid-body, tail, and double contacts between the bar and the body were all observed, as well as failures where the animals slid off of the landing bar. Future kinematic experiments, coupled with modeling, can help answer how flying snakes are able to land on a variety of surfaces. Additionally, we observed the

snakes using their neck to grip around small branches and leaves when landing on a tree placed behind the horizontal bar. The “head hook” behavior can also be induced by placing the animal’s head on a branch and then gently pulling the animal backwards. The forces produced during head hooks, as well as the forces for different sized branches, can be tested explicitly using force sensors attached to both rigid and compliant branches.

Flying snakes also show deviations from their standard aerial kinematics that can be explored further. These include botched jumps and body collisions. We observed botched jumps in the Cube trials from *C. ornata*. Many of these animals were heavy, and the jump from the launch branch was ineffective at giving a significant horizontal velocity. Generally, these animals would fall head down, appearing to flip over in the air. However, inspection of the high-speed footage indicated that the head orientation was always maintained. Control over head orientation was also observed in the landing trials. Inertial control of the body to maintain head orientation could likely be used to understand how these animals cope with perturbations.

In addition to botched jumps, we also observed several body collisions, in which the tail or posterior body would contact the body and distort the aerial undulation waveform. In some cases, the tail wrapped completely around the body. However, even with the body perturbed, the animals did not tumble in the air. The motion capture data of these trials were difficult to recover because the different landmark points along the body could not be discerned, but the overhead video footage clearly indicates a robustness to perturbations. Experimentally investigating how flying snakes respond to perturbations is likely to be a fruitful approach, but will be hampered by recording a significant number of trials, as well as forcing different types of perturbations.

Lastly, the discovery and analysis of the horizontal and vertical bending waves, as well as dorsoventral bending, suggest that the physical properties of the body are highly relevant. This includes the skeletal structure (ribs, vertebra, etc.), muscle and ligament connections, as well as neuromuscular activation patterns. Associated with the skeletal structure are how the body is able to flatten, as well as support the out-of-plane twisting motion. Future studies involving snake dissections and laser scanning of the individual vertebra should provide insights as to if the skeletal system of flying snakes differs from non-flying snakes. Computed tomography scans may be another avenue to measure the skeleton and connective tissue. For flattening, flying snake rib motion has been suggested to act as a four-bar mechanism, but this has not yet been tested [13]. X-ray imaging, such as XROMM (X-ray reconstruction of

moving morphology), could provide insights into the dynamics of rib motion [93].

The neuromuscular system is likely more difficult to probe, especially during glides. In snakes, the muscle activation patterns underlying undulation can vary depending on the physical medium [74, 75]. The ‘S’-shaped body could therefore arise due to cues of being airborne (physical medium change), inertial effects from undulation, as well as the structure of the musculoskeletal system. The kinematic data indicated only certain horizontal wave configurations were used; uncovering how these shapes are formed will likely require measurements of muscle activation patterns in flying snakes during glides, or in wing tunnel measurements in equilibrium-type configurations. A possible future study could investigate muscle activation patterns in the same individual in different environments: flat surface, rough terrain, climbing incline surfaces, sand, swimming, and aerial undulation. These could be investigated one-after-another in a lab setting and could help elucidate the unique control adaptations that enable snake flight.

## References

- [8] J. J. Socha, T. O’Dempsey, and M. LaBarbera. A 3-D kinematic analysis of gliding in a flying snake, *Chrysopelea paradisi*. *J. Exp. Biol.* 208 (2005), p. 1817–1833. DOI: 10.1242/jeb.01579.
- [9] J. J. Socha and M. LaBarbera. Effects of size and behavior on aerial performance of two species of flying snakes (*Chrysopelea*). *J. Exp. Biol.* 208 (2005), p. 1835–1847. DOI: 10.1242/jeb.01580.
- [13] J. J. Socha. Gliding flight in *Chrysopelea*: turning a snake into a wing. *Integ. Comp. Biol.* 51 (2011), p. 969–982. DOI: 10.1093/icb/icr092.
- [74] B. C. Jayne. Muscular mechanisms of snake locomotion: An electromyographic study of lateral undulation of the Florida banded water snake (*Nerodia fasciata*) and the yellow rat snake (*Elaphe obsoleta*). *J. Morphol.* 197 (1988), p. 159–181. DOI: 10.1002/jmor.1051970204.
- [75] G. B. Gillis. Neuromuscular control of anguilliform locomotion: patterns of red and white muscle activity during swimming in the American eel *Anguilla rostrata*. *J. Exp. Biol.* 201 (1998), p. 3245–3256.

- [93] E. L. Brainerd, S. Moritz, and D. A. Ritter. XROMM analysis of rib kinematics during lung ventilation in the green iguana, *Iguana iguana*. *J. Exp. Biol.* 219 (2016), p. 404–411. DOI: 10.1242/jeb.127928.

# Appendix A

## *Supplemental Information* – Global dynamics of non-equilibrium gliding in animals

### Code repository

Python code to reproduce figures in the manuscript, including velocity polar diagrams and pitch bifurcation diagrams, can be found at <https://github.com/TheSochaLab/Global-dynamics-of-non-equilibrium-gliding-in-animals>.

### A.1 Linear stability analysis

The Jacobian of the polar coordinate equations (2.7) and (2.8) in the main text, evaluated at equilibrium is

$$A_{(\gamma^*, \hat{v}^*)} = \begin{bmatrix} \frac{\partial \gamma'}{\partial \gamma} & \frac{\partial \gamma'}{\partial \hat{v}} \\ \frac{\partial \hat{v}'}{\partial \gamma} & \frac{\partial \hat{v}'}{\partial \hat{v}} \end{bmatrix}_{(\gamma^*, \hat{v}^*)} \quad (\text{A.1.1})$$

After simplification, the partial derivatives are

$$\begin{aligned}\frac{\partial \gamma'}{\partial \gamma} &= -\frac{(C'_L + C_D)}{(C_L^2 + C_D^2)^{1/4}} & \frac{\partial \gamma'}{\partial \hat{v}} &= -2C_L \\ \frac{\partial \hat{v}'}{\partial \gamma} &= \frac{C_L - C'_D}{(C_L^2 + C_D^2)^{1/2}} & \frac{\partial \hat{v}'}{\partial \hat{v}} &= \frac{-2C_D}{(C_L^2 + C_D^2)^{1/4}}\end{aligned}$$

where the lift and drag coefficient values, as well as their slopes  $C'_L$  and  $C'_D$ , are evaluated at the equilibrium angle of attack in radians.

Common types of equilibrium points can be calculated analytically. Saddle point equilibria occur when

$$(C_L/C_D)' < -[1 + (C_L/C_D)^2]$$

and stable equilibria occur when

$$C'_L > -3C_D.$$

Lastly, the equilibrium glide velocities at any equilibrium are

$$\hat{v}^* = (C_L^2 + C_D^2)^{-1/4} \quad \hat{v}_x^* = \hat{v}^* \cos \gamma^* \quad \hat{v}_z^* = -\hat{v}^* \sin \gamma^*. \quad (\text{A.1.2})$$

## A.2 Conversion between dimensional, non-dimensional, and rescaled quantities

Below we list the conversion from dimensional quantities, non-dimensional quantities (with the overbar), and rescaled quantities (with an overhat).

$$t = \sqrt{\frac{c}{g\epsilon}} \hat{t} \quad x = \frac{c}{\epsilon} \hat{x} \quad v = \sqrt{\frac{cg}{\epsilon}} \hat{v} \quad a = g\hat{a} \quad (\text{A.2.1})$$

$$t = \sqrt{\frac{\bar{c}}{g}} \bar{t} \quad x = c\bar{x} \quad v = \sqrt{cg}\bar{v} \quad a = g\bar{a} \quad (\text{A.2.2})$$

$$\bar{t} = \frac{\hat{t}}{\sqrt{\epsilon}} \quad \bar{x} = \frac{\hat{x}}{\epsilon} \quad \bar{v} = \frac{\hat{v}}{\sqrt{\epsilon}} \quad \bar{a} = \hat{a} \quad (\text{A.2.3})$$

The universal glide scaling parameter,

$$\epsilon = \frac{\rho c S}{2 m} = \frac{\rho g}{2} \frac{c}{W_S} \quad (\text{A.2.4})$$

when substituted back into the rescaled terms, results in the wing loading expression in the main text (equation 4.1):

$$t = \sqrt{\frac{2W_S}{\rho g^2}} \hat{t} \quad x = \frac{2W_S}{\rho g} \hat{x} \quad v = \sqrt{\frac{2W_S}{\rho}} \hat{v} \quad a = g \hat{a} \quad (\text{A.2.5})$$

The time, length, and velocity, and acceleration scales are thus

$$T = \sqrt{\frac{2W_S}{\rho g^2}} \quad L = \frac{2W_S}{\rho g} \quad \frac{L}{T} = \sqrt{\frac{2W_S}{\rho}} \quad \frac{L}{T^2} = g \quad (\text{A.2.6})$$

### A.3 Velocity polar diagram when $C_L$ and $C_D$ are constant

When the lift and drag coefficients are constants, only stable equilibria are possible. Additionally, they are of spiral type when the lift-to-drag ratio is less than 0.354. Below is a velocity polar diagram constructed using lift and drag coefficients values reported in Socha *et. al* (2010), table 1, for one configuration used in their simulations. We use ‘Case 6: Average’ with  $C_L = .54$ ,  $C_D = .29$ , and  $C_L/C_D = 1.88$ . They also proposed a definition of equilibrium based on when the glide angle reaches 5% of its asymptotic value; this range is also indicated on the velocity polar diagram.

As is clear, there is strong spiraling behavior around a stable focus equilibrium point. As indicated in figure 3 in the main text, this equilibrium point is far from the boundary between a node and a focus. Additionally, the velocity polar diagram indicates that all initial conditions will lead to a stable glide and that the low acceleration magnitude region is confined around the equilibrium point.

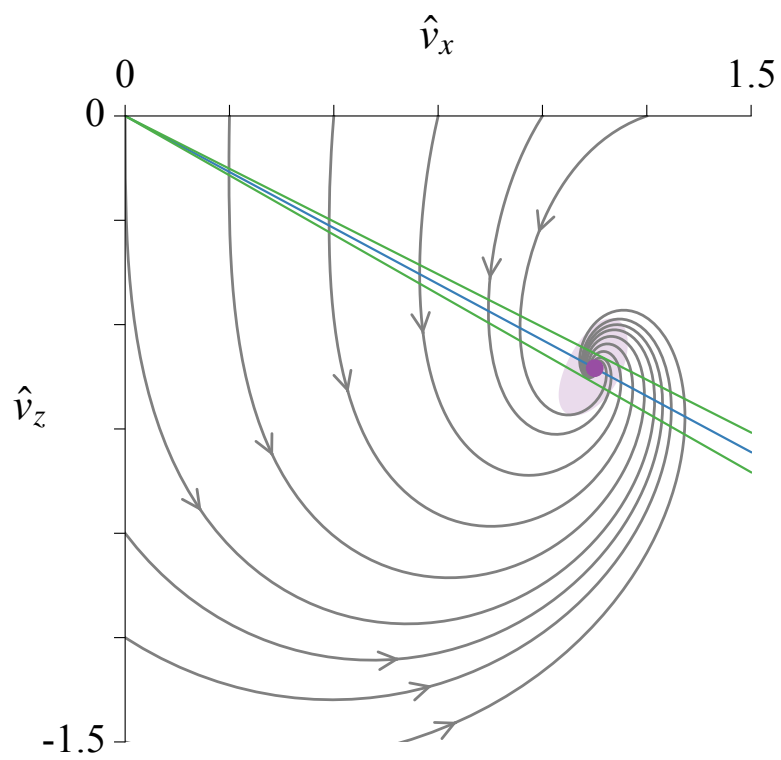


Figure A.1: Velocity polar diagram for constant lift and drag coefficients. The equilibrium condition proposed by Socha *et. al* (2010).

## A.4 Kinematic lift and drag coefficient curves

Here we derive the lift and drag force from the horizontal and vertical forces. The lift and drag force are then used to calculate the lift and drag coefficients. We beginning with the horizontal and vertical forces:

$$\begin{aligned} F_x &= ma_x = F_L \sin \gamma - F_D \cos \gamma \\ F_z &= ma_z = F_L \cos \gamma + F_D \sin \gamma - mg \end{aligned}$$

To calculate the lift force, we multiply the  $x$ -equation by  $\sin \gamma$  and the  $z$ -equation by  $\cos \gamma$  and sum. This gives

$$\begin{aligned} F_x \sin \gamma + F_z \cos \gamma &= F_L(\sin^2 \gamma + \cos^2 \gamma) + \\ &F_D(\cos \gamma \sin \gamma - \cos \gamma \sin \gamma) - mg \cos \gamma, \end{aligned}$$

which simplifies to

$$F_L = F_x \sin \gamma + F_z \cos \gamma + mg \cos \gamma.$$

To obtain the drag force, we multiply the  $x$ -equation by  $-\cos \gamma$  and the  $z$ -equation by  $\sin \gamma$  and sum. This gives

$$\begin{aligned} -F_x \cos \gamma + F_z \sin \gamma &= F_L(\cos \gamma \sin \gamma - \cos \gamma \sin \gamma) + \\ &F_D(\sin^2 \gamma + \cos^2 \gamma) - mg \sin \gamma, \end{aligned}$$

which simplifies to,

$$F_D = -F_x \cos \gamma + F_z \sin \gamma + mg \sin \gamma.$$

The lift and drag coefficients become

$$\begin{aligned} C_L(\gamma + \theta_b) &= \frac{ma_x \sin \gamma + ma_z \cos \gamma + mg \cos \gamma}{\frac{1}{2}\rho v^2 S} \\ C_D(\gamma + \theta_b) &= \frac{-ma_x \cos \gamma + ma_z \sin \gamma + mg \sin \gamma}{\frac{1}{2}\rho v^2 S} \end{aligned}$$

The lift and drag coefficients have been written with explicit dependence on both glide angle and body pitch angle  $\theta_b$ . The glide angle is calculated at each measurement location as  $\gamma = -\tan^{-1} v_z/v_x$ , but the body pitch angle is not accessible from the kinematics data and

must be estimated throughout the entire glide. The body pitch angle was specified to be  $0^\circ$  such that the animal is horizontal to the ground. Short glides presented in [36] of *Glaucomys volans* showed a pitch angle tending towards  $0^\circ$ .

Individual squirrel glide trials presented in the data supplement of [26] were reanalyzed for this study. The data set consists of 59 glides of wild northern flying squirrel (*Glaucomys sabrinus*). A majority of trials, 23 of 59, landed on a tree 18 m from the launch site. We analyze these glides because they were analyzed in detail by in ref. [26] and because longer glides give more opportunity to reach equilibrium. Individual squirrels were not marked, so analyses were performed using an average size squirrel based on previous studies. Therefore, we are calculating ‘equivalent’ lift and drag curves.

Of the 18 m glides, we further restrict the data set to 14 trajectories based on the start and end positions. We require the initial recorded position to be within 3.8 m horizontally and 2 m vertically from the jump point. We also require the trajectories to end with a horizontal distance between 16 m to 18.5 m. These values were selected to ensure the longest possible glides and to capture as much of the transient portion as possible. Note that most of the ballistic phase of the trajectory was not recorded in the original data set.

Velocities and accelerations are calculated using a moving window procedure similar to [26]. Velocities are calculated by iterating through the individual position components and fitting a linear polynomial to the window. The derivative of the window polynomial is evaluated at the current time to calculate velocity. Acceleration was calculated in a similar way, using the velocity time series as input. A half-window is used at the start and end of each time series. The half-window grows until it reaches the set window size. The variable window size increased derivative scatter if a higher-order polynomial was used. This was especially noticeable at the end of the trajectory where reported digitization errors are largest. For all trials, a total window of 81 points, or 0.64 sec, was used. This window uses 40 points before and after the current time step. A large interrogation window was used to obtain the bulk glide performance and smooth out small corrections to the trajectory [26]. Lift and drag coefficient curves were calculated as described above, as was the lift-to-drag ratio. There was significant scatter in the lift and drag curves at small glide angles and therefore angles of attack. This occurred late in the glide, where digitization error was highest. We therefore restricted these curves to start at  $10^\circ$ , and performed glide angle binning from  $10^\circ$  to  $44^\circ$  in  $2^\circ$  increments. Next, a third-order spline was fit to the individual lift and drag coefficient curves. The scatter and binning is shown in figure A.2.

Mean kinematic lift-to-drag ratio curves were calculated by aggregating all glide trials for a particular species. Because glide angle varied continuously during glides, points within a defined glide angle range were averaged. A Taylor moment expansion was used to find the mean and variance of the lift-to-drag-ratio [94, 95]. Naively taking the ratio of lift coefficient to drag coefficient will result in a biased ratio. We use a Taylor series expansion to find the mean and variance of the lift-to-drag ratio in each glide angle bin using

$$\begin{aligned}
 E \left[ \frac{C_L(\alpha_b)}{C_D(\alpha_b)} \right] &\approx E \left[ \frac{C_L(\alpha_b)}{C_D(\alpha_b)} \right] - \frac{\text{cov}[C_L(\alpha_b), C_D(\alpha_b)]}{E[C_D(\alpha_b)]^2} + \frac{E[C_L(\alpha_b)]}{E[C_D(\alpha_b)]^3} \text{var}[C_D(\alpha_b)] \\
 \text{var} \left[ \frac{C_L(\alpha_b)}{C_D(\alpha_b)} \right] &\approx \frac{\text{var}[C_L(\alpha_b)]}{E[C_D(\alpha_b)]^2} - \frac{2E[C_L(\alpha_b)]}{E[C_D(\alpha_b)]^3} \text{cov}[C_L(\alpha_b), C_D(\alpha_b)] \\
 &\quad + \frac{E[C_L(\alpha_b)]^2}{E[C_D(\alpha_b)]^4} \text{var}[C_D(\alpha_b)]
 \end{aligned}$$

where  $\alpha_b = \gamma + \theta_b$  and  $\text{cov}[C_L(\alpha_b), C_D(\alpha_b)]$  is the covariance.

Although the kinematic method of determining aerodynamic coefficients is not ideal, it does provide a measure of the coefficient curves of gliders in their natural setting. Similar techniques have been used for small fixed-wing gliders [96, 97] where multiple markers were placed on the glider, position data differentiated, and aerodynamic parameter calculated. However, this is an idealization of the experimental data available here, including the mass distribution of animal gliders, unsteady fluid mechanics, varying wing size and shape, and time-varying mass distribution.

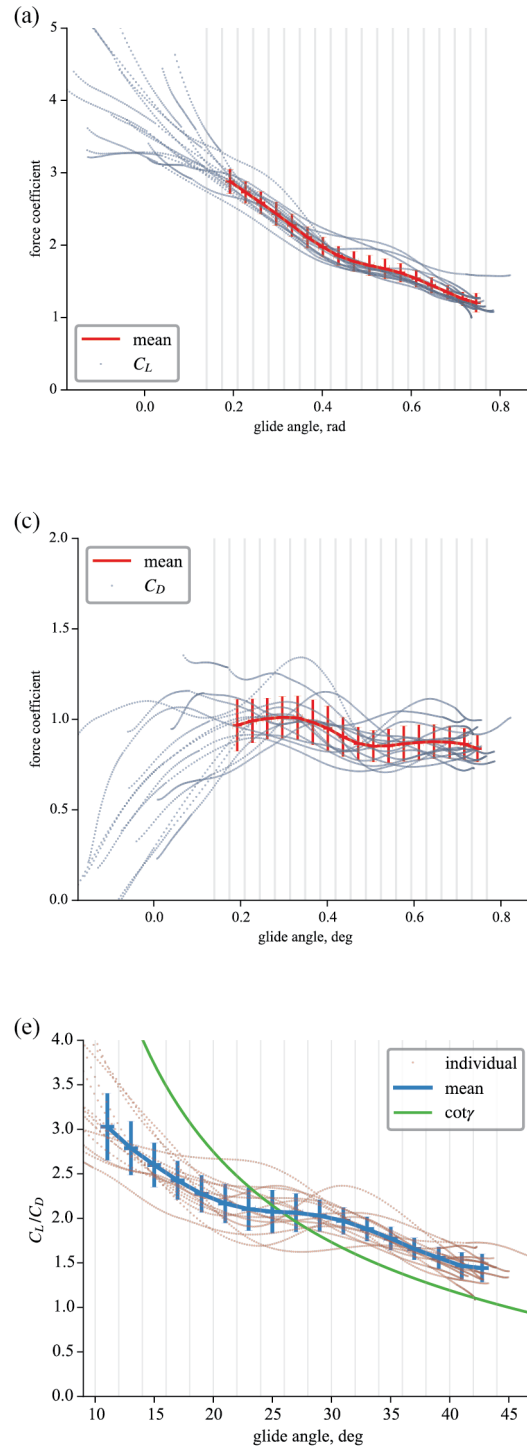


Figure A.2: Mean kinematics-based lift, drag, and lift-to-drag ratio coefficient curves.

## A.5 Numerical implementation of Velocity Polar Diagrams

Velocity polar diagrams are constructed by integrating the Cartesian equations of motion for initial conditions  $(\hat{v}_{0,x}, \hat{v}_{0,z})$  along the perimeter of the velocity space. This technique requires 1) spline fits of the lift and drag coefficients, 2) the measured angle of attack range, and 3) the specified pitch angle of the glider. The horizontal and vertical velocity initial conditions are specified such that  $\alpha_{\min} < \gamma_0 - \theta < \alpha_{\max}$ , where  $\gamma_0 = -\tan^{-1} \hat{v}_{0,z}/\hat{v}_{0,x}$ . This results in the wedge shape of some velocity polar diagrams. Trajectories are found by integrating the equations forward in time using a variable time step fifth-order accurate Dormand-Prince ODE solver until one of the following conditions is met: the angle of attack exceeded the experimentally recorded range; the solver integrates for a total non-dimensional time of 30; or the velocity trajectory leaves the bounding box  $\hat{v}_x \in [0, 1.25]$ ,  $\hat{v}_z \in [0, -1.25]$ . Each trajectory is then plotted to show the phase space flow.

Equilibrium points are found as described in the main text and plotted on the velocity polar diagram. The stable and unstable branches (separatrices) of saddle point equilibria are found by integrating trajectories forward and backwards in time for four initial conditions surrounding the saddle, offset by  $\pm 0.0001$ . The backwards integration identifies the unstable branches and the forward integration specifies the stable branches. Finally, low acceleration regions and nullclines are found by evaluating the Cartesian equations of motion on a fine grid and then plotting contour plots for the following conditions:  $|a| < 0.1$  and  $\hat{v}'_z = 0$ .

## A.6 Stability Analysis and Terminal Velocity Manifold Computation

Below we list the analytical calculation of the terminal velocity manifold and details about the Hopf bifurcation.

The equilibrium condition implies

$$\begin{aligned}\bar{v}^* &= \frac{1}{(C_L(\alpha^*)^2 + C_D(\alpha^*)^2)^{1/4}} \\ \gamma^* &= \cot^{-1} \left( \frac{C_L(\alpha^*)}{C_D(\alpha^*)} \right) \\ \bar{v}_x^* &= \bar{v}^* \cos \gamma^* \\ \bar{v}_z^* &= -\bar{v}^* \sin \gamma^* \\ \alpha^* &= \theta + \gamma^*\end{aligned}$$

### A.6.1 Expansion about the equilibrium

In order to obtain an analytical approximation of the eigenvalues and eigenvectors, and to put the system in a form where we can analytically obtain the glide manifold in the snake phase space, we first do a change of coordinates centered on an equilibrium point. We will work in polar coordinates, since the equations of motion look simpler,

$$\psi = \gamma - \gamma^*, \quad r = \bar{v} - \bar{v}^* \quad (\text{A.6.1})$$

where we are working in non-dimensional and rescaled variables. At equilibrium we know

$$\begin{aligned}\hat{v}' = 0 &\Rightarrow \bar{v}^{*2} C_D(\alpha) = \sin \gamma^* \\ \gamma' = 0 &\Rightarrow \bar{v}^{*2} C_L(\alpha) = \cos \gamma^*.\end{aligned} \quad (\text{A.6.2})$$

In the shifted coordinates, the equilibrium is the origin and the equations of motion are

$$\begin{aligned}\psi' &= -(\bar{v}^* + r) C_L(\gamma^* + \theta^* + \varphi + \psi) + \frac{1}{(\bar{v}^* + r)} \cos(\gamma^* + \psi), \\ r' &= -(\bar{v}^* + r)^2 C_D(\gamma^* + \theta^* + \varphi + \psi) + \sin(\gamma^* + \psi),\end{aligned} \quad (\text{A.6.3})$$

We want to write the right-hand-side of the equations of motion as a power series expansion in  $\psi$  and  $r$ . To start out, we will get this expansion to second-order.

Let's first look at the  $\psi'$  expression. Note that, via Taylor expansion,

$$\frac{1}{(\bar{v}^* + r)} = \frac{1}{\bar{v}^* \left(1 + \frac{r}{\bar{v}^*}\right)} = \frac{1}{\bar{v}^*} \left(1 - \frac{r}{\bar{v}^*} + \left(\frac{r}{\bar{v}^*}\right)^2 - \left(\frac{r}{\bar{v}^*}\right)^3 + \mathcal{O}\left(\frac{r}{\bar{v}^*}\right)^4\right) \quad (\text{A.6.4})$$

Using the cos addition formula,

$$\cos(\gamma^* + \psi) = \cos \psi \cos \gamma^* - \sin \psi \sin \gamma^* \quad (\text{A.6.5})$$

along with (A.6.2), we get

$$\begin{aligned} \frac{1}{\bar{v}^*} \cos(\gamma^* + \psi) &= \frac{1}{\bar{v}^*} [\bar{v}^{*2} C_L(\alpha^*) \cos \psi - \bar{v}^{*2} C_D(\alpha^*) \sin \psi] \\ &= \bar{v}^* [C_L(\alpha^*) \cos \psi - C_D(\alpha^*) \sin \psi] \end{aligned} \quad (\text{A.6.6})$$

so,

$$\begin{aligned} \frac{1}{(\bar{v}^* + r)} \cos(\gamma^* + \psi) &= \bar{v}^* [C_L(\alpha^*) \cos \psi - C_D(\alpha^*) \sin \psi] \left( 1 - \frac{r}{\bar{v}^*} + \left(\frac{r}{\bar{v}^*}\right)^2 - \left(\frac{r}{\bar{v}^*}\right)^3 + \mathcal{O}\left(\frac{r}{\bar{v}^*}\right)^4 \right) \\ &= \bar{v}^* [C_L(\alpha^*) \cos \psi - C_D(\alpha^*) \sin \psi] - r [C_L(\alpha^*) \cos \psi - C_D(\alpha^*) \sin \psi] \\ &\quad + \left( \frac{r^2}{\bar{v}^*} - \frac{r^3}{\bar{v}^{*2}} \right) [C_L(\alpha^*) \cos \psi - C_D(\alpha^*) \sin \psi] + \mathcal{O}(r^4) \end{aligned} \quad (\text{A.6.7})$$

Also note that  $C_L(\gamma^* + \theta^* + \varphi + \psi) = C_L(\alpha^* + \psi)$ , and by Taylor series expansion we have

$$C_L(\alpha^* + \psi) = C_L(\alpha^*) + \psi C'_L(\alpha^*) + \frac{1}{2} \psi^2 C''_L(\alpha^*) + \mathcal{O}(\psi^3) \quad (\text{A.6.8})$$

and similarly for the drag term,

$$C_D(\alpha^* + \psi) = C_D(\alpha^*) + \psi C'_D(\alpha^*) + \frac{1}{2} \psi^2 C''_D(\alpha^*) + \frac{1}{6} \psi^3 C'''_D(\alpha^*) + \mathcal{O}(\psi^4) \quad (\text{A.6.9})$$

so,

$$\begin{aligned} -(\bar{v}^* + r) C_L(\gamma^* + \theta^* + \varphi + \psi) &= -\bar{v}^* [C_L(\alpha^*) + \psi C'_L(\alpha^*) + \frac{1}{2} \psi^2 C''_L(\alpha^*) + \frac{1}{6} \psi^3 C'''_L(\alpha^*) + \mathcal{O}(\psi^4)] \\ &\quad - r [C_L(\alpha^*) + \psi C'_L(\alpha^*) + \frac{1}{2} \psi^2 C''_L(\alpha^*) + \mathcal{O}(\psi^3)] \end{aligned} \quad (\text{A.6.10})$$

So the  $\psi'$  expression becomes

$$\begin{aligned}\psi' &= \bar{v}^* (-C_L(\alpha^* + \psi) + C_L(\alpha^*) \cos \psi - C_D(\alpha^*) \sin \psi) \\ &+ r (-C_L(\alpha^* + \psi) - C_L(\alpha^*) \cos \psi + C_D(\alpha^*) \sin \psi) \\ &+ \left( \frac{r^2}{\bar{v}^*} - \frac{r^3}{\bar{v}^{*2}} \right) [C_L(\alpha^*) \cos \psi - C_D(\alpha^*) \sin \psi] + \mathcal{O}(r^4)\end{aligned}\tag{A.6.11}$$

Note the Taylor series up to 3rd order in  $\psi$  for  $\cos$  and  $\sin$  is,

$$\cos \psi = 1 - \frac{1}{2}\psi^2 + \mathcal{O}(\psi^4), \quad \sin \psi = \psi - \frac{1}{6}\psi^3 + \mathcal{O}(\psi^5)$$

Plugging in all the Taylor series expansions, we get, up through 3rd order in  $\psi$  and  $r$ ,

$$\begin{aligned}\psi' &= \bar{v}^* (-C_L - \psi C'_L - \frac{1}{2}\psi^2 C''_L - \frac{1}{6}\psi^3 C'''_L + C_L - \frac{1}{2}\psi^2 C_L - \psi C_D + \frac{1}{6}\psi^3 C_D) \\ &+ r (-C_L - \psi C'_L - \frac{1}{2}\psi^2 C''_L - C_L + \frac{1}{2}\psi^2 C_L + C_D \psi) \\ &+ \left( \frac{r^2}{\bar{v}^*} - \frac{r^3}{\bar{v}^{*2}} \right) [C_L - C_D \psi] + \mathcal{O}(4)\end{aligned}\tag{A.6.12}$$

where it should be understood that the lift and drag coefficients and all their derivatives (w.r.t. angle of attack) are evaluated at the critical point  $\alpha^*$ , and where  $\mathcal{O}(4)$  stands for terms which are fourth order or higher in the variables  $\psi$  and  $r$ .

Grouping terms by powers in  $\psi$  and  $r$ , we get

$$\begin{aligned}\psi' &= \bar{v}^* [-C'_L - C_D] \psi + 2[-C_L] r \\ &+ \frac{\bar{v}^*}{2} [-C''_L - C_L] \psi^2 + [-C'_L + C_D] \psi r + \frac{1}{\bar{v}^*} [C_L] r^2 \\ &+ \frac{\bar{v}^*}{6} [C_D - C'''_L] \psi^3 + \frac{1}{2} [C_L - C''_L] \psi^2 r + \frac{1}{\bar{v}^*} [-C_D] \psi r^2 + \frac{1}{\bar{v}^{*2}} [-C_L] r^3 + \mathcal{O}(4)\end{aligned}\tag{A.6.13}$$

There are terms linear in  $\psi$  and  $r$ , terms second-order in  $\psi$  and  $r$ , and terms third-order in  $\psi$  and  $r$ .

We can follow a similar procedure for the  $r'$  expression. Using the sin addition formula,

$$\sin(\gamma^* + \psi) = \sin \psi \cos \gamma^* + \cos \psi \sin \gamma^*\tag{A.6.14}$$

along with (A.6.2), we get

$$\begin{aligned}
\sin(\gamma^* + \psi) &= [\bar{v}^{*2} C_L \sin \psi + \bar{v}^{*2} C_D \cos \psi] \\
&= \bar{v}^{*2} [C_L \sin \psi + C_D \cos \psi] \\
&= \bar{v}^{*2} [C_L \psi - \frac{1}{6} C_L \psi^3 + C_D - \frac{1}{2} \psi^2 C_D + \mathcal{O}(4)]
\end{aligned} \tag{A.6.15}$$

Also,

$$\begin{aligned}
-(\bar{v}^* + r)^2 C_D (\alpha^* + \psi) &= -\bar{v}^{*2} [C_D + \psi C'_D + \frac{1}{2} \psi^2 C''_D + \frac{1}{6} \psi^3 C'''_D + \mathcal{O}(4)] \\
&\quad - 2\bar{v}^* r [C_D + \psi C'_D + \frac{1}{2} \psi^2 C''_D + \mathcal{O}(3)] \\
&\quad - r^2 [C_D + \psi C'_D + \mathcal{O}(2)]
\end{aligned} \tag{A.6.16}$$

so we get

$$\begin{aligned}
r' &= \bar{v}^{*2} [-C'_D + C_L] \psi + 2[-\bar{v}^* C_D] r \\
&\quad + \frac{\bar{v}^{*2}}{2} [-C_D - C''_D] \psi^2 + 2\bar{v}^* [-C'_D] \psi r + [-C_D] r^2 \\
&\quad + \frac{\bar{v}^{*2}}{6} [-C_L - C'''_D] \psi^3 + \bar{v}^* [-C''_D] \psi^2 r + \frac{1}{2} [-C'_D] \psi r^2 + [0] r^3 + \mathcal{O}(4)
\end{aligned} \tag{A.6.17}$$

Putting the  $(\psi, r)$  system into matrix form, we have

$$\begin{bmatrix} \psi' \\ r' \end{bmatrix} = \underbrace{\begin{bmatrix} \bar{v}^* [-C'_L - C_D] & [-2C_L] \\ \bar{v}^{*2} [-C'_D + C_L] & [-2\bar{v}^* C_D] \end{bmatrix}}_{\mathbf{A}} \begin{bmatrix} \psi \\ r \end{bmatrix} + \mathbf{F}(\psi, r) + \mathcal{O}(4) \tag{A.6.18}$$

where  $\mathbf{F}(\psi, r)$  stands for second and third-order terms, and is given by

$$\mathbf{F}(\psi, r) = \begin{bmatrix} F^1(\psi, r) \\ F^2(\psi, r) \end{bmatrix} \tag{A.6.19}$$

where

$$\begin{aligned}
F^1(\psi, r) &= \frac{\bar{v}^*}{2} [-C_L - C''_L] \psi^2 + [C_D - C'_L] \psi r + \frac{1}{\bar{v}^*} [C_L] r^2 \\
&\quad + \frac{\bar{v}^*}{6} [C_D - C'''_L] \psi^3 + \frac{1}{2} [C_L - C''_L] \psi^2 r + \frac{1}{\bar{v}^*} [-C_D] \psi r^2 + \frac{1}{\bar{v}^{*2}} [-C_L] r^3
\end{aligned} \tag{A.6.20}$$

and

$$F^2(\psi, r) = \frac{\bar{v}^{*2}}{2} [-C_D - C_D''] \psi^2 + 2\bar{v}^* [-C_D'] \psi r + [-C_D] r^2 + \frac{\bar{v}^{*2}}{6} [-C_L - C_D'''] \psi^3 + \bar{v}^* [-C_D''] \psi^2 r + \frac{1}{2} [-C_D'] \psi r^2 + [0] r^3 \quad (\text{A.6.21})$$

From the  $2 \times 2$  linearization matrix  $\mathbf{A}$  in (A.6.18),

$$\mathbf{A} = \begin{bmatrix} \bar{v}^* [-C_L' - C_D] & [-2C_L] \\ \bar{v}^{*2} [-C_D' + C_L] & [-2\bar{v}^* C_D] \end{bmatrix} \quad (\text{A.6.22})$$

(also given in appendix A), we can analytically determine the eigenvalues and eigenvectors in terms of the equilibrium point and characteristics of the lift and drag curves at that point.

For this simple system, we can write the eigenvalue equation in the standard form as [48, p. 130]

$$\lambda^2 - \bar{\tau}\lambda + \bar{\Delta} = 0,$$

where  $\bar{\tau} = \text{trace}(\mathbf{A})$  and  $\bar{\Delta} = \det(\mathbf{A})$ . The eigenvalues are

$$\lambda_1 = \frac{\bar{\tau} + \sqrt{\bar{\tau}^2 - 4\bar{\Delta}}}{2}, \quad \lambda_2 = \frac{\bar{\tau} - \sqrt{\bar{\tau}^2 - 4\bar{\Delta}}}{2}$$

The trace of  $\mathbf{A}$  is

$$\bar{\tau} = \bar{v}^* [-C_L' - 3C_D]$$

and the determinant of  $\mathbf{A}$  is

$$\bar{\Delta} = 2\bar{v}^{*2} [C_L^2 + C_D^2 + C_L' C_D - C_D' C_L]$$

So,

$$\begin{aligned} \bar{\tau}^2 - 4\bar{\Delta} &= \bar{v}^{*2} [(C_L' + 3C_D)^2 - 8(C_L^2 + C_D^2 + C_L' C_D - C_D' C_L)] \\ &= \bar{v}^{*2} [C_L'^2 + C_D^2 - 2C_L' C_D - 8C_L^2 + 8C_D' C_L] \\ &= \bar{v}^{*2} [(C_D - C_L')^2 - 8C_L(C_L - C_D')] \end{aligned} \quad (\text{A.6.23})$$

and the eigenvalues are

$$\lambda_{1,2} = \frac{\bar{\tau} \pm \sqrt{\bar{\tau}^2 - 4\bar{\Delta}}}{2}$$

We can write the eigenvalues more compactly by introducing  $\tau$  and  $\Delta$ ,

$$\begin{aligned}\tau &= (C'_L/C_D) + 3 \\ \Delta &= (C_L/C_D)' + (C_L/C_D)^2 + 1\end{aligned}\tag{A.6.24}$$

such that

$$\begin{aligned}\bar{\tau} &= -\frac{C_D}{(C_L^2 + C_D^2)^{1/4}}\tau \\ \bar{\Delta} &= 2\frac{C_D^2}{(C_L^2 + C_D^2)^{1/2}}\Delta\end{aligned}\tag{A.6.25}$$

in which case,

$$\lambda_{1,2} = \frac{C_D}{2(C_L^2 + C_D^2)^{1/4}} \left( -\tau \pm \sqrt{\tau^2 - 8\Delta} \right)\tag{A.6.26}$$

and since the prefactor

$$\frac{C_D}{2(C_L^2 + C_D^2)^{1/4}}\tag{A.6.27}$$

is always a positive scalar, the location of the eigenvalues on the complex plane is given solely by  $\tau$  and  $\Delta$ .

## A.6.2 Hopf bifurcation case

We often view the pitch variable  $\theta$  as a bifurcation parameter. A Hopf bifurcation occurs when  $\bar{\tau} = 0$  and  $\bar{\Delta} > 0$ , so the eigenvalues are purely imaginary,

$$\lambda_{\pm} = \pm i\omega$$

where  $\omega = \sqrt{\bar{\Delta}} > 0$ . Suppose this occurs along the branch of equilibria at a particular value of  $\theta$  which we'll call  $\bar{\theta}$ . By the assumption of  $\bar{\tau} = 0$ , we conclude that

$$C'_L = -3C_D\tag{A.6.28}$$

and from  $\bar{\Delta} > 0$ , we conclude that

$$C_L > \frac{1}{2} \left( C'_D + \sqrt{C_D'^2 + 8C_D^2} \right) \quad \text{or} \quad C_L < \frac{1}{2} \left( C'_D - \sqrt{C_D'^2 + 8C_D^2} \right)\tag{A.6.29}$$

Notice that the sign of

$$d = \frac{d}{d\theta} (\operatorname{Re}(\lambda(\theta))) \Big|_{\theta=\bar{\theta}} = \frac{1}{2}\bar{\tau}' = \frac{1}{2}\bar{v}^*(-C_L'' - 3C_D') \quad (\text{A.6.30})$$

is an indication of the type of bifurcation. If, as  $\theta$  increases, the equilibrium point is going from a stable to unstable focus, then  $\bar{\tau}' > 0$ . Otherwise,  $\bar{\tau}' < 0$ . Note that

$$\begin{aligned} C_L'' < -3C_D' & \text{ going from stable to unstable, } \bar{\tau}' > 0 \\ C_L'' > -3C_D' & \text{ going from unstable to stable, } \bar{\tau}' < 0 \end{aligned} \quad (\text{A.6.31})$$

For the case of purely imaginary eigenvalues, we have

$$\mathbf{A} = \begin{bmatrix} \bar{v}^*2C_D & -2C_L \\ \bar{v}^{*2}(-C_D' + C_L) & -\bar{v}^*2C_D \end{bmatrix} \quad (\text{A.6.32})$$

where the eigenvalues are  $\pm i\omega$ , where

$$\omega = \bar{v}^*\sqrt{2}\sqrt{C_L^2 - C_L C_D' - 2C_D^2} \quad (\text{A.6.33})$$

is positive. We solve for the generalized eigenvectors  $\mathbf{u}$  and  $\mathbf{v}$ ,

$$\mathbf{u} = \begin{bmatrix} 2C_L \\ \bar{v}^*2C_D \end{bmatrix} \quad \mathbf{v} = \begin{bmatrix} 0 \\ \omega \end{bmatrix} \quad (\text{A.6.34})$$

Define the matrix  $\mathbf{P}$  as

$$\mathbf{P} = [\mathbf{u} \quad \mathbf{v}]$$

so  $\mathbf{u}$  is the first column of  $\mathbf{P}$  and  $\mathbf{v}$  is the second column of  $\mathbf{P}$ . This matrix defines a linear transformation to the eigenbasis  $(x, y)$  via

$$\begin{bmatrix} \psi \\ r \end{bmatrix} = \mathbf{P} \begin{bmatrix} x \\ y \end{bmatrix}$$

so the  $x$  coordinate is along the  $\mathbf{u}$  direction and the  $y$  coordinate is along the  $\mathbf{v}$  direction.

Note that

$$\begin{aligned}\psi &= 2C_L x \\ r &= \bar{v}^* 2C_D x + \omega y\end{aligned}\tag{A.6.35}$$

The dynamics in the eigenbasis are

$$\begin{bmatrix} x' \\ y' \end{bmatrix} = \begin{bmatrix} 0 & -\omega \\ \omega & 0 \end{bmatrix} \begin{bmatrix} x \\ y \end{bmatrix} + \mathbf{P}^{-1} \mathbf{F}(2C_L x, \bar{v}^* 2C_D x + \omega y) + \mathcal{O}(4)\tag{A.6.36}$$

where  $\mathbf{F}$ , from (A.6.19), includes the 2nd and 3rd order terms and where

$$\mathbf{P}^{-1} = \begin{bmatrix} \frac{1}{2C_L} & 0 \\ -\frac{\bar{v}^* C_D}{\omega C_L} & \frac{1}{\omega} \end{bmatrix}\tag{A.6.37}$$

We will re-write the nonlinear terms, defining  $\mathbf{f}(x, y) = \mathbf{P}^{-1} \mathbf{F}(2C_L x, \bar{v}^* 2C_D x + \omega y)$ , so the resulting equation now has the form,

$$\begin{bmatrix} x' \\ y' \end{bmatrix} = \begin{bmatrix} 0 & -\omega \\ \omega & 0 \end{bmatrix} \begin{bmatrix} x \\ y \end{bmatrix} + \begin{bmatrix} f^1(x, y) \\ f^2(x, y) \end{bmatrix}\tag{A.6.38}$$

The coefficient  $a$ , from [98] and [99], which determines what kind of Hopf bifurcation will occur, can be calculated as

$$\begin{aligned}a &= \frac{1}{16} [f_{xxx}^1 + f_{xyy}^1 + f_{xxy}^2 + f_{yyy}^2] \\ &\quad + \frac{1}{16\omega} [f_{xy}^1 (f_{xx}^1 + f_{yy}^1) - f_{xy}^2 (f_{xx}^2 + f_{yy}^2) - f_{xx}^1 f_{xx}^2 + f_{yy}^1 f_{yy}^2]\end{aligned}\tag{A.6.39}$$

where all partial derivatives are evaluated at the bifurcation point,  $\theta = \bar{\theta}$ ,  $x = 0$ ,  $y = 0$ ,

$$\begin{aligned}
F_{xx}^1 &= \bar{v}^*(4C_L^3 - 4C_L^3 C_L'' + 36C_L C_D^2) \\
F_{xy}^1 &= \omega 12C_L C_D \\
F_{yy}^1 &= \bar{v}^* 4C_L (C_L^2 - C_L C_D' - 2C_D^2) \\
F_{xx}^2 &= -\bar{v}^{*2} (4C_L^2 C_D + 8C_D^3 + 4C_L^2 C_D'' + 16C_L C_D C_D') \\
F_{xy}^2 &= -\bar{v}^* \omega (C_L C_L' + C_D^2) \\
F_{yy}^2 &= -\bar{v}^{*2} 4C_D (C_L^2 - C_L C_D' - 2C_D^2) \\
F_{xxx}^1 &= -\bar{v}^* (8C_L^3 C_L''' + 24C_L^2 C_D C_L'' + 96C_L C_D^3 - 32C_L^3 C_D) \\
F_{xyy}^1 &= -\bar{v}^* 32C_D C_L (C_L^2 - C_L C_D' - 2C_D^2) \\
F_{xxy}^1 &= \bar{v}^* (4[C_L - C_L''] C_L^2 (\frac{\omega}{\bar{v}^*}) - 40C_L C_D^2 (\frac{\omega}{\bar{v}^*})) \\
F_{yyy}^1 &= -\bar{v}^* 12C_L (C_L^2 - C_L C_D' - 2C_D^2) (\frac{\omega}{\bar{v}^*}) \\
F_{xxy}^2 &= -\bar{v}^* \omega (8C_L^2 C_D'' + 8C_L C_D C_D') \\
F_{yyy}^2 &= 0
\end{aligned} \tag{A.6.40}$$

and we get the partial derivatives of  $\mathbf{f}(x, y)$  from the relationship

$$\mathbf{f}(x, y) = \mathbf{P}^{-1} \mathbf{F}(x, y)$$

which give us

$$\begin{aligned}
f^1(x, y) &= \frac{1}{2C_L} F_1(x, y) \\
f^2(x, y) &= -\frac{\bar{v}^* C_D}{\omega C_L} F_1(x, y) + \frac{1}{\omega} F_2(x, y)
\end{aligned} \tag{A.6.41}$$

Knowing the sign of  $a$  along with the sign of  $\tau'$  will determine which of the four cases of Hopf bifurcation is present, via the Poincaré-Andronov-Hopf Bifurcation Theorem ([98]).

For example, for the pitch bifurcation diagram of the ‘kinematic squirrel’, we see a Hopf bifurcation for a critical  $\bar{\theta}$  near 0. We can see that  $d < 0$  (eigenvalues going from right half-plane to left half-plane as  $\theta - \bar{\theta}$  increases through zero). The numerically determined unstable limit cycle exists for  $\theta > \bar{\theta}$ , which is consistent with  $a > 0$ , so we predict that calculating (A.6.39) will give  $a > 0$ . We also predict that the limit cycle will have a period of approximately  $T = \frac{2\pi}{\omega}$  where  $\omega$  is given from (A.6.33), and that the radius of the limit

cycle in the  $(x, y)$  plane, close to the pitch value  $\bar{\theta}$ , is given by

$$\rho = \sqrt{-\frac{d}{a}(\theta - \bar{\theta})} \quad (\text{A.6.42})$$

Notice that the dependence of  $\rho$  on the constants  $a$  and  $d$ , as well as distance away from the bifurcation point,  $(\theta - \bar{\theta})$ , reveal how ‘quickly’ the size of the limit cycle grows. The amplitude of the limit cycle in terms of glide angle  $\gamma$  is provided from (A.6.35) as,

$$\rho_\gamma = 2C_L\rho = 2C_L\sqrt{-\frac{d}{a}(\theta - \bar{\theta})} \quad (\text{A.6.43})$$

### A.6.3 Stable node case

If  $\bar{\tau} < 0$  and  $\bar{\tau}^2 - 4\bar{\Delta} > 0$  (so  $\sqrt{\bar{\tau}^2 - 4\bar{\Delta}} > 0$ ), then we have two real, and negative, eigenvalues. The larger magnitude eigenvalue is

$$\lambda_{ss} = \frac{\bar{\tau} - \sqrt{\bar{\tau}^2 - 4\bar{\Delta}}}{2} = \frac{1}{2}\bar{v}^* \left( -C'_L - 3C_D - \sqrt{(C_D - C'_L)^2 - 8C_L(C_L - C'_D)} \right), \quad (\text{A.6.44})$$

and the smaller magnitude eigenvalue is

$$\lambda_s = \frac{\bar{\tau} + \sqrt{\bar{\tau}^2 - 4\bar{\Delta}}}{2} = \frac{1}{2}\bar{v}^* \left( -C'_L - 3C_D + \sqrt{(C_D - C'_L)^2 - 8C_L(C_L - C'_D)} \right), \quad (\text{A.6.45})$$

so  $\lambda_{ss} < \lambda_s < 0$ , where ‘s’ denotes *stable* and ‘ss’ denotes *super stable*. Let the corresponding eigenvectors be  $\mathbf{e}_{ss}$  and  $\mathbf{e}_s$ , respectively, understood as column vectors.

Now  $\bar{\tau} < 0$  implies that

$$C'_L > -3C_D$$

, and  $\bar{\tau}^2 - 4\bar{\Delta} > 0$  implies that

$$(C_D - C'_L)^2 > 8C_L(C_L - C'_D)$$

We can solve for  $\mathbf{e}_s$ , since it will give us a local approximation of the *terminal velocity manifold* described in the text. All we want is the slope  $\bar{m}$  (in  $(\psi, r)$  coordinates), so we let

$\mathbf{e}_s = [-1, -\bar{m}]^T$ . From the eigenvector formula

$$\mathbf{A}\mathbf{e}_s = \lambda_s \mathbf{e}_s$$

where

$$\mathbf{A} = \begin{bmatrix} a & b \\ c & d \end{bmatrix} \quad (\text{A.6.46})$$

we have

$$\bar{m} = \frac{\lambda_s - a}{b} \quad (\text{A.6.47})$$

and using (A.6.22) and (A.6.53), we get

$$a = \bar{v}^* [-C'_L - C_D], \quad b = [-2C_L]$$

and thus,

$$\bar{m} = \frac{\bar{v}^*}{4C_L} \left( C_D - C'_L - \sqrt{(C_D - C'_L)^2 - 8C_L(C_L - C'_D)} \right) \quad (\text{A.6.48})$$

We want the slope  $m$  in  $(\bar{v}_x, \bar{v}_z)$  coordinates, so, using the relationship between the cartesian and polar coordinates,

$$\bar{v}_x = \bar{v} \cos \gamma$$

$$\bar{v}_z = -\bar{v} \sin \gamma$$

we write the transformation between local vectors,

$$\begin{bmatrix} d\bar{v}_x \\ d\bar{v}_z \end{bmatrix} = \begin{bmatrix} -\bar{v}^* \sin \gamma^* & \cos \gamma^* \\ -\bar{v}^* \cos \gamma^* & -\sin \gamma^* \end{bmatrix} \begin{bmatrix} d\psi \\ dr \end{bmatrix} \quad (\text{A.6.49})$$

and letting  $dr = \bar{m} d\psi$ , we get the slope of the terminal velocity manifold,

$$m = \frac{d\bar{v}_z}{d\bar{v}_x} = \frac{\bar{v}^* \cos \gamma^* + \bar{m} \sin \gamma^*}{\bar{v}^* \sin \gamma^* - \bar{m} \cos \gamma^*} \quad (\text{A.6.50})$$

with  $\bar{m}$  as in (A.6.56). Note, this is the *local* slope of the terminal velocity manifold, as evaluated at the stable node point. The slope may change, i.e., the manifold may be curved, as explored in the next case.

For completeness, we also compute the eigenvector  $\mathbf{e}_{ss} = [-1, -\bar{n}]^T$ , and get

$$\bar{n} = \frac{\bar{v}^*}{4C_L} \left( C_D - C'_L + \sqrt{(C_D - C'_L)^2 - 8C_L(C_L - C'_D)} \right) \quad (\text{A.6.51})$$

#### A.6.4 Saddle case

If  $\bar{\Delta} < 0$ , so  $\bar{\Delta} = -|\bar{\Delta}|$ , then  $\sqrt{\bar{\tau}^2 - 4\bar{\Delta}} = \sqrt{\bar{\tau}^2 + 4|\bar{\Delta}|} > |\bar{\tau}|$ , then we have two real eigenvalues, one negative ( $\lambda_s$ ) and one positive ( $\lambda_u$ ). The negative eigenvalue is

$$\lambda_s = \frac{\bar{\tau} - \sqrt{\bar{\tau}^2 - 4\bar{\Delta}}}{2} = \frac{1}{2}\bar{v}^* \left( -C'_L - 3C_D - \sqrt{(C_D - C'_L)^2 - 8C_L(C_L - C'_D)} \right), \quad (\text{A.6.52})$$

and the positive eigenvalue is

$$\lambda_u = \frac{\bar{\tau} + \sqrt{\bar{\tau}^2 - 4\bar{\Delta}}}{2} = \frac{1}{2}\bar{v}^* \left( -C'_L - 3C_D + \sqrt{(C_D - C'_L)^2 - 8C_L(C_L - C'_D)} \right), \quad (\text{A.6.53})$$

Let the corresponding eigenvectors be  $\mathbf{e}_s$  and  $\mathbf{e}_u$ , respectively, understood as column vectors.

We can solve for  $\mathbf{e}_u$ , since it will give us a local approximation of the *terminal velocity manifold* described in the text. All we want is the slope  $\bar{m}$  (in  $(\psi, r)$  coordinates), so we let  $\mathbf{e}_u = [-1, -\bar{m}]^T$ . From the eigenvector formula

$$\mathbf{A}\mathbf{e}_u = \lambda_u\mathbf{e}_u$$

where

$$\mathbf{A} = \begin{bmatrix} a & b \\ c & d \end{bmatrix} \quad (\text{A.6.54})$$

we have

$$\bar{m} = \frac{\lambda_u - a}{b} \quad (\text{A.6.55})$$

and using (A.6.22) and (A.6.53), we get

$$a = \bar{v}^* [-C'_L - C_D], \quad b = [-2C_L]$$

and thus,

$$\bar{m} = \frac{\bar{v}^*}{4C_L} \left( C_D - C'_L - \sqrt{(C_D - C'_L)^2 - 8C_L(C_L - C'_D)} \right) \quad (\text{A.6.56})$$

We want the slope  $m$  in  $(\bar{v}_x, \bar{v}_z)$  coordinates, so, using the relationship between the cartesian and polar coordinates,

$$\begin{aligned}\bar{v}_x &= \bar{v} \cos \gamma \\ \bar{v}_z &= -\bar{v} \sin \gamma\end{aligned}\tag{A.6.57}$$

we write the transformation between local vectors,

$$\begin{bmatrix} d\bar{v}_x \\ d\bar{v}_z \end{bmatrix} = \begin{bmatrix} -\bar{v}^* \sin \gamma^* & \cos \gamma^* \\ -\bar{v}^* \cos \gamma^* & -\sin \gamma^* \end{bmatrix} \begin{bmatrix} d\psi \\ dr \end{bmatrix}\tag{A.6.58}$$

and letting  $dr = \bar{m} d\psi$ , we get the slope of the terminal velocity manifold,

$$m = \frac{d\bar{v}_z}{d\bar{v}_x} = \frac{\bar{v}^* \cos \gamma^* + \bar{m} \sin \gamma^*}{\bar{v}^* \sin \gamma^* - \bar{m} \cos \gamma^*}\tag{A.6.59}$$

with  $\bar{m}$  as in (A.6.56). Again, this is the *local* slope of the terminal velocity manifold, as evaluated at the saddle point, and may be different from the local slope of the terminal velocity manifold as evaluated at the stable node, if the manifold is curved.

For completeness, we also compute the eigenvector  $\mathbf{e}_s = [-1, -\bar{n}]^T$ , and get

$$\bar{n} = \frac{\bar{v}^*}{4C_L} \left( C_D - C'_L + \sqrt{(C_D - C'_L)^2 - 8C_L(C_L - C'_D)} \right)\tag{A.6.60}$$

**Higher order approximation of terminal velocity manifold.** Define the matrix  $\mathbf{P}$  as

$$\begin{aligned}\mathbf{P} &= [\mathbf{e}_u \quad \mathbf{e}_s] \\ &= \begin{bmatrix} -1 & -1 \\ -\bar{m} & -\bar{n} \end{bmatrix}\end{aligned}$$

so  $\mathbf{e}_u$  is the first column of  $\mathbf{P}$  and  $\mathbf{e}_s$  is the second column of  $\mathbf{P}$ .

This matrix defines a linear transformation to the eigenbasis  $(x, y)$  via

$$\begin{bmatrix} \psi \\ r \end{bmatrix} = \mathbf{P} \begin{bmatrix} x \\ y \end{bmatrix}$$

so the  $x$  coordinate is along the  $\mathbf{e}_u$  direction and the  $y$  coordinate is along the  $\mathbf{e}_s$  direction.

Note that

$$\begin{aligned}\psi &= -x - y \\ r &= -\bar{m}x - \bar{n}y\end{aligned}\tag{A.6.61}$$

and

$$\mathbf{P}^{-1} = \frac{1}{\bar{m} - \bar{n}} \begin{bmatrix} \bar{n} & -1 \\ -\bar{m} & 1 \end{bmatrix}\tag{A.6.62}$$

Considering (A.6.18), we have

$$\begin{bmatrix} x' \\ y' \end{bmatrix} = \underbrace{\mathbf{P}^{-1}\mathbf{A}\mathbf{P}}_{\mathbf{\Lambda}} \begin{bmatrix} x \\ y \end{bmatrix} + \mathbf{P}^{-1}\mathbf{F}(x, y)\tag{A.6.63}$$

where  $\mathbf{\Lambda}$  is the diagonalized matrix,

$$\mathbf{\Lambda} = \begin{bmatrix} \lambda_u & 0 \\ 0 & \lambda_s \end{bmatrix}$$

and where care must be taken to calculate the second-order terms,  $\mathbf{P}^{-1}\mathbf{F}(x, y)$ , in terms of  $x$  and  $y$ , where  $\mathbf{F}(x, y)$  is given as in (A.6.19)-(A.6.21).

We will re-write the nonlinear terms, defining  $\mathbf{f}(x, y) = \mathbf{P}^{-1}\mathbf{F}(-x - y, -\bar{m}x - \bar{n}y)$ , so

$$\mathbf{f}(x, y) = \frac{1}{\bar{m} - \bar{n}} \begin{bmatrix} \bar{n} & -1 \\ -\bar{m} & 1 \end{bmatrix} \begin{bmatrix} a_1x^2 + a_2xy + a_3y^2 \\ b_1x^2 + b_2xy + b_3y^2 \end{bmatrix} + \mathcal{O}(3)$$

where

$$\begin{aligned}
a_1 &= a^1 + b^1 \bar{m} + c^1 \bar{m}^2 \\
a_2 &= 2a^1 + b^1(\bar{m} + \bar{n}) + 2c^1 \bar{m} \bar{n} \\
a_3 &= a^1 + b^1 \bar{n} + c^1 \bar{n}^2 \\
b_1 &= a^2 + b^2 \bar{m} + c^2 \bar{m}^2 \\
b_2 &= 2a^2 + b^2(\bar{m} + \bar{n}) + 2c^2 \bar{m} \bar{n} \\
b_3 &= a^2 + b^2 \bar{n} + c^2 \bar{n}^2 \\
a^1 &= \frac{\bar{v}^*}{2} [-C_L - C_L''] \\
b^1 &= [C_D - C_D'] \\
c^1 &= \frac{1}{\bar{v}^*} [C_L] \\
a^2 &= \frac{\bar{v}^{*2}}{2} [-C_D - C_D''] \\
b^2 &= 2\bar{v}^* [-C_D'] \\
c^2 &= [-C_D]
\end{aligned}$$

We will refer to the components of  $\mathbf{f}$  as  $(f, g)$ .

The resulting equation now has the form,

$$\begin{bmatrix} x' \\ y' \end{bmatrix} = \begin{bmatrix} \lambda_u & 0 \\ 0 & \lambda_s \end{bmatrix} \begin{bmatrix} x \\ y \end{bmatrix} + \begin{bmatrix} f(x, y) \\ g(x, y) \end{bmatrix} \tag{A.6.64}$$

where

$$\begin{aligned}
f(x, y) &= c_1 x^2 + c_2 xy + c_3 y^2 + \mathcal{O}(3) \\
g(x, y) &= d_1 x^2 + d_2 xy + d_3 y^2 + \mathcal{O}(3)
\end{aligned} \tag{A.6.65}$$

where

$$\begin{aligned}
c_i &= \frac{1}{\bar{m} - \bar{n}} (\bar{n} a_i - b_i) \\
d_i &= \frac{1}{\bar{m} - \bar{n}} (-\bar{m} a_i + b_i)
\end{aligned}$$

We will end up with the expansion about the equilibrium in a form where we can now

calculate the terminal velocity manifold. We re-write (A.6.64) as,

$$\begin{aligned}x' &= \lambda_u x + f(x, y) \\y' &= \lambda_s y + g(x, y)\end{aligned}\tag{A.6.66}$$

where  $f(x, y)$  is second-order and higher in  $x$  and  $y$ , as is  $g(x, y)$ .

We assume the terminal velocity manifold is given by  $y = h(x)$ , where  $h(x)$  has the Taylor series expansion form,

$$h(x) = ax^2 + bx^3 + \mathcal{O}(x^4)\tag{A.6.67}$$

We can solve for the coefficients  $a$  and  $b$  by taking the time derivative of  $y = h(x)$ , which gives

$$\frac{\partial h}{\partial x} x' - y' = 0$$

i.e.,

$$\frac{\partial h}{\partial x} [\lambda_u x + f(x, h(x))] - [\lambda_s h(x) + g(x, h(x))] = 0$$

and equating like powers of  $x$ ,

$$(2ax + 3bx^2 + \mathcal{O}(x^3)) [\lambda_u x + c_1 x^2 + \mathcal{O}(x^3)] - [\lambda_s a x^2 + d_1 x^2 + \mathcal{O}(x^3)] = 0$$

i.e.,

$$[a(2\lambda_u - \lambda_s) - d_1] x^2 = 0$$

so

$$a = \frac{d_1}{(2\lambda_u - \lambda_s)}$$

Thus, to a second-order approximation in the  $(x, y)$  coordinates, the terminal velocity manifold is expressed as

$$y = h(x) = \frac{d_1}{(2\lambda_u - \lambda_s)} x^2 + \mathcal{O}(x^3)$$

thus, in general the manifold will be curved. To get the curvature up through third-order terms, we need  $b$ , so we would have to have  $\mathbf{f}(x, y)$  calculated up to the third-order terms. We note that this whole process can be automated using automatic power series expansion tools [100].

To get the terminal velocity manifold in the original  $(\bar{v}_x, \bar{v}_z)$  coordinates, we use (A.6.61),

(A.6.1), and (A.6.57), to get a parametric curve,

$$\begin{aligned}\bar{v}_x(u) &= (\bar{v}^* - \bar{m}u - \bar{n}h(u)) \cos(\gamma^* - u - h(u)) \\ \bar{v}_z(u) &= -(\bar{v}^* - \bar{m}u - \bar{n}h(u)) \sin(\gamma^* - u - h(u))\end{aligned}\tag{A.6.68}$$

parametrized by a curvilinear coordinate  $u$  which we take to be in some interval  $I \subset \mathbb{R}$ , where the function  $h$  is as in (A.6.67).

We can determine the lowest order non-linear approximation of the vector field *along the 1-dimensional terminal velocity manifold*, as

$$\begin{aligned}u' &= \lambda_u u + f(u, h(u)) \\ &= \lambda_u u + c_1 u^2 + \mathcal{O}(u^3)\end{aligned}\tag{A.6.69}$$

where we are using  $u$  as a curvilinear (arc-length) coordinate along the terminal velocity manifold. This is the analytical formula for the ‘speed’ (actually, acceleration) along the terminal velocity curve vs. location along that curve. This tells us that a second equilibrium point (stable) will show up along the terminal velocity manifold at  $u = -\lambda_u/c_1$ , which is an approximation of where the stable node is located.

It is interesting that the local approximation of the dynamics around the saddle point can imply the existence of the stable point. Also noteworthy is the fact that the terminal velocity manifold constructed from the saddle point to the stable node is a heteroclinic trajectory (backward asymptotic to the saddle point and forward asymptotic to the stable node) along which the relative speed varies according to (A.6.69).

To find out what role the shape of the terminal velocity manifold plays in modifying the vector field along it, we must consider third-order terms in (A.6.18), which would give us

$$\begin{aligned}u' &= \lambda_u u + f_2(u, h(u)) + f_3(u, h(u)) + \mathcal{O}(u^4) \\ &= \lambda_u u + c_1 u^2 + c_2 a u^3 + k_1 u^3 + \mathcal{O}(u^4) \\ &= \lambda_u u + c_1 u^2 + \left[ c_2 \frac{d}{(2\lambda_u - \lambda_s)} + k_1 \right] u^3 + \mathcal{O}(u^4)\end{aligned}\tag{A.6.70}$$

where  $f_2(x, y) = c_1 x^2 + c_2 x y + c_3 y^2$  and  $f_3(x, y) = k_1 x^3 + k_2 x^2 y + k_3 x y^2 + k_4 y^3$  are the second and third order terms in the  $x'$  equation of (A.6.66), respectively.

Note that

$$k_1 = \frac{1}{\bar{m}-\bar{n}}(\bar{n}\tilde{a}_1 - \tilde{b}_1)$$

where

$$\begin{aligned}\tilde{a}_1 &= -(A_1 + A_2\bar{m} + A_3\bar{m}^2 + A_4\bar{m}^3) \\ \tilde{b}_1 &= -(B_1 + B_2\bar{m} + B_3\bar{m}^2 + B_4\bar{m}^3)\end{aligned}$$

and where the  $A_i$  and  $B_i$  come from the third-order coefficients in (A.6.20) and (A.6.21), respectively,

$$\begin{aligned}A_1 &= \frac{\bar{v}^*}{6}[C_D - C_L'''] \\ A_2 &= \frac{1}{2}[C_L - C_L''] \\ A_3 &= \frac{1}{\bar{v}^*}[-C_D] \\ A_4 &= \frac{1}{\bar{v}^{*2}}[-C_L] \\ B_1 &= \frac{\bar{v}^{*2}}{6}[-C_L - C_D'''] \\ B_2 &= \bar{v}^*[-C_D''] \\ B_3 &= \frac{1}{2}[-C_D'] \\ B_4 &= 0\end{aligned}$$

We note that the third-order coefficient  $b$  is given by

$$b = \frac{g_1 - a(2c_1 - d_2)}{3\lambda_u - \lambda_s}$$

where

$$g_1 = \frac{1}{\bar{m}-\bar{n}}(-\bar{m}\tilde{a}_1 + \tilde{b}_1)$$

### A.6.5 Terminal velocity manifold as slow manifold

In the previous sections, we have looked for local approximations of the terminal velocity manifold near an equilibrium point, building off of the invariant manifold structure near the equilibrium. However, we may be able to consider another, more global approach, inspired by singular perturbation theory [48]. In some systems, one can identify a fast variable and a slow variable when a small parameter appears in one of the ODEs. The dynamics of the fast

variable quickly collapse onto a lower dimensional manifold on which the dynamics evolve more slowly (the slow variable). In the re-scaled gliding equations of motion for  $(\bar{v}_x, \bar{v}_z)$ , no slow-fast structure can be identified in the equations themselves (i.e., there is no natural choice of a small parameter), yet a slow manifold appears to exist. While we do not consider it here, there may methods to obtain the approximate slow manifold [101, 102], based on the extended zero derivative principle, even if fast and slow variables have not been identified.

### A.6.6 Acceleration along the terminal velocity manifold

In figure 5bii of the text, we include an inset showing the approximation of the terminal velocity manifold in the vicinity of the saddle point equilibrium. Below we show the acceleration magnitude of the glider along the manifold using both the 2<sup>nd</sup>-order and 3<sup>rd</sup>-order approximations.

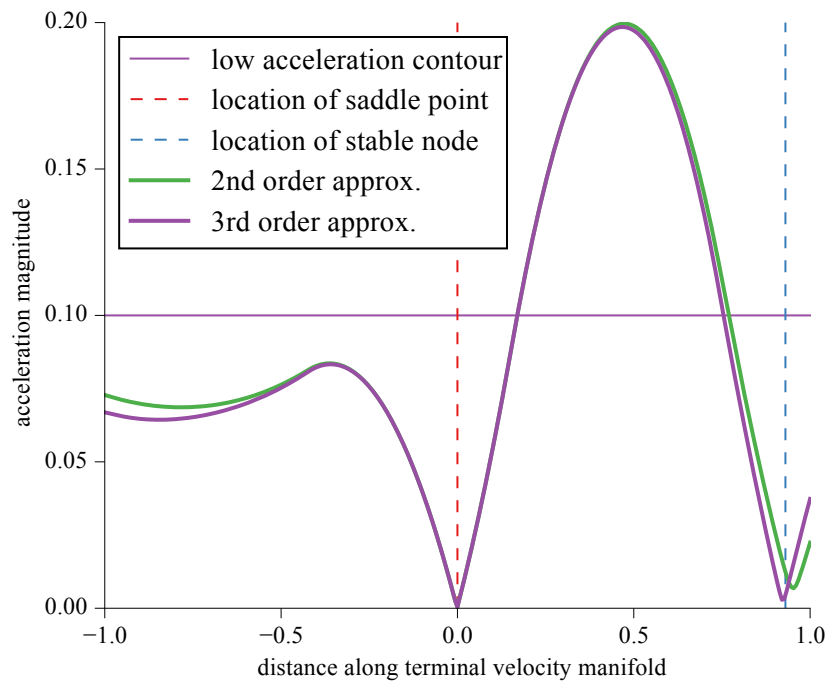


Figure A.3: Acceleration along the terminal velocity manifold for the airfoil snake at a pitch angle of  $\theta = 5^\circ$

## References

- [26] J. W. Bahlman, S. M. Swartz, D. K. Riskin, and K. S. Breuer. Glide performance and aerodynamics of non-equilibrium glides in northern flying squirrels (*Glaucomys sabrinus*). *J. R. Soc. Interface* 10.20120794 (2013). DOI: 10.1098/rsif.2012.0794.
- [36] K. L. Bishop. The relationship between 3-D kinematics and gliding performance in the southern flying squirrel, *Glaucomys volans*. *J. Exp. Biol.* 209 (2006), p. 689–701. DOI: 10.1242/jeb.02062.
- [48] S. H. Strogatz. *Nonlinear Dynamics and Chaos: With Applications to Physics, Biology, Chemistry, and Engineering*. Perseus Books Publishing, LLC, 2001.
- [94] H. Benaroya, S. M. Han, and M. Nagurka. *Probability Models in Engineering and Science*. Vol. 193. CRC Press, 2005.
- [95] A. Papanicolaou. Taylor approximation and the delta method. 2009.
- [96] B. F. Mettler. Extracting micro air vehicles aerodynamic forces and coefficients in free flight using visual motion tracking techniques. *Exp. Fluids* 49 (2010), p. 557–569. DOI: 10.1007/s00348-009-0803-6.
- [97] D. V. Uhlig and M. S. Selig. Determining aerodynamic characteristics of a micro air vehicle using motion tracking. *J. Aircr.* 50 (2013), p. 1481–1490. DOI: 10.2514/1.C031996.
- [98] S. Wiggins. *Introduction to Applied Nonlinear Dynamical Systems and Chaos*. Vol. 2. Springer Science & Business Media, 2003.
- [99] J. Marsden and M. McCracken. *The Hopf Bifurcation and Its Applications*. New York, Heidelberg, Berlin: Springer-Verlag, 1976.
- [100] G. Gómez, W. S. Koon, M. W. Lo, J. E. Marsden, J. Masdemont, and S. D. Ross. Connecting orbits and invariant manifolds in the spatial three-body problem. *Nonlinearity* 17 (2004), p. 1571–1606.
- [101] M. Brøns. An iterative method for the canard explosion in general planar systems. *Discrete and Continuous Dynamical Systems Supplement 2013* (2013), p. 77–83.
- [102] M. Brøns and K. Uldall Kristiansen. On the approximation of the canard explosion point in epsilon-free systems. *ArXiv e-prints* (2015). arXiv: 1504.07752 [math.DS].

# Appendix B

## *Supporting Information* – Undulation enhances stability, enabling gliding in flying snakes

### B.1 Flying snake glide experiments

Glides from the paradise tree snake, *Chrysopelea paradisi* (7 individuals, mass: 37.3–107.2 g, length: 63–88 cm) were recorded in a large indoor arena in the Moss Arts Center at Virginia Tech. Trials were conducted in “The Cube,” a four story black box theater prepared to meet Virginia Tech Animal Care and Use Protocol Committee requirements. The facility is 9.1 m high, 12.5 m wide, and 14.9 m long. To prevent the snakes from landing on three circumferential walkways, black plastic sheeting was hung along the sides and back wall and curtains pulled over the walkway railing. To prevent snake injury, the floor was covered with sheets of 5 cm soft foam padding. An artificial tree covered with fake leaves and vines was placed in the center of the glide arena to encourage jumps and a consistent landing location. A scissor lift, with an oak launch branch, was used to raise the snakes to a height of 8.3 m for jumps and glides. The scissor lift was draped with black cloth to prevent the snakes from contacting the lift mechanism.

A 23 camera Qualisys Oqus 500 motion capture system, recording at 179 frames/s, was used to record infrared markers placed along the snake’s dorsal surface. Three cameras were

placed along the top of the glide arena to record the initial portion of the glide trajectory. The other 20 cameras were placed along the walkway railings. The motion capture system was calibrated at the start of each testing day. Calibrations were done by removing one foam sheet and placing an inertial coordinate system marker on the floor. Next, a calibration wand was used to paint the measurement volume that approximated the glide path of the snakes. This procedure started at the top of scissor lift, and moved downward to the arena floor.

Two high-speed cameras (Photron APX-RS, 500 frames/s) were placed on the ceiling of the glide arena. One camera was positioned directly above the launch branch and the other halfway between the launch branch and the landing tree. A Sony 4K camera was placed orthogonal to the launch branch to record the jump, and a Fastec TS3 was placed 2 m above the ground to record late-phase gliding and landing.

Glide trials were conducted over nine consecutive days in May 2015. Snakes were transported from their animal care facility to the Cube in reptile bags placed in a heated cooler. Snakes were then transferred to an incubator heated to 33 °C. The temperature of the glide arena was set to 26 °C to 28 °C. Between 11 and 17 infrared reflective tape markers ( $\rho_{\text{tape}} = 0.02 \text{ g/cm}^2$ , approximately  $1 \times 1 \text{ cm}^2$ ) were placed along the dorsal surface. A marker was placed at the top of the head, the vent, and tip of the tail. Depending on the size and length of the animal, two or three markers were placed along the tail, and the remaining markers distributed along the body. To ensure the tape did not affect the snake's flattening, the skin was stretched ventrally and tape placed over the ribs, but not contacting the keel. Missing tape markers were replaced at the start of each day of testing.

Snakes were transported in reptile bags from the incubator to the scissor lift and brought to a height of approximately 8.3 m. The height from the tip of the launch branch to the foam floor was measured with a Bosch laser range finder ( $\pm 1.6 \text{ mm}$ ). The cameras and motion capture system were then set to record, and the snake removed from the reptile bag and placed on the launch branch. All glides originated with a volitional jump from the launch branch. Gentle prodding was used if the animal did not immediately jump. Once the animal jumped and glided to the ground, an assistant would capture the animal, re-bag it, and place it back into the incubator. The camera and motion capture systems were then manually triggered and the data transferred to a computer. Snakes were allowed to rest between glides.

At the end of each day of recording, an overhead image was taken of each snake next to a calibration target. The snake's backbone in these images was digitized by hand and used to

measure the length between markers.

## B.2 3D data processing

A total of 131 glides were recorded, and for each trial, the raw landmark points were labeled and exported using Qualisys Track Manager. Based on data quality (number of missing markers, length of time markers were missing), 36 *C. paradisi* trials from seven animals were selected for further processing. For each trial, time series were truncated to start and end times when no markers were missing. Gaps of recorded marker locations were filled separately for each marker using an unscented Kalman filter (UKF) with Rauch-Tung-Striebal smoothing [103, 104]. The filter provides smoothed estimates of the  $[x, y, z]$  positions of the marker, while also incorporating estimates of the velocities and accelerations. Only the gap regions are filled in the resulting time series.

To remove noise from the marker position time series, a forward-backward second-order Butterworth filter was applied. The optimal filter cutoff frequencies were found separately for each marker's  $[x, y, z]$  times series. This approach gives equal weight to both signal distortion and noise passed through the filter [89]. The technique involves fitting linear regressions of the  $L^2$ -norm residual error w.r.t. frequency at high cutoff frequencies until the R-squared of the linear fit drops below 0.95. The y-intercept of the linear regression defines the noise floor; the frequency at which a horizontal line from the y-intercept intersects the residual curve defines the optimal cutoff frequency.

Splines were used to reconstruct the snake's backbone position, given as  $\mathbf{r}(s, t) = [x(s, t), y(s, t), z(s, t)]$ . At each time step, a global natural cubic spline was fit to the filtered positions [105]. The spline is evaluated with the measured arc length coordinate,  $s$ . Overhead movies of gliding indicate the snake has a neck region directly behind the head that does not bend. We model this region by constraining the spline with a virtual marker placed directly behind the head and halfway between the head and second marker on the body. The direction behind the head was determined from the inertial velocity of the head marker, as the neck region and head move together as the snake undulates.

We quantified the spatio-temporal characteristics of aerial undulation using complex orthogonal decomposition (COD) [76, 77] separately on the horizontal and vertical waves, with the linear fit to the vertical wave removed. COD decomposes oscillatory motion into time-varying

modal shapes. The modes are ranked by the amount of explained variance, with only a few modes needed to describe the wave. The spatial mode encodes the spatial frequency and the modal activity encodes the undulation frequency. The spatial mode and modal activity are both complex functions with real and imaginary components. The spatial and temporal frequencies are calculated as the number of revolutions the modes make in the complex plane.

### B.2.1 Complex orthogonal decomposition

Here we provide details of complex orthogonal decomposition and how it was used to quantify the horizontal and vertical waves. For a full discussion, see [76, 77, 106]. We begin with the horizontal and vertical bending angle data in 2D form,

$$\Theta = \begin{bmatrix} \bar{\theta}_1 & \bar{\theta}_2 & \dots & \bar{\theta}_n \\ | & | & & | \\ | & | & & | \\ | & | & & | \\ | & | & & | \end{bmatrix} \quad (\text{B.2.1})$$

$$\Psi = \begin{bmatrix} \bar{\psi}_1 & \bar{\psi}_2 & \dots & \bar{\psi}_n \\ | & | & & | \\ | & | & & | \\ | & | & & | \\ | & | & & | \end{bmatrix} \quad (\text{B.2.2})$$

where each column of  $\Theta$  and  $\Psi$  are the horizontal and vertical waves sampled at times  $t_1, \dots, t_n$ , and each row is the spline location from  $s_1, \dots, s_m$ . At each time point, the horizontal wave has the mean removed, and the vertical wave has the mean and a linear fit removed. Each matrix is of size  $m \times n$ .

The decomposition method requires converting the measured signals  $\Theta$  and  $\Psi$  into complex analytic signals using the Hilbert transform. This transform is performed along the rows of the measured bending angles, i.e., how the angle at a particular location along the body varies in time. Denoting the Hilbert transform as  $\mathcal{H}$  and the complex analytic signal as  $\mathbf{z}$ , we have

$$\mathbf{z}_\theta(s_i, t) = \mathcal{H}(\bar{\theta}(s_i, t)) \quad (\text{B.2.3})$$

$$\mathbf{z}_\psi(s_i, t) = \mathcal{H}(\bar{\psi}(s_i, t)) \quad (\text{B.2.4})$$

where  $1 \leq i \leq m$ , where  $m$  is the number of points the spline is evaluated at. We then form

the complex ensemble matrix  $\mathbf{Z}$  as

$$\mathbf{Z} = \begin{bmatrix} | & | & & | \\ \mathbf{z}_1 & \mathbf{z}_2 & \dots & \mathbf{z}_n \\ | & | & & | \end{bmatrix} \quad (\text{B.2.5})$$

The  $i$ th row of  $\mathbf{Z}$  is the time series of the bending angle at the  $i$ th location along the body. The complex ensemble matrix is of size  $m \times n$ . We then form the complex correlation matrix,

$$\mathbf{R} = \frac{\mathbf{Z}\bar{\mathbf{Z}}^T}{n} \quad (\text{B.2.6})$$

where the overbar indicates complex conjugation and  $\mathbf{R}$  is of size  $m \times m$ . Complex orthogonal decomposition requires solving the eigenvalue problem

$$\mathbf{R}\mathbf{W} = \lambda\mathbf{W} \quad (\text{B.2.7})$$

where the columns of  $\mathbf{W}$  (size  $m \times m$ ) are the eigenvectors called the complex orthogonal modes and the  $m$  eigenvalues  $\lambda$  are called the complex orthogonal values. We sort the eigenvalues based on their magnitude and then rearrange the columns of  $\mathbf{W}$  accordingly. The motion associated with each complex orthogonal mode is found using the complex modal coordinate ensemble  $\mathbf{Q}$ . The complete analytical signal can be recovered as

$$\mathbf{Z} = \mathbf{Q}\mathbf{W} \quad (\text{B.2.8})$$

where the columns of  $\mathbf{W}$  are the modal vectors and the rows of  $\mathbf{Q}$  (size  $m \times n$ , same as  $\mathbf{Z}$ ) are samples of the modal coordinates. Solving for  $\mathbf{Q}$ ,

$$\mathbf{Q} = \mathbf{W}^{-1}\mathbf{Z} = \bar{\mathbf{W}}^T\mathbf{Z} \quad (\text{B.2.9})$$

## B.2.2 Quantifying aerial undulation

The complex orthogonal modes (columns of  $\mathbf{W}$ ) encompass the spatial characteristics of the bending waves, and the complex modal coordinate ensemble (rows of  $\mathbf{Q}$ ) encompass the temporal wave characteristics. Both matrices are complex. The units of  $\mathbf{Q}$  are time;  $\mathbf{W}$  is unitless and must be scaled by  $\sqrt{\lambda}$  to have units of degrees. We use the mean whirl rate —

how each mode moves in the complex plane (figure B.4A,B) — to quantify the horizontal and vertical waves. For the analysis presented in the paper, we use the first (dominate) mode for each wave. To quantify the whirl rate, we “unwrap” each mode by calculating the angle of each mode in the complex plane,

$$\angle W = \tan^{-1} \frac{\text{Im}(W)}{\text{Re}(W)} \quad (\text{B.2.10})$$

$$\angle Q = \tan^{-1} \frac{\text{Im}(Q)}{\text{Re}(Q)} \quad (\text{B.2.11})$$

which we unwrap such that there are no  $2\pi$  discontinuities. The slope of  $\angle W$  w.r.t.  $s$  is the number of spatial periods  $\nu$ , and the slope of  $\angle Q$  w.r.t.  $t$  is the undulation frequency  $f$  (figure B.4C,D). The number of spatial periods,  $\nu$ , is found by the slope of a linear fit to the unwrapped mode  $\mathbf{w}$  against the non-dimensional arc length  $s/SVL$  as

$$\nu_\theta = \frac{m_{\mathbf{w},\theta}}{2\pi} \quad (\text{B.2.12})$$

$$\nu_\psi = \frac{m_{\mathbf{w},\psi}}{2\pi} \quad (\text{B.2.13})$$

The undulation frequency is found from the slope of the best-fit line to the unwrapped  $\mathbf{q}$  against time as

$$f_\theta = \frac{m_{\mathbf{q},\theta}}{2\pi} \quad (\text{B.2.14})$$

$$f_\psi = \frac{m_{\mathbf{q},\psi}}{2\pi} \quad (\text{B.2.15})$$

$$(\text{B.2.16})$$

where  $m$  is the slope. The spatial and temporal frequency ratios are therefore  $\nu_\psi/\nu_\theta$  and  $f_\psi/f_\theta$ , respectively (figure 3.2E).

The horizontal and vertical wave amplitudes (figure 3.2F,G) are found by reanimating the horizontal and vertical waves using enough modes to recover 95% of the observed variance (figure B.1). This procedure removes noise present in the higher modes and the full waveforms. Each mode is reanimated separately and then combined together to form the filtered signal. For each mode  $k$

$$\mathbf{z}_k(t) = \sqrt{\lambda_k} e^{2\pi f_k t i} \mathbf{w}_k \quad (\text{B.2.17})$$

for  $t_1 \leq t \leq t_n$ . Each frequency component is found as described above, and the modal

shapes  $\mathbf{w}$  are from columns of  $\mathbf{W}$ . Between two and four modes are combined to form the complex filtered signal, and the resulting real signal is recovered as  $Re(\mathbf{z}_k(t))$ . The amplitude is found as half of the average peak-to-peak value.

### B.3 Snake morphometrics

We used measured width and mass distributions of *C. paradisi* to make the model more anatomically accurate (figure B.5). We measured the width distribution of flying snakes from mid-glide silhouette images. From underside views of each snake, the images were thresholded to separate the snake from the background. The Euclidean distance transform (EDT) was used to quantify the distance of each pixel within the thresholded snake body to the edge; the midline of the snake has the largest EDT value. The midline was found by skeletonizing the thresholded image such that the image was a continuous line one pixel wide; the EDT was then sampled along the skeleton. Pixel distances were scaled to physical units using the arc length of the snake, found by integrating distance along the skeleton. Width distributions were measured from six images from three different animals and averaged together for one width distribution. A bias correct was applied to the width distribution as the maximum width from the above procedure was 3% lower than the maximum width previously reported.

We measured the linear mass density of flying snakes by sectioning three frozen snakes. The snakes were cut into approximately 10 mm sections and each piece was weighed with a Mettler Toledo scale with an accuracy of  $\pm 0.1$  mg. The mass distribution for each animal was normalized by the average density,  $\bar{\rho} = m_{\text{total}}/\text{SVL}$ , and then averaged. The width and mass density distributions were fit with second-order polynomials for use in the simulation. The mass density was fit with two parabolas because the head was comparatively more massive than the body.

### B.4 Theoretical model of snake flight

To test the effect of horizontal and vertical waves of bending on limbless flight dynamics, we formulate a theoretical model of snake gliding. This anatomically accurate model complements previous reduced-order models of snake gliding [17, 91] and more recent kinematic chain models [72]. The model consists of three components: the kinematic equations

of motion, the equations of motion, and the aerodynamic force model. We define the body kinematics in a local “co-moving” frame that is centered at the center of mass. We define how the body moves in this frame using the aerial serpenoid equations presented in the main text. The co-moving frame then translates and rotates under the translational and rotational equations of motion subject to gravity, aerodynamic forces, and inertial forces due to the prescribed undulation.

### B.4.1 Kinematic model — Aerial serpenoid curve

We model the instantaneous body posture relative to a center of mass frame with the aerial serpenoid curve, a compound space curve with traveling waves of horizontal and vertical bending. We modify the standard serpenoid curve used for modeling snake-like locomotion [63, 80] to better approximate flat-top vertical wave. The horizontal and vertical bending waves are

$$\bar{\theta}(s, t) = \theta_m \sin \left[ \frac{\pi}{2} \cos \left( \frac{2\pi\nu_\theta}{L} s - 2\pi f_\theta t + \phi_\theta \right) \right] \quad (\text{B.4.1})$$

$$\bar{\psi}(s, t) = \psi_m \cos \left( \frac{2\pi\nu_\psi}{L} s - 2\pi f_\psi t + \phi_\psi \right) + \frac{d_\psi}{L} s \quad (\text{B.4.2})$$

where  $s$  is the arc-length coordinate in meters,  $t$  is time,  $\theta_m$  and  $\psi_m$  are the maximum lateral and vertical bending angles,  $\nu$  is the number of spatial waves,  $f$  is the undulation frequency,  $\phi$  is a phase shift, and  $d$  is the dorsoventral bending angle. The lateral and vertical waves are coupled, reducing the kinematics model to five variables to define the body shape:  $\theta_m$ ,  $\psi_m$ ,  $\nu_\theta$ ,  $f_\theta$ , and  $d_\psi$ , with  $\nu_\psi = 2\nu_\theta$ ,  $f_\psi = 2f_\theta$ , and  $\phi_\psi = 2(\phi_\theta - \pi/2)$ . The horizontal wave phase shift,  $\phi_\theta$ , is used to minimize the initial inertial moments on the body (discussed below), but is not a shape parameter.

The position of the body in the co-moving frame satisfies  $\partial_s x = \cos \bar{\psi} \sin \bar{\theta}$ ,  $\partial_s y = -\cos \bar{\psi} \cos \bar{\theta}$ ,  $\partial_s z = \sin \bar{\psi}$ . When the horizontal and vertical waves are prescribed, the instantaneous body

position in the co-moving frame is found by integration,

$$\begin{aligned}
 \mathbf{x}(s, t) &= \int_0^s \cos \bar{\psi} \sin \bar{\theta} ds' \\
 \mathbf{y}(s, t) &= \int_0^s -\cos \bar{\psi} \cos \bar{\theta} ds' \\
 \mathbf{z}(s, t) &= \int_0^s \sin \bar{\psi} ds' \\
 \mathbf{r}(s, t) &= [\mathbf{x}(s, t), \mathbf{y}(s, t), \mathbf{z}(s, t)]
 \end{aligned}
 \tag{B.4.3}$$

where  $\mathbf{r}$  is the position of an infinitesimal element of the snake, and the sign convention is such that the head points in the positive  $+y$ -direction, the right flank is in the  $+x$ -direction, and the dorsal surface is in the  $+z$ -direction. The velocity,  $[\dot{\mathbf{r}}]$ , and acceleration,  $[\ddot{\mathbf{r}}]$ , of the body are found from fourth-order accurate finite-differences as the position is not defined analytically.

The anterior body kinematics are modified to meet the physiological observation of proprioceptive head control and orientation. We modify the first 7.5% of the lateral and vertical waves such that they are linear functions, which results in the head and neck of the snake oriented in the forward direction (the head points in the  $+y$ -direction [107]). We match the angles at the end of the neck region for both the horizontal and vertical wave,

$$c_{\theta, \text{neck}} = \frac{\theta(s_{\text{neck}}, t)}{s_{\text{neck}}} \tag{B.4.4}$$

$$c_{\psi, \text{neck}} = \frac{\psi(s_{\text{neck}}, t)}{s_{\text{neck}}} \tag{B.4.5}$$

and the horizontal and vertical waves in the neck region become

$$\theta(0 \leq s \leq s_{\text{neck}}) = c_{\theta, \text{neck}} \cdot s \tag{B.4.6}$$

$$\psi(0 \leq s \leq s_{\text{neck}}) = c_{\psi, \text{neck}} \cdot s \tag{B.4.7}$$

## B.4.2 Airfoil coordinate system

Lastly, we model the flattened airfoil orientation using the ‘‘airfoil coordinate system’’ which defines how the local airflow interacts with the body. The airfoil coordinate system is defined

by the local tangent direction

$$\hat{\mathbf{t}}(s, t) = \frac{\partial_s \mathbf{r}(s, t)}{\|\partial_s \mathbf{r}(s, t)\|}, \quad (\text{B.4.8})$$

and the co-moving frame vertical  $\hat{\mathbf{z}} = [0, 0, 1]$  direction. We take the width as the chord-line direction and constrain it to reside in the co-moving frame horizontal plane. The chord-line direction,  $\hat{\mathbf{c}}$ , is defined as

$$\hat{\mathbf{c}} = \frac{\hat{\mathbf{z}} \times \hat{\mathbf{t}}}{\|\hat{\mathbf{z}} \times \hat{\mathbf{t}}\|} \quad (\text{B.4.9})$$

and the back-bone direction is defined as

$$\hat{\mathbf{b}} = \hat{\mathbf{t}} \times \hat{\mathbf{c}} \quad (\text{B.4.10})$$

### B.4.3 Dynamic model — Variable-geometry rigid-body formulation

The translational and rotational equations of motion are found using the Newton-Euler method,

$$\int_0^L (\vec{f}_L + \vec{f}_D) ds - m\vec{g} = m\ddot{\vec{R}}_o \quad (\text{B.4.11})$$

$$\vec{M}_A = \mathbf{I}_o \cdot \dot{\vec{\omega}} + \vec{\omega} \times (\mathbf{I}_o \cdot \vec{\omega}) + [\dot{\mathbf{I}}_o] \cdot \vec{\omega} + \vec{\omega} \times \vec{h}_o + [\dot{\vec{h}}_o] \quad (\text{B.4.12})$$

where each term is time-varying, overdots denote inertial time derivatives, brackets denote co-moving frame time derivatives expressed in the inertial frame,  $m$  is the total snake mass,  $\vec{g}$  is gravitational acceleration, and  $\mathbf{I}_o$  is the nine-component inertia dyadic. The angular velocity  $\vec{\omega}$  and center of mass velocity and position,  $\vec{R}_o$  and  $\vec{R}_o$ , are solved for numerically using a standard Dormand-Prince method. The aerodynamic moments are

$$\vec{M}_A = \int_0^L \vec{r} \times (\vec{f}_L + \vec{f}_D) ds \quad (\text{B.4.13})$$

where  $\vec{f}_L$  and  $\vec{f}_D$  are the lift and drag force densities per length; the total lift and drag forces,  $\vec{F}_L$  and  $\vec{F}_D$ , are found by integrating the densities along the body. The angular momentum is

$$[\vec{h}_o] = \int_0^L \mathbf{r} \times \dot{\mathbf{r}} \rho(s) ds \quad (\text{B.4.14})$$

and the angular momentum rate is

$$[\dot{\vec{h}}_o] = \int_0^L \mathbf{r} \times \ddot{\mathbf{r}}\rho(s)ds \quad (\text{B.4.15})$$

where  $\rho(s)$  is the linear mass density

#### B.4.4 Orientation of the body

We specify the orientation of the co-moving frame using Euler angles and the time evolution of these angles with the kinematic differential equations. Traditional aircraft Euler angles (3-2-1 Euler angles) use three successive rotations about the yaw, pitch, and roll axes, with the yaw axis ( $z$ -axis) pointing downward, the pitch axis ( $y$ -axis) to the right, and the roll axis ( $x$ -axis) through the front of the aircraft. Because we have modified the co-moving frame such that the  $z$ -axis is vertical, the  $y$ -axis is the forward direction, and the  $x$ -axis is to the right, we use the same notation, but modify the rotation order to keep the same convention of positive pitch resulting in a nose-up rotation and a positive roll resulting in rotation to the right. We therefore use 2-1-3 Euler angles as defined in [108] to construct a rotation matrix that rotates vectors in the inertial frame into the body frame,

$$\hat{\mathbf{b}} = \mathbf{C}\hat{\mathbf{n}} \quad \hat{\mathbf{n}} = \mathbf{C}^T\hat{\mathbf{b}} \quad (\text{B.4.16})$$

where  $\hat{\mathbf{b}}$  signifies quantities in the co-moving (body) frame,  $\hat{\mathbf{n}}$  signified quantities in the inertial frame, and  $(\cdot)^T$  is the matrix transpose. The rotation matrix is found by successive premultiplications of rotations about each axis,

$$\mathbf{C} = \mathbf{C}_2(\phi)\mathbf{C}_1(\theta)\mathbf{C}_3(\psi) \quad (\text{B.4.17})$$

where a rotation about the pitch axis ( $x$ -axis) is

$$\mathbf{C}_1(\theta) = \begin{bmatrix} 1 & 0 & 0 \\ 0 & \cos \theta & \sin \theta \\ 0 & -\sin \theta & \cos \theta \end{bmatrix} \quad (\text{B.4.18})$$

a rotation about the roll axis ( $y$ -axis) is

$$\mathbf{C}_2(\phi) = \begin{bmatrix} \cos \phi & 0 & -\sin \phi \\ 0 & 1 & 0 \\ \sin \phi & 0 & \cos \phi \end{bmatrix} \quad (\text{B.4.19})$$

and a rotation about the yaw axis ( $z$ -axis) is

$$\mathbf{C}_3(\psi) = \begin{bmatrix} \cos \psi & \sin \psi & 0 \\ -\sin \psi & \cos \psi & 0 \\ 0 & 0 & 1 \end{bmatrix} \quad (\text{B.4.20})$$

Singularities occur with any Euler angle convention. For our convention, we limit angles to

$$0 \leq \psi < 2\pi, \quad \frac{\pi}{2} \leq \theta \leq \frac{\pi}{2}, \quad 0 \leq \phi < 2\pi$$

Therefore, the snake pointing vertically upwards or downwards results in a singularity. However, this condition is never reached in the simulations, as we stop the simulation when any of the angles exceed  $85^\circ$ .

The kinematic differential equations complete the rotational equations of motion and are found by relating the change in co-moving frame orientation (Euler angle rates) to the angular velocity as

$$\dot{\vec{\theta}} = \mathbf{K}^B \vec{\omega} = \mathbf{K} \mathbf{C} \vec{\omega} \quad (\text{B.4.21})$$

where  ${}^B \vec{\omega}$  is the angular velocity expressed in the co-moving frame. Written in detail we have

$$\begin{bmatrix} \dot{\psi} \\ \dot{\theta} \\ \dot{\phi} \end{bmatrix} = \begin{bmatrix} -\sin \phi / \cos \theta & 0 & \cos \phi / \cos \theta \\ \cos \phi & 1 & \sin \phi \\ \sin \phi \tan \theta & \tan \theta & -\cos \phi \tan \theta \end{bmatrix} \begin{bmatrix} \omega_x \\ \omega_y \\ \omega_z \end{bmatrix}^B \quad (\text{B.4.22})$$

For completeness, the Euler angle accelerations are found by taking the inertial derivative of the kinematic differential equations and applying the product rule,

$$\ddot{\vec{\theta}} = \dot{\mathbf{K}} \mathbf{C} \vec{\omega} + \mathbf{K} \dot{\mathbf{C}} \vec{\omega} + \mathbf{K} \mathbf{C} \dot{\vec{\omega}} \quad (\text{B.4.23})$$

The derivative of the rotation matrix is derived from the complete set of Poisson equa-

tions [109]

$$\dot{\mathbf{C}} = -{}^B\tilde{\omega}\mathbf{C} \quad (\text{B.4.24})$$

where  ${}^B\tilde{\omega}$  is the cross product matrix of the angular velocity expressed in the co-moving frame coordinate system given as

$$\tilde{\omega} = \begin{bmatrix} 0 & -\omega_z & \omega_y \\ \omega_z & 0 & -\omega_x \\ -\omega_y & \omega_x & 0 \end{bmatrix} \quad (\text{B.4.25})$$

The angular acceleration  $\dot{\vec{\omega}}$  is an output of the dynamics simulation and is therefore readily available. The derivative of the kinematic differential equations is

$$\dot{\mathbf{K}} = \frac{1}{c_\theta} \begin{bmatrix} -\dot{\theta}s_\phi t_\theta - \dot{\phi}c_\phi & 0 & \dot{\theta}c_\phi t_\theta - \dot{\phi}s_\phi \\ -\dot{\phi}s_\phi c_\theta & 0 & \dot{\phi}c_\phi c_\theta \\ \dot{\phi}c_\phi s_\theta + \dot{\theta}s_\phi/c_\theta & \dot{\phi}/c_\theta & \dot{\phi}s_\phi s_\theta - \dot{\theta}c_\phi/c_\theta \end{bmatrix} \quad (\text{B.4.26})$$

where  $s_{(\cdot)}$ ,  $c_{(\cdot)}$ , and  $t_{(\cdot)}$  are the sine, cosine, and tangent of the respective angle. Combining the above expressions, the final form of the Euler angle accelerations is

$$\ddot{\vec{\theta}} = \dot{\mathbf{K}}\mathbf{C}\vec{\omega} - \mathbf{K}{}^B\tilde{\omega}\mathbf{C}\vec{\omega} + \mathbf{K}\mathbf{C}\dot{\vec{\omega}} \quad (\text{B.4.27})$$

For time simulation initial conditions (discussed below), we rearrange (B.4.21) to solve for the angular velocity. The resulting expression is

$${}^B\vec{\omega} = \mathbf{K}^{-1}\dot{\vec{\theta}} \quad (\text{B.4.28})$$

where the inverse of the kinematic differential equations is

$$\mathbf{K}^{-1} = \begin{bmatrix} -\cos\theta \sin\phi & \cos\phi & 0 \\ \sin\theta & 0 & 1 \\ \cos\theta \cos\phi & \sin\phi & 0 \end{bmatrix} \quad (\text{B.4.29})$$

Lastly, the yaw, pitch, and roll angles can be extracted from the components of the rotation

matrix  $\mathbf{C}$  as

$$\begin{bmatrix} \psi \\ \theta \\ \phi \end{bmatrix} = \begin{bmatrix} \text{atan2}(-c_{21}, c_{22}) \\ \text{asin}(c_{23}) \\ \text{atan2}(-c_{13}, c_{33}) \end{bmatrix} \quad (\text{B.4.30})$$

where  $c_{ij}$  are components of  $\mathbf{C}$ .

### B.4.5 Aerodynamic lift and drag

The lift and drag forces are the result of local fluid velocity, location along the body, and body orientation

$$\begin{aligned} \vec{f}_L &= \frac{\rho U_\perp^2}{2} \cdot c(s) \cdot C_L(\alpha, Re) \cdot \hat{\mathbf{L}} \\ \vec{f}_D &= \frac{\rho U_\perp^2}{2} \cdot c(s) \cdot C_D(\alpha, Re) \cdot \hat{\mathbf{D}} \end{aligned} \quad (\text{B.4.31})$$

which depends explicitly on the width length  $c(s)$  of the animal (figure B.5A). The lift and drag coefficients are angle-of-attack and Reynolds number dependent and taken from previous studies of flying snake aerodynamics [14, 15] (figure B.6).

We use simple sweep theory to account for the non-perpendicular airflow interacting with the body. The aerodynamic force coefficients were measured for a section of the snake's body perpendicular to the flow. However, the modeled snake has sections that are not perpendicular to the flow. To model these forces, we only use the component of the velocity that is perpendicular to the body, i.e., the velocity component that resides in the  $\hat{\mathbf{c}}\text{-}\hat{\mathbf{b}}$  frame. We calculate the angle of attack and Reynolds number as

$$\alpha = \cos^{-1} \left( \frac{\dot{\mathbf{R}}_{CB} \cdot \hat{\mathbf{c}}}{U_\perp} \right) \quad Re(s, t) = \frac{\|\dot{\mathbf{R}}\|c(s)}{\nu} \quad (\text{B.4.32})$$

where  $\dot{\mathbf{R}}_{CB}$  is the component of the inertial velocity  $\dot{\mathbf{R}} = \ddot{\mathbf{R}}_o + \vec{\omega} \times \mathbf{r} + [\dot{\mathbf{r}}]$  of a body element in the  $\hat{\mathbf{c}}\text{-}\hat{\mathbf{b}}$  plane, where  $\hat{\mathbf{c}}$  is the chord-line unit vector expressed in the inertial frame. The normal velocity is then  $U_\perp = \|\dot{\mathbf{R}}_{CB}\|$ .

The lift and drag unit vectors,  $\hat{\mathbf{L}}$  and  $\hat{\mathbf{D}}$ , are calculated such that the drag force acts along

the perpendicular velocity and lift acts normal to the perpendicular velocity. That is,

$$\hat{\mathbf{D}} = -\dot{\mathbf{R}}_{BC}/U_{\perp} \quad \hat{\mathbf{L}} = \hat{\mathbf{t}} \times \hat{\mathbf{D}} \quad (\text{B.4.33})$$

Using the above expression, the orientation of the drag vector will always point in the correct direction, but the lift vector can be flipped by  $180^\circ$  about  $\hat{\mathbf{D}}$ . We account for this by checking which quadrant around the cross-section the velocity vector is located in, and then modifying the sign of the angle of attack and orientation of the unit lift vector as (figure B.7)

$$\alpha, \hat{\mathbf{L}} = \begin{cases} \alpha, \hat{\mathbf{L}} & \text{if } \alpha_c < 90^\circ \text{ and } \alpha_b \geq 90^\circ \\ -\alpha_c, \hat{\mathbf{L}} & \text{if } \alpha_c < 90^\circ \text{ and } \alpha_c < 90^\circ \\ \alpha_c - 180^\circ, -\hat{\mathbf{L}} & \text{if } \alpha_c \geq 90^\circ \text{ and } \alpha_b < 90^\circ \\ 180^\circ - \alpha_c, -\hat{\mathbf{L}} & \text{if } \alpha_c \geq 90^\circ \text{ and } \alpha_b \geq 90^\circ \end{cases} \quad (\text{B.4.34})$$

where  $\alpha_c$  and  $\alpha_b$  are the angles between the perpendicular velocity  $\dot{\mathbf{R}}_{CB}$  and the  $\hat{\mathbf{c}}$  and  $\hat{\mathbf{b}}$  directions, respectively.

### B.4.6 Extending the lift and drag coefficients

The experimentally available lift and drag coefficients were measured over an angle-of-attack range of  $-10^\circ$  to  $60^\circ$ , while the simulation needs values up to  $90^\circ$ . We extrapolated the measured lift and drag coefficients over this  $30^\circ$  range by first modeling the drag coefficient in the extrapolated region as a parabola with the vertex at  $90^\circ$ .

$$C_D(\alpha) = a_D \alpha^2 + b_D \alpha + c \quad (\text{B.4.35})$$

with the constraints

$$C_D(\alpha = 90^\circ) = C_{D,90^\circ} \text{ from theory/experiments} \quad (\text{B.4.36})$$

$$C_D(\alpha = 60^\circ) = C_{D,60^\circ} \text{ from experiments} \quad (\text{B.4.37})$$

The first (vertex) constraint can be written as

$$\frac{-b_D}{2a_D} = 90 \quad (\text{B.4.38})$$

$$c_D - \frac{b_D^2}{4a_D} = C_{D,90^\circ} \quad (\text{B.4.39})$$

which implies

$$b_D = -180a_D \quad c_D = C_{D,90^\circ} + \frac{b_D^2}{4a_D} \quad (\text{B.4.40})$$

The second constraint implies

$$a_D \cdot 60^2 + b_D \cdot 60 + c_D = C_{D,60^\circ}, \quad (\text{B.4.41})$$

which rearranging for  $a_D$  yields

$$a_D = \frac{C_{D,60^\circ} - C_{D,90^\circ}}{60^2 - 180 \cdot 60 + 180^2/4} \quad (\text{B.4.42})$$

To close the equations,  $C_{D,90^\circ}$  is estimated to be between 2–2.1 [90, Chapter 3, figure 33], with the particular value specified by the Reynolds number (evenly selected between 2 and 2.1 for the seven Reynolds numbers measured in experiments).

The lift coefficient is approximated with a third-order polynomial

$$C_L(\alpha) = a_L\alpha^3 + b_L\alpha^2 + c_L\alpha + d_L \quad (\text{B.4.43})$$

with the constraints

$$C_L(\alpha = 90^\circ) = 0 \quad (\text{B.4.44})$$

$$C_L(\alpha = 60^\circ) = C_{D,60^\circ} \text{ from experiments} \quad (\text{B.4.45})$$

$$\frac{\partial C_L}{\partial \alpha}(\alpha = 60^\circ) = \frac{\partial C_{L,60^\circ}}{\partial \alpha} \text{ from experiments} \quad (\text{B.4.46})$$

where the lift coefficient derivative is determined by second-order accurate finite differences,

$$\frac{\partial C_{L,60^\circ}}{\partial \alpha} = \frac{3}{2}C_{L,60^\circ} - 2C_{L,55^\circ} + \frac{1}{2}C_{L,50^\circ} \quad (\text{B.4.47})$$

We have an underdetermined system, as we need to determine four parameters for the

polynomial, but have only three constraint equations. We solve this in matrix form using a least-squares solution to the system

$$\begin{bmatrix} 0 \\ C_{D,60^\circ} \\ \frac{\partial C_{L,60^\circ}}{\partial \alpha} \end{bmatrix} = \begin{bmatrix} 90^3 & 90^2 & 90 & 1 \\ 60^3 & 60^2 & 60 & 1 \\ 3 \cdot 60^2 & 2 \cdot 60 & 0 & 0 \end{bmatrix} \begin{bmatrix} a_L \\ b_L \\ c_L \\ d_L \end{bmatrix} \quad (\text{B.4.48})$$

To calculate the lift and drag values, we use bivariate splines with no smoothing (linear interpolation) to form two two-dimensional surfaces that are evaluated at  $(\alpha, Re)$  separately for each location along the body. If  $Re < Re_{\min}$  or  $Re > Re_{\max}$ , the Reynolds number is set to within these bounds.

### B.4.7 Complete dynamical model

The complete model consists of specifying the body kinematics using Eqs. (B.4.1), (B.4.2), and (B.4.3) by selecting the number of spatial periods  $\nu_\theta$ , horizontal wave amplitude  $\theta_m$ , vertical wave amplitude  $\psi_m$ , undulation frequency  $f_\theta$ , and dorsoventral bending angle  $d_\psi$ . With the kinematics specified, the equations of motion Eqs. (3.2.4) and (3.2.5) and kinematic differential equations (B.4.22) are integrated, with external aerodynamic forces given by (B.4.31). The rotationally invariant model consists of the above, except that (3.2.5) is not integrated and the force and moment histories are recorded.

### B.4.8 Glide simulations

Glides were simulated by integrating the equations of motion forward in time using a fifth-order accurate Dormand-Prince method until the center of mass contacted the ground with  $R_{o,z} < 0$ .

### B.4.9 Simulation initial conditions

The kinematics model, Eqs. (B.4.1) and (B.4.2), require specifying the number of waves on the body,  $\nu$ , undulation frequency,  $f$ , and phase shift,  $\phi$ . The number of body waves and undulation frequency are set from the parameter space given in the manuscript.

The horizontal phase shift,  $\phi_\theta$ , plays an important role because of the high inertial torques on the body about the yaw axis (figure 3.5B,C), especially at the beginning of the glide when aerodynamic forces are small. We therefore bias the undulation at the start of each glide to minimize this effect. This is done by setting the phase shift to minimize  $L^2$ -norm of the the angular momentum expressed in the co-moving frame

$$\left\| [\vec{h}_o] \right\| = \left\| \int_0^L \mathbf{r} \times \dot{\mathbf{r}} \rho(s) ds \right\| \quad (\text{B.4.49})$$

A non-zero angular momentum would cause the simulated snake to rotate in place. For planar undulation, the angular momentum only has a  $z$  component, so it is always possible to find an initial phase shift such that the angular momentum is zero. This norm is not guaranteed to be zero when the vertical wave is incorporated, as the vertical wave moves angular momentum into the other two axes.

The equations of motion require initial conditions, including the jump height, velocity, angular velocity, and yaw, pitch, and roll Euler angles. The height and velocity were set to  $z_0 = 10$  m and horizontal velocity of  $v_{y,0} = 1.7$  m/s. The angular velocity was set to zero, such that the yaw, pitch, and roll rates are zero. The initial Euler angles were found such that average angle deviations were zero. The initial angles were found by simulating one undulation cycle of the snake with gravity and aerodynamic turned off. The initial yaw, pitch, and roll angles are found as the negative of the average of each Euler angle time series.

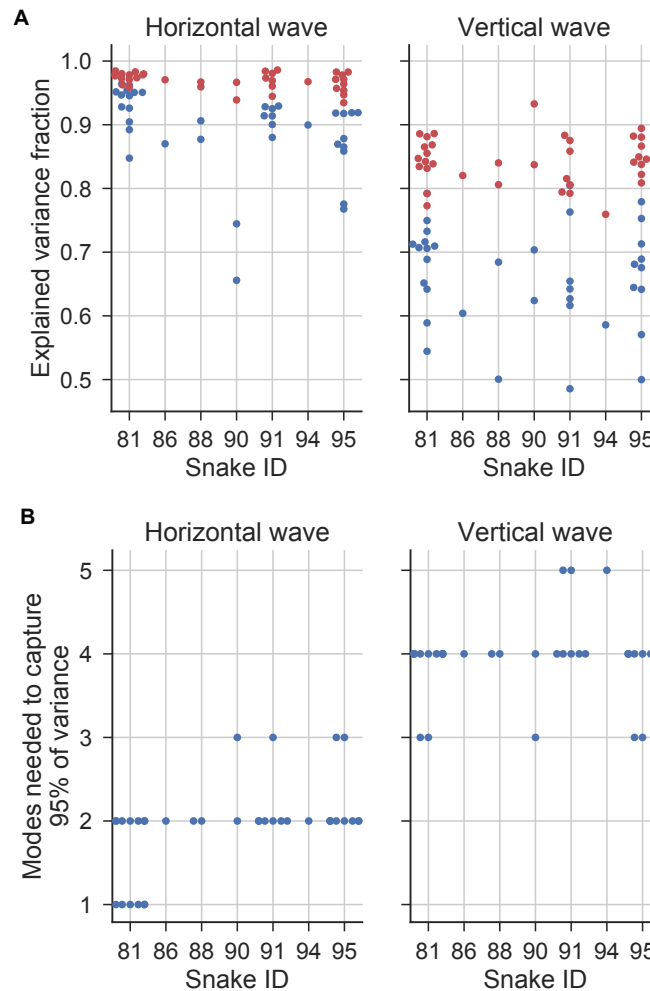


Figure B.1: Summary of complex orthogonal decomposition analysis. (A) The explained variance fraction for the different animals for the horizontal and vertical waves. Summing all modes results in a variance fraction of 1 (explaining all of the modal activity). The blue dots are the explained variance fraction for the first mode, while the red dots are the explained variance of the first and second modes combined. The horizontal wave is more organized, with a single mode accounting for much of the variance. (B) The number of modes required to account for 95% of the variance. Generally two modes are required for the horizontal, while three or four modes are required for the vertical wave.

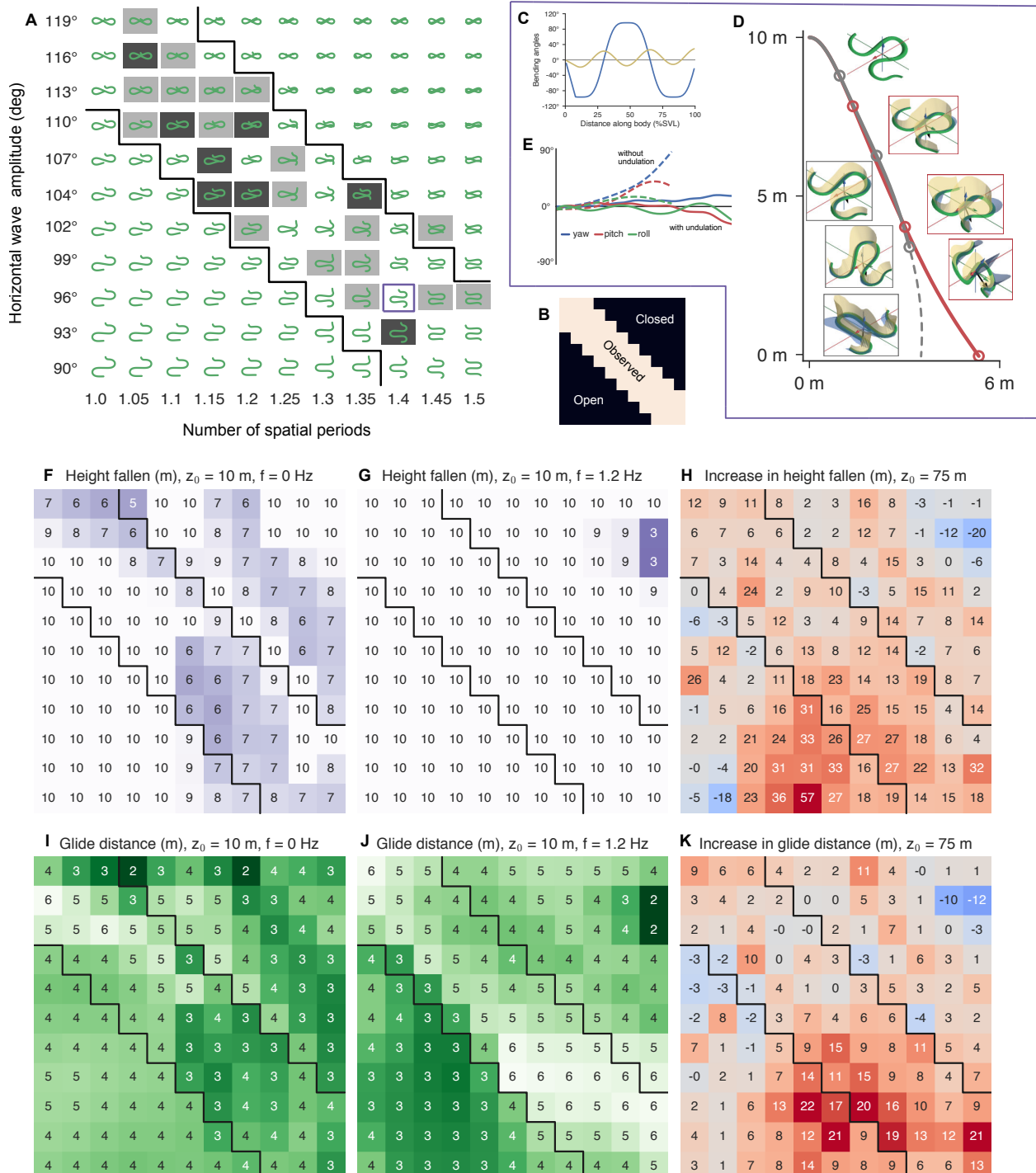


Figure B.2: Caption on next page.

Figure B.2: (Previous page.) Simulated flying snake glides. (A) Shape space used for simulated glides. Gray and black boxes indicate counts (one or two, respectively) of experimentally observed body shapes (figure 3.2F). The purple box indicates the shape shown in detail in (C)-(E) (B) The shape space is naturally demarcated along the diagonal of observed body shape, “open” shapes in the lower left, and “closed” shapes in the upper right. (C) Horizontal and vertical bending angles for a simulated glide with 1.4 spatial periods and a  $96^\circ$  horizontal wave amplitude. (D) Center of mass trajectory with and without undulation (red and gray, respectively). Snapshots of the body orientation are shown, with the lift (blue) and drag (yellow) forces overlaid at the start, 1/3, 2/3, and the end of the trajectories. (E) Yaw, pitch, and roll Euler angles for the glides shown in (D), with no undulation indicated by dashed lines and undulation with solid lines. Without undulation, this particular glide becomes unstable in roll. (F,G) Summary of height fallen before becoming unstable for different body shapes, undulation frequency, and launch heights. The gray bands demarcate the observed body shapes from the kinematics measurements. (H) Increase in height fallen in meters due to undulation from a 75m launch height. (I,J) Horizontal glide distance with and without undulation. (K) Increase in horizontal glide distance in meters due to undulation.

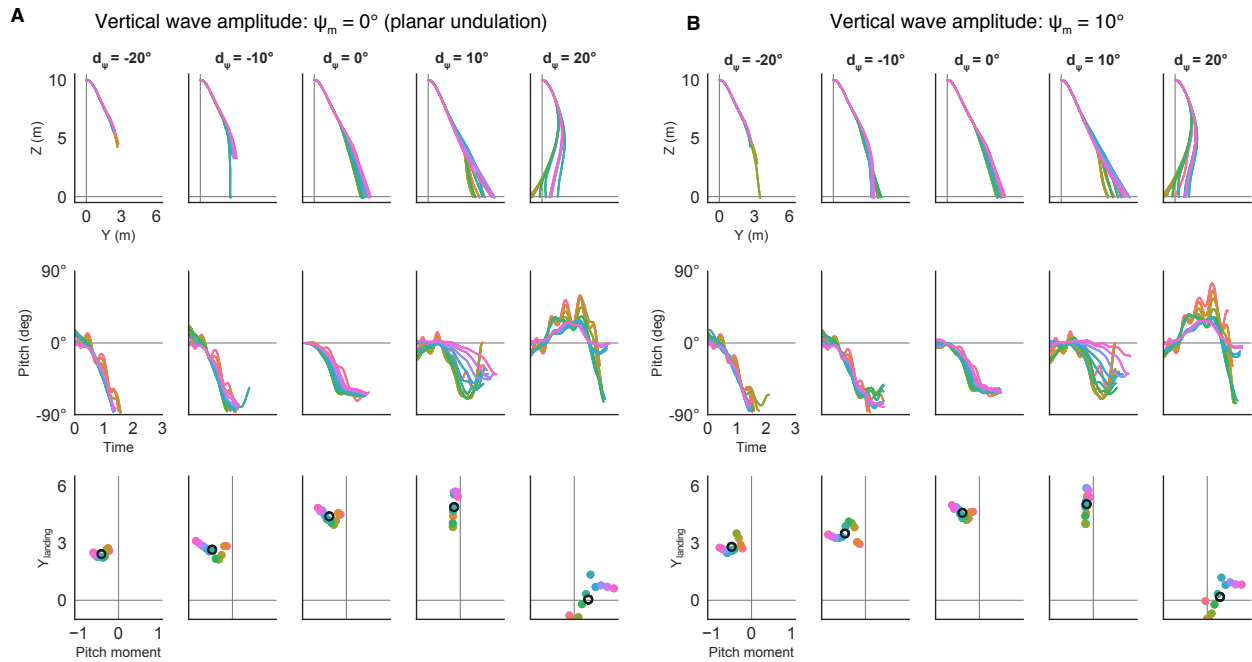


Figure B.3: Effect of the vertical wave amplitude  $\psi_m$  and dorsoventral bending  $d_\psi$  (columns) on glide performance for different dorsoventral flexion angles and number of spatial periods. See figure 3.4 for details. (A) Simulated glides with planar undulation performed worst, although the behavior for different dorsoventral bending angles (moving across the columns) is the same in (B) for  $\psi_m=10^\circ$ . Negative dorsoventral bending is associated unstable glides and poor performance due to pitching down and a net negative phase-averaged pitch moment. Positive dorsoventral bending is associated with stable glides with poor performance due to pitching-up. The pitch moment is in physical units of Nmm.

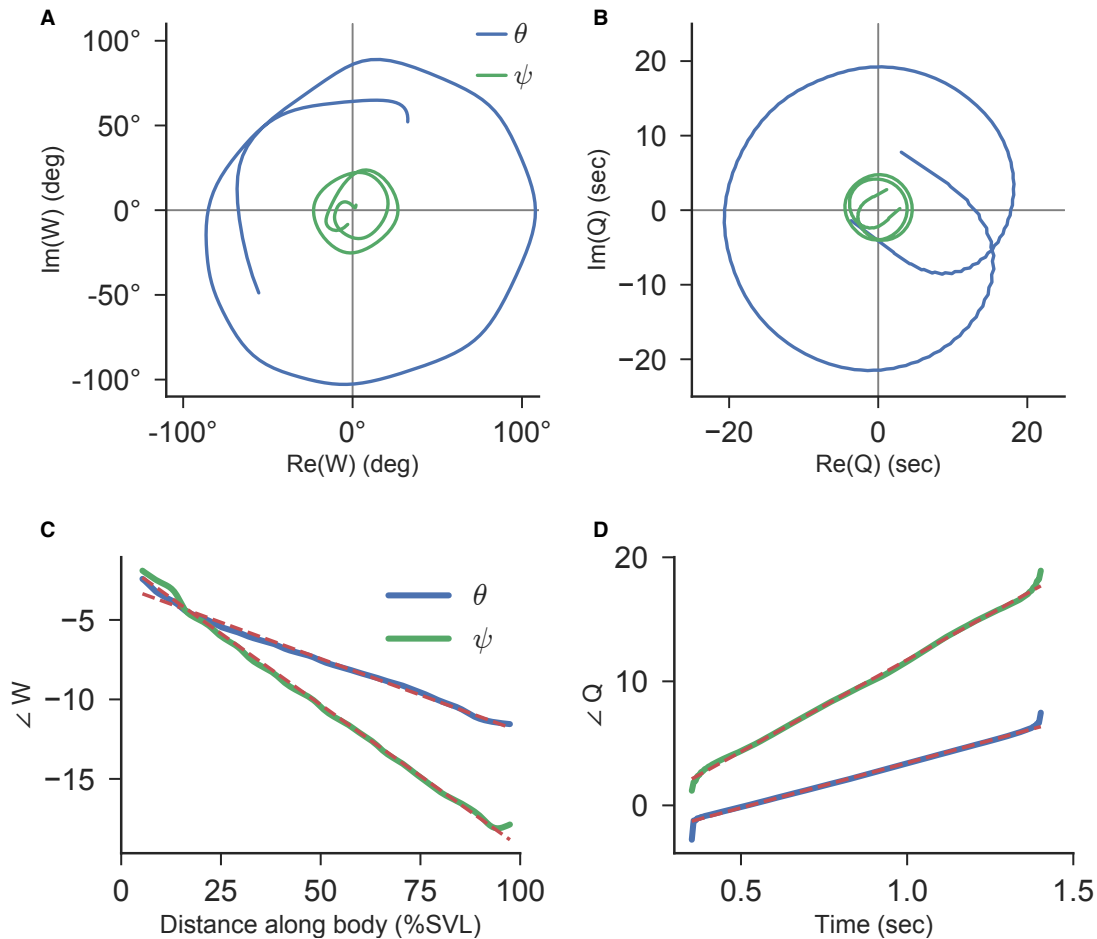


Figure B.4: Overview of complex orthogonal decomposition analysis for the glide shown in figure 3.2 of the main paper. (A) First scaled complex orthogonal model,  $\sqrt{\lambda_1} \mathbf{w}_1$  for the horizontal ( $\theta$ ) and vertical ( $\psi$ ) waves. The diameter of the circular spectrum is roughly the peak-to-peak amplitude of the waves (figure 3.2A). One revolution indicates one complete period of bending on the body. (B) First row of the complex modal coordinate ensemble matrix  $\mathbf{q}$  encompassing the undulation frequency information. One revolution indicates one complete period of undulation of the mode. (C) The complex numbers indicated in (A) are visualized as unwrapped angles to quantify the average whirl rate. The slope of the best-fit line is the number of spatial periods  $\nu$ . The slope for the vertical wave  $\psi$  is twice as great as for the horizontal wave  $\theta$ . (D) The slope of the line indicates the number of undulation periods during the glide. The slope of the vertical bending wave line is twice as great as the horizontal bending wave line.

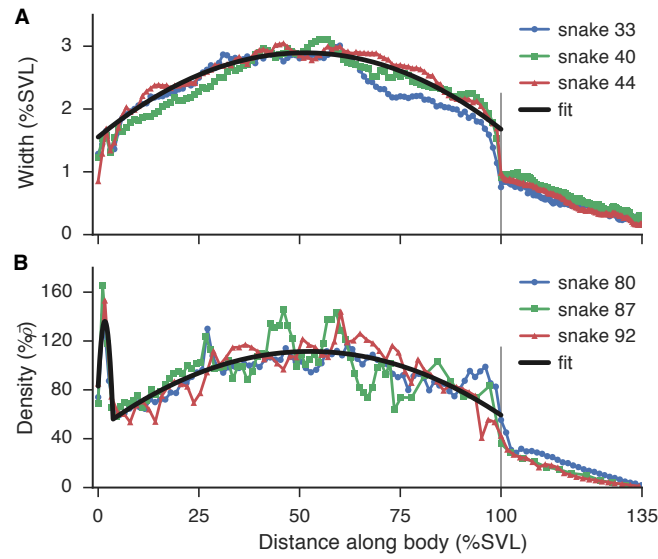


Figure B.5: Width and mass distributions of flying snakes. (A) Width distribution along the length of the animal as percent of the snout-vent length (SVL) of the snake for three different animals, and a parabolic fit. (B) Density distribution as percent of the average snake density,  $\bar{\rho} = m_{\text{tot}}/\text{SVL}$  for three different snakes. The head has higher density than the body, but both are modeled by two parabolas. The tail is included, although the tail dynamics was not modeled.

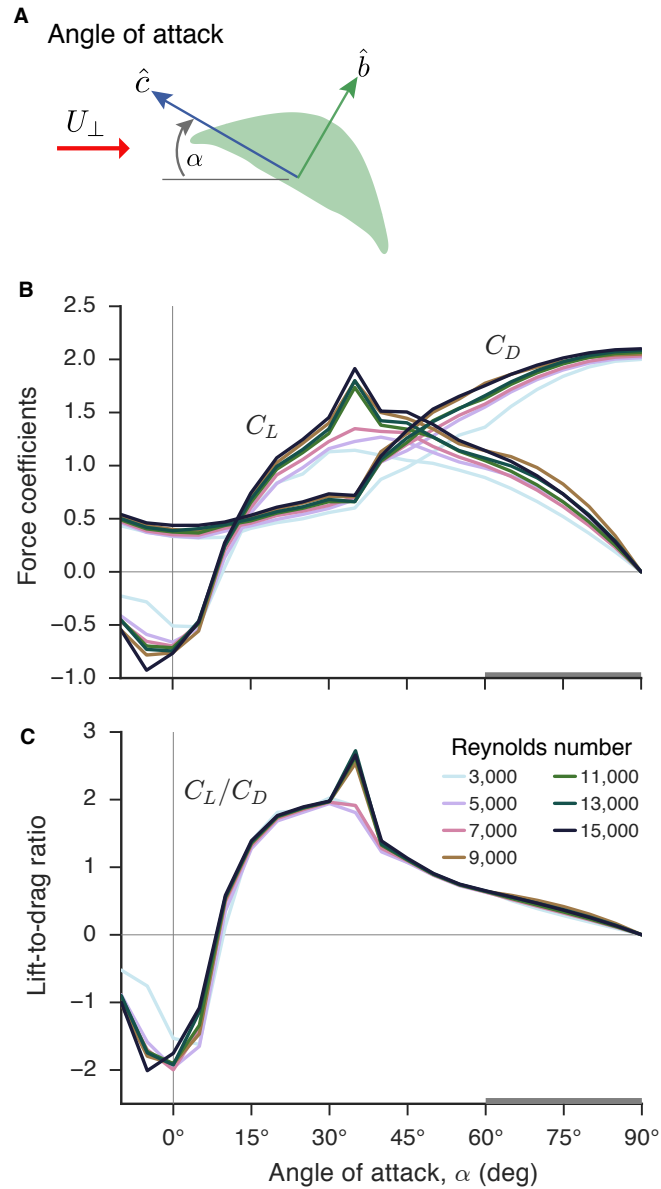


Figure B.6: Lift and drag coefficients of flying snakes. The data is from [14]. (A) Definition of the angle of attack,  $\alpha$ , as the angle between the chord-line direction  $\hat{c}$  and the velocity component locally perpendicular to the body. (B) Lift and drag coefficients as functions of angle of attack and Reynolds number. The extrapolated region is demarcated by the gray band on the horizontal axis between  $60^\circ$  and  $90^\circ$ . (C) Lift-to-drag ratio, with the characteristic peak at an angle of attack of  $35^\circ$ .

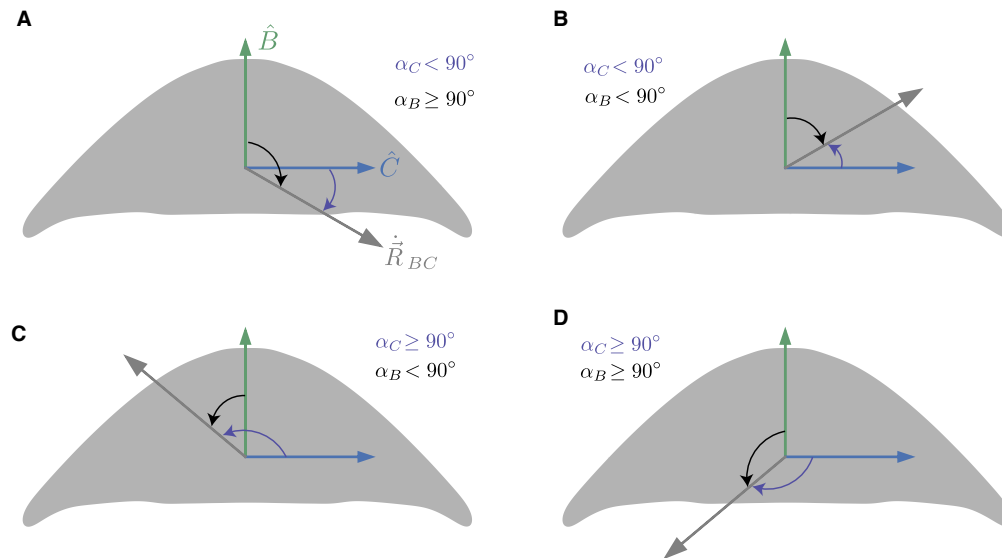


Figure B.7: Ensuring the correct angle of attack and lift vector direction based on the orientation of the body with the free-stream airflow. (A)-(D) match the cases in (B.4.34).

## References

- [14] D. Holden, J. J. Socha, N. D. Cardwell, and P. P. Vlachos. Aerodynamics of the flying snake *Chrysopelea paradisi*: how a bluff body cross-sectional shape contributes to gliding performance. *J. Exp. Biol.* 217 (2014), p. 382–394. DOI: 10.1242/jeb.090902.
- [15] A. Krishnan, J. J. Socha, P. P. Vlachos, and L. A. Barba. Lift and wakes of flying snakes. *Phys. Fluids* 26.031901 (2014). DOI: 10.1063/1.4866444.
- [17] F. Jafari, S. D. Ross, P. P. Vlachos, and J. J. Socha. A theoretical analysis of pitch stability during gliding in flying snakes. *Bioinspir. Biomim.* 9.025014 (2014). DOI: 10.1088/1748-3182/9/2/025014.
- [63] S. Hirose. *Biologically Inspired Robot*. Oxford University Press, 1993.
- [72] F. Jafari, S. Tahmasian, S. D. Ross, and J. J. Socha. Control of gliding in a flying snake-inspired n-chain model. *Bioinspir Biomim* 12 (2017), p. 066002. DOI: 10.1088/1748-3190/aa8c2f.
- [76] B. F. Feeny and A. K. Feeny. Complex modal analysis of the swimming motion of a whiting. *J Vib Acoust.* 135.021004 (2013). DOI: 10.1115/DETC2011-48204.

- [77] B. F. Feeny, P. W. Sternberg, C. J. Cronin, and C. A. Coppola. Complex orthogonal decomposition applied to nematode posturing. *J Comput Nonlinear Dyn* 8.041010 (2013). DOI: 10.1115/1.4023548.
- [80] M. Saito, M. Fukaya, and T. Iwasaki. Modeling, analysis, and synthesis of serpentine locomotion with a multilink robotic snake. *IEEE Control Syst Mag* 22 (2002), p. 64–81.
- [89] D. A. Winter. *Biomechanics and Motor Control of Human Movement*. John Wiley & Sons, 2009.
- [90] S. F. Hoerner. *Fluid-dynamic drag: practical information on aerodynamic drag and hydrodynamic resistance*. Hoerner Fluid Dynamic, 1965.
- [91] I. J. Yeaton, J. J. Socha, and S. D. Ross. Global dynamics of non-equilibrium gliding in animals. *Bioinspir Biomim* 12 (2017), p. 026013. DOI: 10.1088/1748-3190/aa60e2.
- [103] R. Labbe. FilterPy - Kalman filters and other optimal and non-optimal estimation filters in Python. 2017.
- [104] H. E. Rauch, F. Tung, and C. T. Striebel. Maximum likelihood estimates of linear dynamic systems. *AIAA J* 3.8 (1965), p. 1445–1450. DOI: 10.2514/3.3166.
- [105] G. D. Knott. *Interpolating Cubic Splines*. Birkhäuser, 2000.
- [106] B. F. Feeny. A complex orthogonal decomposition for wave motion analysis. *J Sound Vib* 310 (2008), p. 77–90. DOI: 10.1016/j.jsv.2007.07.047.
- [107] H. Yamada, M. Mori, and S. Hirose. Stabilization of the head of an undulating snake-like robot. *IEEE/RSJ IROS*. 2007, p. 3566–3571. DOI: 10.1109/IROS.2007.4399390.
- [108] J. Diebel. Representing attitude: Euler angles, unit quaternions, and rotation vectors. *Matrix* 58.15-16 (2006), p. 1–35. DOI: 10.1093/jxb/erm298.
- [109] D. T. Greenwood. *Advanced Dynamics*. Cambridge University Press, 2006.

# Appendix C

## Reconstructing the flying snake from motion capture data

### C.1 Overview of data processing

From the raw 3D coordinates of infrared markers measure in the Cube, we need to reconstruct the body of the snake. The reconstruction analysis requires:

1. Select trials to analyze in detail
2. Fill in missing data gaps with *Kalman filtering*
3. Smooth position data with a *Butterworth filter*, with the cutoff frequency optimally selected for each trial
4. *Spline fitting* of the marker coordinates to reconstruct the backbone
5. Calculating horizontal and vertical bending waves
6. Complex orthogonal decomposition to quantify the bending waves
7. Measured linear mass distribution and calculation of center of mass
8. Calculating kinematic variables, velocities, and accelerations
9. Rotating the snake's body into the *straightened* and into the *glide* frames

10. Overlaying the *body coordinate system* for the local orientation of the snake's triangular cross section.
11. Measuring and overlaying the snake's flattened body width
12. Calculating aerodynamic forces and simple sweep theory
13. 3D visualization in Python

In this appendix, we list the details of each step that are not described in detail in the manuscript or the supplemental information to the manuscript. We note that steps 2–4 of the reconstruction analysis are performed in order. That is, the gaps in the data must first be filled, then filtered, and then the splines can be fit. For the gap filling and filtering, the individual marker time series are treated independently, i.e. the position of a nearby marker is not used to provide better estimates for the missing marker. However, the spline fit in step 4 requires all of the markers at each time step.

## C.2 Trial selection using trajectory summary plots

From 131 glides recorded over nine days of testing, 52 trials were analyzed in detail (table C.1). Each trial had different levels of data quality, indicated by the amount of missing data. We used trajectory summary plots to determine which trials to process further (figures C.3–C.14). Each figure shows all trials for a particular individual. The y-label is the unique trail ID, where the first number is the day of testing and the remaining numbers indicate the trial number within each day. Bold trial ID numbers indicate glides that were analyzed in detail.

Within each figure, the colored bars show time along the x-axis and markers along the y-axis; the tail markers are indicated in darker shading. Very thin plots indicate that only a few markers were placed on the snake; these trials were excluded from the analysis because the body could not be recovered. The length of the bar indicates the length of the recorded time series and are comparable within each figure. Black indicates where there is missing data. The vertical red line indicates the first time point where all markers were present, and the purple vertical line the last time point. Gaps between these time points were filled with Kalman filters (discussed below). Trial 413 in figure C.4 had no missing data for a majority of the glide and was used to build-up the processing code. The effect of missing data is discussed in detail in section C.9.

The trials that were analyzed in detail were chosen by inspecting the trajectory summary plots and selecting trials with long segments of no missing data and smaller clusters of missing data. The time and marker selection criteria results are shown in figure C.1. Summary histograms of the data selection process are shown in figure C.2 for the 36 trials used the complex orthogonal decomposition analysis (COD), the 52 selected trials to analyze in detail, the 79 trials excluded from the detailed analysis, and all of the 131 trials included together. Generally, the trials used in the COD analysis had fewer gaps, longer time series (covered more vertical distance), and glided further. The main distinguishing feature between these trials and the 52 trials analyzed in detail are 1) only *C. paradisi* were analyzed, and 2) greater glide distances were covered. The main distinguishing feature between the unanalyzed 79 excluded trials and the 52 selected trials are the number of gaps, the height recorded, and the glide distance.

Table C.1: Overview of *C. paradisi* and *C. ornata* glides analyzed and animal sizes. Of 131 recorded glides, 51 were analyzed in detail, with 42 from *C. paradisi* and 9 from *C. ornata*.

Snake	Glides analyzed	Mass (g)	SVL (mm)	VTL (mm)	Total (mm)
81	14	107.2	850	295	1145
91	7	71.0	766	296	1062
95	12	37.3	644	250	894
88	2	71.9	888	308	1196
90	4	39.7	672	217	1196
86	3	54.5	810	266	1076
94	1	49.9	731	267	998
30	1	132.3	789	247	1036
31	1	164.3	750	346	1096
32	2	52.5	662	256	918
33	2	272.5	918	312	1230
35	2	141.0	828	269	1097

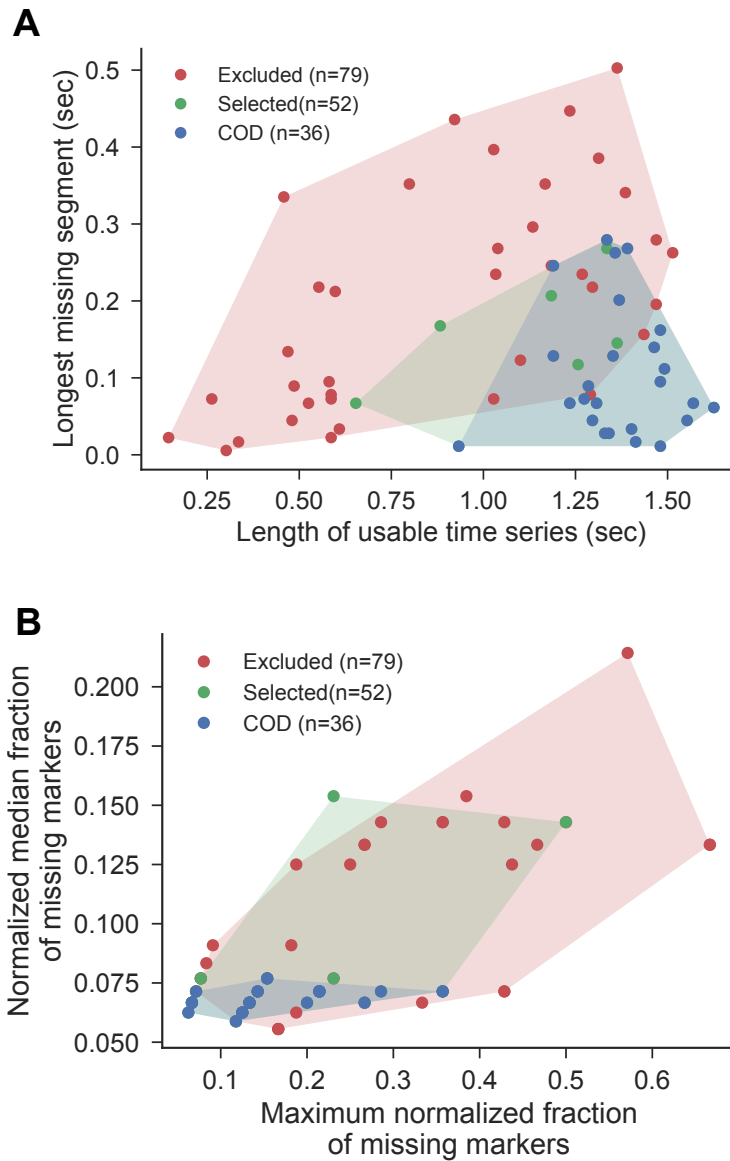


Figure C.1: Quantified selection criteria from the trajectory summary plots. Red markers are trials that were excluded, green markers are trials that were selected for further processing, and blue markers were used in the complex orthogonal decomposition (COD) analysis. The shaded areas are the convex hulls of the respective markers. (A) The time component of selection. The abscissa indicates the total length of usable time series and the ordinate indicates the largest gap length. (B) The marker component of selection. The abscissa indicates the maximum number of missing markers on the snake's body, normalized by the total number of markers on the body. The ordinate indicates the median number of missing markers, normalized by the total number of markers on the body.

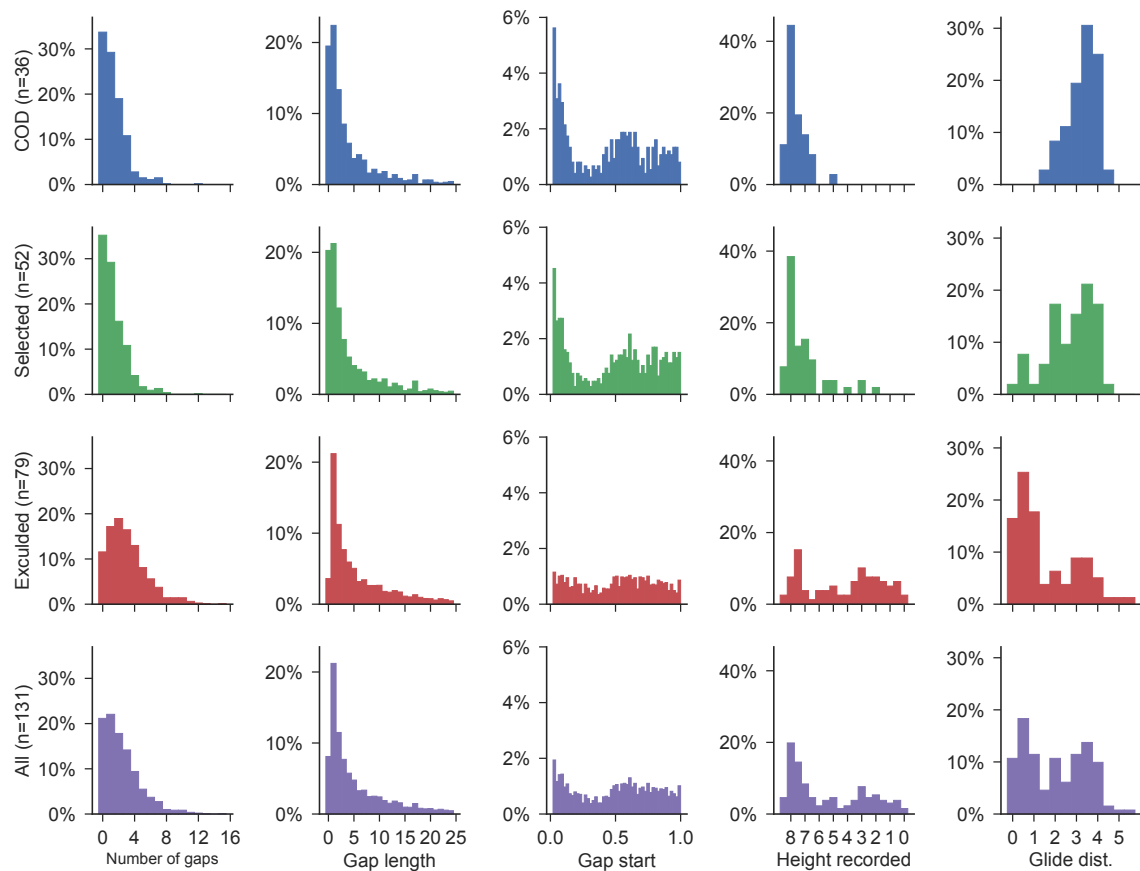


Figure C.2: Summary histograms of missing data, including the number of gaps in the time series, the length of the individual gaps, where the gaps occur in the time series, the amount of vertical glide distance recorded, and the horizontal glide distance, for the different trials analyzed. The first row are for 36 trials used for the complex orthogonal decomposition analysis, which are a subset of the 52 trials shown on the second row that were analyzed in detail. These 52 trials are indicated by bold labels in figures C.3–C.14. The third row indicates the 79 trials that were excluded from further analysis. These trials generally had more gaps, with longer lengths, shorter heights recorded, and much shorter glide distances recorded. The last row is the summary histograms for all of the recorded trials. Note that the first three columns treat each marker time series separately (i.e. between 11 and 17 time series per trial per snake), while the last two columns are summaries for each trial and calculated from the head marker position at the start and end of the usable data region (between the red and purple vertical lines in the trajectory summary plots).

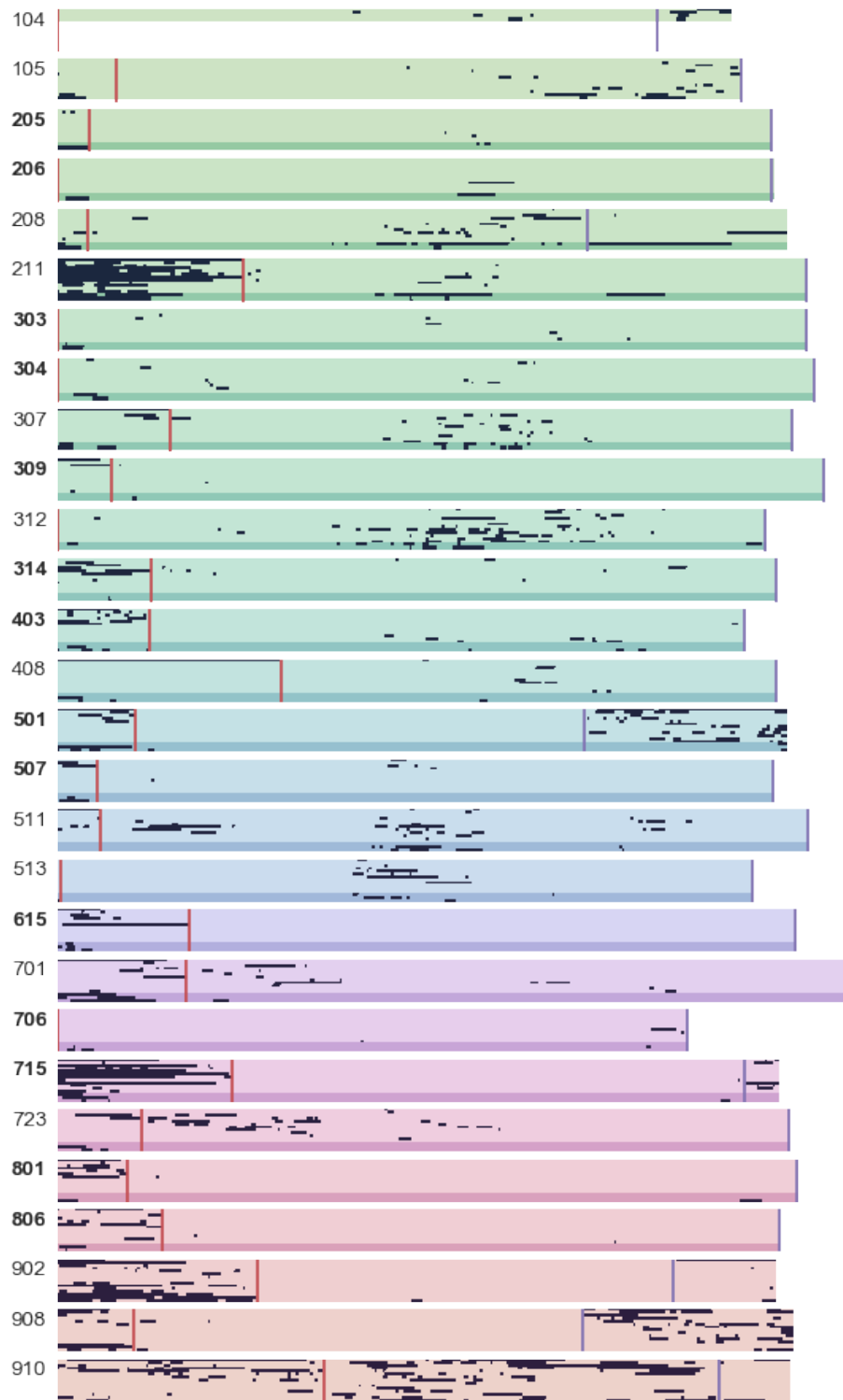


Figure C.3: *Chrysopelea paradisi* 81.

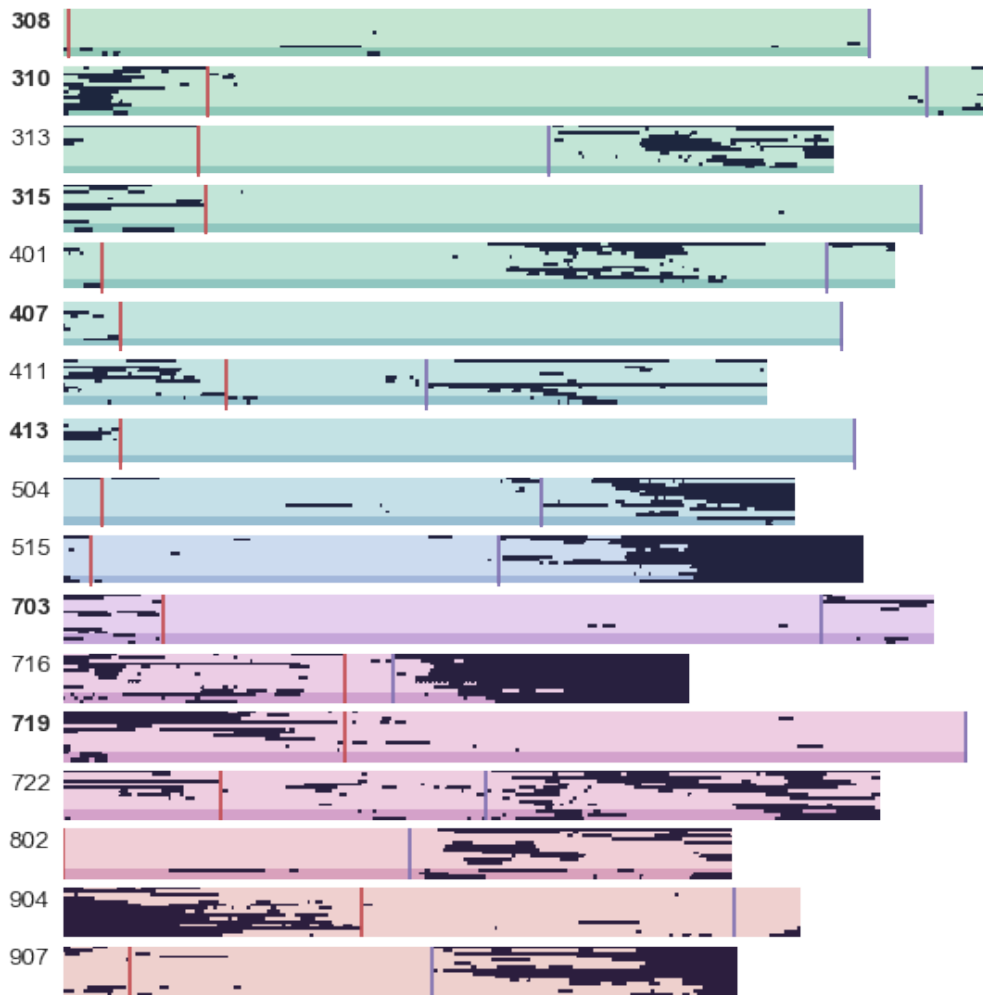


Figure C.4: *Chrysopelea paradisi* 91.

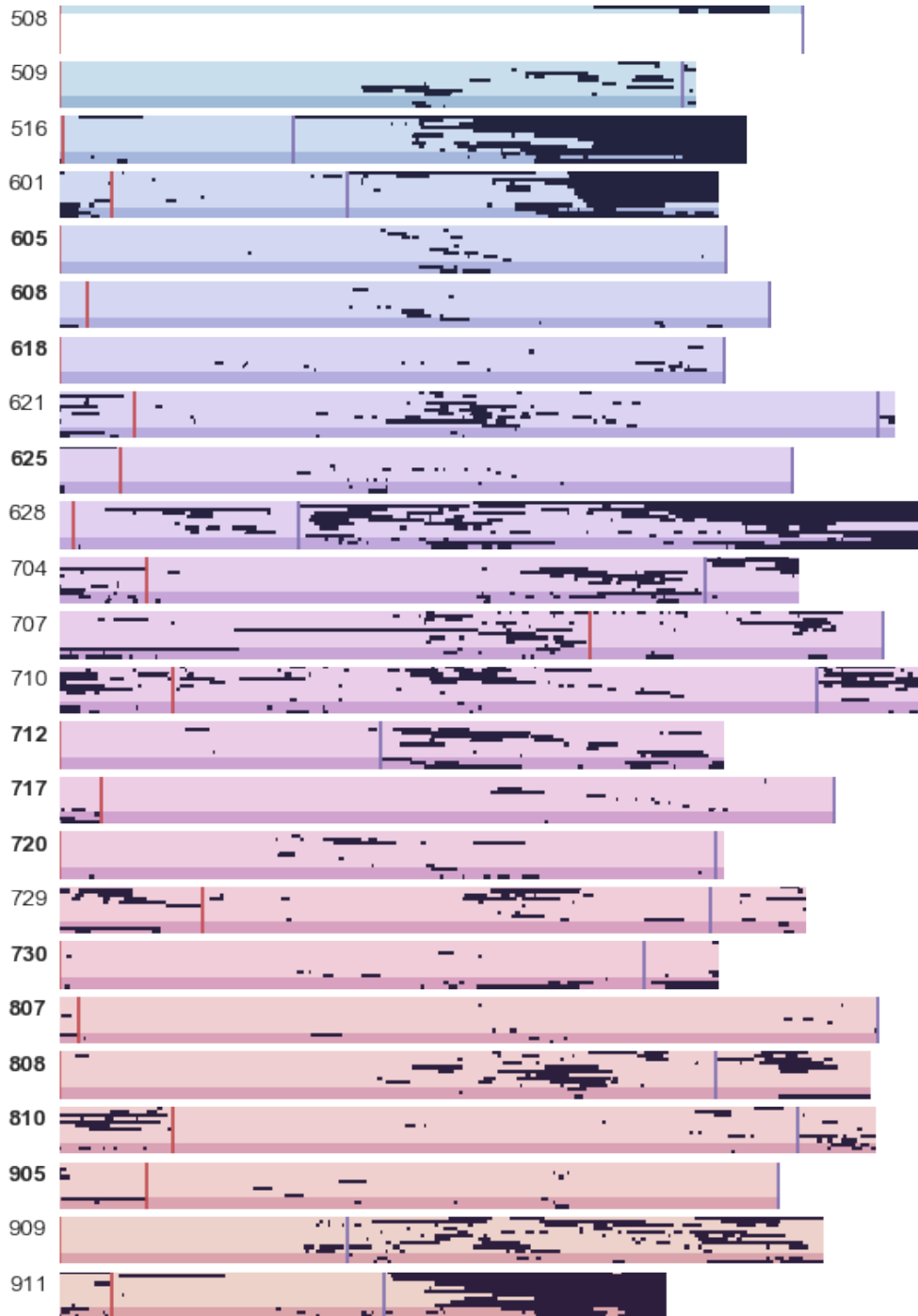


Figure C.5: *Chrysopelea paradisi* 95.

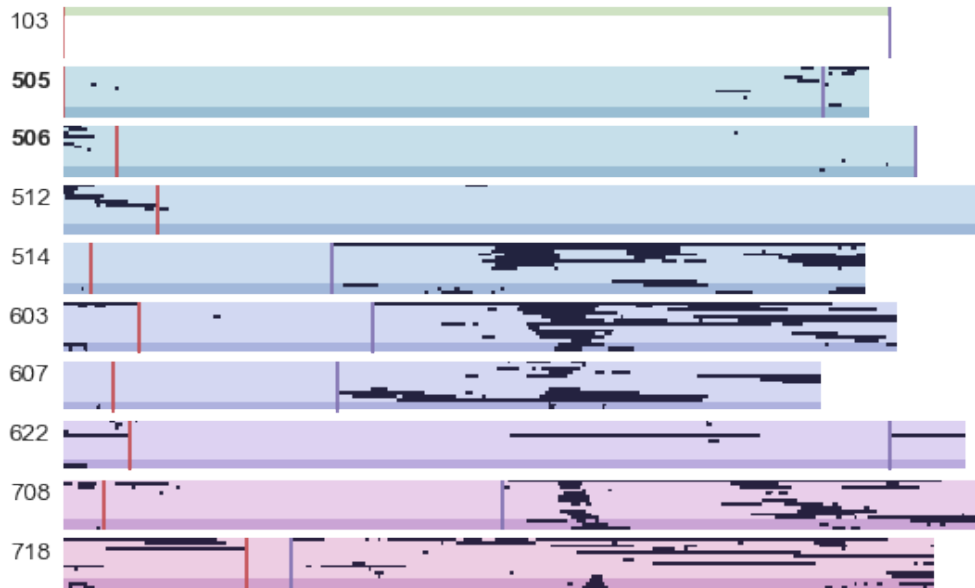


Figure C.6: *Chrysopelea paradisi* 88.

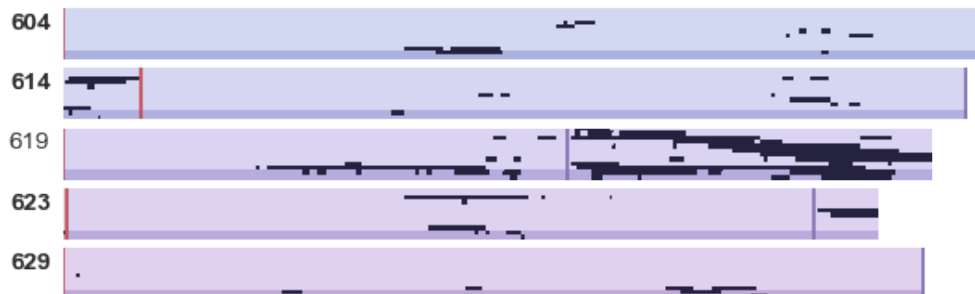


Figure C.7: *Chrysopelea paradisi* 90.

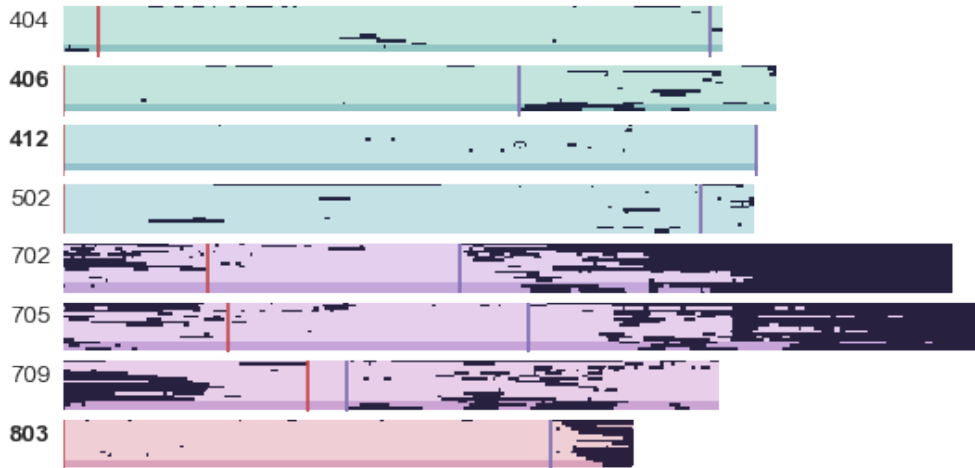


Figure C.8: *Chrysopelea paradisi* 86.

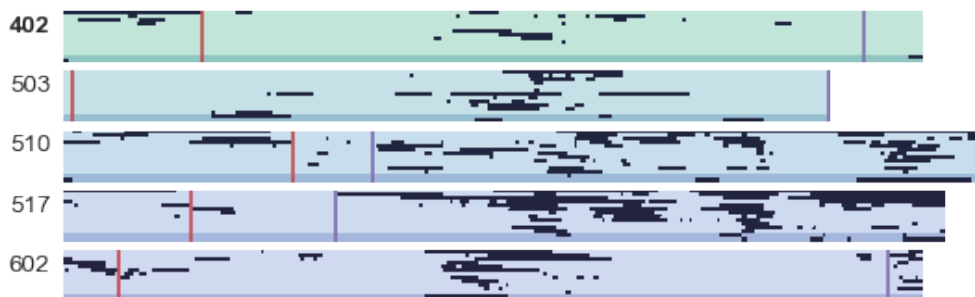


Figure C.9: *Chrysopelea paradisi* 94.

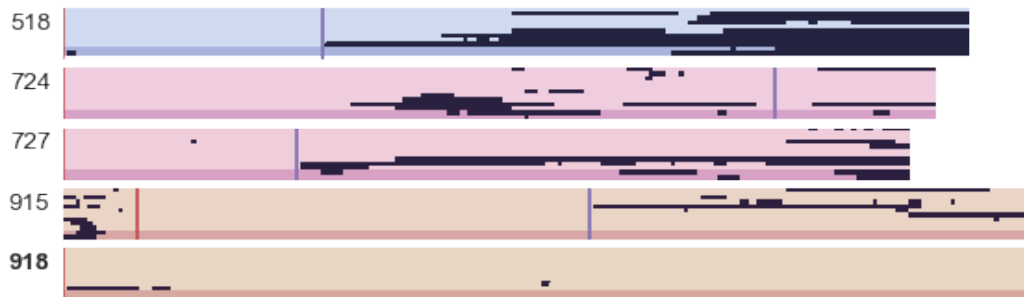


Figure C.10: *Chrysopelea ornata* 30.

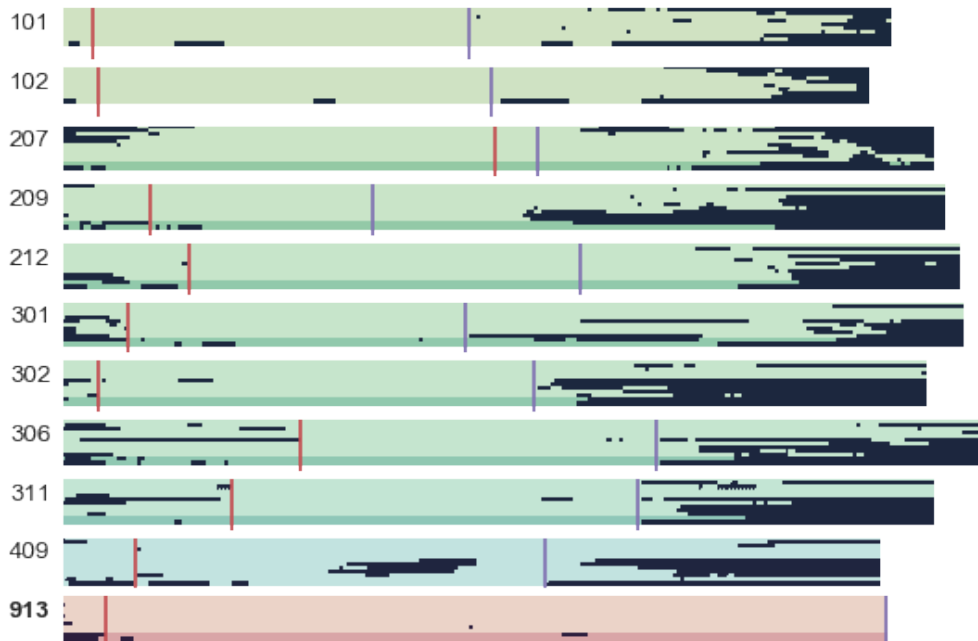


Figure C.11: *Chrysopelea ornata* 31.

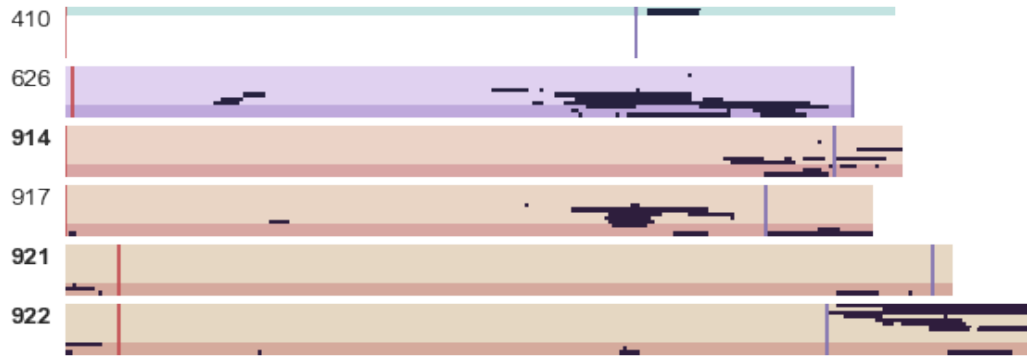


Figure C.12: *Chrysopelea ornata* 32.

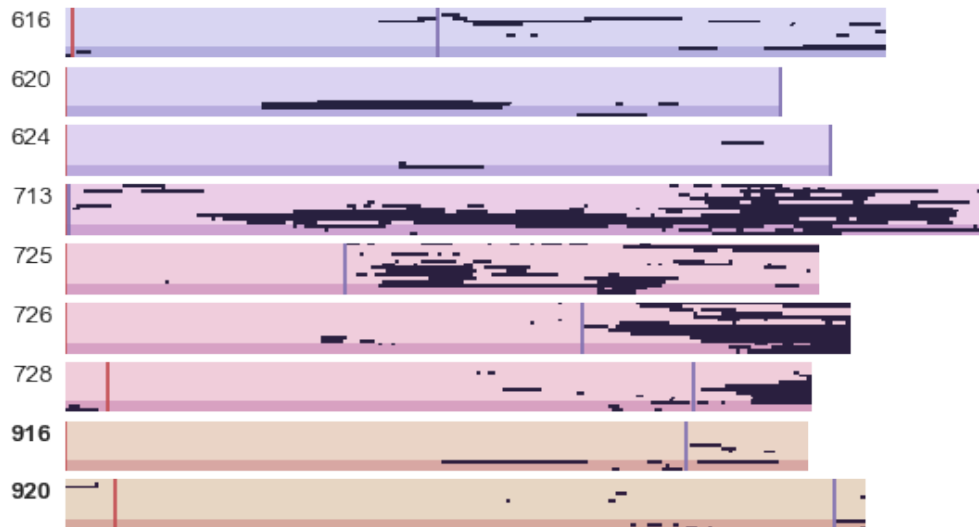


Figure C.13: *Chrysopelea ornata* 33.

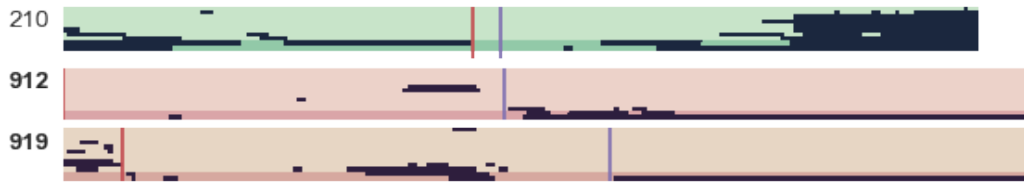


Figure C.14: *Chrysopelea ornata* 35.

### C.3 Gap filling with Kalman filters

The recorded IR marker trajectories had sections where the data is missing. These data gaps needed to be filled in order to spline fit the snake's body. There are several possible reasons for gaps in the data, including marker occlusions due to part of the body covering the marker, poor camera coverage in a particular region of the glide arena, two markers being difficult to distinguish when reconstructing the 3D points, or a combination of the above. The statistics of the missing data are shown in figure C.32, indicating that nearly 40% of the marker time series had at least one gap, and that the gap location is likely at the beginning of the glide or in the last of the half of the glide. Additionally, 30% of the gaps had a length of one time point, while the majority of gaps being under five time points long.

We addressed the data gaps by using unscented Kalman filters to fill only the time points where there are gaps, with the filling process applied to each marker time series separately. We use the Python package `filterpy` [103] to perform the filtering. Below we describe the necessary components to implement the filter used for the Cube data.

The filtering process involves using the known measurement  $\vec{p}(t)$  for the  $x, y, z$  positions, while using the filter to estimate the velocities and accelerations,  $\vec{v}(t)$  and  $\vec{a}(t)$ . We denote the system state estimate vector as  $\vec{x}(t)$ , given by

$$\vec{x} = [p_x, v_x, a_x, p_y, v_y, a_y, p_z, v_z, a_z]^T \quad (\text{C.3.1})$$

with initial conditions

$$\vec{x}_0 = [p_x(t_0), 0, 0.1g, p_y(t_0), 500, 0.1g, p_z(t_0), 1000, -0.5g]^T \quad (\text{C.3.2})$$

where the initial velocities are in mm/s and the accelerations in mm/s<sup>2</sup>. At each time step, the filter uses the measured positions, given by the measurement function  $H$ .  $H$  is a  $3 \times 9$  matrix that gives the measured state at the current time point (i.e. maps from physical space to the measurement space)

$$H = \begin{bmatrix} 1 & 0 & 0 & 0 & 0 & 0 & 0 & 0 & 0 \\ 0 & 0 & 0 & 1 & 0 & 0 & 0 & 0 & 0 \\ 0 & 0 & 0 & 0 & 0 & 0 & 1 & 0 & 0 \end{bmatrix} \quad (\text{C.3.3})$$

where the measurements at time  $t_i$  are

$$\vec{x}(t_i) = H \cdot \vec{x}(t_i) \quad (\text{C.3.4})$$

The state transition matrix,  $F$ , transitions from the state  $\vec{x}(t)$  to the new state  $\vec{x}(t + \Delta t)$ , and is given by

$$F = \begin{bmatrix} 1 & \Delta t & 0.5\Delta t^2 & 0 & 0 & 0 & 0 & 0 & 0 \\ 0 & 1 & \Delta t & 0 & 0 & 0 & 0 & 0 & 0 \\ 0 & 0 & 1 & 0 & 0 & 0 & 0 & 0 & 0 \\ 0 & 0 & 0 & 1 & 0 & 0 & 0 & 0 & 0 \\ 0 & 0 & 0 & 0 & 500 & 0 & 0 & 0 & 0 \\ 0 & 0 & 0 & 0 & 0 & 2g & 0 & 0 & 0 \\ 0 & 0 & 0 & 0 & 0 & 0 & 1 & 0 & 0 \\ 0 & 0 & 0 & 0 & 0 & 0 & 0 & 500 & 0 \\ 0 & 0 & 0 & 0 & 0 & 0 & 0 & 0 & 2g \end{bmatrix} \quad (\text{C.3.5})$$

where the positions, velocities, and accelerations are found from simple finite differences,

$$\vec{p}(t + \Delta t) = \vec{p}(t) + \vec{v}(t)\Delta t + \frac{1}{2}\vec{a}(t)\Delta t^2 \quad (\text{C.3.6})$$

$$\vec{v}(t + \Delta t) = \vec{v}(t) + \vec{a}(t)\Delta t \quad (\text{C.3.7})$$

$$\vec{a}(t + \Delta t) = \vec{a}(t) \quad (\text{C.3.8})$$

The measurement noise matrix is a  $3 \times 3$  matrix that quantifies our uncertainty in the measured IR marker positions. It is given as

$$R = \begin{bmatrix} \sigma_m^2 & 0 & 0 \\ 0 & \sigma_m^2 & 0 \\ 0 & 0 & \sigma_m^2 \end{bmatrix} \quad (\text{C.3.9})$$

where  $\sigma_m = 5$  mm is the measurement reconstruction error from the wand calibration, re-

turned from the Qualisys software. The initial covariance matrix is

$$P = \begin{bmatrix} 1 & 0 & 0 & 0 & 0 & 0 & 0 & 0 & 0 \\ 0 & 500 & 0 & 0 & 0 & 0 & 0 & 0 & 0 \\ 0 & 0 & 2g & 0 & 0 & 0 & 0 & 0 & 0 \\ 0 & 0 & 0 & 1 & 0 & 0 & 0 & 0 & 0 \\ 0 & 0 & 0 & 0 & 500 & 0 & 0 & 0 & 0 \\ 0 & 0 & 0 & 0 & 0 & 2g & 0 & 0 & 0 \\ 0 & 0 & 0 & 0 & 0 & 0 & 1 & 0 & 0 \\ 0 & 0 & 0 & 0 & 0 & 0 & 0 & 500 & 0 \\ 0 & 0 & 0 & 0 & 0 & 0 & 0 & 0 & 2g \end{bmatrix} \quad (\text{C.3.10})$$

The process uncertainty (noise) matrix of the unmodeled behavior is given by the Discrete Constant White Noise Model for three dimensions, with a variance of  $\sigma^2 = (0.5g)^2$ . The submatrices along the diagonal are

$$Q = \sigma^2 \begin{bmatrix} \frac{\Delta t^4}{4} & \frac{\Delta t^3}{2} & \frac{\Delta t^2}{2} \\ \frac{\Delta t^3}{2} & \Delta t^2 & \Delta t \\ \frac{\Delta t^2}{2} & \Delta t & 1 \end{bmatrix} \quad (\text{C.3.11})$$

which becomes

$$Q = \begin{bmatrix} 0.0059 & 2.1 & 375.4 \\ 2.1 & 750.9 & 134408 \\ 375.4 & 134408 & 24059025 \end{bmatrix} \quad (\text{C.3.12})$$

with the values substituted in. Lastly, the unscented Kalman filter requires sigma points which all the filter to estimate the mean and variance. We use the suggested Merwe Scaled Sigma Points from the package documentation, with the suggested parameters  $\alpha = 0.001$ ,  $\beta = 2$ , and  $\kappa = 0$ .

With the filter parameters specified, we batch process each of the time series independently. After the batch processing, we additionally apply the Rauch-Tung-Striebal Kalman smoother technique to provide a better estimate of the smoothed data. Once the gaps in the data have been filled, we select only those times points with missing data and fill the original time series. We chose to use Butterworth filters (discussed below) to filter all of the data, as there are standard biomechanics techniques to do so.

## C.4 Butterworth filtering and filter cutoff frequency calculation

To remove noise from the gap filled, but raw position data, we used a forward-backward pass of a second-order Butterworth filter. This requires selecting the cutoff frequency of the filter. For this, we use the technique from Winter [89] to select the filter cutoff frequency separately for each  $x$ ,  $y$ ,  $z$  time series that equally balances the signal distortion and the noise passed through the filter. We demonstrate this technique in figure C.15 for trial 413\_91 to show how the cutoff frequency changes depending on the individual marker (size, motion through the calibrated volume), and its times series (faster oscillations depending on the location along the body). We begin by find the residual line ( $R$ ) of each  $x$ ,  $y$ ,  $z$  component for each marker at filter cutoff frequencies of  $1 \leq f_c \leq 35$  Hz in 0.5 Hz increments, using the RMS error [89],

$$R(f_c) = \sqrt{\frac{1}{N} \sum_i^N (p_i - \hat{p}_i)^2} \quad (\text{C.4.1})$$

where  $f_c$  is the cutoff frequency,  $p_i$  is any of the raw  $x$ ,  $y$ ,  $z$  time series components, and  $\hat{p}_i$  is the filtered data using a forth-order zero-lag Butterworth filter. This residual line (figure C.15a-c) is high at low frequencies (large errors due to signal distortion), and decreases, eventually becoming near linear. We use a best-fit line to this linear region, by starting at the residual at 35 Hz and including successively more points at lower frequency values until the  $r^2$  of the fit drops below 0.95. We then taken the proceeding linear regression such that  $r^2 > 0.95$ , and find the  $y$ -intercept. This gives the RMS value of the noise. This intercept is then projected onto the residual curve (black lines in figure C.15). The frequency of this intersection (red lines) is the cutoff frequency used. This gives an equal weight to signal distortion and noise passed through the filter, both of which are the vertical distance between the residual curve and the linear fit at the selected cutoff frequency.

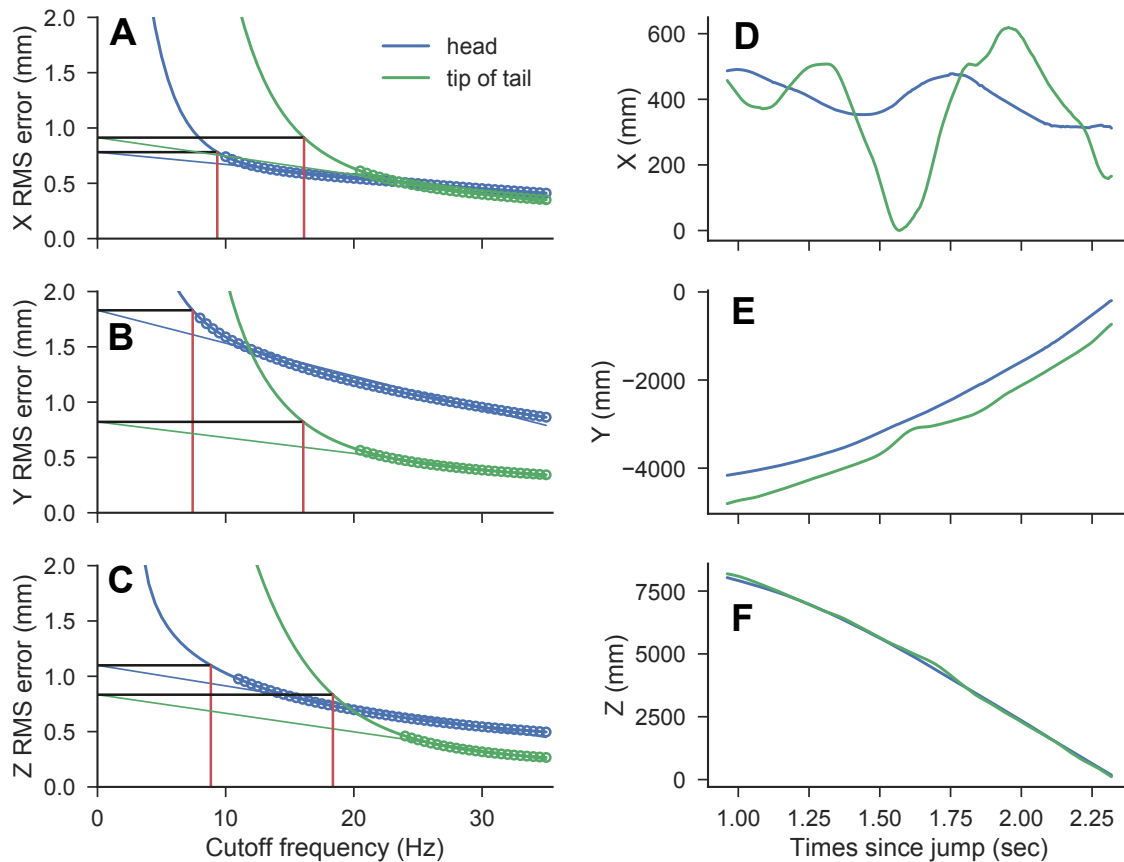


Figure C.15: Filter cutoff frequency selection for a forward-backward Butterworth filter. (a-c) Root-mean-square errors for the head (blue) and tip of the tail (green) marker time series for different filter cutoff frequency, with the selected cutoff frequencies indicated by the vertical red lines. The times series (d-f) for marker about each direction has different characteristics and results in different cutoff frequencies. In (a-c), the frequency selection algorithm begins by calculating the RMS error residual line for cutoff frequencies from  $1 \leq f_c \leq 35$  Hz in 0.5 Hz increments, as indicated by the thick blue and green lines. Then, beginning at 35 Hz and decreasing, points are added to a linear regression (open markers), until the  $r^2$  of the fit drops below 0.95; the proceeding frequency is then used such that  $r^2 \geq 0.95$ . Next, the linear fit is extended to the  $y$ -intercept (thin blue and green lines), giving the RMS value of the noise [89]. Next, the intercept is projected (black line) onto the residual line; the frequency of this intersection is the selected cutoff frequency (red line). Using this approach, the signal distortion (the distance between the residual intercept and the linear fit) is equal to the noise passed through the filter.

### C.4.1 Ball drop experiments to test cutoff frequency calculation and error in the measurement system

We tested the motion capture system and the filtering procedure using a ball drop experiment. At the end of the glide trial experiments, we dropped steel balls vertically through the measurement volume and recorded the position time series. At each location (figure C.16a, b), three balls were dropped through the steel grating at the top of the Cube in a  $5 \times 5$  array. However, the lower right and left portions of the grid were too far outside of the camera coverage region for drops to be recorded.

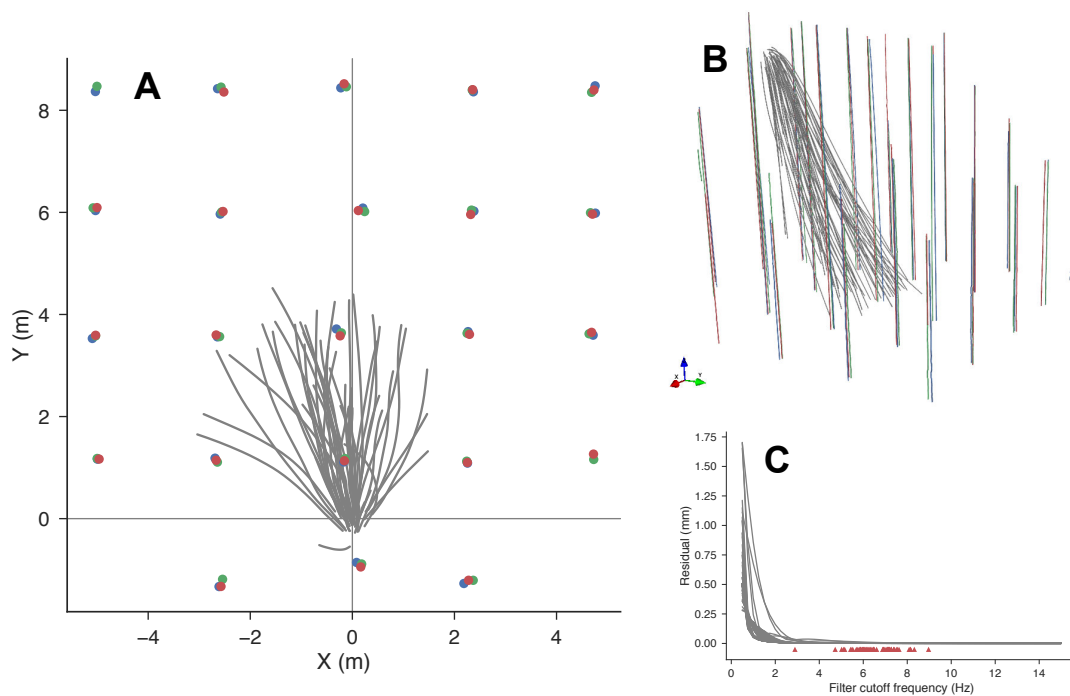


Figure C.16: Ball drop locations used to test the accuracy of the motion capture system. (a) Overhead view of the  $5 \times 5$  measurement grid, where the three ball drops at each site are indicated by the colored markers. Gray lines are the  $X - Y$  center of mass position of the recorded snake glides. The majority of the glides fall within at 7 drop location near the launch height. (b) Three-dimensional analogue of (a). (c) Position residuals for different filter cutoff frequencies for each ball drop trajectory.

From the recorded positions, the  $z$  component was used for further analysis, as this lines-up with the gravitational axis. We used the filtering procedure described above to smooth the raw position data (figure C.16c), and then used finite differences to calculate the velocity and acceleration time series. Given that the balls were dense and small, air drag should

be negligible and the acceleration should be a the gravitation constant  $g = -9.81 \text{ m/s}^2$ . Figure C.17 shows the RMS acceleration error in units of  $g$ , as small multiples of the drop locations. The average error over the height is indicated in each plot, and is between 7% and 12%  $g$  is the locations where glides were recorded.

We found from this analysis that the acceleration errors were large at the start and end end of each ball drop trajectory. This error was also present in the calculated center of mass acceleration from the kinematics data. Visually, we determined that the first 8 and last 10 points contributed most to this error (indicated by the markers in figures C.17 to C.19).

Additionally, we calculated the velocity errors (figures C.18) and position errors (figures C.19) by fitting polynomials to the time series of position. We fit linear and quadratic polynomials to the velocities and positions, respectively, based on simple projectile dynamics, and report the error of the velocity and position relative to the fits. For the velocities, average errors are between 0.03 and 0.05 m/s, and for position, average errors are between 1.4 and 3.7 mm over the vertical distance. We also note that the point reconstruction error from the wand calibration, as reported from the Qualisys software, is 5 mm for the entire measurement volume.

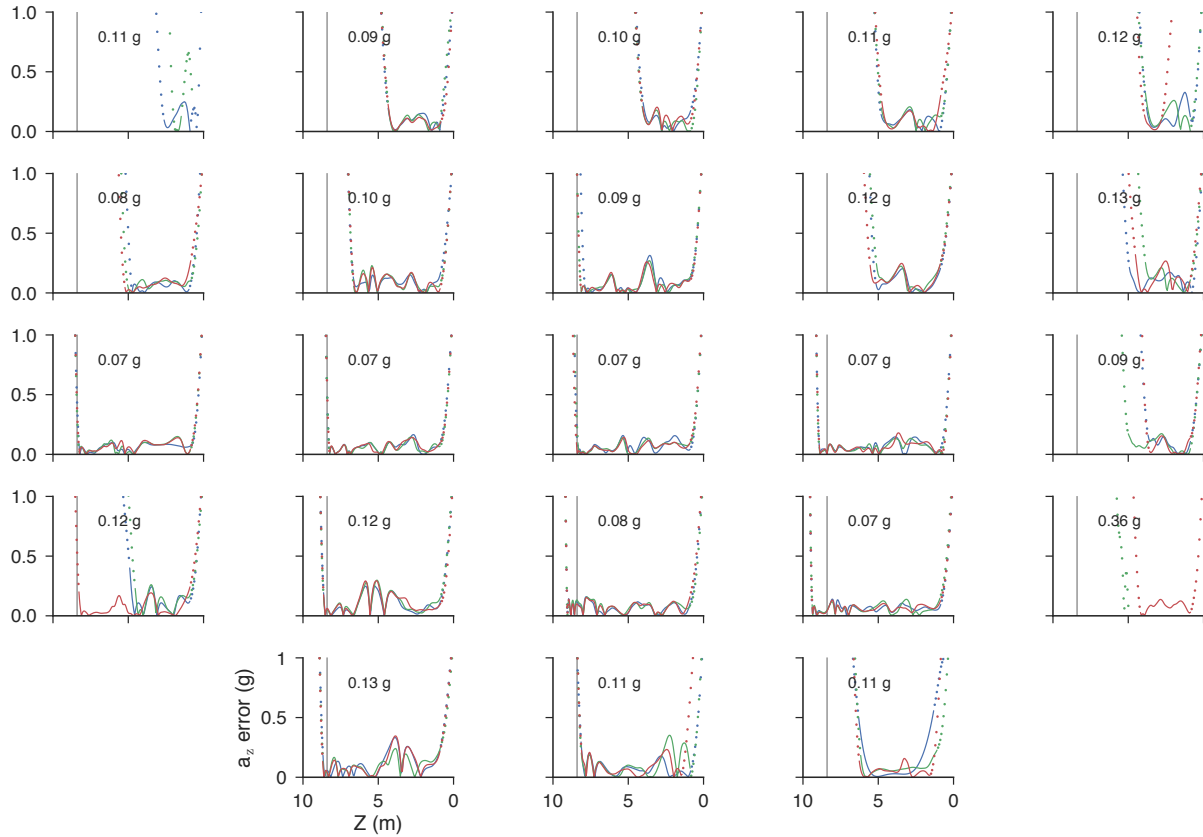


Figure C.17: Ball drop acceleration errors vs. height within the Cube.. The small multiples correspond to the grid of drop locations in figure C.16. Errors are reported in units of gravitational constant  $g$ , and printed values for each plot are the average errors of the solid lines. The markers indicate the errors for the first 8 and last 10 time points, which we determined contributed larger errors and were excluded from the analysis. The vertical gray line indicates the average jump height of 8.4 m.

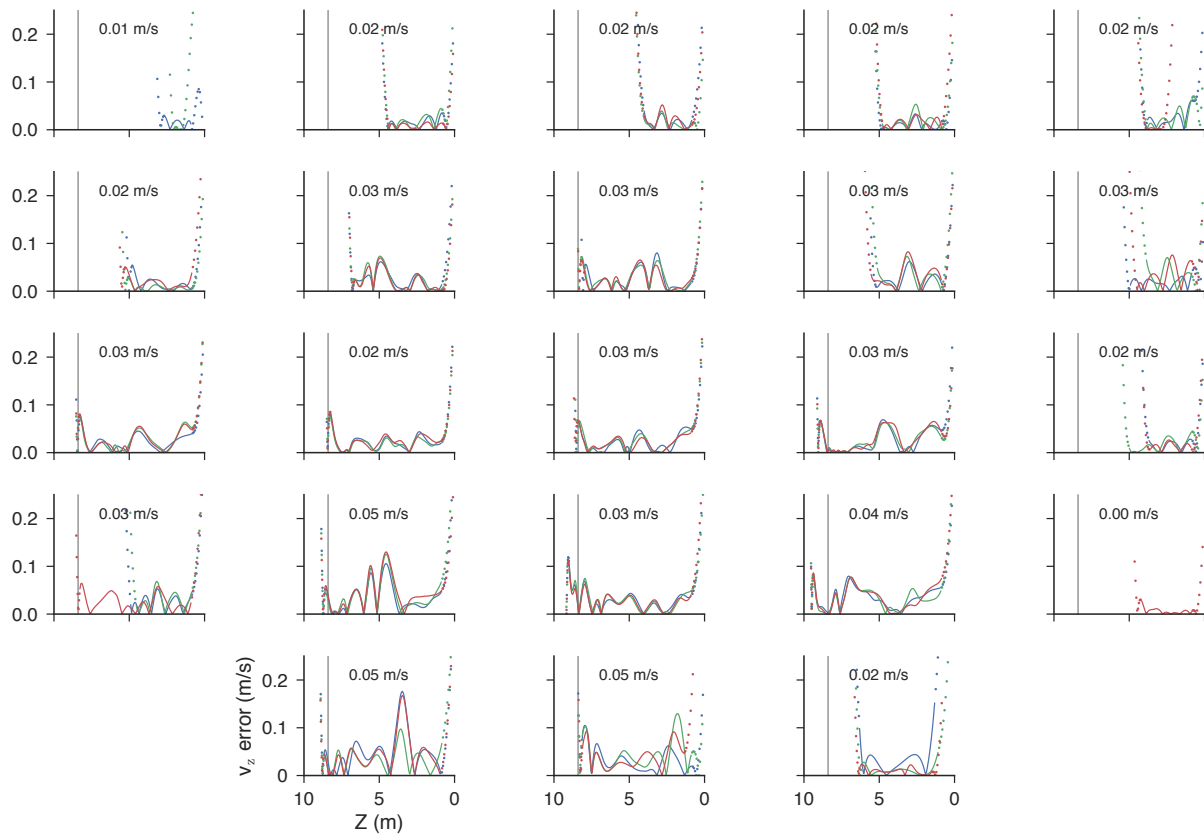


Figure C.18: Ball drop velocity errors found by fitting linear polynomials to the time series data of velocity.

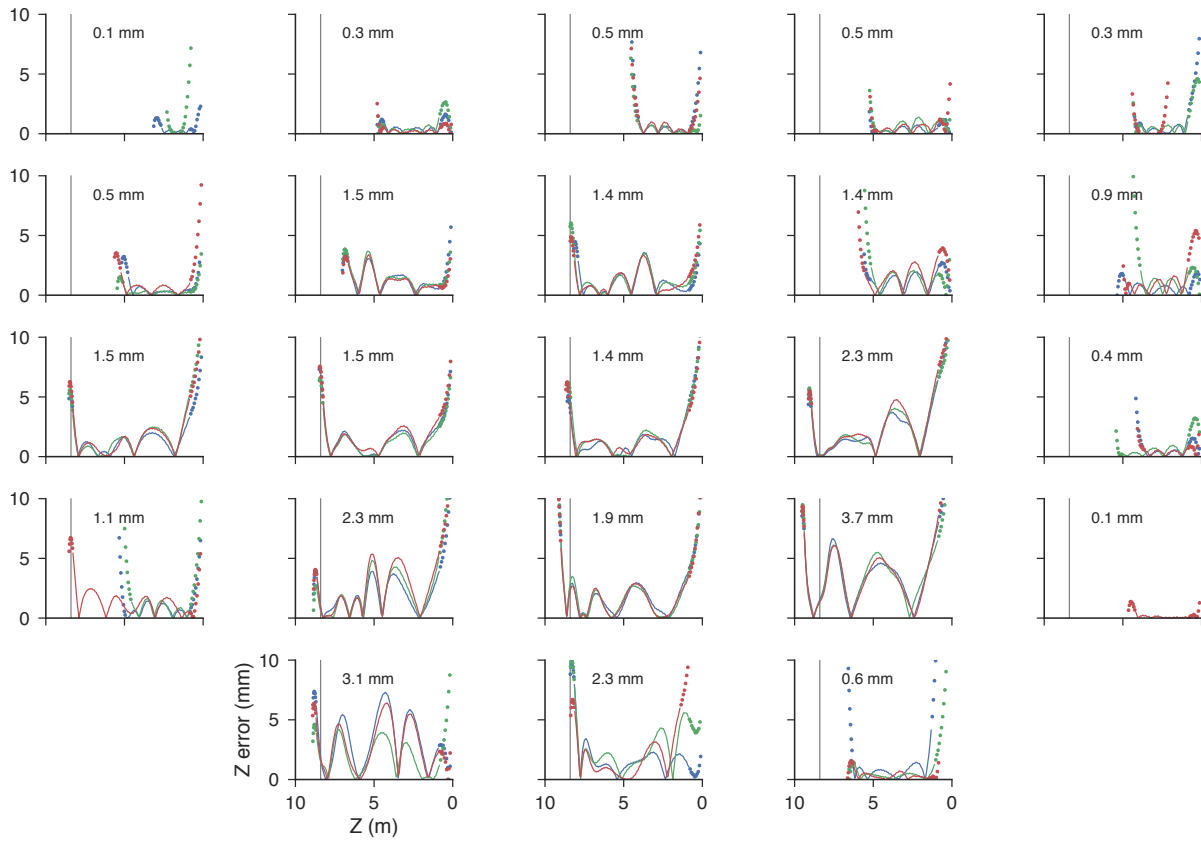


Figure C.19: Ball drop position errors found by fitting quadratic polynomials to the time series data of filtered position.

## C.5 Global natural cubic spline fitting to the snake's body

We fit a cubic polynomial between the recorded points on the snake's body. If there are  $n + 1$  infrared markers on the snake's body, we need to fit  $n$  splines between these points. Each spline has the form

$$\vec{x}_i(t) = \vec{a}_i + \vec{b}_i t + \vec{c}_i t^2 + \vec{d}_i t^3 \quad (\text{C.5.1})$$

where  $\vec{x}_i = [x_i(t), y_i(t), z_i(t)]$  is the spline function,  $t$  is the segment parameter limits, and  $a$ ,  $b$ ,  $c$ , and  $d$  are coefficients that must be determined. We have the following constraints on the spline:

$$\begin{aligned} \vec{x}_i(0) &= \vec{p}_i \\ \vec{x}_i(t_i) &= \vec{p}_{i+1} \\ \vec{x}'_i(0) &= \vec{m}_i \\ \vec{x}'_i(t_i) &= \vec{m}_{i+1} \end{aligned} \quad (\text{C.5.2})$$

where  $p_i$  is the measured marker position,  $m_i$  are the tangent vectors at each marker, and the prime is a derivative with respect to  $t$  (position along the spline). Given these constraints, the three-tuple vector coefficients are

$$\begin{aligned} \vec{a}_i &= \vec{p}_i \\ \vec{b}_i &= \vec{m}_i \\ \vec{c}_i &= 3(\vec{p}_{i+1} - \vec{p}_i) / t_i^2 - (2\vec{m}_i + \vec{m}_{i+1}) / t_i \\ \vec{d}_i &= 2(\vec{p}_i - \vec{p}_{i+1}) / t_i^3 + (\vec{m}_i + \vec{m}_{i+1}) / t_i^2 \end{aligned} \quad (\text{C.5.3})$$

We require second derivative continuity, i.e.  $C^2$  continuous splines, so we need to solve the above equations simultaneously for the  $n - 2$  tangent vectors  $\vec{m}$ . We have two additional constraints for the start and end tangent vectors. For this, we select the natural spline constraints,  $\vec{x}''_1(0) = 0$  and  $\vec{x}''_{n-1}(t_{n-1}) = 0$ . To solve for the tangent vectors, we formulate



spline that represents that backbone of the animal between the  $n + 1$  measured positions. We denote the backbone position as  $\mathbf{r}$  and it is given by

$$\mathbf{r} = [\vec{x}_0, \dots, \vec{n}] \quad (\text{C.5.6})$$

where we select how many evaluation points are in each segment as described above. Since we have analytical expressions for the spline, we can analytically calculate how the spline changes with distance along the body. In full, we have,

$$\mathbf{r} = \mathbf{a} + \mathbf{b}t + \mathbf{c}t^2 + \mathbf{d}t^3 \quad (\text{C.5.7})$$

$$\mathbf{r}' = \mathbf{b} + 2\mathbf{c}t + 3\mathbf{d}t^2 \quad (\text{C.5.8})$$

$$\mathbf{r}'' = 2\mathbf{c} + 6\mathbf{d}t \quad (\text{C.5.9})$$

$$\mathbf{r}''' = 6\mathbf{d} \quad (\text{C.5.10})$$

where the bolds indicate that each variable has a  $[x, y, z]$  component, the prime denotes a derivatives along the spline, i.e.  $\partial/\partial s$ , and  $t$  is understood to include a segment function values. The tangent vector, that is, the unit vector that is tangent to the body and locally points posteriorly down the body, is given by

$$\hat{T} = \frac{\mathbf{r}'}{\|\mathbf{r}'\|} \quad (\text{C.5.11})$$

The signed curvature,  $\kappa$ , determines how fast the unit tangent vector rotates. It is given by the following equivalent expressions based on what information is available:

$$\kappa = \frac{\partial \hat{T}}{\partial s} = \hat{T}' \quad (\text{C.5.12})$$

$$\kappa = \frac{\mathbf{r}' \times \mathbf{r}''}{\|\mathbf{r}'\|^3} \quad (\text{C.5.13})$$

or from the parametric spline curve as

$$\kappa = \frac{(z''y' - y''z') + (x''z' - z''x') + (y''z' - x''y')}{(x'^2 + y'^2 + z'^2)^{3/2}} \quad (\text{C.5.14})$$

For completeness, the torsion is a measure of how much out-of-plane bending occurs for a space curve. It is given by

$$\tau = \frac{(\mathbf{r}' \times \mathbf{r}'') \cdot \mathbf{r}'''}{\|\mathbf{r}' \times \mathbf{r}''\|^2} = \frac{x'''(z''y' - y''z') + y'''(x''z' - z''x') + z'''(y''z' - x''y')}{(z''y' - y''z')^2 + (x''z' - z''x')^2 + (y''z' - x''y')^2} \quad (\text{C.5.15})$$

A limitation with the cubic used here is that the curvature is not a smooth function, but piecewise connected quadratic functions. However, the tangent angle, or any angle derived from the tangent vector, will be a smooth and continuous function. This is shown in figure C.20, where we test the global natural cubic splines on a 2D serpenoid curve. A serpenoid curve is a space curve with a sinusoidally varying curvature; we prescribe a curvature, which defines the tangent angle  $\theta$ , and  $x$  and  $y$  position, and then try to reconstruct these values. These are given by

$$\kappa(s) = \sin s \quad (\text{C.5.16})$$

$$\theta(s) = \int_0^s \sin s' ds' = -\cos s \quad (\text{C.5.17})$$

$$x(s) = \int_0^s \cos \theta(s') ds' \quad (\text{C.5.18})$$

$$y(s) = \int_0^s \sin \theta(s') ds' \quad (\text{C.5.19})$$

Figure C.20a shows the prescribed curvature and tangent angles for  $0 \leq s \leq 2\pi$ , where the markers indicate the angles at the “measurement” positions. We subsample the body at 11 points (figure C.20c) and reconstruct the body using the splines. From the spline, we calculate the tangent vector using (C.5.11), the tangent angle as  $\text{atan2}(\hat{T}_y, \hat{T}_x)$ , and the curvature using (C.5.14). These are shown in figure C.20b as the dashed lines. This plot shows that the tangent angle is recovered, but not the curvature. In fact, the curvature is segments of quadratic functions between the measurement locations and does not recover the sinusoidal curvature well. As noted above, the spline segment parameters are not guaranteed to be the arc length. The arc length is given by

$$s = \int_0^s \sqrt{\left(\frac{\partial x}{\partial t'}\right)^2 + \left(\frac{\partial y}{\partial t'}\right)^2 + \left(\frac{\partial z}{\partial t'}\right)^2} dt' \quad (\text{C.5.20})$$

which we calculate from the spline derivative relative to the selected spine parameter  $t$ . The difference between the segment parameter  $t$  and the arc length  $s$  is shown in figure C.20d.

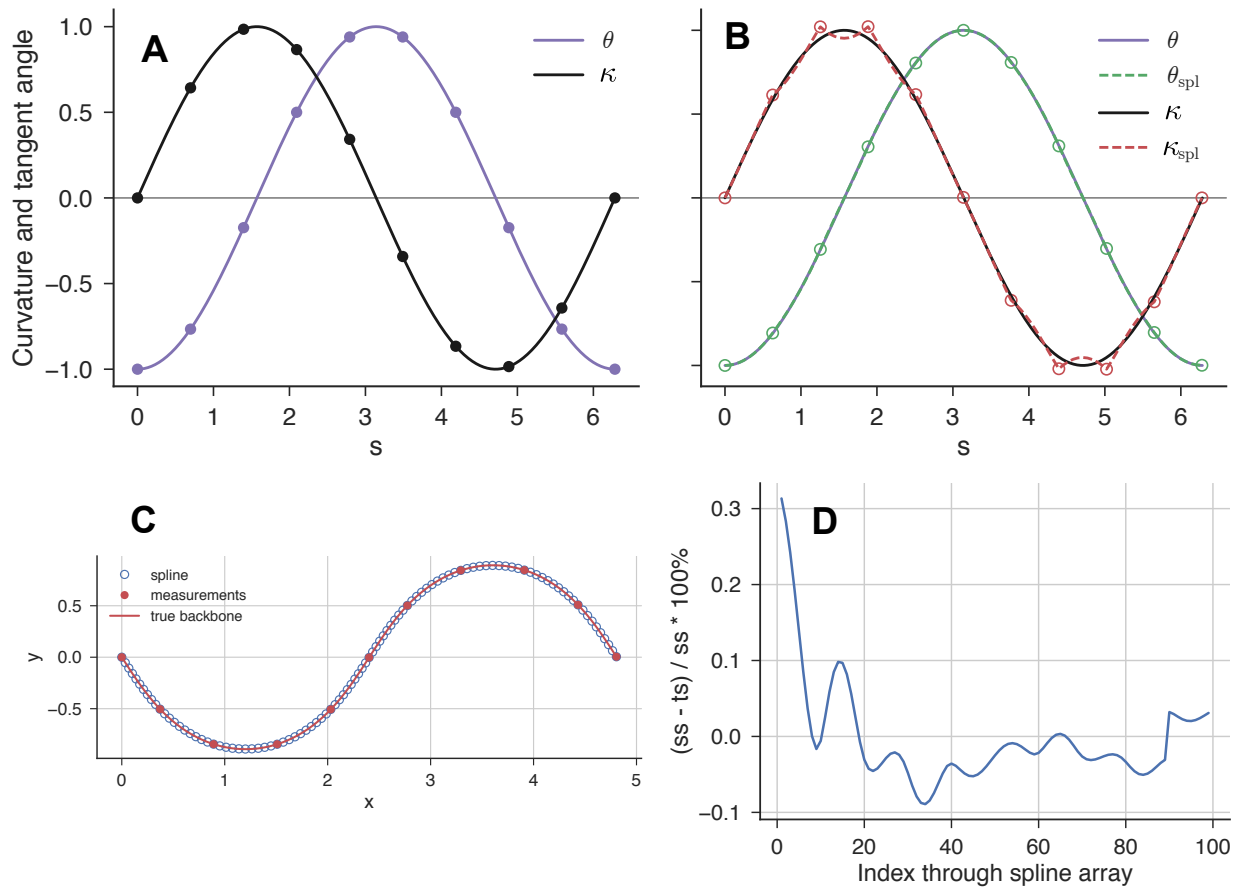


Figure C.20: Numerical test of global natural cubic splines on a 2D serpenoid curve. (a) Prescribe curvature  $\kappa$  (black) and tangent angle  $\theta$  (magenta). (b) Reconstructed curvature and tangent angle from the spline. Note that the curvature is non-smooth. The tangent angle is. (c) Analytical serpenoid curve and the subsampled “measurement” locations (red dots) that the spline were fit to. The spline was sampled at 100 locations and closely matches the body. (d) The error in the arc length of each segment ( $ss$ ) and the length of the segment parameters ( $ts = \Delta t$ ). The length errors are small.

**Digitizing images of snakes to calculate landmark position along the body**

The spline requires the position of each landmark point (infrared marker) along the body. The position of the landmark points varied between individuals and between days when some landmark points had to be replaced. The head, vent, and tip of the tail were always marked, but the number of markers along the body and tail varied with animal size. At the end of each day of testing, photographs of each animal were taken from above, with the animal near a calibration object, such as a ruler or the motion capture system calibration wand. From the photographs, the back of the snake was digitized in ImageJ, with the location of the markers indicated (figure C.21A). A spline was fit to the digitized points, and the arc length distance between the markers calculated (figure C.21B,C). This

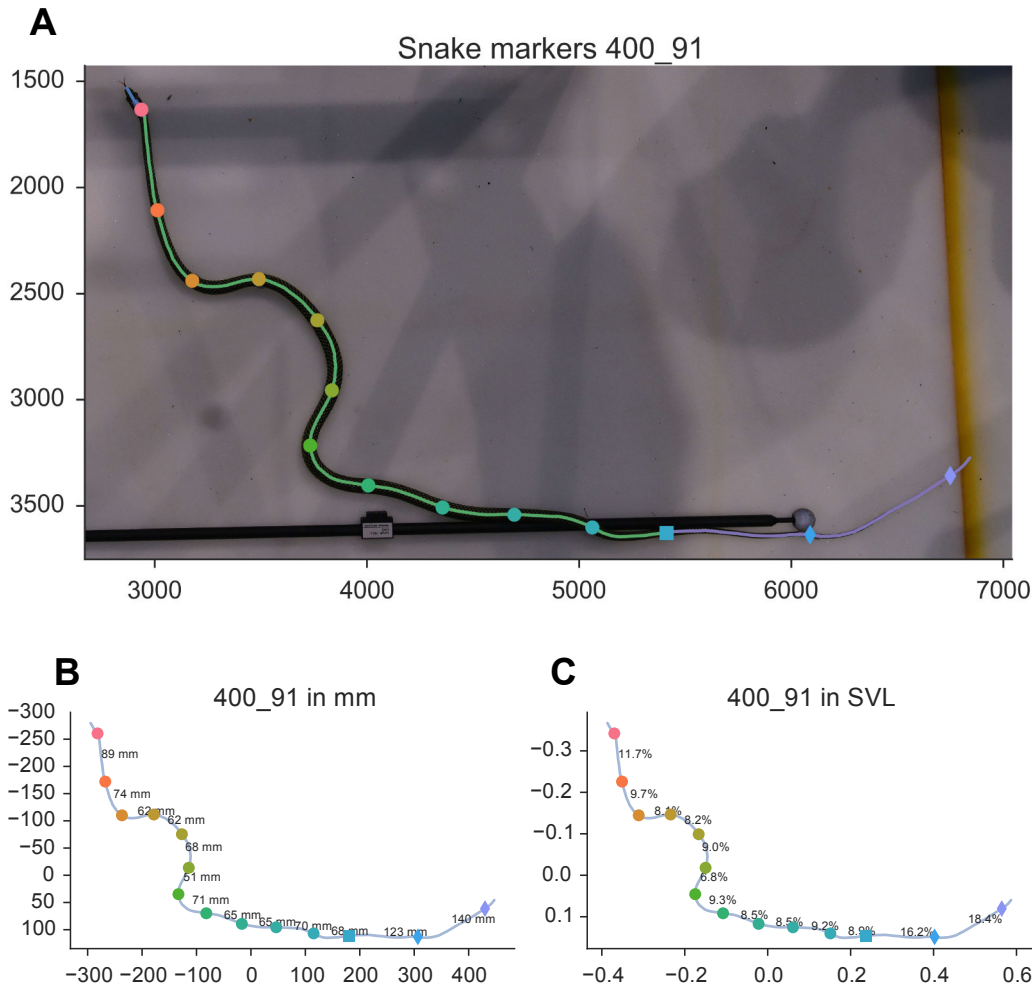


Figure C.21: Digitized snake image to calculate landmark positions along the body. (A) Overhead image of snake 91 at the end of day 4 of trials that was digitized manually. Splines were fit to the digitized points, and separated by different regions of the body, with the head in blue, the body in green, and the tail in purple. The landmarks along the body are denoted by circles, the vent as a square marker, and the landmarks along the tail as diamonds. (B and C) The position between the landmark points was found by integrating along the arc length of the spline in physical units (B) and in units of snout-vent length in (C).

## C.6 Linear mass distribution and calculating center of mass

The spline fit to the snake’s body provides an estimate of the time-varying three-dimensional position of the snake’s backbone as it undulates through the air. From the spline, we superimpose an average the linear mass density,  $\rho(s)$ , where  $\rho$  is the density that varies with distance  $s$  along the body.

### C.6.1 Sectioning measurements

We measured the linear mass density of three snakes by sectioning, from the snout to the tip of the tail, using roughly 10 mm segments. Individual specimens (see table C.2) were removed from the lab freezer and placed under warm flowing water to thaw the body. Once freely movable, the snake was removed from the bag and placed in a long tinfoil tray and straightened along a lab bench. The snake was then placed back into the freezer, as a cold and rigid body cut more cleanly. We performed sectioning on a custom cutting jig. The jig consisted of a rectangular aluminum channel with a horizontal blade channel and small groove along the bottom. A stopper was glued 10 mm from the edge of the blade channel. The whole jig was bolted to a smaller optical breadboard, and the whole unit was placed in the freezer to help slow the warming of the snake body.

Sectioning began at the snout, which was placed against the stopper, and the body held along one side of the aluminum channel. Single pass cuts using an extendable blade X-acto knife were used to cut the body. The individual pieces were then placed into separate aluminum trays, with ten pieces per tray, and placed in the freezer. Once the entire body was sectioned and all pieces were frozen, we measured the mass and length of each section using a Mettler Toledo digital scale and Fisher Scientific digital calipers. Frozen sections gave more consistent results and were easier to handle.

Table C.2: Overview of *C. paradisi* specimens used for the mass distribution measurements.

Snake ID	SVL (cm)	Tail (cm)	Mass (g)	DoD	# segments
80	80.5	20.0	—	2013-06-03	106
87	—	—	—	2013-06-19	86
92	—	—	—	2014-02-17	85



Figure C.22: Snake 87 immediately removed from the lab freezer, shown in (a) dorsal and (b) ventral views. The specimen was kept in the plastic bag and run under warm water to thaw the body. (c) Cross section from a fresh specimen (image from Jake Socha).

### C.6.2 Analysis of linear mass distribution data

Sectioning was performed for three individuals with varying masses and number of sections based on the length of the animal and tail (figure C.23a). The density of each segment  $i$  was calculated as  $\rho_i = m_i/l_i$  (figure C.23b). Lastly, we normalize the density by the average density,  $\bar{\rho} = m_{\text{total}}/\text{SVL}$ . This normalization causes all of the density distributions to collapse onto a single curve (figure C.23c). From the normalized data, we linearly interpolate each snake's distribution onto a grid of  $s = 0, .01, \dots, 1.35$  and average each of the values. This results in the black curve in figure C.23c that was ultimately used to calculate the mass distribution from the splines. We note that the head has higher density than the rest of the body, and that the heart is likely present at  $s \approx 25\%\text{SVL}$ , denoted by the increase in density at that location. Also from the density measurements, we determined that the tail is approximately 35% of the snout-vent length.

### C.6.3 Smoothed mass density used in the dynamical model

We used a parabolic fit to the density data for the head and body as the input density distribution for the glide simulations. This was done to provide a smoothed input. To fit the data, we separated the head and body because they very different densities. We define the head as distances along the body from  $0 \leq s \leq 0.04$  (in units of SVL), and the body

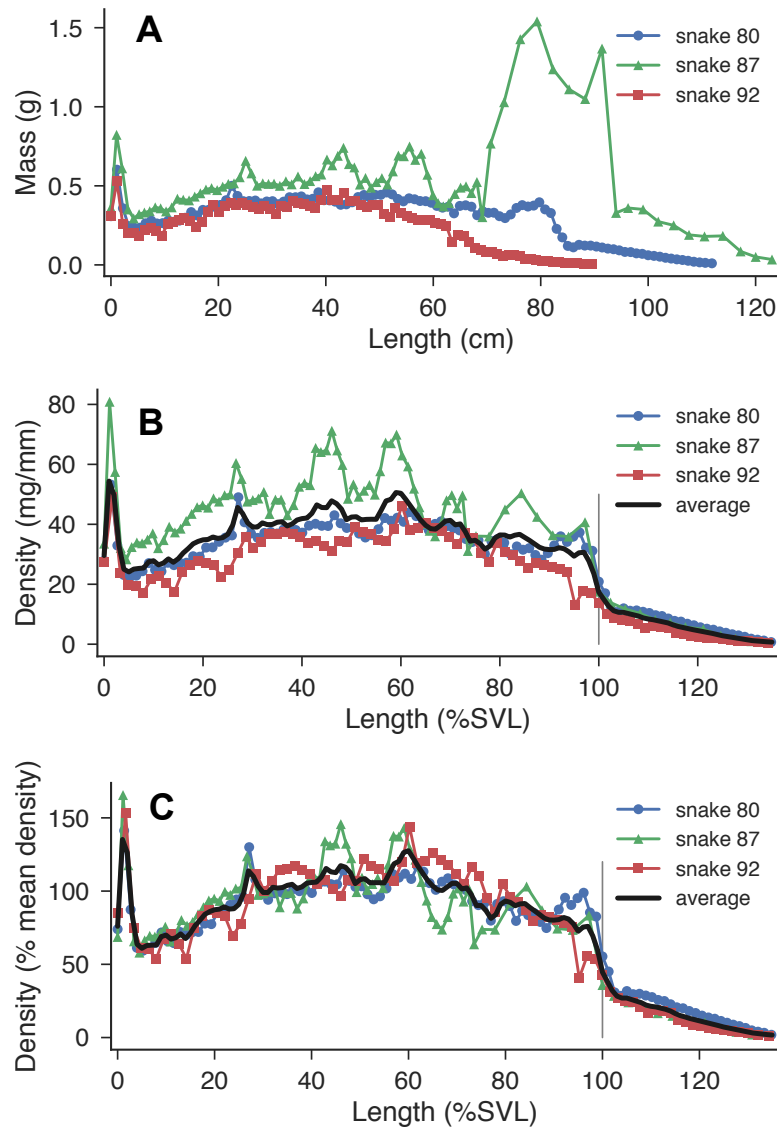


Figure C.23: Raw linear mass density measurements. (a) Measured mass of each  $\approx 10$  mm segment. Specimen 87 showed signs of tissue degradation, so larger sections were used along the posterior section of the body, hence the larger masses of the individual segments. Also, there is more variation with this measurement than the other specimens. (b) Density of each individual segment. (c) Normalized density (density divided by the average density) for each specimen, and the average value (in black) used for mass calculations from the Cube data.

as  $0.04 < s \leq 1$ . The normalized density data (figure C.23) from each snake was grouped and a non-linear least squares parabolic fit was used (figure C.24a). A parabolic fit was selected because visually the distributions appear parabolic and a low order polynomial reduces overfitting. Also, the width distribution is nominally parabolic as well (discussed

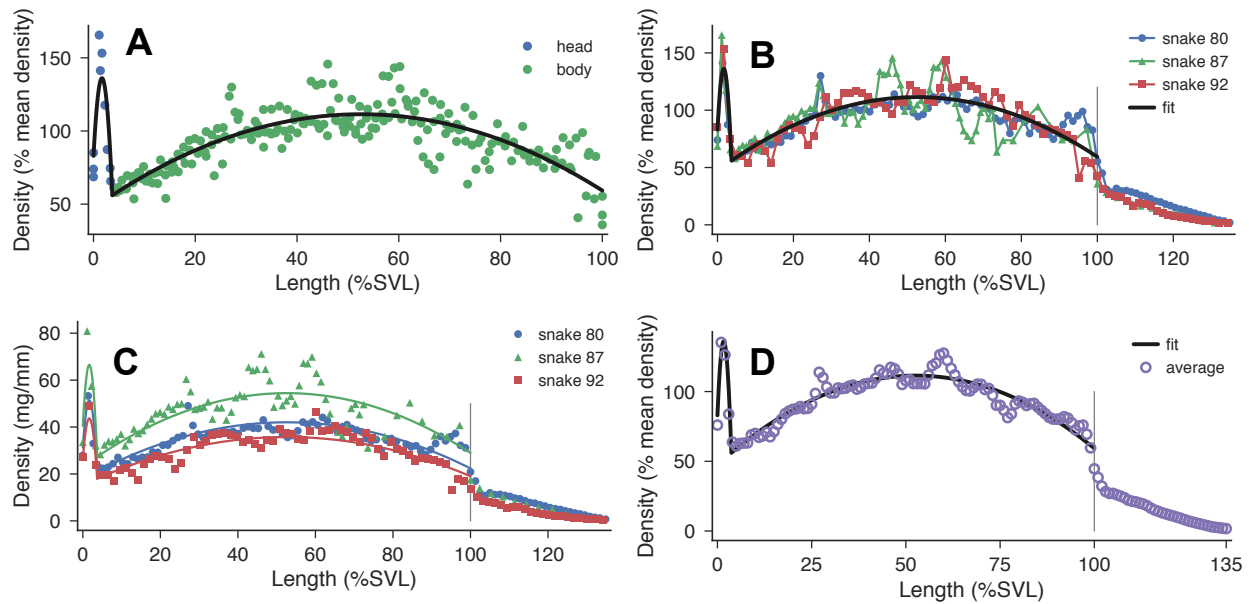


Figure C.24: Parabolic fits to the linear mass density distributions. (a) The head (blue) and body (green) were separated and the data from each specimen grouped together. The parabolic fit for each region is shown with the black line. (b) Comparison of the parabolic fit to the normalized density for each specimen. (c) Comparison of the parabolic fit to the density in physical units for each specimen. (d) Comparison of the parabolic fit to the average normalized density (figure C.23c).

below). The fit has the form

$$\rho = a(s - h)^2 + k \tag{C.6.1}$$

where the sign of  $a$  gives the up/down orientation of the parabola, and the vertex is located at the body position  $h$  and non-dimensional density  $k$ , i.e.  $(h, k)$ . The fit values and errors are shown in table C.3, and the resulting fit is shown in figure C.24b for all of the snake trials. Figure C.24c shows the parabolic fit scaled to physical units for each specimen, and figure C.24d shows that the parabolic fit closely matches the average normalized density (the black line in figure C.23c).

Table C.3: Parabolic fits to the linear mass density data.

Segment	$s$ range (%SVL)	RMS error	$h$	$k$	$a$
Head	$0 \leq s \leq 3.7$	19%	.017	1.36	-1924.4
Body	$3.7 < s \leq 100$	12%	.523	1.11	-2.32

The aerodynamic force produced by each section of the snake's body is proportional to the area of that segment of the body. To provide better estimates of the aerodynamic forces

and to increase the fidelity of our 3D visualizations, we measured the width as a function of distance along the body from three flying snakes shortly after takeoff. For this analysis, we used six images from three snakes of varying mass and length (table C.4).

Figure C.25 depicts the steps to calculate the chord length distribution. First, the images were thresholded using Otsu thresholding, resulting in a binary image of the snake’s body in the ‘S’-shaped glide configuration. Next, the Euclidian distance transform is applied to the image, which measures the distance between each pixel and the closes pixel at the boundary (figure C.26). This is the measure of the width of the the snake. Next, the binary image is skeletonized, such that the body is represented by a continuous line of single pixels. There are spurious branches of the skeleton that are removed by checking the neighbors around the branches. The Euclidean distance transformed image is then sampled along the cleaned skeleton, resulting in the width of the animal in pixels. Next, the snout, vent, and tip of the tail are digitized, and the width is normalized by the SVL, and the data was exported (figure C.27).

The width distributions were fit with a parabola for use in the dynamical model. The fit parameters are shown in table C.5. Looking at the maximum width from the parabolic fit compared to scaling of the maximum width with SVL (figure C.28), the image processing underestimated the with by 13%. The width distributions where then increased by this correction factor and then used in further processing of the data (figure C.27D,E).

Table C.4: Snake and image meta data used along side image processing to measure the width of the snake mid-glide. The snakes used for this analysis are from Socha and LaBarbera (2005) [9].

Snake	File name	Mass (g)	SVL (cm)	Tail (cm)	Wing loading N/m <sup>2</sup>	Total length cm
44	s763_34_03_silhouette.tif	16.3	54.2	19.2	22.6	73.4
44	s763_34_05_silhouette.tif	16.3	54.2	19.2	22.6	73.4
33	s782_39_17_silhouette.tif	35.9	68.5	25.3	31.1	93.8
33	s782_silhouette_S00_39_18.tif	35.9	68.5	25.3	31.1	93.8
40	s845_53_25_silhouette.tif	27.4	63.5	24.4	28.5	87.9
40	s845_53_26_silhouette.tif	27.4	63.5	24.4	28.5	87.9

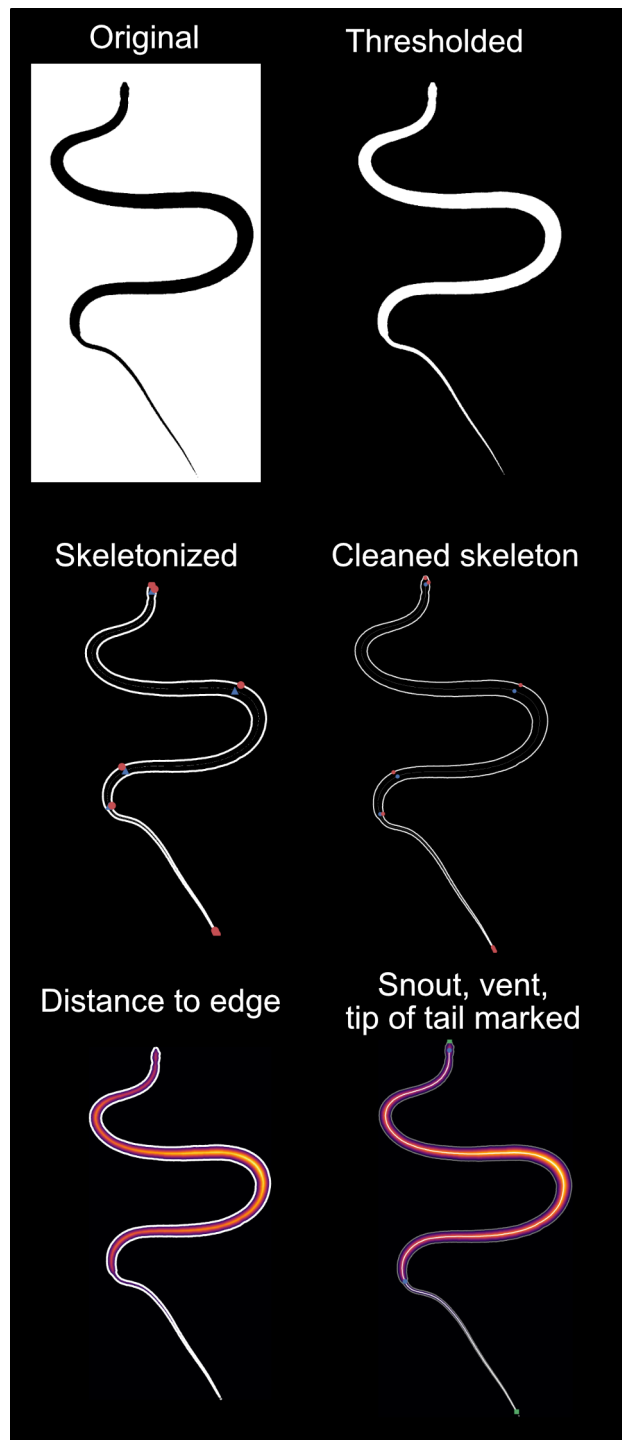


Figure C.25: Image processing steps to calculate the width of the snake as a function of distance along the body.

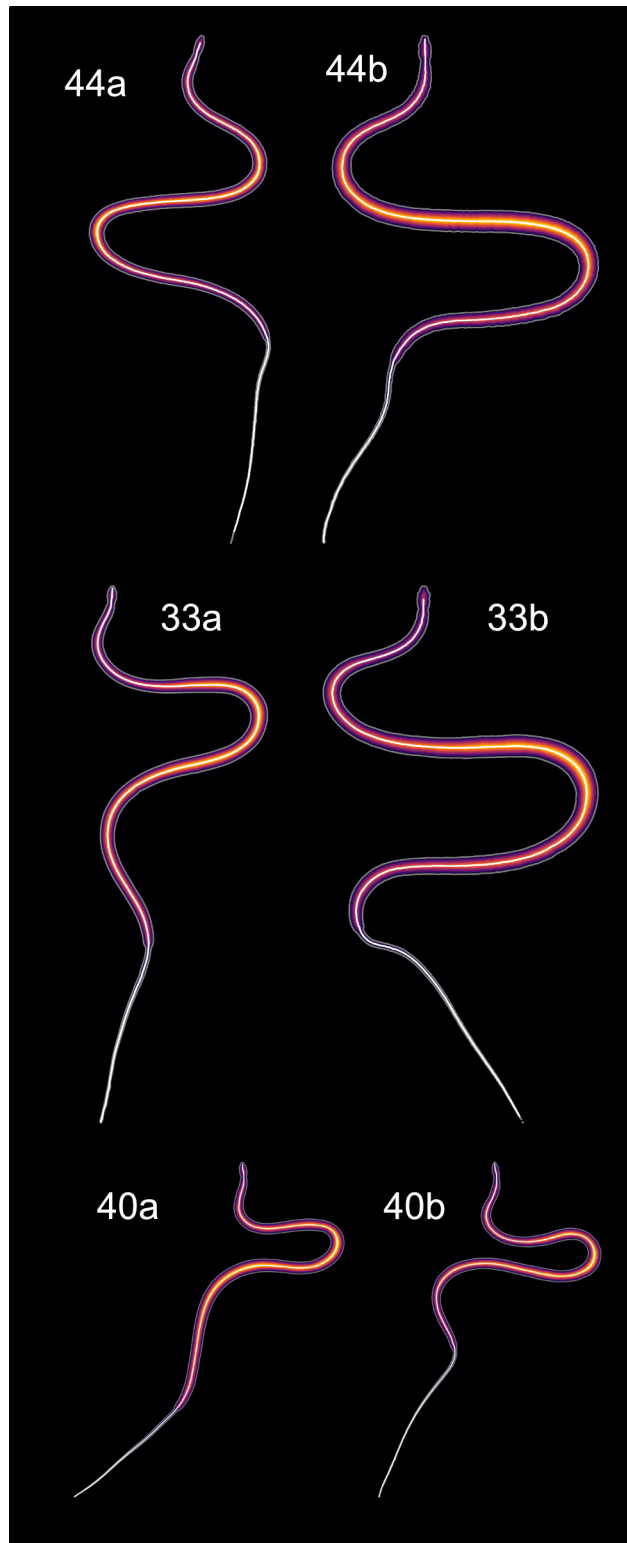


Figure C.26: Pseudo-color images of six snapshots from three individuals used in the width calculations.

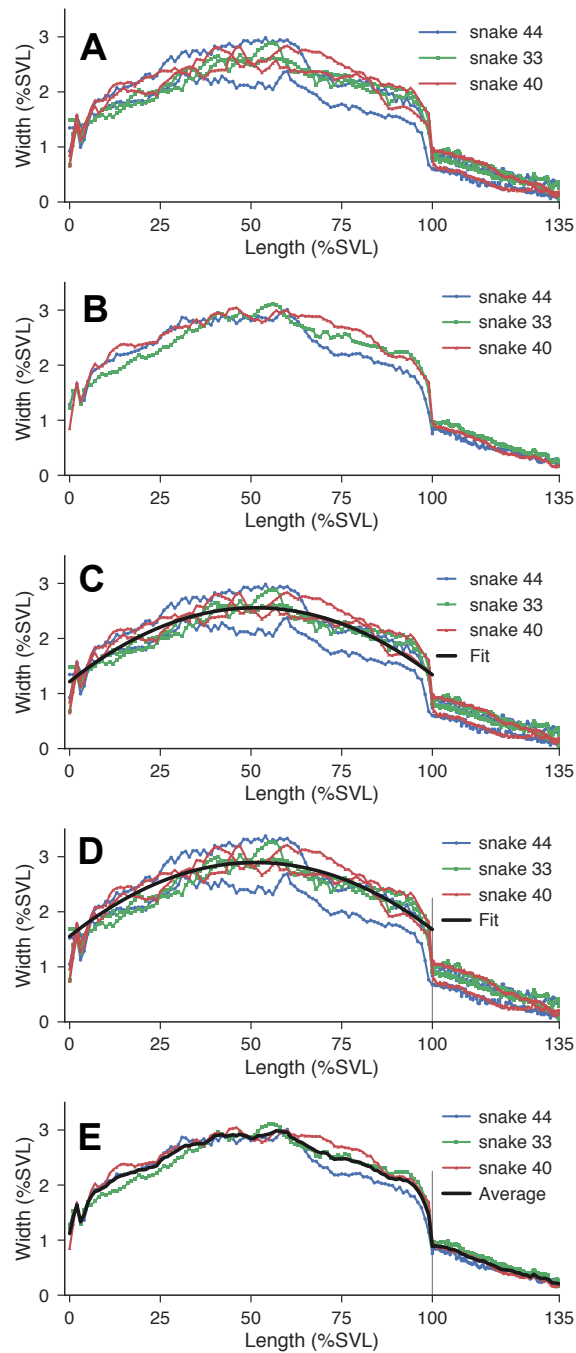


Figure C.27: Build-up for the width distribution. (A) Six width distribution from the image processing steps. (B) Width distributions, where the two measurements per animal have been averaged. (C) Parabolic fit to the width distributions. (D) The width distribution and parabolic fit after the  $1.13\times$  scaling correction has been applied. (E) Average width distribution for the body and tail that was used for further processing.

Table C.5: Parabolic fits to the width distribution.

Type	$s$ range (%SVL)	RMS error	h	k	a
Uncorrected	$0 < s \leq 1$	.15%	.512	0.026	-0.051
Corrected	$0 < s \leq 1$	.15%	.512	0.029	-0.051

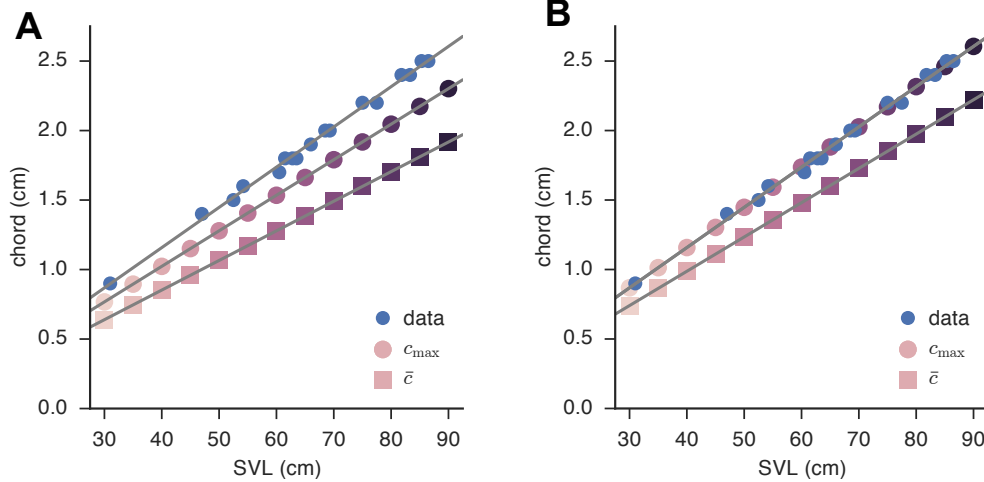


Figure C.28: Scaling of the chord length with SVL. (A) The maximum chord length from the parabolic fit of figure C.27C was too low. (B) The ratio of the slopes of the best fit line resulted in the scaling correction of  $1.13\times$  used in figure C.27D,E.

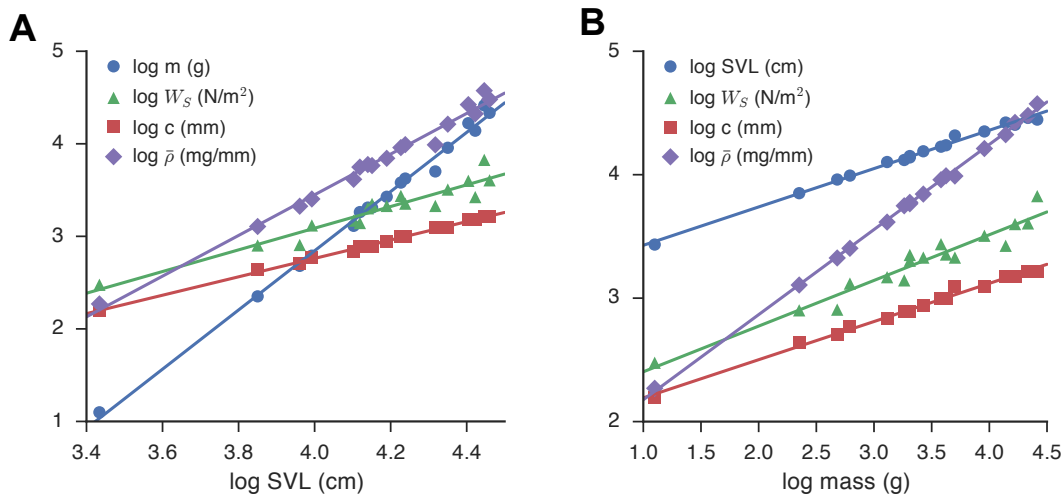


Figure C.29: Scaling of wing loading, maximum width, and average density with (A) SVL and (B) mass. The scaling exponents are presented in table C.6.

## C.7 Flying snake morphometrics

Using data from previous flying snake studies [9, 22], the scaling exponents for flying snake mass, wing loading, chord width, and average density were found. This information was used to scale the dynamical model parameters for a given snake length. These scaling relationships are shown in figure C.29 with SVL or mass as the independent variable. The scaling exponents are presented in table C.6.

Table C.6: Scaling exponents for flying snake morphometrics (figure C.29). Regressions were performed as per [110].

x	y	y-intercept	slope	$R^2$
log(SVL) — cm	log(m) — g	-9.95	3.20	0.9937
log(SVL) — cm	log( $W_S$ ) — N/m <sup>2</sup>	-1.59	1.17	0.9132
log(SVL) — cm	log(c) — mm	-1.21	0.99	0.9963
log(SVL) — cm	log( $\bar{\rho}$ ) — mg/mm	-5.34	2.20	0.9867
log(m) — g	log(SVL) — cm	3.12	0.31	0.9937
log(m) — g	log( $W_S$ ) — N/m <sup>2</sup>	2.03	0.37	0.9393
log(m) — g	log(c) — mm	1.88	0.31	0.9920
log(m) — g	log( $\bar{\rho}$ ) — mg/mm	1.49	0.69	0.9987

## **C.8 Performance comparison between Cube trials and previous flying snake experiments from Socha (2005)**

The recorded glides from the Cube were generally much steeper and covered less horizontal distance than previously recorded glides [8] (figure C.30A,B). Although snakes were released from 9.8 m, compared to 8.3 m from the Cube, they covered upwards of 15 m horizontally. The Cube trials covered up to 5 m. Some of the performance discrepancy is due to the larger snakes used in the Cube study (figure C.31). However, one would still expect the lightest individuals from the Cube trials to perform better. Another possibility is the snakes were less motivated to glide because they were not wild caught and habituated to human contact. Additionally, the Cube trials were the first glides recorded inside, where the visual environment is much different. Although a target tree was placed in the glide arena, this may not have provided the visual cue necessary to elicit higher performance glides.

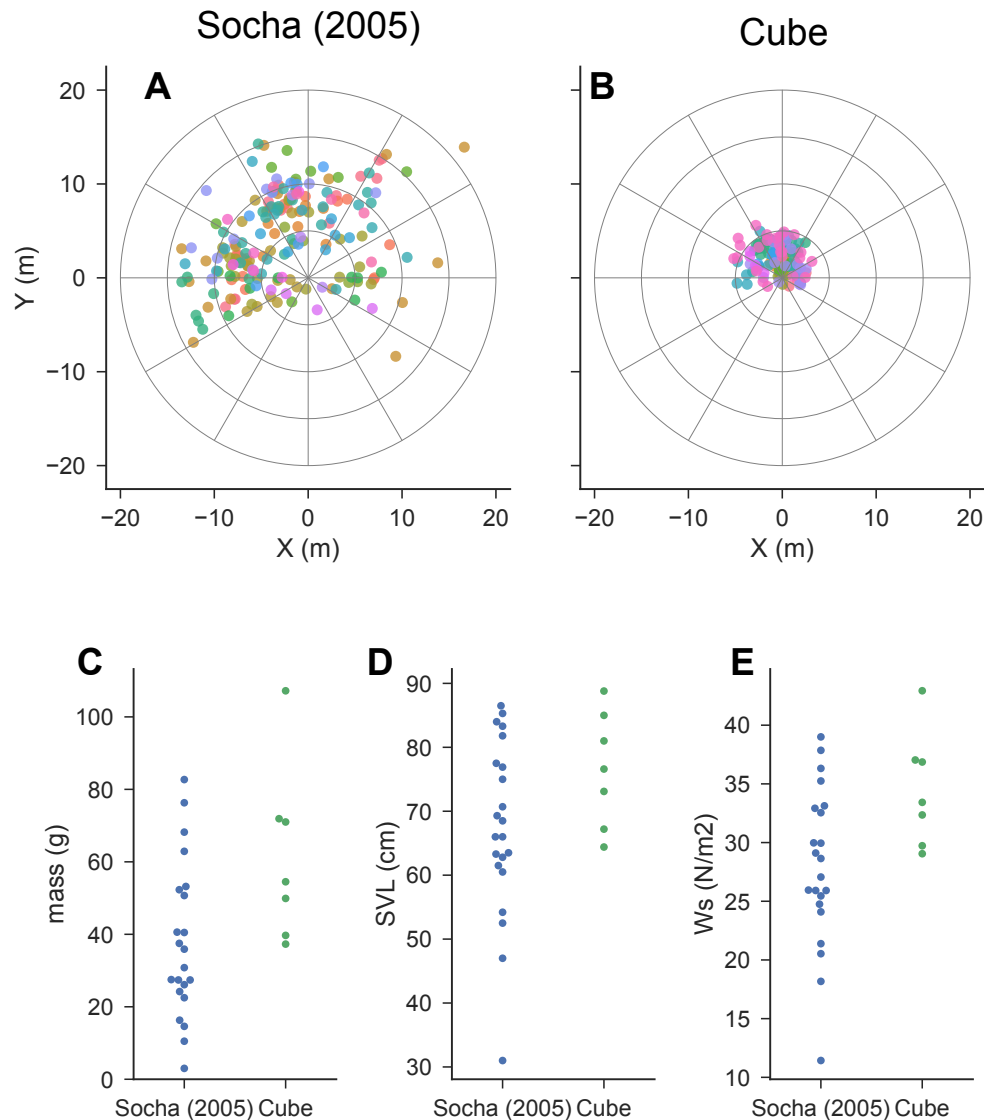


Figure C.30: Comparison of landing location and snake size from Socha, O’Dempsey, and LaBarbera (2005) and this study. (A) Overhead view of landing locations from all glide of Socha, O’Dempsey, and LaBarbera (2005) from a launch height of 9.8 m. Many individuals covered over 10 m horizontally, with many up to 15 m. (B) Overhead view of landing location locations from the Cube trials, from a launch height of 8.3 m. Many snakes did not surpass 5 m horizontally. (C)-(E) Comparison of animal mass, SVL, and wing loading from Socha, O’Dempsey, and LaBarbera (2005) and the Cube trials. The individuals from the Cube were generally longer and more massive, with higher wing loadings. Glide time should scale with  $\sqrt{W_S}$ , and distance covered should scale with  $W_S$ .

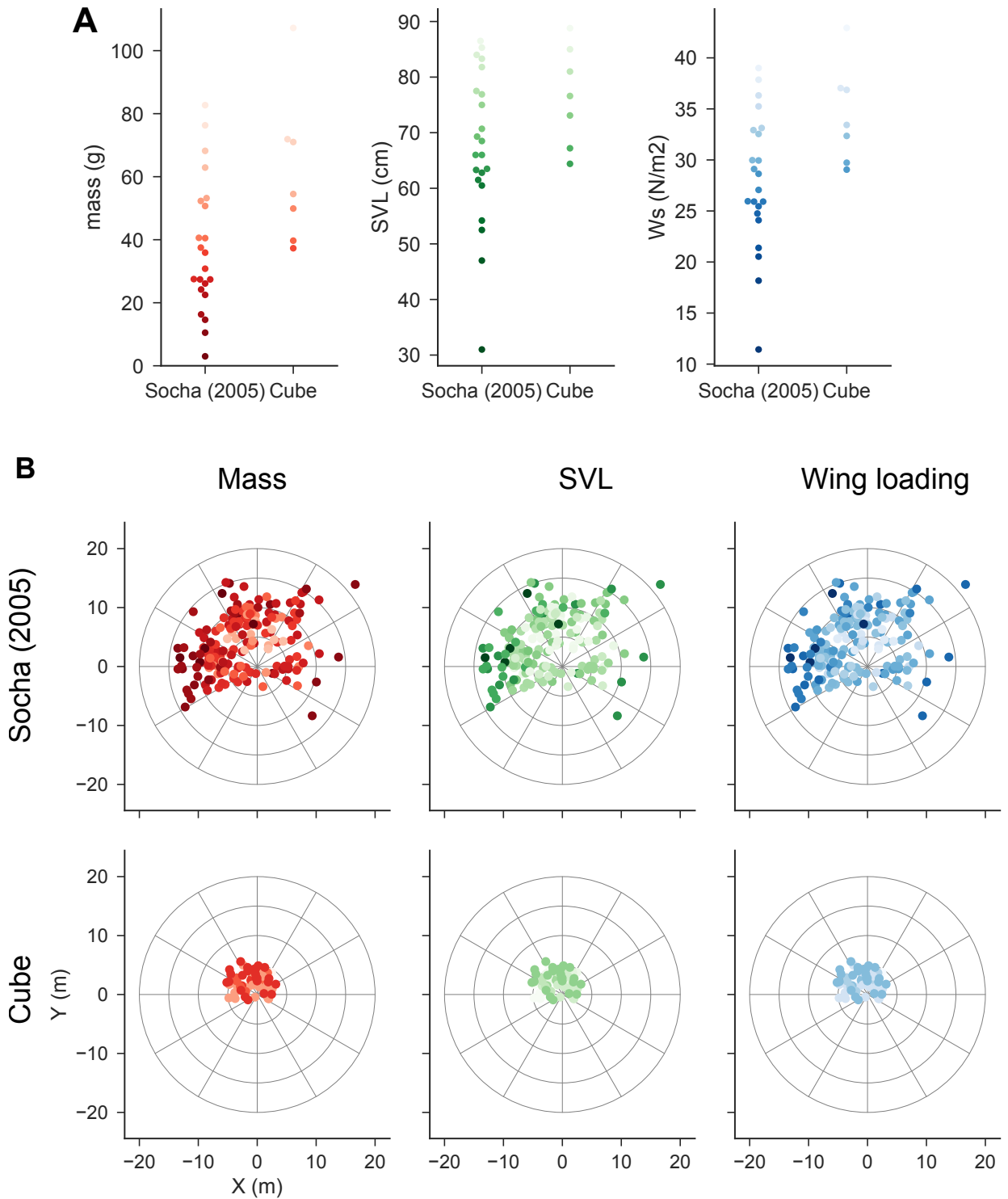


Figure C.31: Comparison of landing location and snake size from Socha, O'Dempsey, and LaBarbera (2005) and this study (same as figure C.30, but color coded by mass, SVL, and wing loading). (A) Ranges of mass, SVL, and wing loading from Socha (2005) and the Cube trials, where darker colors indicate lower values and smaller snakes. (B) Glide distance coded by color for different masses, SVLs, and wing loadings.

## C.9 Effect of missing data

The effect of missing data and the gap filling technique was tested by selecting a trial where there was no missing data (trial 413 from snake 91), and then degrading the time series 100 separate times. The degradation was done for each marker time series according to the statistics of the missing data, and then the full processing pipeline applied to the data. For each time series, the number of gaps is specified by selecting with replacement from the histogram in figure C.32A of number of gaps. Next, where the gaps start in the time series is selected from figure C.32B, and finally the length of the gap from figure C.32C. The percent of missing data from the Cube trials and the degraded time series match closely (figure C.33D).

The center of mass position, velocity, and accelerations, and forces show little variation with the addition of gaps (figure C.33). The accelerations and forces show the most variation, although they still follow the trends of the full time series. The RMS errors (figure C.34) are less than 0.5% for the position, less than 1% for the velocities, and generally less than 5% for the accelerations.

The effect of missing data on the complex orthogonal decomposition results has a larger effect (figure C.35). The temporal frequency ratio is not affected, but the spatial frequency ratio is; there are three outliers which show spurious results (figure C.35A). The horizontal wave amplitude ((figure C.35B) and vertical wave amplitude ((figure C.35C) also show errors, but not the dorsoventral bending angle (figure C.35D). These results indicate that the waveform can become deformed, at least during portions of the glide, which affects the complex orthogonal decomposition analysis.

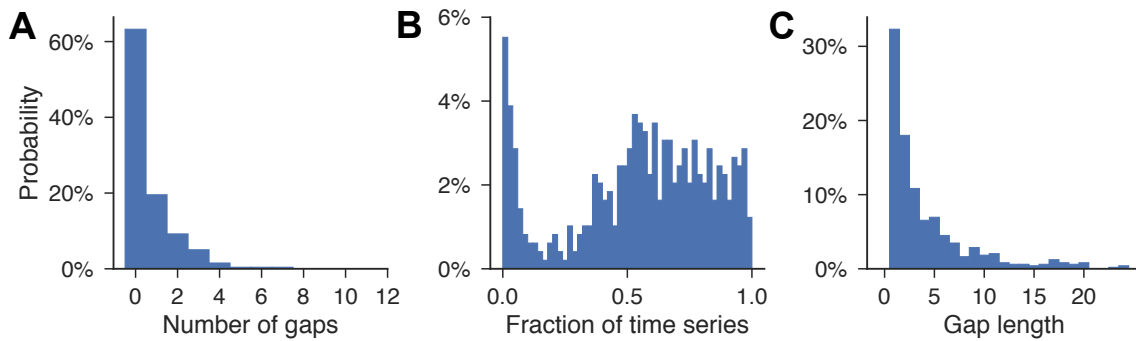


Figure C.32: Missing data statistics from the Cube trials. (A) Probability of any time series having gaps of different lengths. Over 60% of the recorded time series (each marker from each trial is treated separately) had no gaps, while about 20% of trials had one gap. (B) The probability of having a gap depends on where you are in the time series. Data is more likely to be missing at the beginning of the trial. There are fewer gaps one quarter through the trial, and about a 2% chance a gap will occur over 50% through the trial. (C) The gap length is generally small, but there are instances of very long gaps.

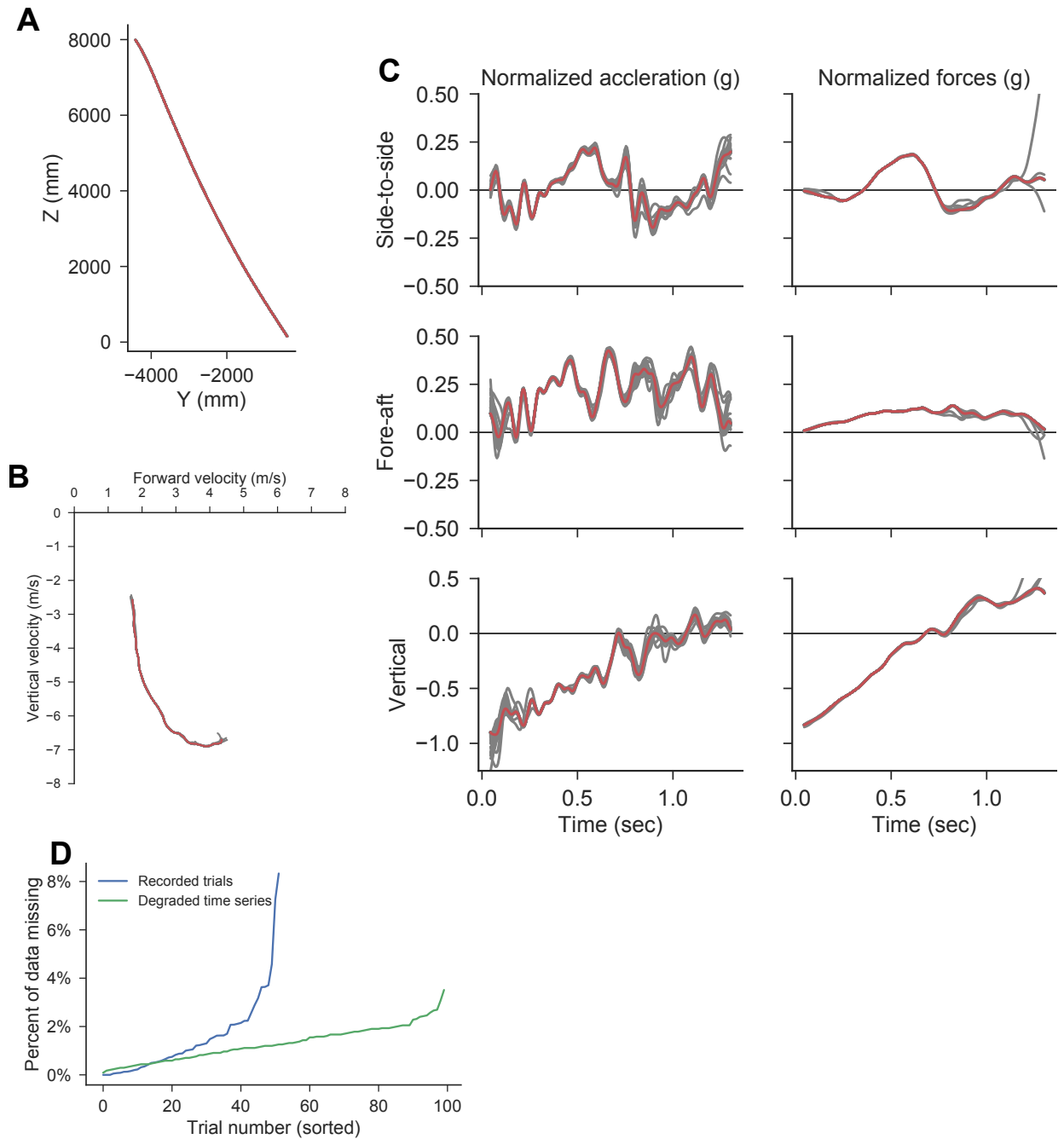


Figure C.33: Effect of missing data on center of mass position, velocity, accelerations, and calculated aerodynamic forces. The complete time series is shown in red, while the 100 degraded time series are shown in gray. (A) Side view of the center of mass position. (B) Velocity polar diagram. (C) Center of mass accelerations and resultant aerodynamic force. (D) Fraction of missing data is similar between the data missing from the Cube trials (blue) and the degraded time series (green).

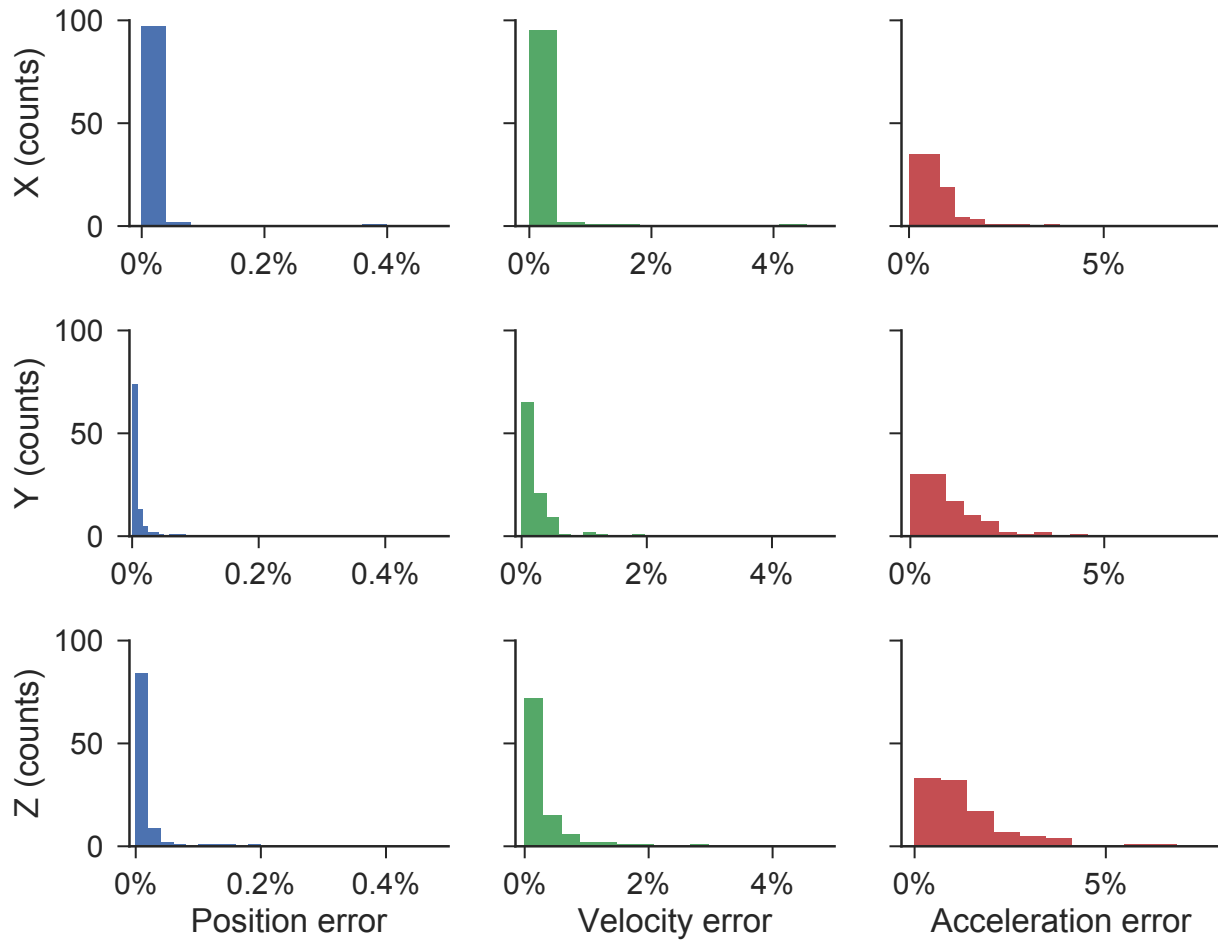


Figure C.34: Histogram of RMSE for the center of mass position, velocity, and acceleration about the X, Y, and Z axes. Position errors are small, while velocity errors are generally less than 1% and acceleration errors are less than 5%.

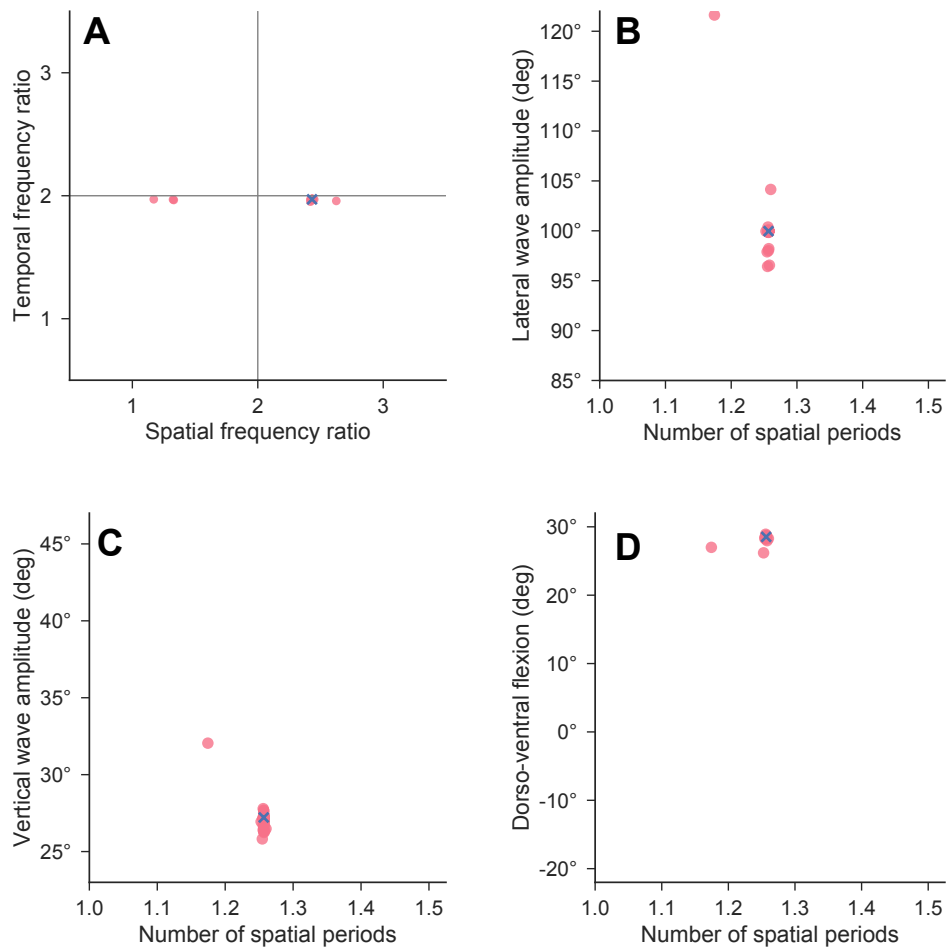


Figure C.35: Effect of missing data on the complex orthogonal decomposition analysis. (A) Temporal frequency ratio is not affected, while spatial frequency ratio is. However, of the 100 degraded time series, only three time series show large errors. (B) Lateral wave amplitude vs. number of spatial periods. (C) Vertical wave amplitude vs. number of spatial periods. (D) Dorsoventral bending angle vs. number of spatial periods. Missing data generally does not have an affect, except for the few trials.

## References

- [8] J. J. Socha, T. O’Dempsey, and M. LaBarbera. A 3-D kinematic analysis of gliding in a flying snake, *Chrysopelea paradisi*. *J. Exp. Biol.* 208 (2005), p. 1817–1833. DOI: 10.1242/jeb.01579.
- [9] J. J. Socha and M. LaBarbera. Effects of size and behavior on aerial performance of two species of flying snakes (*Chrysopelea*). *J. Exp. Biol.* 208 (2005), p. 1835–1847. DOI: 10.1242/jeb.01580.
- [22] J. J. Socha, F. Jafari, Y. Munk, and G. Byrnes. How animals glide: from trajectory to morphology. *Can. J. Zool.* 93 (2015), p. 901–924. DOI: 10.1139/cjz-2014-0013.
- [89] D. A. Winter. *Biomechanics and Motor Control of Human Movement*. John Wiley & Sons, 2009.
- [103] R. Labbe. FilterPy - Kalman filters and other optimal and non-optimal estimation filters in Python. 2017.
- [110] J. Brodziak. *Fitting length-weight relationships with linear regression using the log-transformed allometric model with bias-correction*. Tech. rep. August. 2012, p. 4.

# Appendix D

## Variable-geometry rigid-body model of snake flight

In this appendix, I derive the equations of motion for the variable-geometry rigid-body model for snake flight. Further details are provided in the supplemental information for the manuscript.

### D.1 Dynamic model

Without lack of generality, a rigid body may be considered as a collection of particles defined in a body frame not fixed at the center of mass [111]. The center of mass is a natural choice for most dynamics problems, but due to aerial undulation, its position within the body frame changes continuously. This formulation allows us to define the kinematics of the body relative to a body (co-moving) frame at the center of mass, and then write the equations of motion for how the co-moving frame translates and rotates relative to the inertial frame. We follow Thomson (1986) and Lino (2013) closely in the following derivation.

#### D.1.1 Overview

The snake's body is represented by a collection of  $\mathcal{N}$  point masses, each with mass  $m_i$  and spaced  $ds$  apart along the body. The mass of each body element depends on its location

along the body, as we use the empirical density distribution from snake sectioning.

The center of mass  $\bar{r}$  is given by

$$\bar{r} = \frac{1}{M} \sum_i m_i \vec{r}_i$$

where  $M$  is the total mass,  $\vec{r}_i = \vec{r}(s_i, t)$  from the aerial undulation kinematic equations, and

$$\begin{aligned} s_i &= \frac{ds}{2} + \frac{i-1}{\mathcal{N}}L, \quad i = 1, \dots, \mathcal{N} \\ &= \left[ \frac{ds}{2}, \frac{3}{2}ds, \dots, L - \frac{3}{2}ds, L - \frac{ds}{2} \right] \end{aligned}$$

It follows that

$$m\bar{r} = \sum m_i \vec{r}_i \quad (\text{D.1.1})$$

which can be used to simplify the equations of motion.

The snake kinematics are defined a co-moving reference frame  $\{\hat{b}\}$  given by  $\{\hat{x}_1, \hat{b}_2, \hat{b}_3\} = \{\hat{x}, \hat{y}, \hat{z}\}$ . The co-moving frame translates and rotates relative to the inertial frame  $\{\hat{n}\}$  given by  $\{\hat{n}_1, \hat{n}_2, \hat{n}_3\} = \{\hat{X}, \hat{Y}, \hat{Z}\}$  (figure D.1). The orientation of  $\{\hat{b}\}$  with respect to  $\{\hat{n}\}$  is given by the rotation matrix,

$$\{\hat{b}\} = \mathbf{C}\{\hat{n}\} \quad \{\hat{n}\} = \mathbf{C}^T\{\hat{b}\}$$

The rotation matrix transfers vectors expressed in  $\{\hat{n}\}$  to  $\{\hat{b}\}$ , while the transpose of the rotation matrix,  $\mathbf{C}^T$ , transfers vectors from  $\{\hat{b}\}$  to  $\{\hat{n}\}$ . Therefore, the components of a vector  $\vec{v}$  can be represented in either frame as  ${}^B\vec{v} = \mathbf{C}\vec{v}$ , where the superscript  $B$  indicates the co-moving frame and no superscript indicates a vector expressed in the inertial frame.

The positions, velocities, and accelerations of each mass are known *a priori* in  $\{\hat{b}\}$  from the specified kinematics. However, the position and orientation of the body frame are not known and must be solved for with the dynamic equations. The location of the co-moving frame with reference to the inertial frame is given by  $\vec{R}_o$ . Subsequently, the location of mass element  $i$  in the inertial frame is

$${}^N\vec{R}_i = {}^N\vec{R}_o + \mathbf{C}^T B \vec{r}_i$$

The transport theorem is used to calculate time derivatives in the inertial frame when vectors

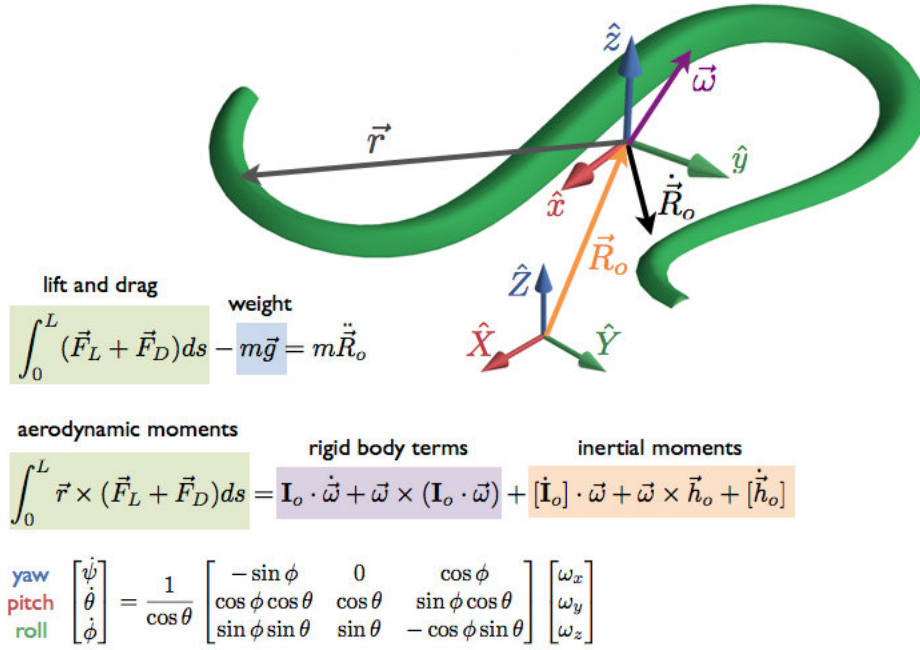


Figure D.1: Schematic of the dynamic model and equations of motion.

are defined in an non-inertial frame. It states

$$\begin{aligned} \dot{\vec{A}} &\equiv \frac{N d}{dt} {}^N \vec{A} = \frac{B d}{dt} {}^B \vec{A} + {}^N \vec{\omega}_{B/N} \times {}^B \vec{A} \\ &= \mathbf{C}^T \frac{B d}{dt} {}^B \vec{A} + {}^N \vec{\omega}_{B/N} \times \mathbf{C}^{TB} \vec{A} \\ &= [\dot{\vec{A}}] + \vec{\omega} \times \vec{A} \end{aligned}$$

where we have introduced the bracket to signify derivatives of body frame vectors expressed in the inertial frame and the angular velocity  $\vec{\omega}$  of  $\{\hat{b}\}$  relative to  $\{\hat{n}\}$ .

Using the transport theorem, the position, velocity, and acceleration of mass element  $i$  defined in the translating and rotating co-moving frame, but expressed in the inertial coordinate system are

$$\begin{aligned} \vec{R}_i &= \vec{R}_o + \vec{r}_i \\ \dot{\vec{R}}_i &= \dot{\vec{R}}_o + [\dot{\vec{r}}_i] + \vec{\omega} \times \vec{r}_i \\ \ddot{\vec{R}}_i &= \ddot{\vec{R}}_o + \dot{\vec{\omega}} \times \vec{r}_i + \vec{\omega} \times (\vec{\omega} \times \vec{r}_i) + 2\vec{\omega} \times [\dot{\vec{r}}_i] + [\ddot{\vec{r}}_i] \end{aligned}$$

which are standard formulas given in dynamics texts [109]. To further clarify our time derivative notation,

$$\vec{r}_i = {}^N\vec{r}_i = \mathbf{C}^T {}^B\vec{r}_i \quad [\dot{\vec{r}}_i] = \mathbf{C}^T \frac{{}^B d}{{}^B dt} \vec{r}_i \quad [\ddot{\vec{r}}_i] = \mathbf{C}^T \frac{{}^B d^2}{{}^B dt^2} \vec{r}_i$$

### D.1.2 Conservation of linear momentum

Newton's law for a single particle states

$$\vec{F}_i = m_i \ddot{\vec{R}}_i,$$

that is, the sum of forces acting on the mass equals the mass of the particle times its acceleration in the inertial frame. Both external forces due to gravity and aerodynamic effects, as well as internal forces act on each particle. However, internal forces do not contribute to the dynamics as they cancel pairwise when summed over the body. The force can be written as

$$\vec{F}_i = \vec{F}_{i,\text{grav}} + \vec{F}_{i,\text{aero}}$$

and are described later. Writing Newton's laws for the entire body with the simplifying steps,

$$\begin{aligned} \sum \vec{F}_i &= \sum m_i \ddot{\vec{R}}_i \\ &= \sum m_i \left[ \ddot{\vec{R}}_o + \dot{\vec{\omega}} \times \vec{r}_i + \vec{\omega} \times (\vec{\omega} \times \vec{r}_i) + 2\vec{\omega} \times \dot{\vec{r}}_i + \ddot{\vec{r}}_i \right] \\ &= \sum m_i \ddot{\vec{R}}_o + \sum -m_i \vec{r}_i \times \dot{\vec{\omega}} + \sum \vec{\omega} \times (\vec{\omega} \times m_i \vec{r}_i) \\ &\quad + 2 \sum \vec{\omega} \times m_i [\dot{\vec{r}}_i] + \sum m_i [\ddot{\vec{r}}_i] \end{aligned}$$

Writing this in detail, Newton's law is

$$\begin{aligned} \sum \vec{F}_{i,\text{grav}} + \sum \vec{F}_{i,\text{aero}} &= \sum m_i \ddot{\vec{R}}_o + \sum -m_i \vec{r}_i \times \dot{\vec{\omega}} + \sum \vec{\omega} \times (\vec{\omega} \times m_i \vec{r}_i) \\ &\quad + 2 \sum \vec{\omega} \times m_i [\dot{\vec{r}}_i] + \sum m_i [\ddot{\vec{r}}_i] \end{aligned} \quad (\text{D.1.2})$$

Simplifying this expression using equation (D.1.1) we have

$$\begin{aligned} \sum \vec{F}_{i,\text{grav}} + \sum \vec{F}_{i,\text{aero}} &= m \ddot{\vec{R}}_o - m \vec{r} \times \dot{\vec{\omega}} + \vec{\omega} \times (\vec{\omega} \times m \vec{r}) \\ &\quad + 2 (\vec{\omega} \times m [\dot{\vec{r}}]) + m [\ddot{\vec{r}}] \end{aligned}$$

### D.1.3 Conservation of angular momentum

Conservation of angular momentum states that the sum of applied moments is equal to the time rate of change of the angular momentum. Internal forces do not change the momentum of the body (Euler's first law), so we only consider gravitational and aerodynamic moments. Writing moments about the co-moving reference frame origin, using the total acceleration in the inertial frame,

$$\sum \vec{M}_i = \sum \vec{r}_i \times m_i \left[ \ddot{\vec{R}}_o + \dot{\vec{\omega}} \times \vec{r}_i + \vec{\omega} \times (\vec{\omega} \times \vec{r}_i) + 2\vec{\omega} \times [\dot{\vec{r}}_i] + [\ddot{\vec{r}}_i] \right] \quad (\text{D.1.3})$$

where

$$\sum \vec{M}_i = \sum \vec{r}_i \times \vec{F}_{i,\text{grav}} + \sum \vec{r}_i \times \vec{F}_{i,\text{aero}}$$

Combining the above expressions, the conservation of angular momentum expression for the variable geometry rigid body is

$$\begin{aligned} \sum \vec{r}_i \times (\vec{F}_{i,\text{grav}} + \vec{F}_{i,\text{aero}}) &= \sum m_i \vec{r}_i \times \ddot{\vec{R}}_o + \sum \vec{r}_i \times (\dot{\vec{\omega}} \times m_i \vec{r}_i) \\ &+ \sum \vec{r}_i \times (\vec{\omega} \times (\vec{\omega} \times m_i \vec{r}_i)) \\ &+ 2 \sum \vec{r}_i \times (\vec{\omega} \times m_i [\dot{\vec{r}}_i]) + \sum \vec{r}_i \times m_i [\ddot{\vec{r}}_i] \end{aligned} \quad (\text{D.1.4})$$

### D.1.4 Alternative derivation of the moment equation

Alternatively, the moment equation can be derived from the angular momentum. Defining the angular momentum of the snake about the co-moving frame origin,

$$\vec{h}_o = \sum \vec{r}_i \times m_i \dot{\vec{R}}_i$$

where  $\dot{\vec{R}}_i$  is the absolute velocity of mass  $m_i$  and all quantities are expressed in the inertial frame. Differentiating the angular momentum,

$$\dot{\vec{h}}_o = \sum \dot{\vec{r}}_i \times m_i \dot{\vec{R}}_i + \sum \vec{r}_o \times m_i \ddot{\vec{R}}_i \quad (\text{D.1.5})$$

Substituting  $\dot{\vec{R}}_i = \dot{\vec{R}}_o + \dot{\vec{r}}_i$  into the first term on the right-hand side above,

$$\begin{aligned}\sum \dot{\vec{r}}_i \times m_i \dot{\vec{R}}_i &= \sum \dot{\vec{r}}_i \times m_i (\dot{\vec{R}}_o + \dot{\vec{r}}) \\ &= \sum \dot{\vec{r}}_i \times m_i \dot{\vec{R}}_o \\ &= -\dot{\vec{R}}_o \times m \dot{\vec{r}}\end{aligned}$$

The second term of equation (D.1.5) is the sum of external moments acting on the snake's body about the co-moving frame origin,  $\vec{M}_o$ . Rearranging (D.1.5),

$$\vec{M}_o = \dot{\vec{h}}_o + \dot{\vec{R}}_o \times m \dot{\vec{r}}$$

Substituting equation (D.1.5) into the above expression,

$$\begin{aligned}\vec{M}_o &= -\dot{\vec{R}}_o \times m \dot{\vec{r}} + \sum \vec{r}_i \times m_i \ddot{\vec{R}}_i + \dot{\vec{R}}_o \times m \dot{\vec{r}} \\ &= \sum \vec{r}_i \times m_i \ddot{\vec{R}}_i\end{aligned}$$

which is the same expression as in equation (D.1.3) after substituting in the total acceleration.

### D.1.5 Matrix formulation

The six, coupled, non-linear equations (D.1.2) and (D.1.4) above are more easily solved by arranging them in a matrix form of

$$\mathbf{M}(\vec{r}_i) \dot{\mathbf{x}} + \mathbf{N}(\mathbf{x}, \mathbf{r}, \theta) = \mathbf{0} \quad (\text{D.1.6})$$

where  $\mathbf{M}$  and  $\mathbf{N}$  have been written to show explicit dependence on our state vector  $\mathbf{x}$ , its time derivative  $\dot{\mathbf{x}}$ , the kinematics vector  $\mathbf{r}$ , and the body orientation  $\theta$ . These dependencies in detail are

$$\begin{aligned}\mathbf{x} &= [\dot{R}_{o,X}, \dot{R}_{o,Y}, \dot{R}_{o,Z}, \omega_X, \omega_Y, \omega_Z] \\ \dot{\mathbf{x}} &= [\ddot{R}_{o,X}, \ddot{R}_{o,Y}, \ddot{R}_{o,Z}, \dot{\omega}_X, \dot{\omega}_Y, \dot{\omega}_Z] \\ \mathbf{r} &= [\vec{r}_i, [\dot{\vec{r}}_i], [\ddot{\vec{r}}_i]]\end{aligned}$$

To formulate the matrix expression, we begin by defining the skew-symmetric cross-product matrix

$$\vec{A} \times \vec{B} = \tilde{A}\vec{B} = \begin{bmatrix} 0 & -A_z & A_y \\ A_z & 0 & -A_x \\ -A_y & A_x & 0 \end{bmatrix} \begin{bmatrix} B_x \\ B_y \\ B_z \end{bmatrix}$$

which can be rearranged by reversing the cross-product as

$$\vec{A} \times \vec{B} = -\vec{B} \times \vec{A} = \tilde{B}^T \vec{A}$$

We will now analyze each term in equations (D.1.2) and (D.1.4) related to a  $\dot{\mathbf{x}}$  and determine the  $3 \times 3$  submatrices of  $\mathbf{M}(\vec{r}_i)$ :

$$\sum m_i \ddot{\vec{R}}_o = \sum m_i \begin{bmatrix} 1 & 0 & 0 \\ 0 & 1 & 0 \\ 0 & 0 & 1 \end{bmatrix} \ddot{\vec{R}}_o \quad (\text{D.1.7})$$

$$\sum \dot{\vec{\omega}} \times m_i \vec{r}_i = \sum m_i \begin{bmatrix} 0 & -r_{i,Z} & r_{i,Y} \\ r_{i,Z} & 0 & -r_{i,X} \\ -r_{i,Y} & r_{i,X} & 0 \end{bmatrix}^T \dot{\vec{\omega}} \quad (\text{D.1.8})$$

$$\sum m_i \vec{r}_i \times \ddot{\vec{R}}_o = \sum m_i \begin{bmatrix} 0 & -r_{i,Z} & r_{i,Y} \\ r_{i,Z} & 0 & -r_{i,X} \\ -r_{i,Y} & r_{i,X} & 0 \end{bmatrix} \ddot{\vec{R}}_o \quad (\text{D.1.9})$$

$$\sum \vec{r}_i \times (\dot{\vec{\omega}} \times m_i \vec{r}_i) = \sum m_i \begin{bmatrix} 0 & -r_{i,Z} & r_{i,Y} \\ r_{i,Z} & 0 & -r_{i,X} \\ -r_{i,Y} & r_{i,X} & 0 \end{bmatrix} \begin{bmatrix} 0 & -r_{i,Z} & r_{i,Y} \\ r_{i,Z} & 0 & -r_{i,X} \\ -r_{i,Y} & r_{i,X} & 0 \end{bmatrix}^T \dot{\vec{\omega}} \quad (\text{D.1.10})$$

where cross-product matrices have been transposed to reverse the cross product so unknown quantities are on the right-hand side. The above matrix elements are embedded in  $\mathbf{M}$  in the upper-left, upper-right, lower-left, and lower-right quadrants, respectively. The elements of  $\mathbf{N}$ , a  $6 \times 1$  column vector, are found from the remaining terms in (D.1.2) and (D.1.4). Writing these in detail, we have

$$\mathbf{N}_{1,2,3,4} = \sum \vec{\omega} \times (\vec{\omega} \times m_i \vec{r}_i) + 2 \sum \vec{\omega} \times m_i [\dot{\vec{r}}_i] + \sum m_i [\ddot{\vec{r}}_i] - \sum \vec{F}_i^a \quad (\text{D.1.11})$$

and for the moment equation

$$\begin{aligned} \mathbf{N}_{5,6,7,8} = & \sum \vec{r}_i \times (\vec{\omega} \times (\vec{\omega} \times m_i \vec{r}_i)) + 2 \sum \vec{r}_i \times (\vec{\omega} \times m_i [\dot{\vec{r}}_i]) + \\ & + \sum \vec{r}_i \times m_i [\ddot{\vec{r}}_i] - \sum \vec{r}_i \times \vec{F}_i^a \end{aligned} \quad (\text{D.1.12})$$

### D.1.6 Initial conditions

We now have to solve twelve equations  $\dot{\vec{R}}_o$ ,  $\ddot{\vec{R}}_o$ ,  $\dot{\vec{\omega}}$ , and  $\dot{\vec{\theta}}$  given twelve initial conditions  $\vec{R}_o(0)$ ,  $\dot{\vec{R}}_o(0)$ ,  $\vec{\theta}(0)$ , and  $\vec{\omega}(0)$ .

#### Angular velocity

Initial conditions for the angular velocity  $\vec{\omega}(0)$  can be specified manually or from the initial Euler angle rates  $(\dot{\psi}, \dot{\theta}, \dot{\phi})$ . The body-axis components of the absolute angular velocity in terms of Euler angle rates are [109]

$$\vec{\omega}_o = \mathbf{C}^T \begin{bmatrix} -\sin \theta_o & 0 & 1 \\ \cos \theta_o \sin \phi_o & \cos \phi_o & 0 \\ \cos \theta_o \cos \phi_o & -\sin \phi_o & 0 \end{bmatrix} \begin{bmatrix} \dot{\psi}_o \\ \dot{\theta}_o \\ \dot{\phi}_o \end{bmatrix}$$

#### Angular momentum

Zero angular momentum “jumps” in the co-moving frame are specified using offset angle  $\phi$  in the curvature definition. We constrain the angular momentum in the co-moving frame to be zero at  $t = 0$ ,

$${}^B \vec{h}_o(t = 0) = \sum {}^B \vec{r}_i \times m_i \frac{{}^B d}{{}^B dt} {}^B \vec{r}_i = 0$$

Because the snake is planar, adjusting  $\phi$  such that  $\hat{z}$  component of  ${}^B \vec{h}_o$  ensure we have selected a portion of the kinematics with zero angular momentum. If  ${}^B \vec{h}_o$  is not zero, the simulated trajectory would be biased to a yaw turn. Additionally, if gravity and aerodynamic forces were set to zero, and all other initial conditions were set to zero, the snake would not return to the initial yaw angle after one undulation cycle. We specify  $\phi$  using a Newton root finding method for the  $\hat{z}$  component of  ${}^B \vec{h}_o$ .

### D.1.7 General form of Euler's equation

The moment equations (D.1.4) can be simplified such that they take-on a more traditional form from rigid body dynamics [111, 112]. The moment equation,

$$\begin{aligned}\vec{M}_o &= \sum m_i \vec{r}_i \times \ddot{\vec{R}}_o + \sum \vec{r}_i \times (\dot{\vec{\omega}} \times m_i \vec{r}_i) + \sum \vec{r}_i \times (\vec{\omega} \times (\vec{\omega} \times m_i \vec{r}_i)) \\ &\quad + 2 \sum \vec{r}_i \times (\vec{\omega} \times m_i [\dot{\vec{r}}_i]) + \sum \vec{r}_i \times m_i [\ddot{\vec{r}}_i]\end{aligned}$$

can be simplified by using the definition of center of mass and by introducing the standard Euler rigid body terms with the inertia diadic terms [111]

$$\begin{aligned}\mathbf{I}_o \cdot \dot{\vec{\omega}} &= \sum \vec{r}_i \times (\dot{\vec{\omega}} \times m_i \vec{r}_i) \\ \vec{\omega} \times (\mathbf{I}_o \cdot \vec{\omega}) &= \sum \vec{r}_i \times (\vec{\omega} \times (\vec{\omega} \times m_i \vec{r}_i))\end{aligned}$$

such that the second and third terms on the right-hand side of the moment equation are

$$\begin{aligned}\vec{M}_o &= -\ddot{\vec{R}}_o \times m \vec{r} + \mathbf{I}_o \cdot \dot{\vec{\omega}} + \vec{\omega} \times (\mathbf{I}_o \cdot \vec{\omega}) \\ &\quad + 2 \sum \vec{r}_i \times (\vec{\omega} \times m_i [\dot{\vec{r}}_i]) + \sum \vec{r}_i \times m_i [\ddot{\vec{r}}_i]\end{aligned}$$

The variable-geometry terms,

$$VGT = 2 \sum \vec{r}_i \times (\vec{\omega} \times m_i [\dot{\vec{r}}_i]) + \sum \vec{r}_i \times m_i [\ddot{\vec{r}}_i]$$

are simplified [112] by adding and subtracting

$$\sum [\dot{\vec{r}}_i] \times (\vec{\omega} \times \vec{r}_i)$$

and splitting the first term in the VGT expression above. We obtain,

$$VGT = \sum [\dot{\vec{r}}_i] \times (\vec{\omega} \times \vec{r}_i) - \sum [\dot{\vec{r}}_i] \times (\vec{\omega} \times \vec{r}_i) + \quad (D.1.13)$$

$$\sum \vec{r}_i \times (\vec{\omega} \times m_i [\dot{\vec{r}}_i]) + \sum \vec{r}_i \times (\vec{\omega} \times m_i [\dot{\vec{r}}_i]) + \sum \vec{r}_i \times m_i [\ddot{\vec{r}}_i] \quad (D.1.14)$$

The first and third terms are combined into the identity

$$[\dot{\mathbf{I}}_o] \cdot \vec{\omega} = \sum [\dot{\vec{r}}_i] \times (\vec{\omega} \times \vec{r}_i) + \sum \vec{r}_i \times (\vec{\omega} \times m_i [\dot{\vec{r}}_i])$$

where the inertia dyad is

$$\mathbf{I}_o = \sum m_i \begin{bmatrix} r_{i,Y}^2 + r_{i,Z}^2 & -r_{i,X}r_{i,Y} & -r_{i,X}r_{i,Z} \\ -r_{i,X}r_{i,Y} & r_{i,X}^2 + r_{i,Z}^2 & -r_{i,Y}r_{i,Z} \\ -r_{i,X}r_{i,Z} & -r_{i,Y}r_{i,Z} & r_{i,X}^2 + r_{i,Y}^2 \end{bmatrix}$$

and the inertial dynamic time derivative is

$$[\dot{\mathbf{I}}_o] = \sum m_i \begin{bmatrix} 2(r_{i,Y}\dot{r}_{i,Y} + r_{i,Z}\dot{r}_{i,Z}) & -(\dot{r}_{i,X}r_{i,Y} + r_{i,X}\dot{r}_{i,Y}) & -(\dot{r}_{i,X}r_{i,Z} + r_{i,X}\dot{r}_{i,Z}) \\ -(\dot{r}_{i,X}r_{i,Y} + r_{i,Y}\dot{r}_{i,Y}) & 2(r_{i,X}\dot{r}_{i,X} + r_{i,Z}\dot{r}_{i,Z}) & -(\dot{r}_{i,Y}r_{i,Z} + r_{i,Y}\dot{r}_{i,Z}) \\ -(\dot{r}_{i,X}r_{i,Z} + r_{i,X}\dot{r}_{i,Z}) & -(\dot{r}_{i,Y}r_{i,Z} + r_{i,Y}\dot{r}_{i,Z}) & 2(r_{i,X}\dot{r}_{i,X} + r_{i,Y}\dot{r}_{i,Y}) \end{bmatrix}$$

Switching the cross product of the second term of (D.1.13) and combining the above identity,

$$VGT = [\dot{\mathbf{I}}_o] \cdot \vec{\omega} + \sum (\vec{\omega} \times \vec{r}_i) \times [\dot{\vec{r}}_i] + \sum \vec{r}_i \times (\vec{\omega} \times m_i[\dot{\vec{r}}_i]) + \sum \vec{r}_i \times m_i[\ddot{\vec{r}}_i] \quad (\text{D.1.15})$$

The remaining three terms can be recognized by recognizing the inertial derivative of [112]

$$\vec{\gamma} = \sum \vec{r}_i \times m_i[\dot{\vec{r}}_i]$$

Therefore, the general form of Euler's equation is

$$\vec{M}_o = -\ddot{\vec{R}}_o \times m\vec{r} + \mathbf{I}_o \cdot \dot{\vec{\omega}} + \vec{\omega} \times (\mathbf{I}_o \cdot \vec{\omega}) + [\dot{\mathbf{I}}_o] \cdot \vec{\omega} + \vec{\gamma} \quad (\text{D.1.16})$$

The first term is zero if the origin of the co-moving frame is located at the center of mass. Furthermore, we can use the definition of the angular momentum in the co-moving frame to arrive at the expression in the main text,

$$\vec{M}_o = \mathbf{I}_o \cdot \dot{\vec{\omega}} + \vec{\omega} \times (\mathbf{I}_o \cdot \vec{\omega}) + [\dot{\mathbf{I}}_o] \cdot \vec{\omega} + \vec{\omega} \times \vec{h}_o + [\dot{\vec{h}}_o] \quad (\text{D.1.17})$$

where

$$\vec{h}_o = \int_0^L \vec{r} \times \rho(s)\dot{\vec{r}}ds \quad (\text{D.1.18})$$

$$[\dot{\vec{h}}_o] = \int_0^L \vec{r} \times \rho(s)\ddot{\vec{r}}ds \quad (\text{D.1.19})$$

The translational equations of motion are

$$\int_0^L (d\vec{F}_L + d\vec{F}_D) ds - m\vec{g} = m\ddot{\vec{R}}_o \quad (\text{D.1.20})$$

### D.1.8 Center of pressure

The center of pressure is the location where the resultant aerodynamic force acts, i.e. the vector sum of lift and drag integrated over the simulated snake body. We include the procedure to calculate the center of pressure here, although it was not included in the analysis presented in the main dissertation. The aerodynamic moment is

$$\vec{M}_{\text{aero}} = \sum \vec{r}_i \times \vec{F}_{i,\text{aero}} = \vec{p} \times \vec{F}_{\text{aero,total}} \quad (\text{D.1.21})$$

where  $\vec{p}$  is the position of the center of pressure. The line of action of the total aerodynamic force, which is simply the vector sum of lift and drag along the snake's body, is easily determined. The center of pressure determines where along the line of action the vector is placed and requires additional constraints. We consider two possibilities. In the first, the center of pressure is located the shortest distance from the center of mass. This constraint is

$$p_X F_X + p_Y F_Y + p_Z F_Z = 0$$

where all quantities above are expressed in the inertial frame. In the other formulation, we require the center of pressure to lie within the plane of the snake, i.e.  $p_z = 0$ . The center of pressure is calculated using a least-squares solution given the four equations (the three equations in (D.1.21) and one constraint equation).

The moment used in the center of pressure calculations is the aerodynamic moment with the portion of the moment parallel to the resultant aerodynamic force removed. That is,

$$\vec{M} = \vec{M}_{\text{aero}} - \vec{M}_{\parallel} \quad (\text{D.1.22})$$

where  $\vec{M}_{\parallel}$  is found by projecting the aerodynamic moment along the force unit vector,

$$\hat{f} = \frac{\vec{F}_{\text{aero,total}}}{|\vec{F}_{\text{aero,total}}|}$$

using

$$\vec{M}_{\parallel} = (\vec{M}_{\text{aero}} \cdot \hat{f}) \hat{f}$$

The center of pressure lying closest to the origin is found with a least-squares solution for  $\vec{p}$  given

$$\begin{bmatrix} M_X \\ M_Y \\ M_Z \\ 0 \end{bmatrix} = \begin{bmatrix} 0 & F_Z & -F_Y \\ -F_Z & 0 & F_X \\ F_Y & -F_X & 0 \\ F_X & F_Y & F_Z \end{bmatrix} \begin{bmatrix} p_X \\ p_Y \\ p_Z \end{bmatrix} \quad (\text{D.1.23})$$

where all quantities are calculated with values expressed in the inertial frame and the components of the moment and total aerodynamic force are explicitly written.

The center of pressure lying in the  $\hat{x}$ - $\hat{y}$  plane of the co-moving frame, the plane in which we prescribe the planar body kinematics, is found from a least-squares solution to

$$\begin{bmatrix} M_x \\ M_y \\ M_z \\ 0 \end{bmatrix} = \begin{bmatrix} 0 & F_z & -F_y \\ -F_z & 0 & F_x \\ F_y & -F_x & 0 \\ 0 & 0 & 1 \end{bmatrix} \begin{bmatrix} p_x \\ p_y \\ p_z \end{bmatrix} \quad (\text{D.1.24})$$

where all quantities are must be expressed in the co-moving frame.

## D.2 Effects of snake size and undulation frequency on glide dynamics

We performed a parametric sweep of body shape (along the observed diagonal within the horizontal wave shape space of Chapter 3. The analysis performed in the modeling chapter consisted of a snake with a length of 70 cm, with a mass, average density, and maximum chord length determined from the scaling relationships presented in Appendix C.

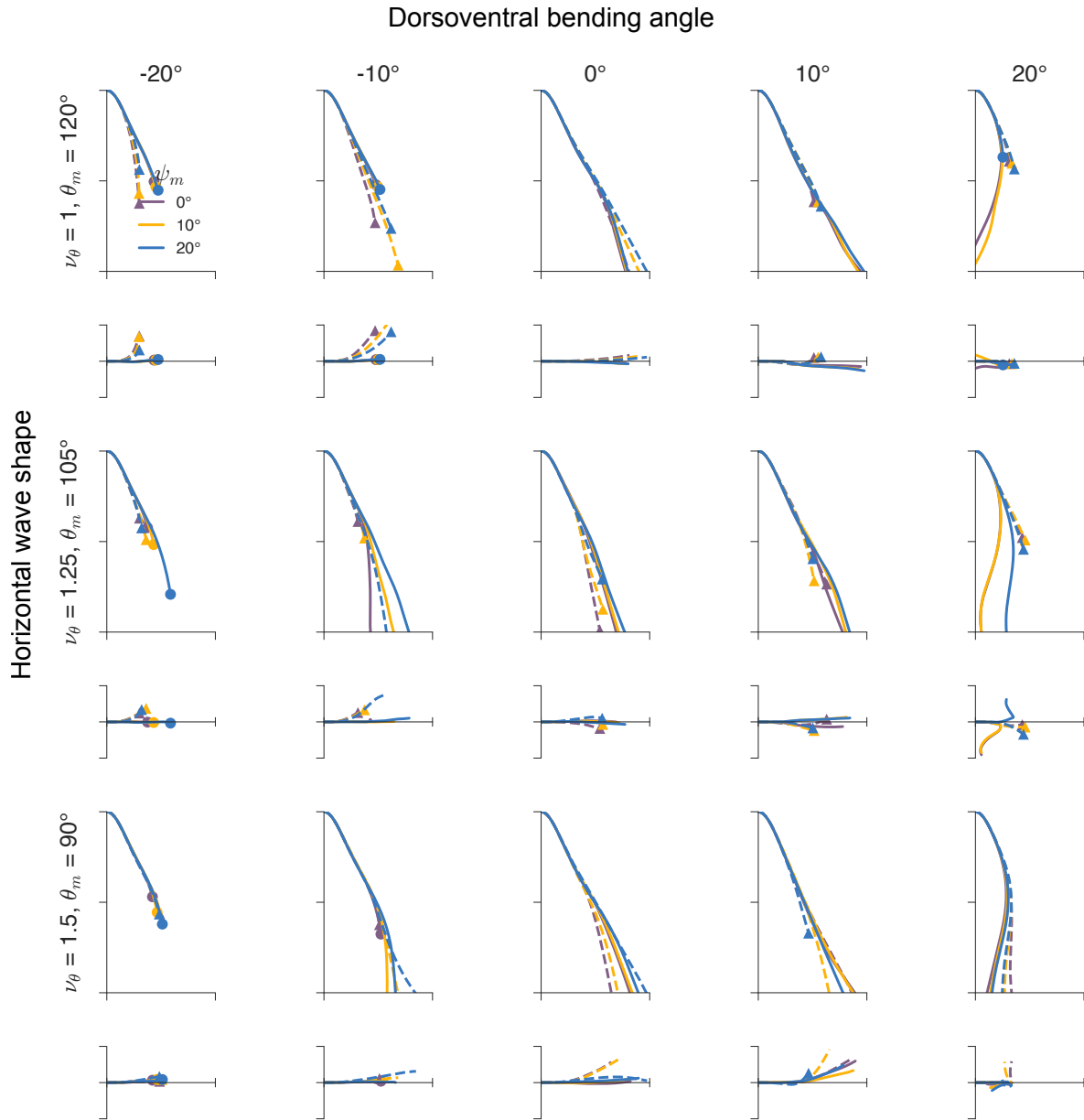


Figure D.2: Effect of dorsoventral bending angle,  $d_\psi$ , and vertical wave amplitude,  $\psi_m$ , on center of mass motion. The three rows are combinations of number of body waves,  $\nu_\theta$ , and horizontal wave amplitude,  $\theta_m$ , along the observed diagonal of the horizontal wave shape space. The top row within each horizontal wave shape is the side view of  $Z$  vs.  $Y$  motion of the center of mass, and the bottom row is the top view of  $X$  vs.  $Y$ .

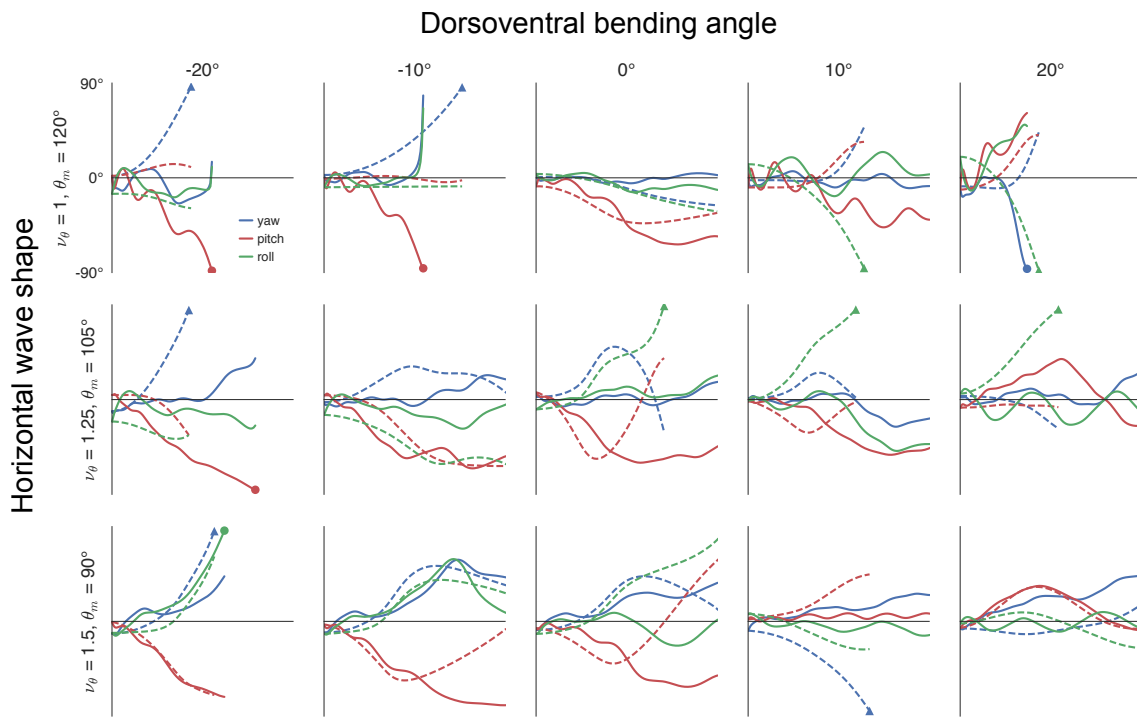


Figure D.3: Effect of dorsoventral bending angle,  $d_\psi$ , and vertical wave amplitude,  $\psi_m$ , on yaw, pitch, and roll Euler angles. This is for  $\nu_\theta=1.25$  and  $\theta_m = 105^\circ$ .

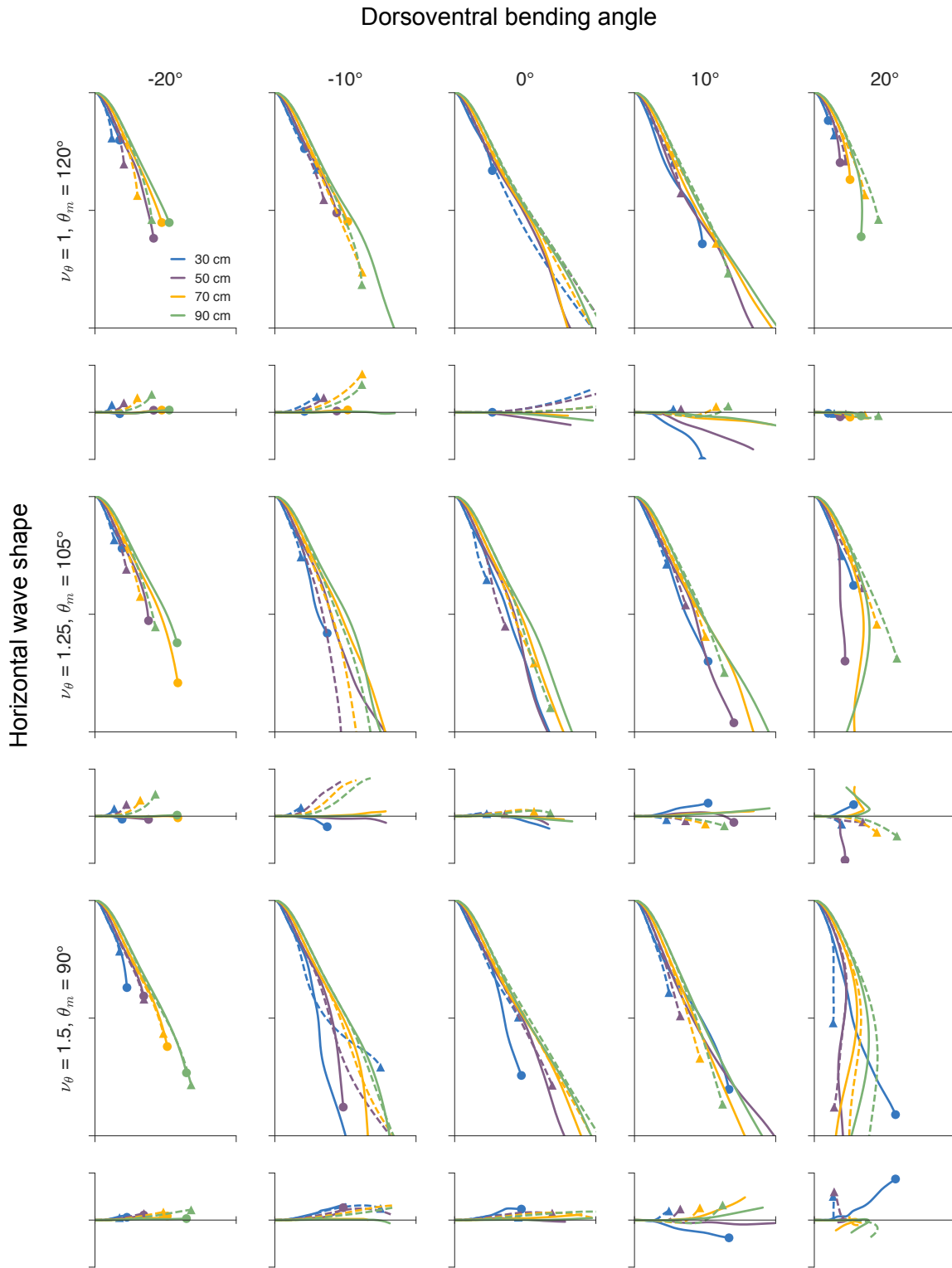


Figure D.4: Effect of snake length and dorsoventral bending angle on center of mass motion.

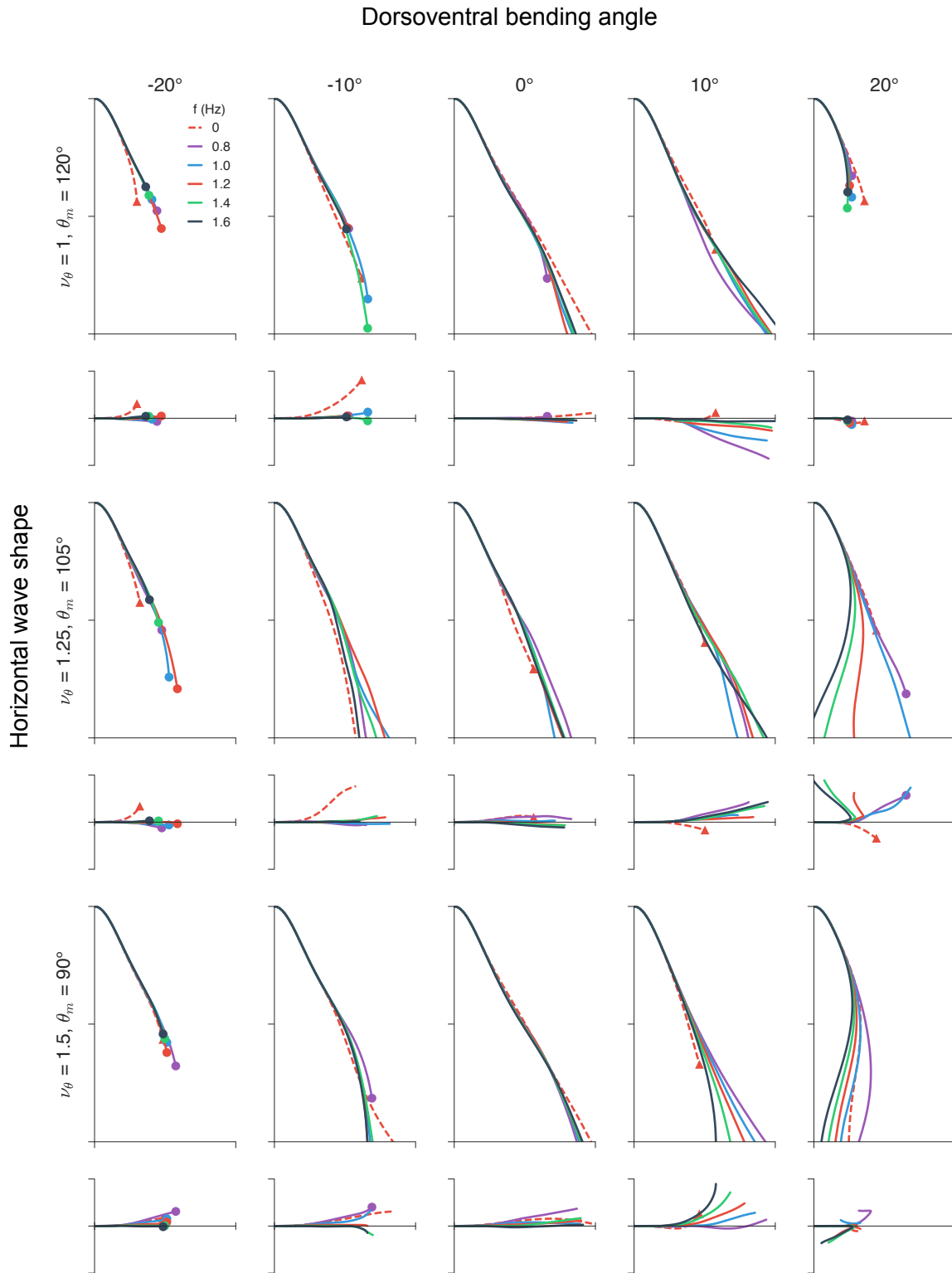


Figure D.5: Effect of undulation frequency and dorsoventral bending angle on center of mass motion.

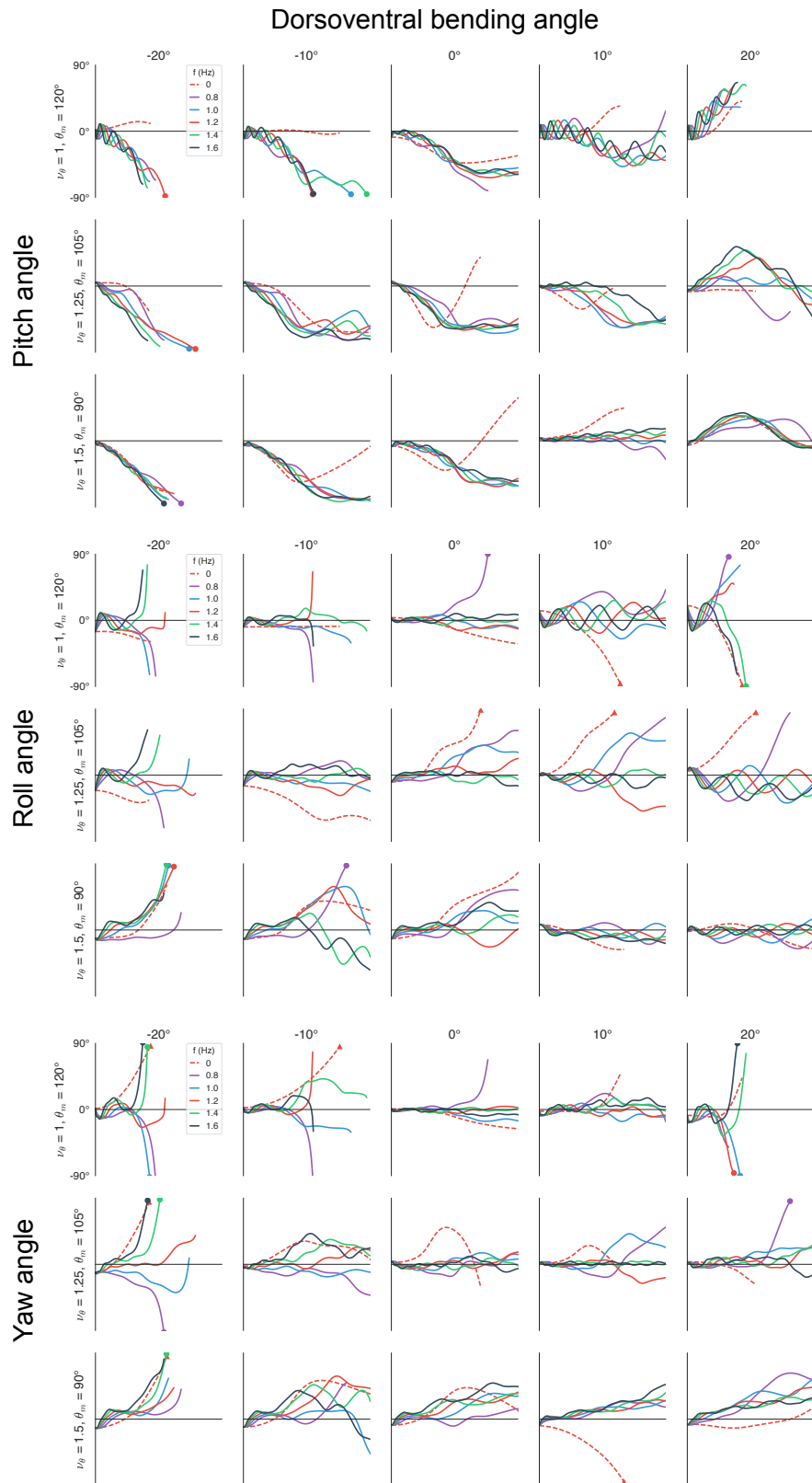


Figure D.6: Effect of undulation frequency and dorsoventral bending angle on pitch, roll, and yaw Euler angles.

### **D.3 Effects of corrected lift and drag forces on glide dynamics and stability**

In Chapter 4, we found that quasi-steady theory under-predicted the lift force and over-predicted the drag force. I applied the lift and drag multipliers (figure 4.6B) to the model of snake snake flight to determine if our conclusions were valid given modified forces. Our conclusions do hold. The modified forces result in the simulated snake covering more horizontal distance, but the main effects of horizontal wave shape, vertical bending angle amplitude, and dorsoventral bending hold. The model results are given below for the key figures, with the uncorrected forces given by “L and D” and the corrected forces given by “1.36L and 0.6D”. The multipliers were the average for the three individuals that gave the greatest number of glides.

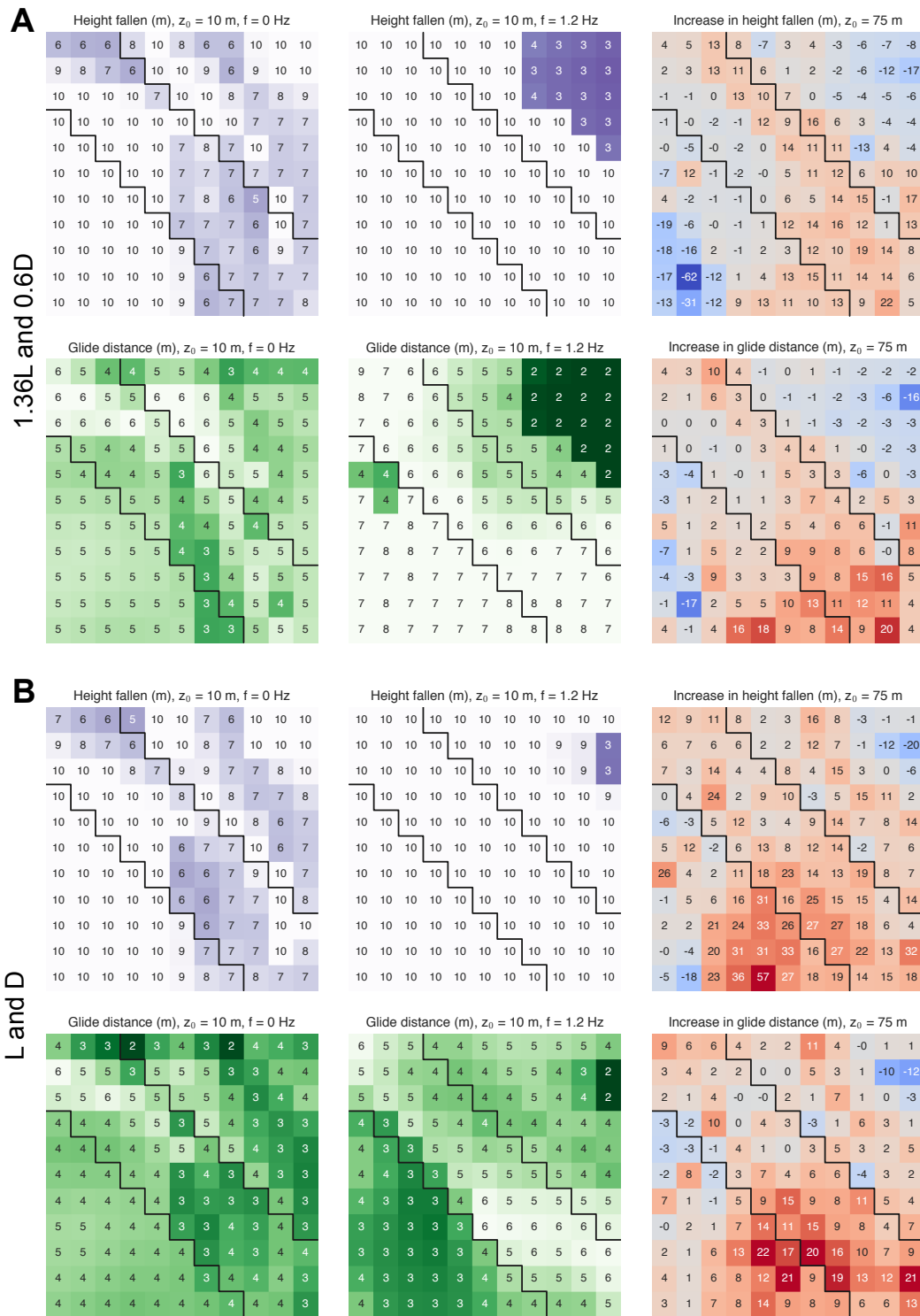


Figure D.7: Effect of corrected forces on glide distance and glide distance.

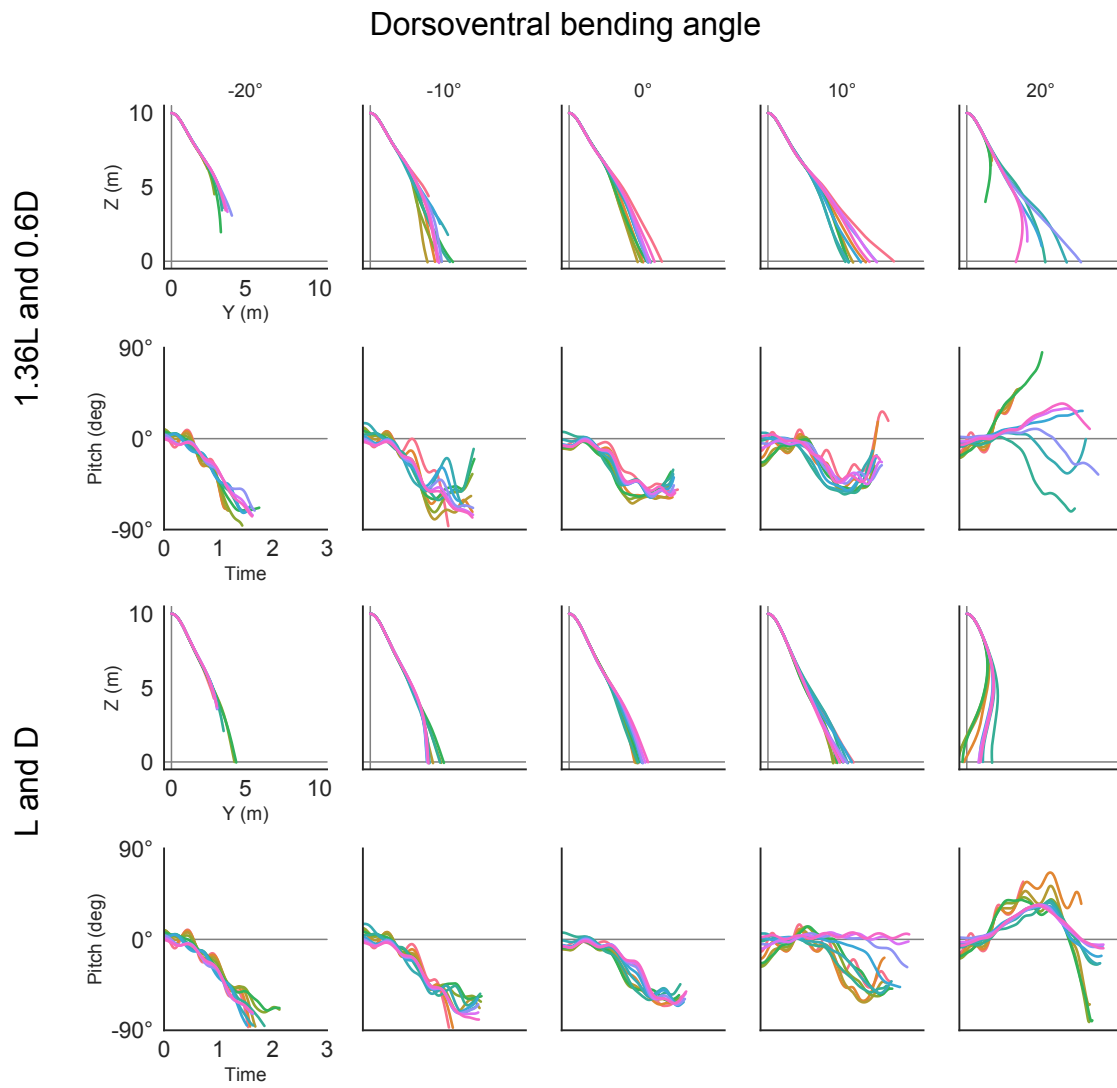


Figure D.8: Effect of corrected forces and dorsoventral bending on glide performance and pitch dynamics for a vertical wave amplitude of  $\psi_m=20^\circ$ .

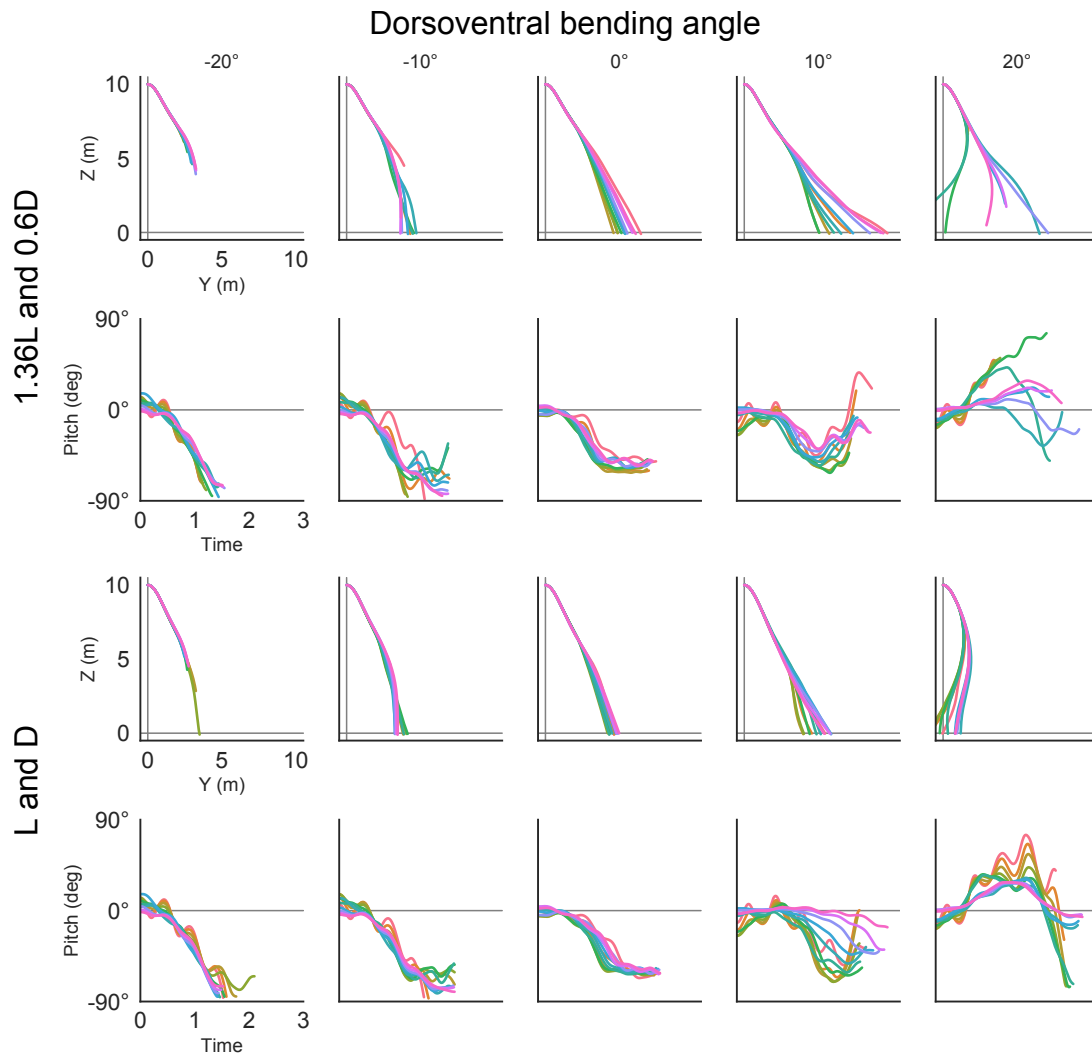


Figure D.9: Effect of corrected forces and dorsoventral bending on glide performance and pitch dynamics for a vertical wave amplitude of  $\psi_m=10^\circ$ .

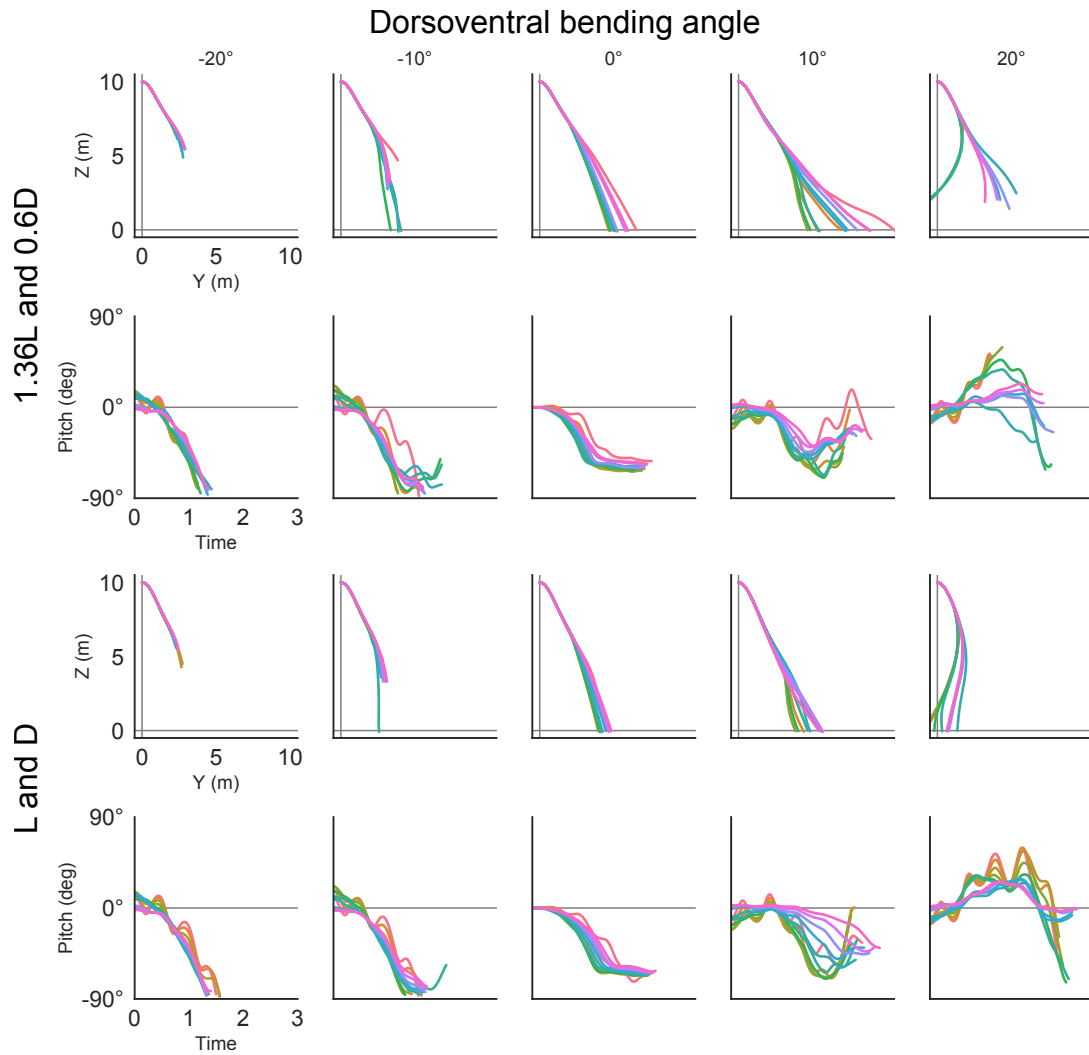


Figure D.10: Effect of corrected forces and dorsoventral bending on glide performance and pitch dynamics for a vertical wave amplitude of  $\psi_m=0^\circ$ .

## References

- [109] D. T. Greenwood. *Advanced Dynamics*. Cambridge University Press, 2006.
- [111] W. T. Thomson. *Introduction to Space Dynamics*. Dover, 1986.
- [112] M. F.G.d. M. Lino. Design and Attitude Control of a Satellite with Variable Geometry. PhD thesis. Técnico Lisboa, 2013.